Towards Quantitative Intra-Nuclear Dose Mapping of Auger Emitting Radionuclides used for Targeted Radiotherapy

A thesis submitted for the degree of

Doctor of Philosophy

University of Oxford

Georgina L. Royle

CRUK/MRC Oxford Institute for Radiation Oncology

Trinity College, University of Oxford
Trinity Term, 2016

Abstract

Towards Quantitative Intra-Nuclear Dose Mapping of Auger Emitting Radionuclides used for Targeted Radiotherapy

Georgina L. Royle, Trinity College
Submitted for the degree of Doctor of Philosophy,
Trinity Term 2016

Targeted radiotherapy (TRT) is a technique which allows for individual cancer cells to be targeted by radiation. However, there is variation in uptake at the whole body, organ, cellular and subcellular levels. This distribution affects the biological efficacy of the TRT agents. To address this problem, novel techniques have been developed and demonstrated. These aim to provide quantitative information about the spatial distribution of Auger electron (AE) emitting radiopharmaceuticals at the subcellular level.

Two methods have been developed. The first, photoresist autoradiography (PAR), uses photoresists as an autoradiography substrate, and the second uses microautoradiography (MAR) and a transmission electron microscope (TEM). The techniques have been demonstrated using the AE emitter indium-111.

Firstly, PAR is demonstrated using poly (methyl methacrylate) (PMMA). Photoresists were exposed to indium-111 which had been internalised into cells, and the photoresists were analysed using atomic force microscopy (AFM). The technique has a theoretical resolution in the nanometre range and was able to demonstrate cellular patterns on the micron scale. To gain quantitative information, the photoresist response (depth of pattern) was calibrated as a function of electron fluence and a model of the patterns was created. Combining the calibration data with the point source model allowed the position and intensity of the internalised source terms to be estimated using the PAR method.

Secondly, a technique for electron microscope-microautoradiography (EM-MAR) was developed. The processing conditions of the MAR technique were determined and staining techniques developed, to produce high quality TEM micrographs. A time course experiment showed the distribution and variation in the uptake of the radiopharmaceutical at the cellular level.

Both techniques are able to provide information about the subcellular distribution of the radioactivity at a higher resolution than current techniques. Both enable the collection of information which can be used in microdosimetric calculations.

Declaration

This thesis is a presentation of my original research work. Wherever contributions of others are involved, every effort is made to indicate this clearly.

Work Previously Accepted for Submission

Figure 4.1: Electron beam calibration, Chapter 4, Page 98, has been adapted from previous work submitted for the degree of Master of Engineering, at the University of Oxford (Royle, 2012).

Contributions of Others

Experimental work and preparation of Figure 4.14: A photoresist exposed to a high electron beam dose, Chapter 4, page 114, was carried out by Dr Sverre Myhra, Department of Materials, University of Oxford.

Part of the experimental work for Table 3.1: The number of epidermal growth factor receptors per cell, Chapter 3, 85 , the determination of the amount of protein per cell by a bicinchoninic assay was carried out by Mrs Sarah Able, Department of Oncology, University of Oxford.

Statistics calculated using a linear mixed effects model, Tables 5.1 and 5.2 page 149 and Table 5.3 page 150**Error! Bookmark not defined.** (Chapter 5, Section 4.2.2) were carried out by Dr Cristiana Kartsonaki, Nuffield Department of Population Health, University of Oxford.

Modelling of the indium-111 in appendix 1, page 237 was carried out by Dr Nadia Falzone, Department of Oncology, University of Oxford.

Acknowledgements

First and foremost, I would like to thank my supervisors Professor Katherine Vallis and Dr Nadia Falzone and to express thanks to Dr Sverre Myhra for being the final member of my thesis committee. Thank you for giving me the patience to develop my own ideas and the help and inspiration when needed.

I would like to thank the people who supported me in this project from across the University: Drs Radka Chakalova, Alison Crossley and Colin Johnson in the Department of Materials and Drs Errin Johnson and Anna Pielach at the Dunn School of Pathology, without whom this project would not have been possible. I would also like to gratefully thank Dr Cristiana Kartsonaki for help with statistical work and Dr Danny Allen for help with Matlab. I would like to thank those who gave me support with my disabilities, Marion Frostick and David Human.

I would like to thank and apologise to the members of the Vallis group past and present, particularly Sarah Able, for putting up with my odd requests and Anne-Marie Honeyman-Tafa for her practical advice. Thanks also to those in the department, especially Dr Graham Brown and Mick Woodcock, for technical help, as well as the graduate supervisory team: Professor Nicola Sibson and Associate Professor Ester Hammond for guidance as Directors of Graduate Studies and Dr Sarah Norman and Katy Higgins for administrative assistance. Thank you also to Dr Mark Hill and Associate Professor Mike Partridge for assessing my transfer and confirmation.

I could not have completed my time in Oxford without all those friends who have supported me throughout the many years in Oxford. There were those who were in it for the short haul and those who decided to take a slightly more protracted path. Your distractions, insights and cooking will remain some of my fondness memories of my time in Oxford.

Thanks to my parents, who provided encouragement and support but allowed me to develop into my own person and make my own choices. And finally, to Matt, for showing me that there is life outside the bubble and without whom this journey would have felt far more lonely. Thank you.

List of Publications

Papers

Internalization of Auger electron-emitting isotopes into cancer cells: A method for spatial distribution determination of equivalent source terms
ROYLE, G., FALZONE, N., CHAKALOVA, R., VALLIS, K. A. & MYHRA, S.
International Journal of Radiation Biology, 92, 633-640.
2016

Spatial distribution of Auger electrons emitted from internalised radionuclides in cancer cells: the photoresist autoradiography (PAR) method
ROYLE, G., MYHRA, S., CHAKALOVA, R., VALLIS, K. A. & FALZONE, N.
Radiation Protection Dosimetry, 166, 1-5.
2015

Talks

PMMA Photoresists for Nanoscale Quantifiable Dosimetry for Auger-Electron Emitting Radiotherapeutics
ROYLE, G., MYHRA, S., CHAKALOVA, R., VALLIS, K. A. & FALZONE, N
MICROS 2013 - 16th International Symposium on Microdosimetry
20–25 October 2013, Treviso, Italy

Posters

A 3-D model to determine the spatial distribution of internalized radioisotopes into individual cancer cells
ROYLE, G., FALZONE, N., CHAKALOVA, R., VALLIS, K. A. & MYHRA, S.,
National Cancer Research Institute Caner Conference, 2015
1–4 November 2015, Liverpool, UK

A novel quantitative method in determining the spatial distribution of Auger electron-emitting radiopharmaceuticals used in targeted radiotherapy
ROYLE, G., MYHRA, S., CHAKALOVA, R., VALLIS, K. A. & FALZONE, N
Society of Nuclear Medicine and Molecular Imaging, Annual Meeting 2014
7–11 June 2014, St Louis, USA

A Novel Quantitative Method using PMMA Photoresists to Determine the Spatial Distribution of Auger Electron-Emitting Radiotherapeutics
ROYLE, G., MYHRA, S., CHAKALOVA, R., VALLIS, K. A. & FALZONE, N
Association of Radiation Research annual meeting, 2014
29 June–2 July 2014, Brighton, UK

Prizes

Determining the sub-cellular distribution of internalized source terms from radiopharmaceuticals, a 3-D model
ROYLE, G., FALZONE, N., CHAKALOVA, R., VALLIS, K. A. & MYHRA, S.,
3rd CRUK/MRC Oxford Institute for Radiation Oncology Symposium
10 & 11 September 2015, Oxford, UK
Won Best Poster

A Novel Quantitative Method using PMMA Photoresists to Determine the Spatial Distribution of Auger Electron-Emitting Radiotherapeutics
ROYLE, G., MYHRA, S., CHAKALOVA, R., VALLIS, K. A. & FALZONE, N
The British Institute of Radiology/Internal Users Dosimetry Group -Molecular Radiotherapy Dosimetry,
4 June 2014, Oxford, UK
Won Best Poster

Table of Contents

Table of Figures

Chapter 5: Exploration of Photoresist Autoradiography for Quantitative Single Cell Dosimetry

Chapter 6: Microautoradiography using the Transmission Electron Microscope

Table of Tables

List of Abbreviations

%ID/g	percentage of injected dose per gram
^{111}In-DTPA-hEGF	indium labelled human epidermal growth factor
AE	Auger electron
AFM	atomic force microscope
BCA	bicinchoninic acid assay
BDMA	benzyl dimethylamine
BrdU	bromo-deoxyuridine
BSA	bovine serum albina
CARs	chemically amplified photoresists
d.d.H_2O	double distilled water
d.H_2O	distilled water
DM	direct application method
DMEM	Dulbecco's modified eagle's medium
DMSO	dimethyl sulfoxide
DPTA	diethylenetriaminepentaacetic acid
DSBs	double-strand breaks
DTPA	diethylenetriaminepentaacetic acid dianhydride
EBRT	external beam radiotheapy
EGF	epidermal growth factor
EGFR	epidermal growth factor receptor
EM-MAR	electron microscopy microautoradiograph
EMPA	electron microprobe analysis
hEGF	human epidermal growth factor
HMPAO	hexamethyl-propylene-aminoxime
IM	indirect application method
IMFP	inelastic mean free path
IPA	isopropyl alcohol
ITLC	instant thin-layer chromatograph
IUDR	iodo-deoxyuridine
LET	linear energy transfer
mAb	monoclonal antibody
MAR	microautoradiography
MC	Monte Carlo
MIBG	metaiodobenzylguanidine
MIBI	methoxyisobutyl isonitrile
MIBK	4-methyl-2-pentanone
MIRD	medical internal radiation dose
NanoSIMS	nanoscale secondary ion mass spectrometry
NLS	nuclear localization sequence
PAR	photoresist autoradiography
PBS	phosphate-buffered saline
pDTPA	p-SCN-Bn-DTPA
PET-CT	positron emission tomography computed tomography
PFA	paraformaldehyde
PIPES Buffer	1,4-piperazinediethanesulfonic acid buffer

PMMA	poly (methyl methacrylate)
RBE	relative biological effectiveness
RMS	root mean squared
RNA	ribonucleic acid
SE	standard error of the mean
SEM	scanning electron microscope
SIMS	secondary ion mass spectrometry
SPECT	single-photon emission computed tomography
TCH	thiocarbohydrazide
TEM	transmission electron microscope
TFO	triplex-forming oligonucleotides
TPS	treatment planning system
TRT	targeted radiotherapy

Chapter 1:
Introduction

Chapter 1

Introduction

In 1906, Ehrlich envisaged a magic bullet of cancer therapy that was specific and universal to tumour cells, with a cytotoxic and short range effect such that only tumour cells would be damaged (Bosch and Rosich, 2008). Unlike external beam (EBRT) or brachytherapy, with targeted radiotherapy (TRT) it is not necessary to image the tumour volume to target the tumour, as cancer cells are targeted by exploiting characteristics that differentiate them from normal cells (Alberts, 2002). This is particularly advantageous when the primary tumour has metastasised as small metastases may fall below the detection limit of imaging techniques such as positron emission tomography–computed tomography (PET-CT) or single-photon emission computerized tomography (SPECT) which have a resolution of approximately 2 mm (Bal et al., 2014).

One of the challenges of using TRT is that there is heterogeneous distribution of internalised radionuclides at the multicellular, cellular and subcellular levels (Roeske et al., 2008, Bolch et al., 1999). This heterogeneity in the distribution of radionuclides leads to non-uniformity of the absorbed dose and may be a cause of TRT failure (McGowan and Guy, 2015).

The aim of this thesis is to develop ways of imaging and quantifying these variations in the spatial non-uniformity of radionuclides within individual cells, to provide more accurate information for small-scale dosimetry. The following paragraphs discuss the reasons for using TRT and the importance of cellular dosimetry for TRT. In addition, the techniques which are currently used to inform cellular dosimetry and spatial distribution are evaluated.

1.1 Types of Radionuclides used in Systemic Radiotherapy

There are three main types of emissions from radionuclides which are used for TRT: alpha particles, beta electrons and Auger electron (AE) emitters. Within the cell the main radiation target is the DNA, with DNA double-strand breaks (DSBs) being particularly deleterious (Radford et al., 1988). Other radiation-sensitive targets in cells include the mitochondria (Murphy et al., 2005) and the cell membrane (Alper, 1963). Radiation can also cause activation of growth factors and death receptors, as well as triggering downstream signalling pathways (Pouget et al., 2011), inducing the bystander effect (Shao et al., 2004).

The amount of radiation damage that is done to the targeted cell and the cells around it is related to the linear energy transfer (LET). This is the energy deposited per unit track length expressed as keV/μm. High LET particles are more cytotoxic at equivalent absorbed doses compared with low LET-type radiation (Howell et al., 1993, Goddu et al., 1996). Modelling studies have shown that about 30–40% of low LET induced DSBs are complex, with the yield increasing to greater than 90% for high LET radiation (Nikjoo et al., 1999, Datta et al., 2006). Complex DSB consist of a standard simple DSB with one or more additional lesions (e.g. base damage, abasic sites, stand breaks) within about 10 base pairs. These complex DSBs are difficult to repair. Radiation causes both direct damage to DNA and also the ionisation of water. This leads to the generation of reactive oxygen species which can cause indirect damage to DNA and other effects such as peroxidation of membrane lipids (Adelstein, 1993).

Alpha particles, which are helium^{2+} nuclei, have a range of a few cell diameters (50–100 μm). For those cells that are not specifically targeted, this short range can limit the fraction of cells traversed. (Sgouros et al., 2010); this is known as the cross-fire

effect. Alpha particles have an energy of 5–10 MeV, a LET of 50–230 keV/μm and a relative biological effectiveness (RBE) of 5–20 if within a cell, when compared to beta particles. They are used for the therapy of single cells or microscopic cell clusters (Speer, 2011). Xofigo, containing the alpha emitter radium-223 chloride, is now an approved drug and has been studied in the treatment of metastatic hormone-refractory prostate cancer (Nilsson et al., 2007). Other alpha-emitting radionuclides that are being explored for TRT include astatine-211, bismuth -212 and -213 and lead-212 (Wadas et al., 2014).

Beta particles, typically used in radioimmunotherapy have a range of up to 100s of cell diameters (0.05–12 mm) (Pouget et al., 2011) and can therefore be used to treat larger bulk tumours since the cross-fire effect allows for cells to be irradiated, even if they are not directly targeted. They have an energy of 50–2,300 keV, a LET of 0.2 keV/μm and a RBE of approximately 1 (Speer, 2011). Iodine-131, lutetium-177 and rhodium-186 are used in the treatment of minimal residual disease due to their different path lengths, while rhenium-188 and yittrum-90 are used for the treatment of large tumour masses (Sharkey et al., 1997, Koppe et al., 2005). Beta particles have low LET-type radiation and are therefore sparsely ionising radiation.

Electrons can be emitted from atoms undergoing decay by electron capture and/or internal conversion, these can have energies ranging from a few electron volts to 100s of kilo-electron volts (Kassis, 2004). These electrons can consist of energetic electrons which have a low LET (~0.2 keV/μm) and a range of up to 1 cm in tissue. Or low energy AE that have an energy range from 12 eV to 26 keV (Kassis, 2003) with corresponding tissue ranges between microns and nanometres (Kassis, 2004). Although most have low energies (< 500 eV) and correspondingly short ranges (several

nanometres) in biological material (O'Donoghue and Wheldon, 1996). The LET depends on the energy of the electron, with lower energy electrons having a higher LET. The LET of individual AE ranges from 4–26 keV/μm, however multiple AE from a point source results in an additional increase in localised ionisation density and therefore clustering of damage. As a result the decay of an Auger emitter located in the cell nucleus emitting multiple AE, has an associated RBE of 5–10 when compared to beta particles (Speer, 2011). AE are emitted by around half of the radionuclides that decay by electron capture or internal conversion (Adelstein, 1993). During electron capture or internal conversion, a vacancy is formed in an inner electron shell. To increase the stability of the atom, this vacancy is transferred to the outermost shell by a cascade of electron transitions. The energy that is gained in these transitions is transferred via the electrostatic interaction to another bound electron which is emitted from the atom (Kassis, 2004, Kassis, 2011). This emitted electron is known as an AE. The kinetic energy of the AE is the difference between the energy of the initial electronic transition to the K-shell (inner most shell) and the ionization energy for the electron which is emitted from the highest energy shell (McGraw-Hill, 2005). Non-radiative transitions are classified into Auger, Coster–Kronig and super-Coster–Kronig processes, depending on the relationship between the electron shells involved (Sastry, 1992).

AE emitters used in TRT include indium-111, iodine -123 and -125 and gallium-67. Due to the short range of AE, the cross-fire effect is minimized (Vaidyanathan and Zalutsky, 2011). This makes TRT with AE emitters well-suited to the treatment of single cells and microscopic tumours. For example indium-111 decays by electron capture to cadmium-111, it has a half-life of 2.8 days. It emits 0.171 and 0.245 MeV gamma rays as well as electrons, consisting of on average 7.43 AE per decay with an

energy of, between 0.345 – 25.58 keV with an range between 0.02–10 μm and 0.16 internal conversion electrons with an energy of between 144.6 and 245 keV and a range between 200–500 μm (Capello et al,. 2003).

1.2 Auger Electrons for Targeted Radiotherapy

AE, with their short range and high cytotoxicity, have been studied for targeted radiotherapy since the 1970s (Hofer and Hughes, 1971, Chan et al., 1976, Bloomer and Adelstein, 1977). Comparing them with energetic electrons, which have a LET of approximate 0.2 keV/μm along their path length and a range of 1 cm in tissue, AE have a LET of up to 26 keV/μm and a highly localized deposition of energy of a few nanometres around the decay site (Cole, 1969). Approximately 90% of the radiotoxicity is caused by indirect mechanisms (Walicka et al., 2001, Walicka et al., 1999, Walicka et al., 1998, Walicka et al., 2000, Bishayee et al., 2000). These indirect mechanisms occur as AE generate a high density of oxygen free radicals around the site of decay. These free radicals, generated by the ionisation of nearby water molecules, diffuse over approximately 4 nm and can damage DNA (Adelstein, 1993).

Targets of radiation in the cell include cell membrane, mitochondria, although the main radiosensitive target in the cell is the DNA. This is a double strand helix with a diameter of 2 nm. Coincidently, the highest energy deposition of an AE occurs within a sphere with a radius of approximately 1–2 nm (Kassis et al., 1987). AE-emitting radionuclides can be directly targeted to DNA (Buchegger et al., 2006). Examples of AE emitters being directly incorporated into the DNA include the AE emitters iodine -125 or -123 and bromine-77 which can be labelled to deoxyuridine to create iodo-deoxyuridine ($^{125/123}$IUdR) or bromo-deoxyuridine (^{77}BrUdR). These are directly incorporated into DNA as nucleosides. The radiobiological damage produced by the AE

when located close to the DNA is similar to that produced by high LET-type alpha particle emitters (Hofer and Hughes, 1971, Chan et al., 1976, Porteous, 1971, Kassis et al., 1982). The local energy density created by the AE was comparable to that of an alpha particle in volumes between 5 and 50 nm^3 (Charlton et al., 1978). The RBE can be attributed to radiation-induced ionisations and excitations from the emitted electron, and processes that occur at the atomic level because of the radioactive decay. These include the kinetic energy of nuclear recoil (which occurs as momentum transfers to the atomic nucleus as whole) (Demekhin et al., 2009) and chemical transmutation and local charge effects (Kassis, 2004). A comparison of the absorbed dose of iodine-131, a beta and gamma emitter, and iodine-125, an AE emitter, showed that iodine-131 deposited more dose but iodine-125 produced higher levels of cell kill when applied in the form of IUdR (Chan et al., 1978, Hofer, 1980). Studies have looked at the range of AE by looking at the fragmentation pattern produced by the incorporation of a single iodine-125 labelled deoxycytidine into a DNA duplex of defined sequence. Phosphorus-32 labelled cleavage products allowed the detection of DNA fragments from each strand of DNA, after the DNA was denatured. This was detected on high-resolution polyacrylamide gels. The relative amounts of the shorter DNA fragments were determined by scanning the autoradiogram with a densitometer. It was shown that 70% of DNA strand breaks occurred within 1.0–1.5 nm of the site of incorporation of iodine-125 (Martin and Haseltine, 1981). There was also DNA damage, leading to fragmentation of the DNA molecule up to 7 nm from the incorporation site. Since only phosphorus-32 labelled DNA fragments are detected, there is an experimental bias toward measurement of the shorter DNA products. These findings demonstrate the very short-range effects of AE-emitting radionuclides when incorporated close to DNA within cells.

AE emitters can also target the DNA by being conjugated to DNA-binding molecules. For example, the AE emitter iodine-125 was non-covalently linked to the DNA. The iodine -125 still produced the type of survival curve characteristic of high-LET radiation (Kassis et al., 1989), but with a lower RBE (RBE: 1.7-1.9) in comparison to when iodine-125 was incorporated into the DNA (RBE: 7.3), when comparing the mean lethal dose to the nucleus (delivered over the 18 h incubation) to the mean lethal dose of 5.80 Gy following exposure of the same cell line to 250 kV_p X-rays. The reduction in RBE is believed to be due to the greater distance between the site of decay and the DNA molecule (Kassis et al., 1989). In another example, by labelling oligonucleotides with iodine-125, sequence-specific DSBs have been induced in a target DNA duplex (Panyutin and Neumann, 1994). The DNA breaks were distributed symmetrically around the target site within a distance of five nucleotides to either side or approximately 1.7 nm (Kassis et al., 1989).

When AE emitted are located outside the cell nucleus, such as bound to the plasma membrane or within the cytoplasm, cell survival curves have initial shoulders and much shallower slopes typical of low LET type radiation (O'Donoghue and Wheldon, 1996). Microdosimetric modelling has shown when the AE emitters are localized in the nucleus of the cells within a cell cluster, the self dose to cross dose ratios are enhanced by between 8 - 35 times compared to when the AE emitter is localized on the cell surface (Goddu et al., 1994b).

The cytotoxicity of AE-emitting radiopharmaceuticals is therefore determined by their subcellular distribution. The cytoplasm of non-targeted normal cells provides sufficient

shielding against AE emitted from targeted cancer cells (Behr et al., 2000). In TRT with beta-emitters, exposure of hematopoietic stem cells in the bone marrow results in dose-limiting toxicity. The bone-marrow would not be affected by AE emitters (Aghevlian et al., In Press).

Limitations associated with the use of AE-emitting radioisotopes include the heterogeneity of radionuclide uptake. Due to their short path length, as the heterogeneity of uptake increases the potential for killing all targeted cells diminishes. Assuming a normal distribution, as heterogeneity of uptake increases there will be more cells which are "overkilled"; i.e. they would have died with a much lower uptake of the radiopharmaceutical. Likewise, there will be an equal number of cells that have had a sub-lethal uptake. Those cells in the low uptake tail of the distribution allow the tumour to continue to progress. AE have a negligible cross-fire effect which could irradiate and kill cells that are not targeted by the radionuclide (Humm, 1986). Therefore, for AE TRT, the therapeutic outcome will be dominated by the sub-populations of tumour cells with insufficient accumulation of radionuclide and relatively reduced adverse biological effects (O'Donoghue and Wheldon, 1996).

However, this limitation may be offset by the radiation-induced bystander effect which can lead to cell killing of non-targeted cells (Mairs et al., 2007). This phenomenon has been demonstrated in medium transfer experiments. Clonogenic survival was reduced when cancer cells were exposed to medium from cells that bound iodine-123 labelled metaiodobenzylguanidine (^{123}I-MIBG) (Boyd et al., 2006). A bystander effect has also been shown to occur in animal studies when using DNA-bound ^{125}IUdR (Xue et al., 2002). In these studies mixed-cell suspensions containing two million cells were injected into mice, 1 x 10^6 live cells and 1 x 10^6 cells, which were either ^{125}IUdR-

labelled cells or dead cells. Increasing the number of labelled cells (and reducing the number of dead cells) caused statistically significant slower tumour growth, producing a tumour growth delay of between 2 and 4 days. It was also shown that the growth delay could not be explained by a minor radiation exposure of non-pre-labelled cells from the gamma-radiation of iodine-125, since much higher EBRT doses were required to diminish tumour growth to a similar degree. Although typically only a fraction of the unirradiated cells will be killed (Hei et al., 2008). Another effect which has been observed, is a localized cross-fire effect (a cross-dose effect), in which targeted cells irradiate neighbouring cells, although this is less important for AE compared to alpha and beta emitters (Goddu et al., 1994a). Cross-dose and bystander effects may improve the effectiveness of AE TRT for the treatment of cancer (Cai et al., 2010). However, AE TRT requires targeting of most cancer cells and therefore may not be suitable for large tumours (Aghevlian et al., In Press).

1.2.1 Targeting the Cell Nucleus with Auger Electron-Emitting Radionuclides

The biological effects of AE-emitting radionuclides are critically dependent on their subcellular location and therefore, for maximum cytotoxicity, the maximum radiation absorbed dose needs to be delivered to the cell nucleus. The target needs to have specificity exclusively with tumour cells, ideally at the DNA level. This target needs to be present in all tumour cells. To achieve this, different targeting mechanisms have been investigated. These exploit different characteristics of the cancer cells to deliver radiation specifically to cancer cells. Targeting mechanisms include using antibodies, small molecules, oligonucleotides, peptides, proteins and nanoparticles.

1.2.1.1 Antibodies

Antibodies can be developed against a large number of targets, but they have a long circulation time, or biological half-life, due to their large size (~150 kDa). This can lead to a high dose to the bone marrow. One internalising monoclonal antibody (mAb) which has been used in AE TRT is CO17-1A. This was labelled with the AE emitters (indium-111 and iodine-125) and beta emitters (iodine-131 and yittium-90). The AE-emitting version had a therapeutic advantage when internalised (Behr et al., 2000). In other studies when CO17-1A was radiolabelled with iodine-125, it was shown to be selectively radiotoxic and caused more chromosomal damage and micronuclei than the non-internalising ^{125}I-R11D10 mAb (Woo et al., 1989). However, in another study when using iodine-125 labelled internalizing and not internalizing mAbs, it was shown that when the cell membrane was targeted there was a greater cytotoxicity compared to when the cytoplasm was targeted (Pouget et al., 2008).

1.2.1.2 Small Molecules

Small molecules have a molecular weight of less than 900 Da and help to regulate biological processes. In TRT, AE were first used in the direct targeting of DNA by the use of ^{125}IUdR in the 1970s (Bloomer and Adelstein, 1977). Clinical studies have used both ^{125}IUdR and ^{123}IUdR to treat liver metastases from colorectal cancer using a continous infusion (Macapinlac et al., 1996, Mariani et al., 1996), as well as other cancers (Bodei et al., 2003).

Another small molecule is MIBG which was labelled with iodine -123 and -131. This is actively transported into neuroblastoma cells by the norecinechrine transporter (Tepmongkol and Heyman, 1999). Iodine-125 can be used to produce an AE-emitting radiopharmaceutical, which has shown some promise in a small phase I study in

neuroblastoma patients (Sisson et al., 1990). However, experiments and calculations have shown that the growth inhibiting effect of ^{125}I-MIBG is greater than that of ^{131}I-MIBG only if ^{125}I-MIBG is homogeneously distributed in tumour cell aggregates that have a diameter of less than 100 µm, due to a much higher dose rate (Weber et al., 1996). Experiments with technium-99m compounds have shown that hexamethyl-propylene-aminoxime (^{99m}Tc-HMPAO) had a substantially higher uptake into the nucleus, the membrane, and organelles than ^{99m}Tc-pertechnetate. However when using a clonogenic assay the ^{99m}Tc-pertechnetate and ^{99m}Tc-HMPAO caused a similar reduction in cell survival suggesting extra-nuclear radiosensitive targets are involved in cell inactivation (Maucksch, et al. 2016).

1.2.1.3 Oligonucleotides

Oligonucleotides are single strands of DNA, ribonucleic acid (RNA) or peptic nucleic acid, which are 13 to 25 nucleotides in length and are designed to hybridize specifically to DNA or RNA sequences. They are suitable for AE TRT as they could, in theory, deliver AE on a sequence-specific basis (Martin and Haseltine, 1981). An iodine-125 triple helix forming oligonucleotide (TFO) has been developed against the RNA and DNA encoding the androgen receptor. This is over-expressed in prostate cancer. Studies with mouse models show that protein expression and tumour growth was reduced in the radiolabelled TFO compared with the unlabelled TRO (Zhang et al., 2008).

1.2.1.4 Peptides

Peptides are formed when two or more amino acids are condensed together with the formation of a secondary amide bond. Peptide receptor radionuclide therapy uses their excellent binding efficiencies, selectivity and favourable pharmacokinetic behaviour. Using somatostatins is the recommended first-line therapy for unresectable

neuroendocrine tumour of non-pancreatic origin (Eriksson et al., 2008, Pavel et al., 2012). Somatostatins have been labelled for TRT using indium-111 and have been used in phase I trials where therapeutic effects were seen in 42% of patients (Valkema et al., 2002); in these studies modest uptake was shown in the cell nuclei (Janson et al., 2000).

1.2.1.5 Proteins

Cell surface receptors, which are over-expressed in a large range of cancers, have also been targeted using radiolabelled proteins. These include the epidermal growth factor (EGF), insulin-like growth factor and vascular endothelial growth factor. These bind to cell surface receptors and are internalised into the cell (Wang and Hung, 2009, Firth and Baxter, 2002, Domingues et al., 2011).

One example of a protein TRT agent is ^{111}In-DTPA-human epidermal growth factor (^{111}In-DTPA-hEGF, DTPA is diethylenetriaminepentaacetic acid). *In vitro* studies showed that ^{111}In-DTPA-hEGF was more toxic to epidermal growth factor receptor (EGFR)-overexpressing breast cancer cells when compared to breast cancer cells expressing low levels of EGFR (Bailey et al., 2007, Reilly et al., 2000b). ^{111}In-DTPA-hEGF was shown to interact with EGFR in the cytoplasm and the nucleus, by using fluorescence resonance energy transfer with fluorophore-labelled EGF (Cornelissen et al., 2011). Approximately 10% of the total membrane bound radioactivity translocated to the cell nucleus (Bailey et al., 2007, Reilly et al., 2000a). The uptake of ^{111}In-DTPA-hEGF is proportional to the cancer cells' EGFR expression, with nuclear localization approaching saturation at 6×10^5 EGFR/cell. In cells with a lower expression of EGFR (1×10^4 receptors/cell), nuclear localisation has also been shown (Hu et al., 2007). However, other studies have shown nuclear EGFR only in tumour cells which have a high receptor density (Lin et al., 2001).

A phase I trial of patients with EGFR-positive metastatic breast cancer matched results seen in animal studies (Reilly et al., 2006). The liver and kidneys accumulated ^{111}In-DTPA-hEGF but the mean radiation absorbed dose estimates were within accepted tolerance. Tumour localization was also achieved, although no objective antitumour responses were observed at the doses studied. The study, however, did not achieve maximum tolerable dose but further dose escalation of ^{111}In-DTPA-hEGF is feasible as there was favourable radiation dosimetric data and lack of immunogenicity (Vallis et al., 2014).

1.2.1.6 Nanoparticles

Nanoparticles can be targeted at cancer cells in two ways, by passive and active targeting. In passive targeting, the nanoparticles are delivered to the tumour through the tumour vasculature and are accumulated in the tumour due to the enhanced permeability and retention effect (Maeda et al., 2000). In active targeting, the nanoparticles are engineered so that they are able to target the cancer cells using a variety of mechanisms such as antibody fragments, peptides or small molecules. Nanoparticles have been used with a range of radioisotopes, including AE emitters. Indium-111 was delivered to HER2-positive breast cancer cells using block co-polymer micelles with HER2-specific antibodies and a nuclear localization sequence (NLS) conjugated to the surface. The NLS led to a significant increase in nuclear uptake of the radionuclide (Hoang et al., 2012). Gold nanoparticles have been labelled with indium-111 and EGF in order to target cells over-expressing EGFR (Song et al., 2016). *In vitro* studies have shown more internalisation and cytotoxicity in cells over-expressing EGFR compared to cells with normal expression.

1.3 Dosimetry

As early as 1902, the ability to quantify the delivered radiation dose (dosimetry) from therapy and the establishments of dose–effect relationships led to a significant improvement in patient outcomes (Pouget et al., 2015).

The radiation absorbed dose is strictly defined as the mean energy imparted (by ionizing radiation) per unit mass. It is used to measure the radiation absorbed by an object or person and can be calculated for any type of ionising radiation absorbed by a material. It is used in several circumstances. Firstly, it is used to assess the risk from diagnostic radiological procedures. Secondly, it can be used to evaluate the dangers that people face after a nuclear disaster or accident. Thirdly, it can be used to predict the efficiency of radiotherapy. The dose by itself is a poor predictor of biological effect; other factors which should be taken into account include the time course of the delivery, the LET of the radiation and the biological system such as the radiosensitivity of the tissue (Bolch et al., 2009).

1.3.1 External Beam Dosimetry

In EBRT, the delivered dose needs to be accurate to within ±5% of the prescribed radiation dose (Venselaar et al., 2001). The dosimetry to calculate these doses is standardised and uses computer-based treatment planning systems (TPS) (Mohan et al., 1988). TPS are able to incorporate voxel by voxel considerations of heterogeneous tissues (Reft et al., 2003, Ahnesjö and Aspradakis, 1999).

1.3.2 Systemic Dosimetry

Unlike EBRT, the dosimetry for TRT is less established. Instead of a prescribed radiation dose, an administered activity is given. There are three main ways of calculating the administered activity. Firstly, there is a fixed administered activity

regime, where all patients receive the same administered activity. Secondly, there is a maximum tolerable dose regime, where patients receive an individualised administered activity which aims to deliver the maximum tolerated absorbed dose to the dose-limiting normal tissue. Thirdly, there is a prescribed tumour absorbed dose regime, where patients receive an individualised administered activity projected to deliver a prescribed therapeutic absorbed dose to the tumour (Speer, 2011). However, the actual absorbed radiation dose can only be calculated at the resolution of imaging methods post administration, and this cannot account for variably below this limit. The biological effects on tissue incorporating radionuclides are highly dependent on the type of radiation and on isotopic distribution at macroscopic, microscopic and subcellular levels (Howell et al., 2012, Bolch, 2008, Bousis et al., 2010, Rajon et al., 2011).

Being able to measure the absorbed radiation dose from internally deposited radionuclides, is a key factor when assessing the risk and therapeutic value for new radiopharmaceuticals (Bolch et al., 1999). The absorbed dose in TRT will depend on the pharmacokinetics, the type of emission and the distribution of the radionuclide within the different cells. In EBRT, there is homogeneous irradiation at the high absorbed dose rate (1–2 Gy/min) of low-LET X-rays that target all the cells in the field. In TRT, however, there is a low inhomogeneous absorbed dose rate (<1 Gy/hr) with protracted, heterogeneous and radioactive emissions which have a range of energies (Pouget et al., 2015). There is a heterogeneous distribution of internalised radionuclides at the multicellular, cellular and subcellular levels (Roeske et al., 2008, Bolch et al., 1999), which leads to non-uniformity of the absorbed dose and may be a cause of TRT failure (McGowan and Guy, 2015). It has been shown that there is a poorer tumour response as dose non-uniformity increases and at higher doses this effect is worse. (Zanzonico, 2000, O'Donoghue, 1999). For TRT using AE, conventional dosimetry

does not explain the biological effects (Task Group on Radiation Quality Effects in Radiological Protection, 2003). Instead, microdosimetry is used to quantify exposure of cells to radiopharmaceuticals (Scott and Schollnberger, 2000, Falzone et al., 2011).

1.3.2.1 The Medical Internal Radiation Dose Schema

The most widely used method for internal dose calculations is the medical internal radiation dose (MIRD) Schema. Its traditional application was diagnostic radiopharmaceuticals and calculation of the absorbed dose to organs (Howell, 1994). It assumes that activity and cumulated activity are uniformly distributed within the source regions and the energy is deposited uniformly. The average dose at the organ or voxel level is less meaningful when considering short-range emissions such as AE and the biological effects observed do not correlate well with the mean tumour dose (Speer, 2011, Zanzonico, 2011). However, the MIRD schema can be used for microdosimetry, as the source and target regions can be virtually any size as long as there is an appropriate model and set of biological data.

The cellular S-values (absorbed dose per unit cumulated activity) allow convenient calculation of the mean self-absorbed dose. However, this is the average self-absorbed dose and does not count for differences in size and geometry, differences in intracellular activity or stochastic differences related to the energy deposition events. If there is a wide variation in cellular uptake of radioactivity, the mean absorbed dose across a cell population may not be accurate (Howell, et al., 1997). For proper microdosimetric analysis, the biological data required includes the spatial distribution and size of the source and target regions as well as the activity in each compartment.

$$\overline{D}(r_k \leftarrow r_h) = \overline{A_h}(S(r_k \leftarrow r_h)) \qquad (1.1)$$

$$S(r_k \leftarrow r_h) = \sum_i \frac{\Delta_i \emptyset_i(r_k \leftarrow r_h)}{m_k} \qquad (2.2)$$

Source	Target
Cell	Cell
Cell surface	Cell
Nucleus	Nucleus
Cytoplasm	Nucleus
Cell surface	Nucleus

Figure 1.1: The medical internal radiation dose schema
Radiation is emitted from a source region (r_h) and deposits its energy in a target region (r_k). The mean absorbed dose ($\overline{D}$) to the target region (r_k) from the cumulated activity in the source region (r_h) is described by equation 1.1. This is the cumulated activity ($\overline{A_h}$) in the source region, multiplied by the S-values (S), from a source region (r_h) to a target region (r_k). The S-values are described by equation 1.2 and tables of S-values are available. S-values are the sums of the mean energy emitted by decay(Δ_i) multiplied by the absorbed energy in the target region($\emptyset_i$), from the source region, divided by the mass of the target region (m_k). The table shows the cellular compartments for microdosimetry, which have tabulated S-values. Cellular S-values can be calculated using analytical methods or MC techniques (Howell, 1994, Howell, et al., 1997).

For accurate Monte Carlo (MC) simulations of ionizing radiation for microdosimetry, experimental information is required which provides information on the intracellular micro-dose distribution. To obtain a quantitative measure of the dose distribution at a single cell level, knowledge of the 3-D intracellular distribution of the radiotherapeutic is required. Determining the activity in subcellular compartments is considered to be one of the major sources of error and uncertainty in small-scale dosimetry (Speer, 2011). Attempts have been made to provide S-values for smaller voxels. For example, the MIRD Pamphlet No. 17, has tabulated S-values for 3 mm and 6 mm voxels for the beta emitters: phosphorus-32, strontium-89, yttrium-90 and iodine-131, which also has 0.1 mm voxels and for technetium-99m which decays by isomeric transition and internal conversion (Bolch et al., 1999). The activity distributions were obtained by autoradiography studies. As well as these small voxels, cellular S-values for a range of radioisotopes at different cell (3 to 10 μm) and nucleus (2 to 9 μm) radii have been calculated. These assume cells are perfect spheres and can be used for absorbed dose calculations. These S-values have been calculated using analytical methods assuming

that tissue is equivalent to water. Cellular S-values can also be calculated from MC simulations or dose point kernel approximations (Falzone et al., 2015).

1.3.2.2 A Medical Internal Radiation Dose Calculation

For absorbed dose calculations using the MIRD schema, three pieces of information are used: the biological distribution data, the physical properties of the radionuclide and the method or schema that combines the biological and physical data into the dose estimate. A simple calculation can be carried out using the MIRD schema to work out the dose to the cell nucleus exposed to a radionuclide. For example, If 10^6 cancer cells internalised 2 x 10^4 Bq of indium-111, with 75% of the intracellular activity located in the cell nucleus and a biological clearance of 48 hours, the mean absorbed dose to the cell nucleus can be calculated.

Firstly, the activity in each cell ($A_{o,C}$) is calculated, assuming a uniform distribution:

$$\frac{Total\ Activity}{Number\ of\ cells} = A_{o,C} = 20 * 10^{-3}\ Bq \tag{1.3}$$

Secondly, the effective clearance time is calculated:

$$\frac{1}{T_{eff}} = \frac{1}{T_{Bio}} + \frac{1}{T_{phy}} = \frac{1}{48\ (hours)} + \frac{1}{2.81\ (days)} = 28\ hours \tag{1.4}$$

Thirdly, the accumulated activity is calculated:

$$\tilde{A}_C = 1.44\, T_{eff} A_{o,C} = 3.0 * 10^3 \text{ Bq s} \tag{1.5}$$

Then, tabulated cellular S-values are used to convert the cumulated activity of indium-111 to the cell nucleus into a dose. For the tabulated S-values, the dimension of the cell needs to be known. For example, consider a cell radius of 10 µm and a nucleus radius of 5 µm. The mean absorbed dose to the nucleus from the nucleus (S(N←N)) is 1.48 x 10^{-3} Gy/Bq S and the dose to the nucleus from the cytoplasm (S(N←Cy)) is 8.96 x 10^{-5} Gy/Bq S.

Therefore, the mean absorbed dose to the cell nucleus is:

$$\bar{D}_{N=}\tilde{A}_C([F_N S(N \leftarrow N)] + [F_{Cy} S(N \leftarrow Cy)]) \quad (1.6)$$

$$= 3.0 * 10^3 * (0.75 * 1.48 * 10^{-3} + 0.25 * 8.96 * 10^{-5}) \quad (1.7)$$

$$= 3.2 \text{ Gy.} \quad \text{(Howell et al., 1997)}$$

The example given demonstrates a very simple system. The cells are all assumed to have the same distribution of radioactivity and be perfectly spherical, the same size, with the same size nucleus, in the centre of the cell. However, this is not the case. For example, when ellipsoidal cell geometries were used, there were differences between the calculated S-value between the two geometries (Nettleton and Lawson, 1996). Many cells exhibit irregular geometries and eccentric cell/nucleus arrangements, which lead to inaccuracies in dose when using MIRD tabulated S-values (Falzone et al., 2015).

The radioactivity is also shown not to be uniformly distributed across the cell population (Bolch, 2008, Bousis et al., 2010, Rajon et al., 2011). Therefore, improving the knowledge of the distribution at the cellular level will allow for more accurate calculations to be made.

1.4 Current Methods of Evaluating Radionuclides at Cellular and Subcellular Levels

Evaluation of the intracellular distribution of radionuclides used for TRT is essential for accurate dosimetry. The efficiency of AE-emitting radiopharmaceuticals is determined by their subcellular distribution, which varies between cells. Techniques are required that show and quantify this variation at the nanometre scale, as this is the range of the electrons and size of the DNA target.

There are several methods which are currently used for determining the efficiency of TRT agents in animal models or human studies. These include imaging methods such as SPECT and PET-CT. These are able to detect gamma rays that have been emitted either by a radiotracer or radiopharmaceutical; these images are quantitative, and provide a time course of biodistribution data. The resolution is between 4–6 mm and 8–12 mm for clinical PET-CT and SPECT respectively and 1–2 mm and ≤ 1 mm for preclinical PET-CT and SPECT respectively (Khalil et al., 2011). While the theoretical resolution has not yet been achieved, these imaging techniques will not be able to resolve details from single cells (Moses, 2011). As well as imaging techniques, quantitative non-imaging techniques can be used in human and animal models. These include radiation monitoring, using shielded detectors such as sodium iodide detectors, or measuring the radioactivity present in the blood or in excreta. Blood monitoring can help assess bone marrow dose and excreta monitoring can help estimate the whole body absorbed dose and dose to the bladder. The radioactivity present can be analysed by using calibrated gamma well and liquid scintillation counters (Siegel et al., 1999). The resolution of these non-imaging techniques only allows for the absorbed dose to be calculated at the organ or whole body level.

To develop a system for single cell dosimetry, other techniques have been studied. Some methods, which look at the location of TRT agents at the single cell level, provide information on the efficacy of the treatment, or measure the effects of the radiopharmaceutical. Other techniques directly measure the quantity of radiation. As well as providing information for microdosimetric modelling, they can be used to judge the success of a treatment. Small-scale dosimetry can play an important role in preclinical studies. It may also help to provide information on clinical failures and lead to solutions in overcoming these obstacles (Speer, 2011).

1.4.1 Biological Methods of Evaluating Radionuclides at Cellular and Subcellular Levels

Biological methods are used for the evaluation of radiopharmaceuticals in single cell models and positive results will lead to animal studies. They have a biological endpoint so are influenced by the inherent properties of the cells, not just by the amount of radioactivity that has accumulated in the cell. They are not dosimetry methods but they do provide information about the kinetics, survival fractions and radiation damage, which can help inform dosimetry calculations and determine which radionuclide or TRT agent is most effective. They do not give the distribution of the radiopharmaceutical. Absorbed doses can be calculated by assuming the cellular location or by determining the location by other methods.

1.4.1.1 Cell Viability Assays

Cell viability assays are used to determine the effect of cells exposed to radiopharmaceuticals. Two main types are clonogenic assays, which determine the proliferation potential, and MTT and WST1 assays, which look at metabolic activity (Woodward and Bristow, 2009). However, for cells which have been exposed to

radiation, where cell death is mainly through mitotic catastrophe, clonogenic assays are considered the gold standard.

In clonogenic assays, treated cells are counted and then a known number are reseeded then left for one to two weeks. During this time those cells which are viable will divide and form colonies. These colonies are then counted and the survival fraction calculated. This is the fraction of colonies formed compared to the number of colonies which would have formed with no treatment. They can be used to compare therapeutic efficacy between radiolabelled and non-radiolabelled compounds, as well as the biological equivalent dose. For example, clonogenic assays showed that the monoclonal antibody CSL360–which incorporates a NLS and was radiolabelled to indium-111 (^{111}In-DTPA-NLS-CSL360), at a concentration of 266 nmols/L and labelled with 2.95 MBq–reduced the clonogenic survival by 3.7-fold when compared to control cells (Gao et al., 2016). In another example, gold nanoparticles labelled with indium-111 and using EGF as a targeting mechanism were shown to have a higher radiotoxicity and hence a lower survival fraction than the controls (Song et al., 2016).

Clonogenic assays can also be used to compare the effects of differing isotopes. For example, comparing ^{123}IUdR,^{125}IUdR and ^{131}IUdR showed that, when using the AE emitters iodine -123 and -125, there was a lower survival fraction in single cell models but in spheroids (which were mechanically disaggregated) ^{131}IUdR was shown to be more toxic. These results were predicted from microdosimetric modelling (Neshasteh-Riz et al., 1998). In another example, iodine-125, iodine-131, indium-111 and gallium-67 were radiolabelled to anti-CD20 and anti-MHC antibodies. These antibodies were shown to bind to the cell surface and while some of the anti-CD20 was transported to the juxtanuclear endocytic recycling compartment, a large percentage still remained on

the cell surface. The counts per cell over a time course were measured and the survival fraction was calculated using a clonogenic assay. This showed that where comparing the disintegrations per cell, iodine-131 was more radiotoxic and indium-111 was the least radiotoxic. Dosimetry was then carried out determining the centigray dose delivered per cell, assuming cell surface S-values for both antibodies and for the anti-CD20 intracellular s-values were also calculated. In both cases his showed that the calculated doses for iodine-125 and indium-111 were considerably higher than those for gallium-67 and iodine-131. This variation suggests that the effects of iodine-125 and indium-111 are overestimated by the dose calculation, or the effect of gallium-67 and iodine-131 are underestimated. As well as this when comparing the cell surface and internalized dose calculations as carried out for the anti-CD20 antibody, iodine-125 and gallium-67 have a greater cytotoxic effect when located on the cell membrane, although the assumptions tend to exaggerate the difference between cell surface and cytoplasm (Michel et al., 2003).

The clonogenic assay only evaluates cell survival in monolayers of cells and as such may not model what is seen in cell spheroids or other multiple cell models. For example, when incubated with rapamycin, an mTOR inhibitor, cells in culture did not have a decrease in survival. However, when looking at spheroid or xenograph models, rapamycin was shown to decrease the volume of both spheroids and xenographs (Eshleman et al., 2002).

While the location of the radiopharmaceutical may vary, clonogenic assays do not take into account the variation in location of the radioactivity within the individual cell that led to a colony forming. Clonogenic assays are able to demonstrate dose effects, as well as the minimum incubation time for cells, before effects are seen.

1.4.1.2 Biomarkers

Biomarkers can be useful in a range of circumstances when physical dosimetry is absent. For example, accidental radiation exposure, nuclear warfare or cellular experiments (Rana et al., 2010). Biomarkers can either be prognostic, which could provide an early indication of radiation-induced damage, or diagnostic, which give information about the biological status (Jones et al., 2014). To determine the effect of TRT, diagnostic biomarkers are more appropriate.

Biomarkers can look at different mechanisms within cells which are affected by radiation exposure. These include genomic, transcriptomic, proteomic and metabolomics markers. The main target in AE-emitting TRT is the DNA, therefore transcriptomic biomarkers, which identify DNA damage and repair, are most useful. Biomarkers which are indicators of DNA damage, such as DSBs, can provide information about the localization of the radiopharmaceutical (Rogakou et al., 1998). Detecting the phosphorylation of H2AX (γ-H2AX), is the most commonly used biomarker for this purpose.

If DNA DSBs have occurred there will be phosphorylation of H2AX causing γ-H2AX foci to form at sites of DNA DSBs. Immunohistochemistry, using fluorophore-labelled antibodies which bind to γ-H2AX, allows γ-H2AX foci to be viewed (Qvarnström et al., 2004). The γ-H2AX foci assay is a sensitive and precise marker for DSBs (Sak and Stuschke, 2010). This can then be used as an indirect method of evaluating radionuclide distribution. When using confocal microscopy, the number of foci has been found to correlate closely with the number of DSBs (Rogakou et al., 1999), with approximately one immunohistochemically-detectable focus per DSB (Phillips et al., 2006,

Sedelnikova et al. 2002). There is a linear radiation dose response of the γ-H2AX assay (Rothkamm and Löbrich, 2003, Redon et al., 2010, MacPhail et al. 2003).

The γ-H2AX assay has been used to determine the effect of an iodine-125 radiolabelled TFO. Quantification of the disintegrations has been carried out with approximately 1 decay leading to 0.8 DSBs (Sedelnikova et al., 2002). Studies were conducted to determine the efficiency of ^{125}I-TFO for TRT. DNA-bound ^{125}I-TFO produced more γ-H2AX compared to ^{125}I-iodoantipyrine which does not bind to DNA, giving spatial information about the delivery of the radiopharmaceutical. There was a large variation in γ-H2AX foci due to non-uniform delivery of ^{125}I-TFO. Dosimetry information was not calculated. However, the information allowed for the selection of a TFO with significantly higher targeting efficiency (Sedelnikova et al., 2002, Panyutin et al., 2005). Other AE-emitting radiopharmaceuticals included the monoclonal antibody ^{111}In-NLS-7G3, where γ-H2AX staining showed there was unrepaired DNA DSBs in the nucleus (Leyton et al. 2011).

γ-H2AX detection has also been used in clinical trials, when blood sampling allowed for γ-H2AX measurement. It was concluded that γ-H2AX foci determination in peripheral blood lymphocytes can be used for *in vivo* dosimetry shortly after local radiotherapy (Sak et al., 2007). The γ-H2AX assay is able to detect radiation doses as low as 1.2 mGy (Rothkamm and Löbrich, 2003) and γ-H2AX has been used to determine treatment-induced DNA damage in a tumour after treatment with EBRT (Shah et al., 2016).

Dose-estimates can be determined by comparing the number of foci in cells treated with the radiopharmaceutical, with those cells which have been irradiated using different doses of EBRT. A uniform dose to all cells will be given in a cell population treated

with EBRT. The number of foci at this known dose can be compared to the number of foci after treatment with a radiopharmaceutical, to see how effective the radioisotope is at causing DNA damage. Using γ-H2AX, variations in DNA damage across a cell population can be shown.

Methods of viewing γ-H2AX include flow cytometry for use in the clinic, where peripheral blood mononuclear cells treated with DSB-inducing agents have shown an increase in γ-H2AX. The technique provided enough sensitivity to measure DNA damage in clinic (Johansson et al., 2016). However, the most sensitive method to accurately measure DSBs is by counting γ-H2AX using con-focal microscopy (Mah et al., 2011, Sak and Stuschke, 2010). Con-focal microscopy is operator dependent, time consuming and requires the evaluation of a large number of cells. It is also limited by the resolution limit of optical microscopy.

γ-H2AX expression gives no information about the distribution of the radioisotope, just the effects and only if the radiation is causing DNA damage. Other radiation-sensitive targets may be affected by the radiopharmaceutical but may not lead to detection using a biomarker. The damage repair is not taken into account. Cells which have internalised the radiopharmaceutical and have been repaired over the period of study will have the same response as those cells which have not been exposed to radiation. γ-H2AX foci are at a maximum 30 min after irradiation (Rogakou et al. 1998, Antonelli et al. 2005) and the foci numbers are then reduced (Olive and Banáth, 2004, Banáth et al. 2004).

1.4.2 Direct Measures of Evaluating Radionuclides at Cellular and Subcellular Levels

These techniques are able to directly measure the radiation in cells either by detecting their emissions or looking for the presence of the element.

1.4.2.1 Internalisation Studies

Internalisation studies look at the distribution of radiation within different cellular compartments. The biological material is separated into different fractions, either by centrifugation leading to separation by density gradient, or by using chemicals to disrupt the cell membrane. The radioactivity associated with different cellular compartments can then be determined in a scintillation counter. To ensure that separation of the fractions is complete, the biochemical purity of the fractions is tested by Western blot analysis, probing for proteins known to be included in the specific compartments.

Fractionation studies can be used for cell- and subcellular- scale dosimetry, as they provide quantitative spatial distribution of the radiopharmaceutical. For example, they can be used to determine the presence of AE-emitting isotopes in the cell nucleus. However, since large numbers of cells are used for fractionation analyses, there is no information about the variation in uptake of the radionuclide across the population of cells. Due to its relative simplicity and the quantitative information provided, it is the most widely-used technique for determining the distribution of radiopharmaceuticals (Puncher and Blower, 1994).

Internalisation studies have been used to evaluate the internalisation and pharmacologic properties of novel radiopeptides. For example, the somatastain-binding radiopharmaceuticals [^{111}In-DOTA^{0}-1-Nal^{3}, Thr8]-octreotide and [^{111}In-DOTA^{0}-BzThi^{3}, Thr8]-octreotide were compared to [^{111}In-DOTA-Tyr^{3}]-octreotide, the clinical gold standard. The culture medium, the receptor bound and the internalised fractions were measured. The percentage of internalised peptide at 30 minutes as a function of concentration showed a linear dependence. The internalisation studies formed part of a

set of work that showed that [^{111}In-DOTA^{0}-1-Nal^{3}, Thr8]-octreotide and [^{111}In-DOTA^{0}-BzThi^{3}, Thr8]-octreotide have superior pharmacologic properties when compared with the gold standard, leading to preparation of these peptides for clinical trials. No comment was made about the increase of dose to the cell (Ginj et al., 2005).

Internalisation assays were also carried out to determine the subcellular distribution of the somatostatin receptor ligand, ^{64}Cu-TETA-OC. Uptake of ^{64}Cu-TETA-OC and [^{64}Cu]Cupric Acetate (a non-receptor meditated tracer) was demonstrated in cell nuclei. Incubation with the radioligand in a pulse-chase experiment, before internalisation studies, showed the different in the pharmokinetics of the compounds. In this pulse chase experiment, after incubation with the radioligand, levels of copper-64 from [^{64}Cu]cupric acetate decreased significantly from 4 to 24 hours post-administration and increased between 4 and 24 hours for ^{64}Cu-TETA-OC. Internalisation studies allowed a discussion on the mechanisms which led to ^{64}Cu-TETA-OC being located in the cell nucleus, as currently there is no known pathway for somatostatin receptor ligands to accumulate in the cell nucleus (Wang et al., 2003). As well as determining the amount of radioactivity in the cell nuclei, the radioactivity in the mitochondria, lysosomes and cytosol was also determined. However, in these fractions there were low levels of cross-contamination from each of the other fractions, as determined by their marker enzyme assays.

While it is possible to work out the average dose to a single cell from internalisation studies, it is not commonly done. Instead, internalisation studies are used to provide information about the kinetics and as evidence to move the studies forward to *in vivo* work. Dosimetry information from internalisation studies will only be able to provide

information at the multi-cellular level and not the heterogeneity across a cell population.

While the technique is simple, it is possible that it can give deceptive results, as processing may affect the interaction of the radioligand with its target. If this is the case, the radiopharmaceutical may appear in the cytosolic fraction. For example, internalisation studies carried out on guinea pig hearts of the myocardial perfusion agent ^{99m}Tc-MIBI. This showed that 70–80 % of the internalisation was in the cytosolic fraction. However, studies later showed that ^{99m}Tc-MIBI accumulated in the mitochondria (Piwnica-Worms et al., 1994, Crane et al., 1993).

1.4.2.2 Electron Microprobe Analysis

Electron microprobe analysis (EMPA) is a non-destructive technique which provides micrometre-scale quantitative chemical analysis (Echlin, 2001). To carry out this analysis, a beam of electrons is fired at a sample which then produces backscattered electrons and characteristic X-rays. The element is then identified by its electronic structure. It therefore cannot distinguish radioactive atoms from non-radioactive ones. When carrying out the analysis, the size and current density of the beam determines the trade-off between resolution and time to conduct the analysis.

Samples can be analysed qualitatively and quantitatively to determine the element concentration at the subcellular level (Gardin et al., 1999). While the technique has not been widely used in biological samples, it has been used to determine the intracellular metabolism of gallium. Experiments were carried out using cultured cells or tumours. A transmission electron microscope (TEM) accessory on the electron microprobe allowed for the cell compartment to be determined and allowed EMPA of these compartments. Characteristic X-rays of phosphorus and gallium-67 showed gallium in the lysosomes

of tumour cells in ultrathin sections. These contained small dense clumps of gallium-67, showing that gallium-67 is associated with phosphorus, and suggesting that this element is precipitated as a phosphate salt (Berry et al., 1983).

Another study looked at the presence of ^{99m}Tc-MIBI, a gamma-emitting radiopharmaceutical, which is in clinical use to evaluate myocardial perfusion. This study determined the membrane potential at different concentrations (Piwnica-Worms et al., 1994). Cultured chick heart cells were treated with varying amounts of ^{99m}Tc-MIBI. The presence of technetium-99m was shown in the mitochondria but not in cytoplasm or other subcellular organelles. EMPA was carried out separately in the different cell compartments, after the location of the cell compartments was determined by the TEM. The level of technetium-99m in the mitochondria was quantifiable and the membrane potential was calculated. As well as determining the subcellular localisation and quantifying the amount in different compartments, EMPA allows for the determination of all the elements present and electron microscopy can be carried out alongside EMPA to determine the ultra-structure of the samples.

EMPA is used alongside secondary ion mass spectrometry (SIMS) and TEM. This has allowed for the determination of the subcellular location of indium after administration of indium nitrate to rats (Maghraoui et al., 2011). EPMA was unable to detect the presence of indium in lysosomes of duodenal enterocytes but these were viewed as electron dense inclusions in the TEM. SIMS was able to detect the electron dense inclusions. The EMPA was unable to detect this, as it only determines the chemical composition, not the biological structure. The EMPA chemical analysis was able to determine that indium was concentrated in lysosomes as insoluble phosphate salts. From SIMS data and TEM images it was suggested that that a new function of the

lysosome is to concentrate mineral elements, which are a defensive reaction of the organism against intoxication by foreign elements.

EMPA allows for the chemical composition to be determined but needs to be used alongside other techniques, such as TEM and SIMS. TEM allows the ultra-structure of the sample to be determined after staining with heavy elements and SIMS allows for histological structure to be determined by imaging the distribution of ions such as calcium (Ca^{2+})**,** cyanide **(**CN^-) and phosphorus (PO_4^{-3}). EMPA is unable to detect different isotopes and is limited to counting the elements present and not the compounds. The limit of detection is approximately 0.05 $mmol^{-1}$ of an element in 0.1 nL of a solution (Roinel, 1984). While it is not a destructive technique, the biological samples are altered by exposure to radiation, leading to less accurate spatial information. EMPA is unable to detect the lightest elements, and it is necessary to know the oxidation state as EMPA analyses are reported as oxides of elements.

1.4.2.3 Secondary Ion Mass Spectrometry

SIMS, like EMPA, involves the use of a primary ion beam that is focused on the surface of a resin-embedded biological tissue section (Fourré et al., 1992). Characteristic secondary ions are produced from the sample surface. The secondary ions are focused, energy-filtered and separated by a mass spectrometer on the basis of their mass-to-charge ratio. This leads to an image of the surface representing its chemical composition (Chandra, 2003). To be detected by ion microscopy, a molecule in a biological specimen must contain a specific atom which is not present in the surrounding cell. SIMS can detect molecules that contain a native halogen atom (Clerc et al., 1993, Chéhadé et al., 1996), as they have a high ionization yield compared with other elements, and they also have a low abundance in cell samples. Other molecules

must first be labelled with either a stable isotope such as nitogen-15 or a radioactive isotope such as carbon-14 (Hindie et al., 1992, Peteranderl and Lechene, 2004). Due to the high sensitivity of SIMS, images can be obtained representing the distributions of these elements at a concentration several orders of magnitude lower than that required by EPMA (Galle et al., 2004).

SIMS has been used to study the subcellular location of N-(2-diethylaminoethyl)-4-iodobenzamide (^{127}I-BZA). It has been studied as an unlabelled (without carbon) and also with carbon-14 bound in different places. These studies were carried out in tissue samples from mice bearing pulmonary colonies of melanoma B16 cells (Chéhadé et al., 2005). The distribution of ^{127}I-BZA was shown, and by using carbon-14 bound to different sites on the molecule, information was gained on the structure of the molecule when at its tissue-binding site. Iodine-127 is a readily ionized halogen, it has a stronger SIMS yield than carbon-14 and provides better contrast images. SIMS images showed the distribution of negatively charged cyanide ions, which allows determination of the tissue structure, including the stratum corneum, the other epidermal layers and the superficial dermis. Using the distribution of phosphorus, internal cell structure can be determined, including the cell nuclei, nucleoli and nuclear membrane. TEM micrographs were compared with SIMS images, allowing for the assumption that the iodine-127 hotspots seen in SIMS corresponded to locations in melanosomes. These are intracytoplasmic organelles that synthesize melanin. SIMS images obtained at different time points after injection showed a similar distribution of carbon-14 and iodine-127. These images allowed the biological half-life of ^{127}I-BZA to be determined. Images showed heterogeneous distribution between cells and distinguished between nuclear and cytoplasmic atom localization. The resolution of the micrographs was between 0.5 and 1 μm. The digital images were used to directly assess the distribution of the

radiopharmaceutical for dose calculations on the cell and tissue level. These images are concentration maps of the radioisotopes being investigated. With this information, MC techniques can be used to determine the dose distribution for a given isotope. (Chéhadé et al., 2005).

SIMS has been used to investigate the localization of MIBG. The effects of MIBG depend, firstly, on the capacity of a tumour to take up and retain the tracer and, secondly, on the intratumoural biodistribution (Clerc et al., 1995). SIMS analysis using ^{76}Br-MIBG and unlabelled MIBG was used to demonstrate intratumoural mapping and quantification of ^{76}Br- MIBG. MIBG was used as the reference tracer. It was seen that both compounds accumulated mainly in the cytosol of the tumour cells with a homogeneous distribution pattern, although chemical processing of the sample may have caused passive drug diffusion, and therefore the redistribution of drugs, which may have been stored in other subcellular organelles. The use of cryo-techniques would reduce this possibility. Quantification of the technique was carried out by using a carbon-12 secondary current which led to a larger than expected mean concentration.

SIMS has also been used to detect technetium-99m, where it was able to detect the nuclear and cytoplasmic distribution of technetium-99m in leukocytes (Fourré et al., 1992), and also to detect gallium (Berry et al., 1983).

The application of SIMS to the analysis of biological specimens has so far been limited, mainly due to poor lateral resolution (1–0.5 μm). SIMS has a detection limit of between 10^{12} and 10^{16} atoms/cm^3, with a minimum detectable concentration of about 1 ppm/μm^3 (Fourré et al., 1996). The technique is destructive: as the sample is imaged, so the surface layer is removed. Thus, if scanning for 90 seconds, 100–300 nm may have been etched away leading to a difference in imaging location (Clerc et al., 1995). The SIMS

signal is not only influenced by the number of molecules in the sample but also by the topography of the sample, the instrumental transmission, the detector response and the chemical composition of the sample matrix; as there can be interaction of the matrix with the primary ion beam, these are matrix effects (Burns et al., 1986). The two main issues are: a variation in the number of atoms physically removed (sputtered) and variation in the number of secondary ions produced under given conditions, even if the matrix composition of elements is similar across different samples (Burns, 1988). Therefore, quantification of SIMS images requires the use of an internal standard of known concentration (Ostrowski et al., 2007). For example, a ubiquitous ion ($C_5H_9^+$) signal has been used to normalize the fatty acid fragment signal when detecting cholesterol (Ostrowski et al., 2004, Monroe et al., 2005).

1.4.2.4 Nanoscale Secondary Ion Mass Spectrometry

However, SIMS has been improved through the development of nanoscale SIMS (NanoSIMS) which incorporates a novel ion nanoprobe that increases the lateral resolution to the range 80–100 nm (Elbast et al., 2008, Guerquin-Kern et al., 2005). NanoSIMS can be used to measure the distribution of any stable isotope as well as any radioisotope with a suitable half-life (Lechene et al., 2006). It can simultaneously detect five different ions from the same micro-volume and has very good transmission (the ratio between the number of ions formed and the number of ions detected) even at high mass resolution (Guerquin-Kern et al., 2005). When using NanoSIMS, ultra-structural details show the nucleus, nucleoli and nuclear envelope, although at much lower resolution than TEM imaging. Like TEM, the cell preparation is complicated, and chemical processing might lead to the relocation of cytosolic components such as diffusible ions and small molecules. NanoSIMS is used to look at biological processes as stable isotopes have little or no effect on the biochemical properties of target

molecules. Since NanoSIMS detects a mass/charge ratio it can discriminate between all elements and their isotopes. Like SIMS, halogens have a strong electron affinity and a high effective ionic yield and are therefore easy to detect when using NanoSIMS.

NanoSIMS was able to demonstrate the spatiotemporal distribution of decay events within the thyroid of newborn rats. Before being scarified, rats were injected with iodine-129 and the method was able to distinguish between iodine-129 and iodine-127. Imaging differentiated between the newly organified iodine (iodine-129) and the iodine pool already present (iodine-127). This showed that within the thyroid of newborn rats the distribution is a function of time and there is variation in uptake between follicles, and variation from one thyrocyte to another inside the same follicle. This was able to allow for an improved dynamic model for the dosimetric evaluation of the thyroid cells (Elbast et al., 2008, Guerquin-Kern et al., 2005).

NanoSIMS allows parallel detection of up to five elements and isotopes up to mass 58. However, above this mass, such as iodine -127 and -129, images must be recorded in two separate acquisitions. This is due to mechanical reasons related to the size of the detectors. This leads to a reduction in resolution as multiple scans are required. There is a reduction in the stability of secondary emissions in biological material. This means more time is required to reach a steady secondary ion intensity, leading to greater destruction of the sample. Important modifications of the matrix can occur during high dose irradiation and, like SIMS, as the surface is destroyed so subsequent scans will image different surfaces, reducing the resolution. When using similar masses of the same element, if it is incorrectly assumed that there is a homogeneous signal, the resolution will be reduced (Elbast et al., 2008, Guerquin-Kern et al., 2005).

The majority of NanoSIMS use in biology has been to detect a range of secondary ions from carbon, hydrogen, nitrogen, sulphurm phosphorous, fluorine and calcium compounds in cell samples (Musat et al., 2008, Peteranderl and Lechene, 2004, Galli Marxer et al., 2005), as well as the previous examples using iodine (Elbast et al., 2008, Guerquin-Kern et al., 2005). However, studies have looked at detecting negatively charged arsenic-75 ion in human hair (Audinot et al., 2004). In control hairs, the natural abundance of arsenic ranges from 0.1 to 1.0 ng/mg, which was difficult to image as there was only sufficient signal intensity at a higher current and a longer acquisition time (40 ms per pixel). In hair spiked with arsenic, ion images show higher arsenic levels, with the average arsenic to cyanide ratio being approximately 20×10^{-5} to 30×10^{-5}. Other examples have shown indium and aluminium traces in rat kidneys. Kidney samples were obtained from rats, 6 hours and 8 days after an intraperitoneal injection of 0.01 mg of indium sulphate, followed by a subcutaneous injection of 0.01 mg of aluminium lactate. There was detection of ions from both elements (Galle et al., 2004). The amount of indium and aluminium lactate was not calculated but was described as high concentrations in small volumes. NanoSIMS could provide accurate information on the location of the subcellular distribution of TRT. However, for the detection of non-halogen isotopes it may be difficult to detect the small ratios, especially if a low amount is distributed relatively evenly throughout the cell. The matrix effects which are observed in SIMS are the same as NanoSIMS. Therefore, detecting small amounts of a TRT agent would require a longer detection time and a reduction in resolution.

NanoSIMS has been used alongside various other techniques, for example using TEM before NanoSIMS. This approach is currently being applied to the imaging of hydroxy apatite agglomerate during the biomineralization process. Only 200 atoms are necessary

to obtain a NanoSIMS signal and the lateral resolution remains between 0.2 and 1 μm. Other groups have used NanoSIMS in combination with fluorescence microscopy, atomic force microscopy (AFM) and EMPA (Jiang et al., 2014), although none of these techniques have looked at using it for dosimetry purposes.

1.4.2.5 Autoradiography

For autoradiography, a sample is placed on to photographic X-ray film and the absorption and scattering of radiation within the sample produces an image on the film. The X-ray film is a crystal lattice of silver halide and bromide. The silver bromide crystals are suspended in gelatine, resulting in each crystal acting as an independent detector. When exposed to light or emissions from radioactive decay, the grains are converted into metallic silver to produce a latent image, which is then developed.

Autoradiography has been used extensively to study the macroscopic distribution of radiopharmaceuticals. For example, multicellular models using neuroblastoma spheroids were incubated with ^{125}I-MIBG, the mAb ^{125}I-UJ13A or nerve growth factor ^{125}I-βNGF, to compare the ability of these compounds to penetrate into the multicellular model (Mairs et al., 1991). The radioactive compounds were added to the cell medium, before 20 μm thick sections of the spheroids were used for autoradiography. Autoradiographs showed the superior penetration of radiolabelled MIBG relative to UJ13A. There was reduced uptake of MIBG in necrotic areas of the spheroid (as shown by haematoxylin and esoin staining). The UJ13A mAb was unable to penetrate beyond the outer cell layers, hence the reduced uptake, and localisation was limited to the surface of the spheroid. The sections were placed on X-ray film alongside known concentrations of iodine-125, this allowed for quantitation of the autoradiographs using the optical density of autoradiograms. From this, the average concentrations of MIBG

was calculated to be 0.09, 0.63 and 1.12 MBq/g after 10, 60 and 120 minutes' incubation respectively. The autoradiograms also showed that ^{125}I-βNGF had a uniform distribution but at a much lower concentration, approximately 2–3 % of that of MIBG.

Experiments using autoradiography in human colon carcinoma cells have shown quantification and spatial distribution in the millimetre range when using ^{64}Cu-diacetyl-bis(N^4 -methylthiosemicarbazone) (^{64}Cu-ATSM). The study showed that the peripheral regions of the tumour model were high-uptake regions and the central regions low-uptake regions. A calibration curve which correlated photostimulated luminescence intensity to known concentrations of copper-64 was calculated. This allowed the percentage of injected dose per gram (%ID/g) to be determined from densitometric measurements. For example, a photostimulated luminescence intensity of 50% was approximately equal to 7.5 %ID/g (Yoshii et al., 2016). Double tracer-autoradiography, using different films to detect different isotopes, has been carried out looking at a fludeoxyglucose-18 and ^{64}Cu-ATSM. Uptake was compared on the same sections showing the difference in metabolic activity and uptake of the radiopharmaceutical. This was only possible due to the short half-life of fluoride-18, as the two autoradiographs were carried out at different times (Yoshii et al., 2010). In both cases, images were analysed using a laser scanner and filmless autoradiography, improving the resolution of images and allowing for faster imaging.

The technique is simple, quantifiable and can be carried out with fast automated analysis. Films used are often designed for the detection of tritium, carbon-14, sulphur-35, phosphorus-33 and phosphorus-32 which are used as radioactive tracers to determine the biological processes which occur within cells. The resolution achieved is

in the region of millimetres. Phosphorous screens have a similar, if not worse, resolution than X-ray films, depending on the isotope (Johnström et al., 2012).

1.4.2.6 Microautoradiography

Similar to autoradiography, microautoradiography (MAR) relies on detection of a radioisotope by a silver bromide crystal. In the case of MAR, the crystals are smaller and are suspended in a liquid emulsion, which is applied to single cells or cell sections containing radioactivity. As in autoradiography, the grain density per unit area is proportional to the radioactivity and can therefore be used quantitatively as a measure of radioactive tissue concentration (Puncher and Blower, 1994).

In a study by Puncher and Blower, frozen section MAR has been carried out with indium-111 labelled to oxine (Puncher and Blower, 1995). Firstly, a calibration experiment showed a linear relationship between grain density and specific activity. As well as this standard, the grain density was plotted as a distance from the source edge suggesting that the resolution was approximately 2 µm. When ^{111}In-oxine was mixed with the leukocytes of homogenized rat liver, it was shown that there was variation in uptake of indium-111 across the leukocytes. They were able to identify neutrophils, eosinophils and mononuclear cells, although they could not distinguish between different types of mononuclear cells. With the calibration curve, it was possible to show the difference in uptake at the cellular level and determine the differences.

MAR has been used with spheroid models (Neshasteh-Riz et al., 1997). These have shown different amounts of radioactivity within different regions of the spheroid. Spheroids were grown to between 150 µm and 1000 µm diameter, and incubated with ^{125}IUdR at a concentration 0.06 MBq/ml in 10 mL. Spheroids were then embedded in

mounting medium, cut into 5 µm sections and placed on histology slides. Slides were dipped in emulsion and left for an exposure period of 92 hours. After development, cells in the spheroids sections were classed as either labelled or unlabelled for ^{125}IUdR. A cell which was classed as labelled had ten or more silver grains overlying the nucleus. This allowed for the ratio, described as the labelling indices, to be calculated. The labelling indices were determined as the ratio of labelled cell nuclei to unlabelled cell nuclei in predefined regions of the spheroid sections. These predefined regions were sub-regions of concentric tissue layers; an outer layer, a middle layer and an inner layer. Overall, the results showed that as the size of the spheroid increased, so the labelling index decreased with increasing depth within the spheroid. The labelling index in the inner and middle layer increased as the incubation time increased.

MAR has also been carried out used human tumour specimens (Bodei et al., 2003). Tumours were removed 24 hours after intraumoural injection of ^{125}IUdR and showed accumulation of radioactivity specifically in tumour cells but not in normal cells. There were different levels of uptake in different types of tumour, with the largest number of silver halide grains in colorectal cancer and the lowest number of grains in gastric cancer. MAR was able to show that cell tumour incorporation of ^{125}IUdR is strictly confined to the cell nucleus, and ^{125}IUdR incorporation is confined to cells in the most superficial layers of the bladder cancer. This is not observed in the experimental bladder cancel model. These results suggest that poor diffusion in the tumour mass makes ^{125}IUdR unsuitable for intracavitary therapy of bladder cancer.

To improve the resolution of images, electron microscope-microautoradiography (EM-MAR) can be used which allows the subcellular distribution to be obtained. Studies have been used with ^{111}In-oxide allowing for *in vivo* studies of cell kinetics and cell

distribution of neutrophils, since ^{111}In-labelled cells retain their normal function and physical properties. Experiments were conducted with alveolar macrophages and monocytes which were incubated with 0.5 µg of oxine per 10^6 cells, and radiolabelled at a concentration of 0.37 MBq of indium-111 to 50 µl of oxine (Davis et al., 1980). The silver grains in different cell compartments including nuclei, mitochondria, lysosomal granules, vacuoles, Golgi and other cytoplasmic structures were counted. The number of grains expected over each organelle (if there was uniform distribution) was calculated. This was done by multiplying the total number of grains over the cell by the volume density of each of the organelles. The number of grains actually observed over each organelle was compared to the expected number by χ^2 analysis. This showed greater accumulation in the cell nucleus.

EM-MAR has also been used to look at the radiopharmaceutical [^{111}In-DTPA-$_D$-Phe^1]-octreotide, which targets somatostatin receptors. Tissue samples were taken from patients who had been treated with the radiopharmaceutical 1 day before. Grid sections showed poor morphological staining which occurred as part of the MAR procedure, as control samples not exposed to the emulsion showed good morphological structure. The micrographs showed the location of the radioactivity in the plasma membrane, and within vacuoles in the cell and in the cell nucleus, although quantification was not carried out (Janson et al., 2000). However, the use of EM-MAR for TRT has been limited. EM-MAR has been used for imaging ^{3}H-thyminde for DNA synthesis in cell culture or living tissues and other tritium incorporated molecules, although the techniques and resolution are the same (Lundberg et al., 1996, Marc and Liu, 1984, Zhou et al., 1998, Bard and Abbott, 1979).

Issues with MAR include the difficulty of matching the position in the emulsion with the cellular site of radioactive emission and the difficulty of assessing local concentration, as the yield quantification is imprecise (Crane et al., 1993). When carrying out MAR on whole cells, the internal radioactivity will be shielded by either the cell, as the emissions do not reach the MAR grains, or other radionuclides which are closer to the MAR grains. The MAR grains are a binary detection system so electron emissions which would have been detected by an already converted grain are not. However, when carrying out EM-MAR ultrathin sections (~100 nm) are used, so that shielding of internal emissions does not occur. MAR at the resolution of optical microscopy is not capable of distinguishing between different targets in the cell (Puncher and Blower, 1994). Other problems include a high background and the limited range of detection–there is a narrow range of activities which can be measured in one sample as the development conditions depend on the radioactivity present.

1.4.2.7 Photoresist Autoradiography

Photoresist autoradiography (PAR) was first described by Falzone et al. in 2011 to provide a quantitative autoradiographic technique (Falzone et al., 2011). Three photoresists were used: the organic photoresist poly (methyl methacrylate) (PMMA) and the chemically amplified photoresists (CARs) AZ40XT and UV1116. In summary, the PMMA was able to detect doses of between 10 μC/cm^2 and 1300 μC/cm^2; UV1116 and AZ40XT were both able to resolve patterns of 0.5 nm depth; and shallower patterns could be seen optically but were not resolvable when using the AFM. UV1116 had a detection range of 10 μC/cm^2 to 3000 μC/cm^2. At doses above this, contrast-reversal was seen and at doses below 10 μC/cm^2, swelling was observed. This swelling was not dependent on the dose. Swelling was caused by ingress of fluid during chemical development. To resolve this issue a post-bake was carried out, removing the swelling.

AZ40XT had better contrast at exposure doses above 10 μC/cm^2 but cross-linking took place for exposure doses above 50 μC/cm^2, limiting its dynamic range. For UV1116 and AZ40XT, the relationship between pattern depth and fluence was non-linear but for PMMA, under the development conditions used, there was a near linear log-log dependence on the depths.

The photoresists were exposed to indium-111 which had been internalised into cells after incubation with ^{111}In-DTPA-hEGF. Cells and cell nuclei, which were isolated after incubation with ^{111}In-DTPA-hEGF, were placed on the photoresists. These created patterns in the surface of the UV1116 and AZ40XT. However, cellular patterns were not demonstrated for PMMA as there was not sufficient contrast. The cellular patterns on UV1116 showed swelling as well as depressions, suggesting a range of doses across cells and cell nuclei. AZ40XT was shown to be more sensitive but with lower resolution.

While PMMA is less sensitive that CARs, it has several other advantages over CARs, including a more reproducible development process. The development of CARs are more complex and less robust due to the chemical effects of the acid species which diffuse over several nanometres from the exposed area (Grigorescu and Hagen, 2009). PMMA is relatively insensitive compared with UV1116 over the fluence range 1–33.6 μC/cm^2, although it has been reported that low-energy (10–50 keV) electrons are as efficient in producing damage in PMMA as higher energy electrons (Bermudez, 1999). Therefore, the processing and development conditions were improved in order to allow for cellular patterns to be demonstrated in PMMA (Royle, 2012). Firstly, the resist thickness was varied, as an ultra-thin resist layer suppresses small angle scattering and enhances back-scattering, but a thicker resist layer increases the dynamic range of the

resist. The greatest contrast was seen with the thinner resist layer and so this was used with cellular experiments. Secondly, the development time and developer concentration was varied. A longer development time gave deeper patterns and hence greater sensitivity but increased the surface roughness and reduced the resolution of the PMMA. Increasing the concentration of developer both increased sensitivity and increased the surface roughness. In all cases increasing the surface roughness reduces the resolution. Other developments of the technique included using a gold layer to enhance electron back-scattering. This increased the sensitivity of the photoresist and reduced the resolution. However, the increase in sensitivity was enough to offset the reduction in resolution. These improvements to the processing of the PMMA led to cellular patterns being demonstrated (Royle, 2012).

Photoresists and AFM have also been used to characterise single alpha tracks, where SU-8 and PMMA have been used as negative tone photoresists (Falzone et al., 2013, Myhra et al., 2014). PMMA was shown to have undergone a cross-linking reaction and contrast reversal, believed to occur at fluences greater than 300 $\mu C/cm^2$ (Puttaraksa et al., 2012, Lee et al., 1999), leading to spikes in the photoresist surface. These appear hard when imaged using the AFM in phase contrast mode. The photoresist response was linear with the fluence. The resolution achieved in PMMA was in the order of nanometres. This research did not look at internalised radioisotopes. However, cells were exposed to an external source of radiation to mirror the cross-fire effect. PMMA was able to show spikes corresponding to the location of the alpha tracks.

1.4.3 Summary of Current Methods

Cell variability assays are able to determine if the radiopharmaceutical is effective at causing cell killing and can provide information leading to survival curves and hence

the dose response of cells to a treatment. However, they do not provide quantitative or spatial uptake of the radiopharmaceutical. Biomarkers are able to provide spatial information and quantitative information at the cellular level but are only able to measure the effects of radiation which may or may not be correlated with dose. Internalisation studies provide quantitative information about uptake into subcellular compartments but do not inform the heterogeneity of uptake. These types of studies are often used in combination to inform further research.

EMPA and SIMS provide quantitative spatial information from individual cells but may not be sensitive enough to detect the small quantities of a radiopharmaceutical; they require specialist knowledge and techniques. Autoradiography provides a quantitative and spatial uptake on a multicellular level and MAR provides this information on a cellular level or, if using EM-MAR, a subcellular level. PAR is able to demonstrate nanoscale resolution and a differing response of the photoresists to different fluences, suggests that the technique can be quantitative.

For AE TRT, the most AE have a range in the order of nanometres (O'Donoghue and Wheldon, 1996), hence they need to be located close to their target in order to be effective. Techniques which determine the location of AE need to have a spatial resolution of the same length scale as their range in biological material in order to allow accurate modelling. Therefore, new methods to determine the intracellular distribution of the radionuclides need to be developed, as none of the current techniques are able to provide a high enough resolution or quantitative information about the non-uniform exposure at cellular and subcellular level.

1.5 Aim of the Thesis

The aim of this work is to investigate novel methods for determining the subcellular spatial distribution of AE-emitting radiopharmaceuticals and to investigate methods which allow for the quantification of radionuclide energy deposition. The development of these techniques aims to provide more accurate information for microdosimetric modelling, compared with current techniques available.

To investigate these techniques, ^{111}In-DTPA-hEGF is used as the radiopharmaceutical as it localizes to the cell nucleus. Two novel methods for determining the subcellular spatial distribution are investigated. Firstly, the PAR technique is adapted to consider PMMA as a photoresist substrate. To investigate PMMA, MC modelling looks at the energy deposited in PMMA photoresists and different methods for obtaining PAR images from cells exposed to ^{111}In-DTPA-hEGF are considered. An attempt at quantifying the information gained from cellular experiments is made. Secondly, EM-MAR is explored, aiming to obtain more detailed spatial distribution information about the subcellular location of ^{111}In-DTPA-hEGF.

Chapter 2:
Materials and Methods

Chapter 2:

Materials and Methods

2.1 General Materials and Methods

2.1.1 Cell Culture

Cell lines used in this work were a head and neck squamous cell carcinoma, SQ20B, and the breast cancer cell line, MDA-MB-468. These were obtained from the American Type Tissue Culture Collection. The cells were cultured in Dulbecco's Modified Eagle's medium (DMEM; Sigma-Aldrich, #D5796), supplemented with 10 % foetal calf serum (Gibco, #10270), 100 units/mL penicillin and 100 µg/mL streptomycin (Sigma-Aldrich, #G1146) in a standard humidified incubator at 37°C and 5 % CO_2. Cells were regularly passaged using 0.05 % trypsin-ethylenediaminetetraacetic acid (trypsin, Gibco, #25300-054) when below 80 % confluency. Only cells that had been passaged fewer than 15 times were used for experiments. Cells were routinely tested for mycoplasma infection using the MycoAlert testing kit (Lonza, #LT07) according to the manufacturer's instructions.

Cells were counted using a NucleoCounter (chemometec, NC-100). To do this, 100 µL of DMEM containing cells was mixed with 100 µL of reagent A (chemometec, #910-0003) and reagent B (chemometec, #910-0002). This was added to a NucleoCassette (chemometec, #941-0002) which was placed into the NucleoCounter.

2.1.2 Synthesis of ^{111}In-DTPA-hEGF

The radiopharmaceutical was prepared in two stages. The first stage was the conjugation of diethylenetriaminepentaacetic acid dianhydride (DTPA; Sigma-Aldrich, #D6148) and human epidermal growth factor (hEGF; Peprotech, #AF-100-15). This was used immediately, or refrigerated at 4^{o}C for up to 1 month for later use. The second

step was the radiolabelling of the DTPA-hEGF compound, with indium–111 ($^{111}InCl_3$, Mallinckrodt, #DRN4901) and used immediately.

2.1.2.1 Conjugation on DTPA to hEGF

The DTPA-hEGF was prepared by diluting a five times molar excess of DTPA, (13.5 µg), with 10 µL of dry dimethyl sulfoxide (DMSO; from 1 mg/mL stock solution; Sigma-Aldrich, #276855). The solution was added to hEGF (50 µg) which had been dissolved in 0.1 M sodium bicarbonate (pH 8.3, 1 mg/mL, Sigma-Aldrich, #S5761) and incubated at room temperature for 45 minutes.

To purify the DTPA-hEGF from free DTPA, size exclusion chromatography was performed. The DTPA-hEGF in DMSO was added to a Sephadex G25 size exclusion column (Sigma-Aldrich, #G25150), then 20 fractions of 100 µL phosphate-buffered saline (PBS) were added to the column. The eluate of each fraction was collected in separate centrifuge tubes. The concentration of DTPA-hEGF in each fraction was calculated using a NanoDrop spectrophotometer (NanoDrop, #ND 1000), where the absorbance of each fraction was measured at 280 nm. The five fractions with the highest concentration were combined YM3 column (Amicon µltra YM column, cutoff 3 KDa; Millipore, #UFC500396). The YM3 column was centrifuged (17, 000 x g, 20 minutes) and the eluate discarded.

For buffer exchange, 500 µL of sodium citrate (0.1 M, pH 5.0, Sigma-Aldrich, #71498) was added to the YM3 column and centrifuged (17, 000 x g, 20 minutes). The eluate was discarded and the contents of the YM3 column (DPTA-hEGF) were collected by inverting the YM3 column into a centrifuge tube and centrifuging (900 x g, 3 minutes). The final concentration of DTPA-hEGF was calculated using spectrophotometrical

analysis, at 280 nm, with standard curves. The concentration was between 0.9 and 1.2 µg/µL.

2.1.2.2 Radiolabelling of DTPA-hEGF

Immediately before experiments were carried out, 8 MBq of $^{111}InCl_3$ was added to a centrifuge tube containing 1 µg of DTPA-hEGF and incubated at room temperature for 45 minutes. The radiochemical purity of ^{111}In-DTPA-hEGF was determined by silica gel instant thin-layer chromatography (ITLC) using glass microfibre chromatography paper (Varian, #A120B12), in 0.1 M sodium citrate (pH 5.0) (Reilly et al., 2004). The paper was cut in two (a bound and an unbound fraction) and each half was counted, using an automatic gamma-counter (Wizard^2 3"automatic gamma-counter, Perkin-Elmer, 2480). The binding efficiency ranged from 85 % to 95 %.

2.1.3 Exposure of the Cells to ^{111}In-DTPA-hEGF

Cells were exposed to ^{111}In-DTPA-hEGF at a standard concentration of 40 nM/mL, ten times the dissociation constant of ^{111}In-DTPA-hEGF, which allows for 90.9 % EGFR receptor coverage. A similar amount was used in previous work (Cai et al., 2008).

2.1.4 Statistical Analysis

GraphPad Prism 5 software was used to perform statistical analysis. Where statistical analysis was performed, information regarding the particular statistical test is provided in the figure legend. The statistical significance achieved is indicated as follows: * $P \leq 0.05$; ** $P \leq 0.01$; *** $P \leq 0.001$.

2.2 Characterisation of Cell Lines

2.2.1 Competition Binding

SQ20B and MDA-MB-468 cell lines were plated into a 24-well plate (Greiner bio-one #662 160), at a seeding density of 2 x 10^5, and left to adhere overnight. Cells were washed in cold PBS, then 8 nM ^{111}In-DTPA-hEGF, radiolabelled to a low specific activity (1 MBq/µg), was added to the wells. Unlabelled DTPA-hEGF was added in increasing concentrations (0.01 nM to 1,000 nM) to the wells. The total volume in each well was then made up to 500 µL, by adding cold PBS.

Cells were incubated for 2 hours at 4°C. After this, the PBS (containing the unbound DTPA-hEGF and ^{111}In-DTPA-hEGF) was aspirated. The cells were then washed twice in 500 µL of PBS. Next, 500 µL of sodium hydroxide (0.1 M; Sigma-Aldrich #72068) was added to the cells and incubated at room temperature for 30 minutes. After 30 minutes the sodium hydroxide was removed and added to fresh counting tubes. Cells were washed twice in PBS and the waste was collected in the same tubes as the sodium hydroxide.

Tubes were counted in an automatic gamma-counter (Wizard^2 3"automatic gamma-counter, Perkin-Elmer, 2480). Data was fitted using GraphPad Prism 5.0 and plotted with the inbuilt equation in '*log (inhibitor) vs. response -- variable slope curve'* ($Y = Botton + \frac{Top-Bottom}{1+10^{Log(IC_{50})-x*Hillslope}}$) which was used to calculate the total binding, non-specific binding and B_{max}. This information was used, together with the protein concentration obtained from a bicinchoninic acid assay (BCA), to obtain the number of receptors per cell.

2.2.2 Bicinchoninic Acid Assay

A BCA assay was carried out according to the manufacturers' standard protocol (BCA Assay kit, Thermo scientific #23225), by Mrs Sarah Able. Briefly, SQ20B and MDA-MB-468 cells were grown to 80 % confluency in a T-25 flask (Greiner bio-one, #658170). The DMEM was removed and the cells were washed with PBS. Ice-cold RIPA buffer (1 mL; Sigma-Aldrich, #R0278) containing protease inhibitors (Roche Complete Mini, #836170001) was added and the flask was incubated on ice for 5 minutes. Cells were then removed from the flask with a cell scraper (Sigma-Aldrich; #CLS3010) and the cell suspension was transferred to a 15 mL falcon tube and centrifuged (4°C, 8000 x g, 10 minutes). The supernatant containing cell lysate was maintained on ice throughout the experiment.

A standard curve was constructed by dilution of BSA (Sigma-Aldrich #A7906) solution in RIPA buffer to give concentrations of 2 to 0.025 mg/mL. Standards and samples (25 µL) were added to duplicate wells of a 96-well plate (Greiner bio-one #655101). Working reagent was prepared by mixing solutions A (bicinchoninic acid) and B (cupric sulphate) from the assay kit in a 50:1 ratio. Working reagent (200 µL) was added to each well of the plate. The plate was mixed briefly before being incubated at 37°C for 30 minutes.

The plate was cooled to room temperature and absorbance at 562 nm wavelength was measured using a plate reader (Tecan Infinite Fluorescence plate reader, #M2000). A standard curve was then plotted to determine the protein concentration of the cell lysate.

2.2.3 Flow Cytometry

Cells were harvested by trypsinization (Gibco, #25300-054) and diluted to 1 x 10^6 cells/mL in 15 mL falcon tubes. The cells were centrifugated (500 g, 5 minutes) and the

supernatant removed. Cells were washed twice in PBS and fixed in 4 % PFA (Sigma-Aldrich #252549) for 10 minutes. To permeabilise the cells, 1 % triton (Triton X-100, Sigma-Aldrich, #T9284) was added.

Cells were washed in PBS before being incubated in blocking buffer at room temperature (2 % BSA). After 1 hour, the blocking buffer was removed and the cells washed in PBS. EGF was biotinylated and complexed to Alexa Fluor® 488 Streptavidin (Alexa Fluor® 488 EGF complex, life technologies #E-13345) and 12 nM (30 µL) was added per million cells. Cells were incubated at 4°C with constant shaking (MACSmix Tube Rotator, Miltenyi Biotec Ltd., #130-090-753) for 1 hour.

Cells were pelleted by centrifugation and washed in PBS. They were then stored overnight in the dark in PBS containing 50 µg/mL propidium iodide (life technologies, #P3566) and 20 µg/mL RNase (Ribonuclease A from bovine pancreas (RNAse; Sigma, #R4875).

Flow cytometry was carried out using FACS Calibur, (Becton Dickinson) and Cell Quest Pro software (Becton Dickinson, version 6.0.4). Green and red florescence histograms were collected and data was analysed with Flowjo version 10.1. Data was fitted using GraphPad Prism 5.0.

2.2.4 Internalisation Assay

SQ20B cells were plated into a 24-well plate (Greiner bio-one, #662 160) at a seeding density of 2 x 10^5 and left to adhere overnight. The DMEM was replaced with fresh DMEM immediately prior to the addition of ^{111}In-DTPA-hEGF. Cells were treated for the indicated time (1 or 24 hours) in a total volume of 500 µL of DMEM with 20 nM ^{111}In-DTPA-hEGF (40 nM/mL).

Following incubation the DMEM was aspirated and collected in counting tubes. Cells were then washed twice with PBS (500 μL) and the washes combined with the DMEM to constitute the free-fraction. Cell membranes were washed using 500 μL glycine (0.1 M, pH 2.5, Sigma-Aldrich #G8898) and incubated at 4 °C for 6 minutes. After this, the glycine was collected in counting tubes and then the cells were washed twice with 500 μL PBS. The PBS washes were collected in the same counting tubes. Finally, 500 μL of sodium hydroxide (0.1 M Sigma-Aldrich #72068) was added and plates incubated for 30 minutes at room temperature to lyse the cells. The internalised fraction was then collected and combined with the two PBS washes (500 μL).

The tubes were counted in an automatic gamma-counter (Wizard^2 3"automatic gamma-counter, Perkin-Elmer, 2480). To facilitate counting, PBS was added to fractions to give a final volume of 2 mL. The fractions were stored to allow radioactive decay to a level that did not exceed the range of the detector.

2.3 Photoresist Autoradiography

2.3.1 An Overview of the Photoresist Autoradiographic Technique

Photoresists autoradiography (PAR) utilizes photoresists as a material for the detection of ionizing radiation from intra-cellularly distributed Auger electron (AE) emitting radionuclides. Photoresists are photosensitive materials and different types exist. When exposed to radiation they undergo chemical changes that depend on the type of resist. There are two ways that photoresists can be used: as positive and negative tone resists. Negative tone resists are when the radiation exposure causes a change in the chemical structure and the unexposed region is removed by the developer. This creates raised radiation features. Positive tone resists are when the exposed region is removed by the developer.

The photoresist used in this work was poly (methyl methyl methacrylate) (PMMA) can be used for both negative and positive tone application. In PAR, PMMA is used as a positive tone resist. In this case, exposure of PMMA causes chain-scission of the polymer backbone, this leaves shorter chain fragments within the PMMA. These shorter chain fragments are then removed by the developer (Reichmanis and Thompson, 1989), and cause patterns in the surface of the photoresist. These can be detected by an atomic force microscope (AFM).

The PAR experimental process is shown schematically in Figure 2.1. The sensitivity of the PMMA as a function of fluence and electron energy was calibrated by using an electron beam. An electron beam lithography system is commonly used in the processing of photoresists such as those used in micro-electro-mechanical systems. A beam of electrons is accelerated through a known voltage (25 keV and 50 keV) and

current (10 pA) and the used to create a custom made pattern or latent image in the surface of the photoresists. This pattern is computer generated, and directs the electron beam. For PAR a pattern file with the electron beam exposed 5x5 μm^2 areas to difference fluences was used (Falzone et al. 2012, Royle, 2012, Royle, 2015). The resultant patterns written to the resists were developed and depths were measured from line scans through the AFM image (Figure 2.1a). The volumes of the patterns were related to the known fluence. Functionalized microspheres were radiolabelled to similar activities which have been demonstrated in cellular experiments (Royle et al., 2015) and were used as a model system (Figure 2.1b). The method was then demonstrated for cells and isolated cell nuclei (Figure 2.1c–d).

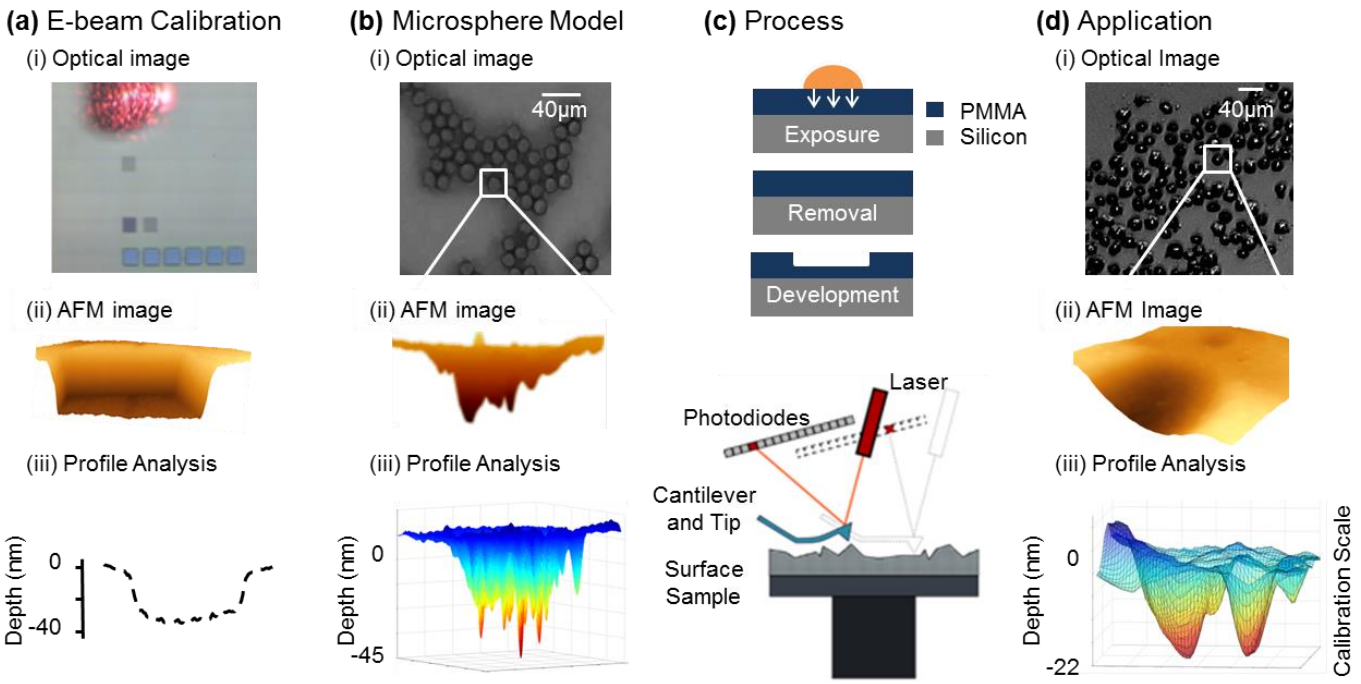

Figure 2.1: Schema of the photoresist autoradiography technique
(a) Electron beam calibration: (i) 5x5 μm^2 patterns of varying fluence incident on the PMMA substrate (the laser reflecting off the AFM probe is shown). (ii) AFM image of 5x5 μm^2 electron beam feature, and (iii) line scan relating depth to electron fluence. (b) Model system consisting of ^{111}In-labelled microspheres: (i) optical image showing the close packing of the microspheres on the PMMA surface, (ii) AFM contour through image of a radiolabelled microsphere pattern and (iii) 3-D generated profile of the AFM feature. (c) Resist exposed to radionuclide treated cells and isolated cell nuclei, followed by removal of biological material and chemical development of the resist and AFM analysis of the pattern. (d) Demonstration of PAR with ^{111}In-DTPA-hEGF treated cells: (i) optical image of radionuclide treated SQ20B cells, (ii) AFM image of an ^{111}In-DTPA-hEGF treated cell pattern and (iii) 3-D generated plot of an AFM image of a cell nucleus.

2.3.2 Photoresist Autoradiography Experimental Protocol

An outline of the PAR methodology is shown below. Briefly, prepared photoresists were exposed to a source of electrons before being developed and analysed using the atomic force microscope (AFM).

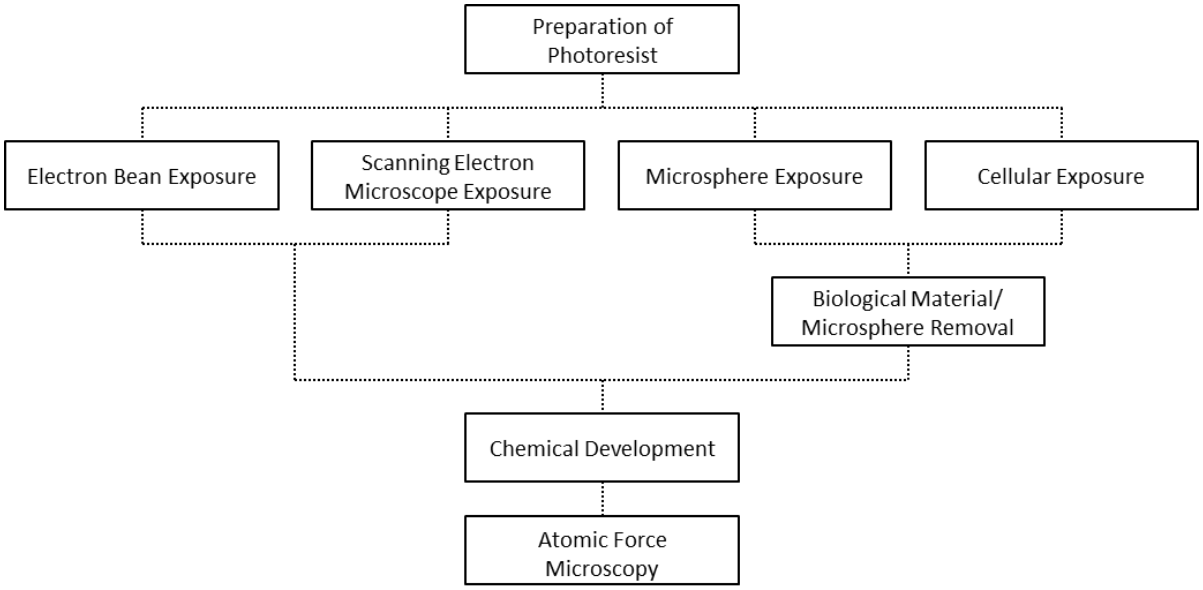

Figure 2.2: A flow diagram of the photoresist autoradiography methodology

2.3.3 Preparation of the Photoresists

Silicon substrates (University wafers, 1317; (100) orientation), with original diameters of 100 mm, were cut into 3 x 5 mm^2 pieces (Electronic Micro Systems Ltd; Micro Ace 3 Dicer Loadpoint). A 5–10 nm thick chrome layer was then thermally evaporated on top of the substrate in a thermal evaporator (Eurocoater thermal evaporator; 18B) with an initial vacuum of better than 10^{-6} mBar. Without breaking the vacuum, a 100 nm thick gold layer was thermally evaporated on top of the chrome layer. The thicknesses of these films were monitored with a quartz thickness monitor within the thermal evaporator and the deposition was stopped when the correct thickness was reached. The prepared substrates were then pre-dehydrated by baking at 140°C for 20 minutes using

a hotplate (Electronic Micro Systems Ltd, Electronic Hot Plate Model 1000-1). For exposure in the scanning electron microscope (SEM), the silicon substrates were diced into 10x10 mm^2 sections and processed as above.

In a yellow room, designed for photolithography, (Class 1000 clean room with all light fittings filtered for photoresist processing) PMMA photoresists (NANO^{TM}PMMA, MicroChem) at two molecular weights, 495, 000 (495 K) and 950,000 (950 K), were dissolved in anisole ($CH_3OC_6H_5$). They were then spin-coated (Electronic Micro Systems Ltd, EMS Spin Coater Model 6000, 500 rpm for 5 seconds, and then 4000 rpm) for 45 seconds to give a thickness of 1.4 μm (MicroChem, 2001). Spin coating was followed by a soft-bake using a hotplate (pre-exposure bake) at 120°C for 90 seconds (Falzone et al., 2012, Royle et al. 2015). For samples exposed in the SEM, a thick layer of PMMA 950 K (3.2 μm) was obtained by drop-casting: a droplet of PMMA is placed on the silicon substrate and then the solvent is allowed to evaporate

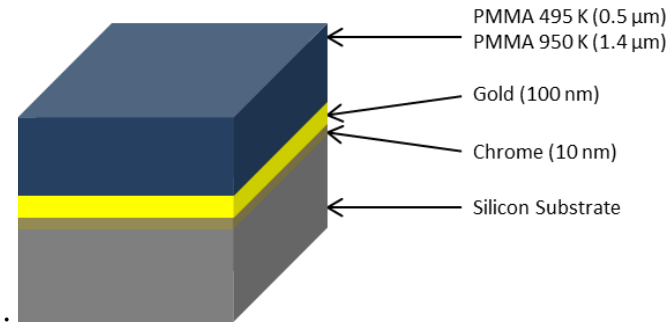

Figure 2.3: A PMMA photoresist

2.3.4 Exposure of the Photoresists

2.3.4.1 Electron Beam Exposure

Electron beam exposure was carried out to relate a particular topographical change of the developed resist to a certain fluence. The electron beam exposure was carried out under yellow room conditions using a JEOL, JBX 5500FS electron beam, with the help of Dr Thomas Altebaeumer (Department of Physics, University of Oxford), and was

operated at accelerating voltages of 50 keV and 25 keV creating a monoenergetic beam, perpendicular to the surface with a beam current of 10 pA, and near the maximum scan rate (12 MHz). The beam size was 2 nm, and the step size varied from 10 - 200 nm. To avoid unwanted pixelation due to the larger step sizes, the electron beam was slightly defocused. Regions (5x5 μm^2) of different exposure doses were written in the photoresists. The divergence of the beam was considered to be negligible due to the patterns sizes being order of magnitude (1000x) greater than the beam size and the two points for depth measurement taken in the centre of the exposed region and distant (micrometers away) from the interface of the exposed and unexposed region. The fluence used to etch the pattern ranged, in logarithmic decrements, from 2.1 x 10^6 $e^-/\mu m^2$ to below the detection limit of the AFM, (6.2 x 10^5 $e^-/\mu m^2$). After exposure resists were chemically developed (Falzone et al., 2012, Royle et al. 2015).

2.3.4.2 Scanning Electron Microscope Exposure

The thick PMMA samples were placed on a SEM stub and into an SEM (JOEL, JSM-6480LV). The photoresists were exposed to the 30 keV electron bean for 1 hour to allow for an exposure dose of approximately 1 x 10^8 electrons (10^3 $\mu C/cm^2$). After exposure resists were chemically developed. This was carried out by Dr Sverre Myhra, Department of Materials, University of Oxford.

2.3.4.3 ^{111}In-labelled Microspheres Exposure

Preparation of Microspheres

To expose the photoresist to electrons with different energies, polystyrene microspheres with a diameter of 6.77 μm and coated in bovine serum albina (BSA), were radiolabelled with indium-111 and left to expose the photoresist for four half-lives. The day before radiolabelling, the BSA-coated microspheres (Spherotech, #PP-60-10)

underwent a buffer exchange. The stock pot was vortexed before being sonicated for 5 minutes, to resuspend the microspheres. Then 250 µL of the microspheres was removed from the stock pot and was pelleted by centrifugation (9.6 x g, 10 minutes). The supernatant was then removed, and the microspheres resuspended in 500 µL of iodogen buffer (Na_2HPO_4, 0.1 M, pH 8.5; Sigma-Aldrich, #255793). The microspheres were sonicated for 5 minutes, pelleted (9.6 x g, 10 minutes) and the supernatant was then removed. Microspheres were resuspended in 500 µL iodogen buffer and sonicated for 30 minutes. Microspheres were then pelleted and the iodogen buffer was replaced and microspheres were stored at 4°C overnight. Before radiolabelling, the microspheres were centrifuged (9.6 x g, 8 minutes) and the supernatant removed.

The microspheres were labelled with p-SCN-Bn-DTPA (pDTPA, Macrocyclics, #B-305). This was dissolved in DMSO (1 µg/µL) and 150 µL of pDTPA-DMSO was added to the prepared microspheres. These were vortexed for 1 minute before being incubated at room temperature for 45 minutes. After incubation, microspheres were centrifuged (9.6 x g, 10 minutes) and washed twice in citrate buffer (sodium citrate, 0.1 M, pH 5; Sigma-Aldrich, #71498). Microspheres were resuspended in citrate buffer (500 µL) and counted using a hymotymeter (on average 10^6 per 100 µL).

Radiolabelling of the Microspheres

To radiolabel the microspheres, pDTPA-coated microspheres (100 µL) were incubated with varying amounts (an average activity per microsphere of 210 mBq, 300 mBq, 420 mBq and 640 mBq) of $^{111}InCl_3$ (Mallinckrodt, #DRN4901) for 1 hour at room temperature. After 1 hour, the microspheres were centrifuged (9.6 x g, 10 minutes) and the supernatant was removed. The microspheres were resuspended in citrate buffer (100µl), and then washed in citrate buffer and resuspended in distilled water (d.H_2O).

The radiolabelling efficiency was calculated to obtain the average activity per sphere. To do this, 2 µL was removed from the radiolabelled microspheres and added to a Y30 column (Amicon µltra YM 30 column, cutoff 30 KDa Millipore, #UFC5030BK) together with 500 µL of d.H_2O. The Y30 column was centrifuged (16.2 x g, 10 minutes), and the eluate from the column was collected and added to a counting tube. Another 500 µL of d.H_2O was added to the Y30 column and it was again centrifuged (16.2 x g, 10 minutes). The eluate was collected and combined with the first eluate and placed in a counting tube. The Y30 column was added to a second counting tube. These were then counted in an automatic gamma-counter ($Wizard_2$ 3" Automatic gamma-counter, Perkin-Elmer 2480). The binding efficiency was calculated as:

$$\frac{YM30}{Eluate+YM30} * 100.$$

Exposure of the Photoresists to Radiolabelled Microsphere

Radiolabelled microspheres (2 µL) were placed on the resists under dark room conditions. The resists were exposed for four half-lives ($T_{1/2}$ indium-111 2.81 days, four half-lives is approximately 10 days), in the dark, and then the microspheres were removed from the resist by washing in double distilled water (d.d.H_2O) for up to 8 minutes. Washing stopped when no debris was seen under an optical microscope (Vickers photoplan, filtered for use in yellow room conditions). The resists were then chemically developed (Royle et al., 2015).

2.3.4.4. Cellular exposure

Photoresists were exposed to cells using two methods: the direct application technique (DM) and the indirect application technique (IM). Photoresists were exposed to cells that had been incubated with ^{111}In-DTPA-hEGF for 1 or 24 hours.

Direct Application Method

For the DM, cells were cultured as previously described in Section 2.1.1. Cells were trypsinized (Gibco, #25300-054) and diluted to 1 x 10^6 cells/mL, in 1 mL centrifuge tubes. Cells were then exposed to ^{111}In-DTPA-hEGF at a concentration of 40 nM/mL, for either 1 or 24 hours.

After exposure to ^{111}In-DTPA-hEGF, cells were pelleted (900 x g, 3 minutes), washed twice in PBS, and resuspended in PBS (1000 µL). Cells (500 µL) were transferred to a second centrifuge tube. Both centrifuge tubes were centrifuged (900 x g, 3 minutes) to pellet the cells. Cells in the first tube were fixed in either 4 % paraformaldehyde (PFA; Sigma-Aldrich, #252549) for 10 minutes at room temperature or in ice cold methanol (Fisher Scientific, #M/4000/PC17) for 6 minutes. After fixation, cells were washed in d.H_2O, and resuspended in 100 µL of d. H_2O.

The second centrifuge tube was used to prepare isolated cell nuclei. Cells were re-suspended in 500 µL lysis buffer (25 mM Potassium chloride Sigma-Aldrich, #P9541; 5 mM Magnesium chloride, Sigma-Aldrich, #M8266; 10 mM Trizma hydrochloride, Sigma-Aldrich, #T5941; 0.5 % Tergitol solution, Sigma-Aldrich, #NP40S) for 6 minutes at 4°C (Cornelissen et al., 2009). Cells were centrifuged (240 x g, for 3 minutes), before an additional washing step (400 x g, 2 minutes) in lysis buffer. Isolation was confirmed by confocal microscopy. Isolated cell nuclei were fixed and washed as described for cells. Cells and isolated cell nuclei were resuspended in 100 µL of d.H_2O before being deposited on the photoresists.

To expose the photoresists, 2 µL of cells or isolated cell nuclei was placed on the resists under dark room conditions. The resists were exposed for four half-lives, in the dark. After this time, cell debris was removed by washing in d.d.H_2O for up to 8 minutes,

under yellow room conditions. Washing was stopped when no debris was seen under an optical microscope (Vickers photoplan, filtered for use in yellow room conditions). The resists were then chemically developed (Falzone et al., 2012, Royle et al., 2015).

Indirect Application Method

For the IM, cells (2 x 10^5) were seeded into a 24-well plate (Greiner bio-one #662160) and left to adhere overnight. The DMEM was replaced with fresh DMEM immediately prior to the addition of ^{111}In-DTPA-hEGF. At the selected time point the DMEM was removed and cells were processed.

After washing, cells were fixed in either 4 % PFA for 10 minutes at room temperature, or in ice cold methanol for 6 minutes on ice. They were then washed twice in d.H_2O and left to air dry. In some cases, cell nuclei were prepared as described above. Cells (or isolated cell nuclei) were then washed twice with 500 µL PBS and fixed as previously described.

Plates were air dried and then photoresists were placed inverted (resist side down) on top of the cells, under dark room conditions. The resists were exposed for four half-lives, in the dark. After this time the biological debris was removed by washing in d.d.H_2O for up to 8 minutes, under yellow room conditions. Washing was stopped when all debris had been removed and this was confirmed using an optical microscope (Vickers photoplan, filtered for use in yellow room conditions). The resists were then chemically developed.

2.3.5 Development of the Resists

Development was carried out in a yellow room designed for photolithography. Individual resists were developed in 2:1 ratio of 4-Methyl-2-pentanone (MIBK, Sigma-Aldrich, #293261) and isopropyl alcohol (IPA, Sigma-Aldrich, #563935). To do this,

resists were placed in a beaker containing the developer and the beaker was stirred for 60 seconds. The resist was then removed and placed in a stopping solution of IPA for 15 seconds. The resists were then dried using a compressed nitrogen gun, boiled from a liquid nitrogen dewer (Falzone et al., 2012, Royle et al., 2015). If a post-bake was carried out, samples were heated to 100°C for 90 seconds using a hotplate (Electronic Micro Systems Ltd, Electronic Hot Plate Model 1000-1).

2.3.6 Analysis using the Atomic Force Microscope

AFM (Park Autoprobe CP-II instrument, Veeco, UK; now Bruker, Cambridge, UK) scans were carried out in the AC intermittent contact mode. This is a dynamic mode where the cantilever is oscillating close to its characteristic resonance frequency. Cantilevers with spring constants in the range 4.5–14 N/m, with a resonance frequency of between 150 and 210 kHz, were used (MicroMasch, Ultralevers, NSC35/AlBS). The radius of curvature of the tip was 10 nm, and the half cone angle of the probe was 10^{o} (Figure 2.4). The fast-scan rate was 1 Hz for an image size of 15x15 μm^2 corresponding to a linear scan rate of 15 μm/s (Falzone et al., 2011, Falzone et al., 2012, Royle et al., 2015).

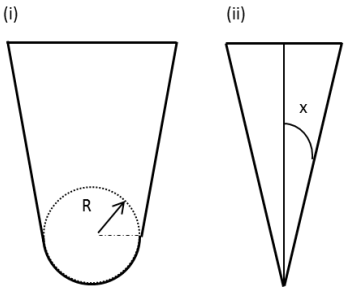

Figure 2.4: The shape of an atomic force microscope tip
A schematic of an AFM tip (i) radius of curvature of the tip at the apex is shown by R (ii) the half cone angle of the probe, is shown by x.

2.3.7 Analysing AFM Scans

AFM scans were analysed using two programmes. WxSM version 5 Develop 8.2 was used to obtain the surface roughness and to obtain the area, maximum depth, average depth and volume of patterns (Horcas et al., 2007). Veeco DI SPMLab NT was used to obtain line scans, maximum depth and radius of the patterns which were analysed for modelling (Veeco, Plainview, NY, version 6.0.2). For all analysis, image data were processed by subtraction of a low-order polynomial plane followed by filtering, taking the average value over a region of 3 x 3 pixels (Falzone et al., 2011, Falzone et al., 2012, Royle et al., 2015).

2.3.8 Monte Carlo Modelling of the Electron Beam

To model the electron beam used in photoresist autoradiography (PAR) experiments, a Monte Carlo (MC) modelling program, CASINO (the name derives from "monte CArlo SImulation of electroN trajectory in sOlids"), was used (Demers et al., 2011). It simulates electron trajectories in solids and is especially designed for low beam interaction in bulk and thin foils. The cut of energy used by CASINO is 50 eV.A geometry was designed that modelled the photoresist structure; the silicon substrate, a 10 nm chrome layer, a 100 nm gold layer and a 1.4 µm thick (PMMA) layer. 6×10^5 electrons were simulated at various beam energies with a beam radius of 10 nm. The distributions obtained were the Z_{max}, and Z_{max} backscattered .

2.4 Optical Microautoradiography

Microautoradiography (MAR) uses a silver bromide emulsion which, when exposed to a source of radiation, causes the bromide crystals to convert to metallic silver. After processing, these grains can be viewed under an optical microscope providing spatial information about the location of the radioactive source.

2.4.1 Preparation of Cells

SQ20B cell lines were plated onto glass coverslips (24 x 24 mm glass coverslips VWR collection, #631-0127) at a seeding density of 2 x 10^5 and left to adhere overnight. Fresh DMEM was added before the addition of ^{111}In-DTPA-hEGF. The cells were incubated with ^{111}In-DPTA-hEGF for 1 or 24 hours.

Cells were then washed twice in PBS and fixed in 4 % PFA (Sigma-Aldrich, #252549) for 10 minutes at room temperature. Cells were then washed twice in d.H_2O. The coverslips were left to air-dry and attached to glass slides (VWR Collection, #631-0108) using strips of double-sided tape (office depot, #545 767).

2.4.2 Application of Autoradiography Emulsion

All work with the emulsion was carried out in a darkroom under red-light conditions. To allow for homogenisation, emulsion was prepared a minimum of 24 hours in advance (Rogers, 1979). The MAR emulsion (Ilford Nuclear Emulsion Type L4, agar scientific, #AGP9282) was placed into a water bath at 43°C for 1 hour and once emulsified it was diluted to 40 % in d.H_2O and stored at 4°C until it was used.

The diluted emulsion was pre-heated to 43°C for 1 hour before use. The emulsion was then poured (slowly, to avoid bubbles) into a coplin jar. Slides containing cells were dipped in to the emulsion and left for 5 seconds, before being removed and the excess

emulsion allowed to run off. Slides were left to dry at air temperature for 1 hour, upright on an absorbent surface to avoid the accumulation of emulsion on the coverslip.

Two blank slides were coated with emulsion. The first was left in dark room conditions (as a negative control) and the second was exposed to white light for 10 seconds (as a positive control). These were stored with the samples and developed at the same time. After drying, cells were stored at 4°C for 24 hours until development.

2.4.3 Development of Emulsion

Slides were developed in coplin jars. The developer (Ilford Phenisol Developer Agar Scientific, #AGP9106) was diluted in a ratio of 1:4 with d.H_2O. Slides were placed in the coplin jar containing the developer for 3 minutes before being placed into a stopping solution (1 % acetic acid, Sigma-Aldrich, #A6283) for 1 minute. The silver halide crystals that formed were then fixed for 6 minutes (Agar Scientific, #AGP9183) at a ratio of 1:4 with d.H_2O. Finally, slides were washed in d.H_2O for 10 minutes with two changes of d.H_2O. Once dry, the glass coverslips were remounted onto fresh slides, prior to image acquisition.

2.4.4 Analysis on Laser-Scanning Confocal Microscope

Images were obtained using a laser scanning Zeiss confocal microscope (Carl Ziess LTD., Zeiss LSM710, AxioObserver). Confocal planes were imaged using line-scanned consecutive acquisition channels through an EC Epiplan-Neofluar 50x/0.8 DIC lens (Carl Ziess LTD., #422372-9901-000) with a pixel dwell time of 0.79 μs, and pin-hole of 1 Airy unit. A second bright field image using reflected light images was obtained.

2.5 Microautoradiography using the Transmission Electron Microscope

The distribution of indium-111 was evaluated in EGFR over expressing head and neck cancer cells. The methods used are detailed in the following pages, with results in Chapter 6 which further explore the rationale for the methods. Microautoradiography using the Transmission Electron Microscope (TEM) was carried out on single cell sections. To image cells by TEM they need to be processed firstly to allow sectioning to nanometre thicknesses so that a beam of electrons from the TEM can pass through the sections and secondly they need to be stained with heavy metals so that different organelles can be imaged in the TEM. Two main preparation techniques were used namely microwave and oven preparation techniques. These techniques evaluated different methods of fixation, dehydration and embedding the cells and are described in the following pages.

As well as different methods of processing the cells, different methods of applying the emulsion and developing the emulsion were used. These were the Chien staining pad and the wire loop method and are again described in the following pages.

2.5.1 Overview of the Final Transmission Electron Microscope Protocol

Figure 2.5 shows an overview of the final electron microscope-microautoradiography (EM-MAR) protocol using TEM which was developed, using *en-bloc* staining and oven polymerisation and application of the emulsion using a wire loop. The various different protocols which were optimised are described below.

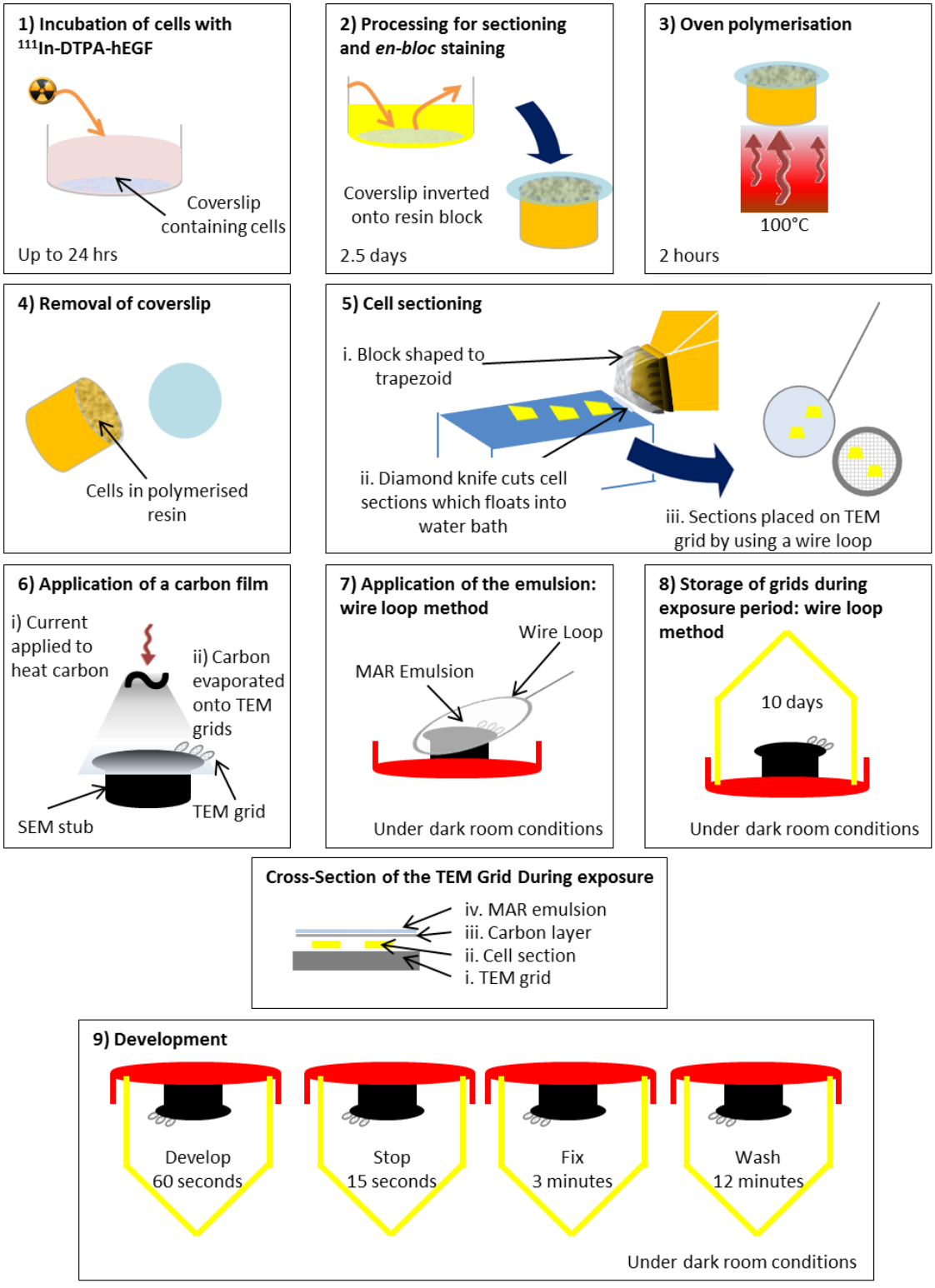

Figure 2.5: Overview of the final electron microscope microautoradiography protocol

2.5.2 Preparation of the Cells for Sectioning

2.5.2.1 Microwave Polymerisation Preparation Method

For microwave processing, SQ20B cells were plated into a T-25 flask (Greiner bio-one, #658170) at a high seeding density of 2 x 10^6 and left to adhere overnight. The DMEM

was replaced with fresh DMEM immediately prior to the addition of ^{111}In-DTPA-hEGF. Cells were then exposed to ^{111}In-DTPA-hEGF, at a concentration of 40 nM/mL, for 24 hours. After incubation with the radiopharmaceutical, the DMEM was removed and cells were washed twice in 1,4-piperazinediethanesulfonic acid buffer (PIPES Buffer, 0.1 M, pH 7.2, Sigma-Aldrich # P8203).

Primary and Secondary Fixation

To fix the cells, the PIPES buffer was removed and the cells were fixed in pre-warmed (37°C) primary fixative (2.5 % glutaraldehyde, Sigma-Aldrich, #G5882; 2 % PFA Fisher Scientific #1044336, in 0.1 M PIPES buffer) for 15 minutes at 37°C. The primary fixative was aspirated and the cells were washed for 10 minutes in 0.1 M PIPES buffer. During this time, the PIPES buffer was changed three times. To fix unsaturated fatty acid and phospholipids in cells, a secondary fixation step was conducted in 2 % osmium tetroxide (Sigma-Aldrich; #201030), in 0.1 M PIPES buffer, for 30 minutes at 4°C. The osmium tetroxide was aspirated and the cells were washed for 15 minutes in ultrapure water, during which period the ultrapure water was changed three times. The T-25 flask cells were scraped (Sigma-Aldrich; #CLS3010) with ultrapure water in the flask and evenly split into two centrifugation tubes.

Dehydration, Embedding and Polymerization

Cells were dehydrated in an ascending series of acetone (Sigma-Aldrich; # 320110). To do this, cells were centrifuged (900 x g, 3 minutes) and then the supernatant removed. Cells were resuspended in 70 % acetone, centrifuged (900 x g, 3 minutes) and then the supernatant removed. This was repeated for 80 % and 90 % acetone. Finally, cells were incubated in 100 % dry acetone for 15 minutes, during which time the acetone was changed three times.

To section the samples, cells are embedded in resin which is then polymerised to create a hard block. Dehydrated cells were embedded in resin by resuspension in a 1:1 ratio of 100 % dry acetone to LR White resin (agar scientific, #AGR1280). Cells were centrifuged (900 x g, 3 minutes) and then supernatant removed. Cells were then resuspended in a 1:3 ratio, centrifuged (900 x g, 3 minutes) and then supernatant removed, before being resuspended in 100 % LR White resin with three solution changes.

Centrifugation tubes containing cells were centrifuged (900 x g, 3 minutes) to create a cell pellet and then polymerised in a microwave (Russell Hobbs #EM820CPT(F)-PM) at 50 % power for 20 minutes. Resin block containing cells were removed from the centrifugation tubes by using a hacksaw and vice.

2.5.2.2 Oven Polymerisation Preparation Method

SQ20B cell lines were plated onto thermanox coverslips (Thermo Scientific, #174950), in 24-well plates (Greiner bio-one #662160) at a seeding density of 2 x 10^5 and allowed to adhere overnight. The DMEM was changed before incubating with 40 nM/mL of ^{111}In-DTPA-hEGF. After incubation with the radiopharmaceutical, the DMEM was removed and cells were washed twice for 5 minutes each in PIPES Buffer.

To fix the cells, the PIPES buffer (0.1 M, pH 7.2, Sigma-Aldrich # P8203) was removed and the cells were fixed in pre-warmed (37°C) primary fixative (2.5 % glutaraldehyde, Sigma-Aldrich, #G5882; 2 % paraformaldehyde Fisher Scientific #1044336, in 0.1 M PIPES buffer) for 1 hour at room temperature. The primary fixative was then aspirated and the cells were washed for 1 hour in 0.1 M PIPES buffer on a shaker. The PIPES buffer was changed four times, with one wash containing 50 mM of glycine (Sigma-

Aldrich, #G889) to neutralise residual glutaraldehydes. Coverslips containing cells were then transferred to a fresh 24-well plate.

Secondary and Tertiary Fixation for Samples that will be Post-stained

If cells were to be post-stained, they underwent a secondary fixation step in 1 % osmium tetroxide (Sigma-Aldrich, #201030) in 0.1 M PIPES buffer, incubated at 4°C for 1 hour and then washed three times in ultrapure water with each wash lasting 10 minutes. Cells underwent a tertiary fix in 0.5 % aqueous uranyl acetate (agar scientific, #R1260A) overnight at 4°C in the dark. Cells were then washed in ultrapure water for 10 minutes with one change, before dehydration.

Secondary and Tertiary Fixation for Samples which will be *En-Bloc* Stained

If cells were to be *en-bloc* stained, they were secondary fixed in osmium. Firstly in osmium ferricyanide, which was made by dissolving 3 % potassium ferricyanide (Sigma-Aldrich, #702587) in 0.2 M PIPES buffer and adding an equal amount 4 % osmium tetroxide in water. Cells were fixed in the osmium ferricyanide solution for 1 hour at 4°C. Cells were then washed in ultrapure water for 30 minutes with three changes. While cells were undergoing fixation in osmium ferricyanide, thiocarbohydrazide (TCH) solution was made. TCH solution is prepared by adding 0.1 g of TCH crystals (Sigma-Aldrich, #223220) to 10 mL of ultrapure water. This was placed in a 60°C embedding oven (agar scientific, #AGB7606) for 1 hour and stirred every 10 minutes. Once the TCH crystals have dissolved, the solution is cooled to room temperature. Immediately before use, the TCH is filtered through a 0.22 µm Millipore syringe filter (Sigma-Aldrich, Z359904). Cells were then incubated in the TCH solution for 20 minutes at room temperature. Cells were then washed in ultrapure water for 30 minutes with three changes before being fixed in 2 % osmium tetroxide (in ultrapure water) for 30 minutes at 4°C. Cells were washed in ultrapure water for 30 minutes with

three changes. A tertiary fixation in 2 % aqueous uranyl acetate in ultrapure water at 4°C was carried out overnight. Cells were then washed in ultrapure water for 30 minutes with three changes.

For *en bloc* staining using lead aspartate, the lead aspartate needs to be made up immediately before use. To do this 0.066 g of lead nitrate (agar scientific, #AGR1217) was added to 10 mL of aspartic acid (0.998 g of L-aspartic acid (Sigma-Aldrich, #A9256) in 250 mL of ultrapure water) and the pH adjusted to 5.5 using a freshly made stock of potassium hydroxide (1 M; Sigma-Aldrich, #484016). The lead aspartate solution was warmed to 60°C in an embedding oven for 30 minutes before being cooled to room temperature. Cells were incubated in lead aspartate for 30 minutes at room temperature and cells were then washed in ultrapure water for 30 minutes before dehydration.

Dehydration, Embedding and Polymerization

For samples which were to be post-stained and samples which were *en-bloc* stained, cells were dehydrated in an ascending series of ethanol. Firstly, cells were incubated in 30 %, 50 %, 70 %, 80 %, 90 % and 95 % ethanol (Sigma-Aldrich, #459844), each for 10 minutes. Finally, they were incubated in 100 % dry ethanol for 30 minutes during which time the ethanol was changed three times.

For oven polymerization, cells were infiltrated and polymerised with Agar100 resin (agar scientific, #R1140). This was achieved by incubating cells for 1 hour in a 3:1 ratio of 100 % dry ethanol to Agar100 resin, then in a 1:1 ratio for 2 hours, and then a 1:3 ratio for 1 hour. Samples were incubated in 100 % Agar100 with benzyl dimethylamine (BDMA; 300 µL for 10 mL of resin; agar scientific, #R1140), an accelerant, for 2 hours before the resin and accelerant were replaced and cells were incubated overnight in 100

% Agar100, including BDMA, at room temperature. The resin was changed and cells were incubated for 2 hours before polymerisation.

Coverslips were removed from the 24-well plate and placed inverted onto flat embedding capsules (Electron Microscopy Sciences, #70021) filled with fresh 100 % Agar100 resin including BDMA. Blocks were polymerised for 2 hours at 100°C in a polymerization oven.

To remove the blocks from the capsules, blocks were dropped into liquid nitrogen for 30 seconds. This allows the coverslips to be removed using tweezers. The capsule was then cut away using a razor blade (Fisher Scientific, #11904325) and capsule splitter (TAAB, #C065). The best blocks, from each experimental condition (as determined by the hardness, lack of air bubbles and layer of cells) were selected for sectioning.

2.5.3 Sectioning

Blocks were sectioned on the ultramicrotome (Leica, #EM Ultracut 7) by shaping them into a trapezoid of approximately 3 mm using a razor blade (Fisher Scientific, #11904325). Once shaped, a diamond knife with a water bath attached (Diatome, #DU4530) was aligned to the surface of the block, and cells sectioned to 90 nm. Sections were used only if there were no visible flaws, such as holes or scratches in the sections. Sections floating in the water bath were manipulated into groups of three using an eyelash. Chloroform (Acros organics # 326821000) was used to expand the sections. These sections were then removed from the water bath by use of the wire loop method; a wire loop (agar scientific, #AGT5112) with a diameter of 5 mm, was used to touch the surface of the water, forming a bubble across the surface of the wire loop containing the cell sections. The loop was then placed onto a nickel TEM grid (150 mesh, agar

scientific, AGG201N) which had been laid out onto filter paper (Whatman No. 1 filter papers, agar scientific, AGL4164). The TEM grid was then left on filter paper to dry.

2.5.4 Application of a Carbon Film

The dry TEM grids were then coated with a layer of carbon, approximately 10 nm thick. This prevents chemographic interactions between the sections and the autoradiographic emulsion and provides more support for the emulsion (Somogyi and Chubb, 1976). To do this, a small section of the TEM grids was stuck down onto SEM stubs (TAAB, #S081) with conductive tape (TAAB, #C249/N). They were then placed in the carbon sputter coater (Quorum Technologies Ltd, #Q150R ES Dual Carbon/Sputter Coater) and the carbon layer was applied using a carbon cord (Quorum Technologies Ltd, C5421) with four pulses.

2.5.5 Microautoradiography

2.5.5.1 Application of the Emulsion

A minimum of 24 hours before the experiment was due to take place, a working solution of emulsion was made up. The stock emulsion (Ilford Nuclear Emulsion Type L4, agar scientific, #AGP9282) was placed into a water bath at 43°C for 1 hour. Then aliquots of 5 mL diluted emulsion were prepared. The emulsion was diluted to 40 % in d.H_2O. For emulsion applied using the wire loop method, 100 µL of 2 % aqueous solution of dioctyl sodium sulfosuccinate (Sigma-Aldrich, #323586) was added (Nagata, 1998). Aliquots were stored at 4°C in the dark until use.

Chien Staining Pad Method

To apply the emulsion using the Chien staining pad method, the TEM grids were placed into a Chien staining pad (agar scientific, #AGG3766) and the emulsion was poured into a small Petri dish until it formed a flat surface. The Chien staining pad was then

inverted into the emulsion. To avoid crumpling of the TEM grids, the Chien staining grid was larger than the Petri dish. The staining grid was removed and left inverted to allow excess emulsion to run off. Sections were then left to expose the emulsion for between two and six half-lives (5 to 14 days), before development.

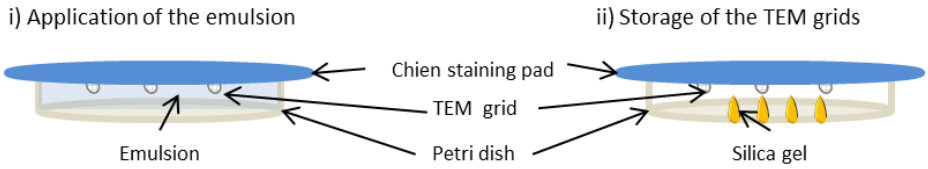

Figure 2.6: Chien stain pad method
TEM grids are placed in the Chien staining pad and (i) inverted into emulsion, (ii) removed and stored in a Petri Dish during the expose period

Wire Loop Technique

To apply a thin layer of emulsion, using the wire loop technique, a small edge of the grid was placed on conductive tape, section-side up, which had in turn been attached to a SEM stub. The SEM stubs were then attached to the lid of 50 mL falcon tubes (Sarstedt, #62.547.004). This allowed the grids to be suspended. Once the TEM grids had been prepared, the diluted emulsion was heated to 43°C in a water bath for 1 hour and then poured into a glass Petri dish, where it was cooled to form a gel-like layer. A platinum wire loop (Sigma-Aldrich, #349402), with a large diameter (2.5 cm), was dipped into the emulsion and placed over the grids. The falcon tube lids were then placed into falcon tubes containing silica gel (Sigma-Aldrich, #10087). Sections were then left to expose the emulsion for between two and six half-lives (5 to 14 days), before development.

Two blank control slides were coated with emulsion. The first was left in dark room conditions (as a negative control) and the second was exposed to white light for 10 seconds (as a positive control). These were stored with the samples and developed at the same time.

2.5.5.2 Development of the Sections

Grids were developed in the developer (Ilford Phenisol Developer, Agar Scientific, #AGP9106) at a ratio of 1:8 with d.H_2O. The development time varied between 30 seconds and 2 minutes.

Chien Staining Pad Method

To develop the grids which had the emulsion applied using the Chien staining pad, the developer was placed into a Petri dish and the Chien staining pad inverted into the Petri dish. To avoid crumpling of the TEM grids, the Chien staining pad was larger than the Petri dish. After development, the Chien staining grid was placed in a Petri dish of 1 % acetic acid (Sigma-Aldrich, #A6283) for 15 seconds before being placed in a Petri dish of fixative (Ilford Hypam Fixer, Agar Scientific, #AGP9183) at a ratio of 1:4 with d.H_2O, for 3 minutes. The TEM grids were then washed in d.H_2O for 12 minutes with the d.H_2O changed every 3 minutes.

Wire Loop Technique

To develop the grids which had the emulsion applied using the wire loop method, the falcon tube lid containing a SEM stub with the TEM grids on was placed into a falcon tube containing developer. The SEM stub containing the TEM grids was then placed into a second falcon tube of 1 % acetic acid for 15 seconds before being placed into a falcon tube of fixative, at a ratio of 1:4 with d.H_2O, for 3 minutes. The TEM grids were then washed in d.H_2O for 12 minutes changing the falcon tube of d.H_2O every 3 minutes.

2.5.6 Post-Staining

If grids had not been *en-bloc* stained they were post-stained to provide contrast in the TEM. This staining was carried out with lead citrate and uranyl acetate. To avoid

carbonisation of the lead citrate and the formation of precipitates, staining was carried out in Petri dishes. These were lined with parafilm and pellets of sodium hydroxide (Sigma-Aldrich #72068) were placed around the edge of the lead citrate staining dish, to absorb carbon. Droplets of the stain and ultrapure water for washing were placed onto the parafilm and the TEM grids were floated section-side down on top of the droplets.

For staining of grids prepared using the microwave technique, sections were stained for 10 minutes in uranyl acetate. Then the grids were washed three times in water for 1 minute each and stained with lead citrate for 10 minutes. Grids were then blotted, twice, with sodium hydroxide (1 M) and washed three times in decarbonised (achieved by boiling the water in a microwave) ultrapure water for 1 minute each. Grids were then stained for 8 minutes in uranyl acetate and washed three times in ultrapure water for 1 minute each.

For staining of the grids which were prepared for oven polymerisation, grids were stained for either 5 minutes in lead citrate or for 10 minutes in uranyl acetate and 10 minutes in lead citrate. After each staining step, samples were washed in a droplet of 37°C decarbonised ultrapure water in the same Petri dish for 1 minute. Sections were then washed a further 6 times on droplets of 37°C decarbonised ultrapure water for 1 minute. Droplets of ultrapure water were only laid out immediately before the grid was to be transferred to the droplet, to avoid carbonisation of these droplets.

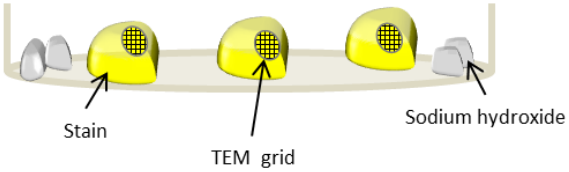

Figure 2.7: Post-staining of the transmission electron microscope grids
A diagram demonstrating how the TEM grids are placed section-side down onto a droplet of stain.

2.5.7 Analysis in the Transmission Electron Microscope

Sections were analysed using a Tecnai 12 TEM (FEI, Tecnai 12). Sections were imaged using a Gatan One View camera and Gatan Digitalmicrograph software (version 3). Images were obtained with an exposure time of 1 second, with a pixel saturation of between 5,000 and 6,000.

2.5.8 Analysis of Transmission Electron Microscope Images

Counting of the MAR grains was performed off-line using a commercial software package (MATLAB 6.1, The MathWorks Inc., Natick, MA, 2000), and an in house MATLAB code.

Chapter 3:
Characterisation of Cell Lines

Chapter 3

Characterisation of Cell Lines

3.1 Introduction

This chapter introduces the biological factors which influence the model system that is being used: SQ20B cells and indium labelled human epidermal growth factor (^{111}In-DTPA-hEGF, DTPA is diethylenetriaminepentaacetic acid). Cells rather than multicellular models were used to reduce the variation in uptake due to geometrical arrangement which is seen across spheroid and tumour models (Neshasteh-Riz et al., 1997; Bodei et al., 2003).

3.1.1 Epidermal Growth Factor

One target which has been used for targeted radiotherapy (TRT) is epidermal growth factor receptor (EGFR). This is a member of the ErbB family. This is a family of proteins containing four type 1 tyrosine kinase receptors. Under normal physiological conditions, the majority of ErbB receptors are located on the cell membrane (Cohen and Carpenter, 1975, Carpenter et al., 1975). Following binding of epidermal growth factor (EGF) to the EGFR, the ligand/receptor complexes are internalised (Jorissen et al., 2003). These complexes are carried in vesicles to cellular locations including the Golgi, endoplasmic reticulum and mitochondria as well as the cell nucleus (Wang and Hung, 2012). Translocation to the nucleus is mediated by a nuclear localising sequence (NLS) (Hsu and Hung, 2007).

After internalisation, the EGF/EGFR complex is degraded (Carpenter and Cohen, 1976) and the receptors are recycled back to the cell membrane (Wiley, 2003). In normal cells this process takes a few hours. In cells with an overexpression of EGFR, the rate of

recycling is faster than internalisation (Sorkin and Goh, 2008). Following internalisation, ^{111}In-DTPA-hEGF was shown, by using fluorescence resonance energy transfer with fluorophore-labelled EGF, to be associated with EGFR in the cytoplasm and the nucleus (Cornelissen et al., 2011).

3.1.2 Aims and Outline

In this chapter, the biological factors that affect the cellular uptake of an exemplar AE-emitting radiopharmaceutical, ^{111}In-DTPA-hEGF, are explored.variation in EGFR expression and uptake of ^{111}In-DTPA-hEGF is explored.

3.2 Results

3.2.1 The Number of Epidermal Growth Factor Receptors on the Cell Surface

To determine the number of EGFR per cell, a competition binding assay (Figure 3.1) and a bicinchoninic acid (BCA) were used. These assays were carried out in SQ20B and MD-MA-468 cells. The competition binding assay allowed the calculation of B_{max}, the total number of receptors expressed in picomoles per milligram of protein and the inhibitory concentration (50 %; IC_{50}; nM) and the BCA assay was used to determine the protein concentration per cell. Together they allow for the calculation of the number of receptors per cell (Table 3.1).

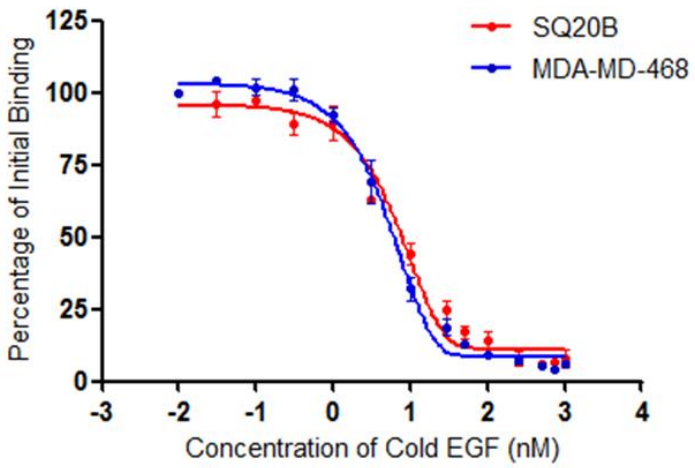

Figure 3.1: Competition binding assay
Competition receptor-binding assay curve for binding of ^{111}In-DTPA-hEGF to MDA-MB-468 and SQ20B cells. Experiments were carried out in quadruplet and from at least three independent experiments.

Table 3.3.1: The number of epidermal growth factor receptors per cell
Summary of the competition binding assays results. Protein per cell (µg) calculated by Mrs Sarah Able, Department of Oncology, University of Oxford.

	SQ20B	MDA-MB-468
IC_{50} (nM)	5	5.2
B_{max} (pmoles/mg protein)	10.61	11.44
Protein per cell (µg)	0.002	0.000165
receptors per cell	$1.28 \times 10^6 \pm 9.30 \times 10^5$	$1.14 \times 10^6 \pm 7.29 \times 10^5$

3.2.2 The Variability in the Number of Epidermal Growth Factor Receptors

To determine the variation in the number of receptors per cell in a population of cells, flow cytometry (Figure 3.2) was carried out using EGF bound Alexa Fluor® 488 Streptavidin.

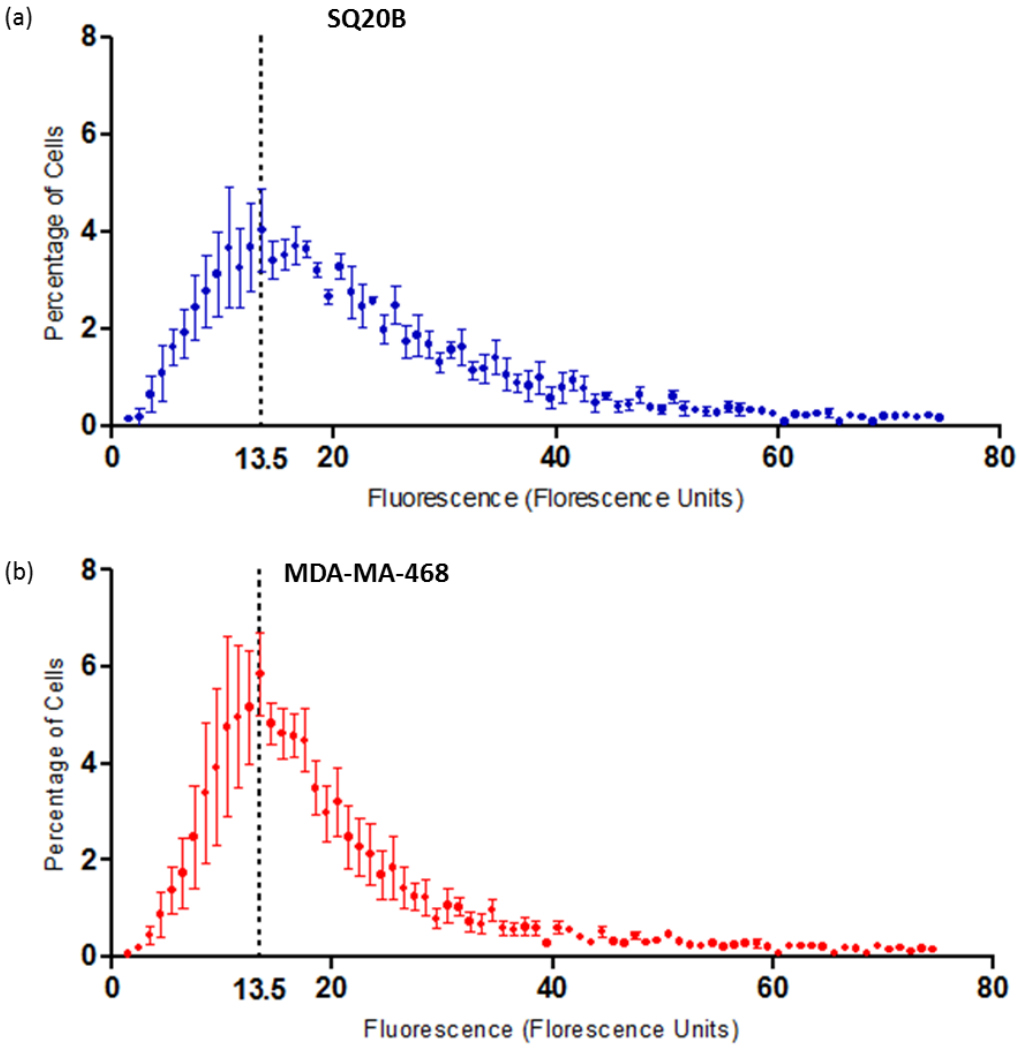

Figure 3.2: The range in the number of epidermal growth factor receptors per cell
Flow cytometry analysis of EGF complexed to Alexa Fluor® 488 Streptavidinon for (a) SQ20B cells and (b) MDA-MB-468 human breast cancer cells; data from three repeat experiments.

Figure 3.2 clearly shows a positively skewed distribution. Table 3.2 shows a summary of these data. Briefly, SQ20B cells have a more skewed distribution and for both cell lines the distribution was non-Gaussian with a high kurtosis (the sharpness of the peak).

Table 3.3.2: A summary of flow cytometry analyses

	SQ20B	MDA-MB-468
Skewness (florescence units)	2.082	1.785
Kurtoness (florescence units)	3.32	1.891
Gaussian distribution –Std. Dev. (florescence units)	17.74	15.85
Mode (florescence units)	13.5	13.5
Mean (florescence units)	27.5	16.5

The distribution can be split into two halves around the mode. By mirroring the distribution around the mode, a Gaussian distribution can be fitted. In this case, for SQ20B cells, the 0-13.5 standard deviation is 4.7 florescence units and the second half is 8.901 florescence units. For MDA-MD-468 cells, these values are 5.649 florescence units and 14.85 florescence units respectively. For both SQ20B cells and MDA-MD-468 cells, the curve fitting can be improve by fitting a Lorentizan distribution (a bell-shaped distribution, but has a much wider tail compared to a Gaussian) with R^2 increasing from 0.84 to 0.89 for SQ20B cells and from 0.9 to 0.94 for MDA-MD-468 cells. Fitting a Lorentizan distribution in both cell lines decreases the width of the peak to 8.3 florescence units for SQ20B cells and 13.68 florescence units for MDA-MD-468 cells.

3.2.3 The Internalization of ^{111}In-DPTPA-hEGF

To identify trends in the uptake of ^{111}In-DTPA-hEGF, internalisation studies were carried out with ^{111}In-DTPA-hEGF and $^{111}InCl_3$ (Figure 3.3). There was a statistically significant difference (*** $P \leq 0.001$) between $^{111}InCl_3$ and ^{111}In-DTPA-hEGF in both the membrane bound and internalised fractions at both time points.

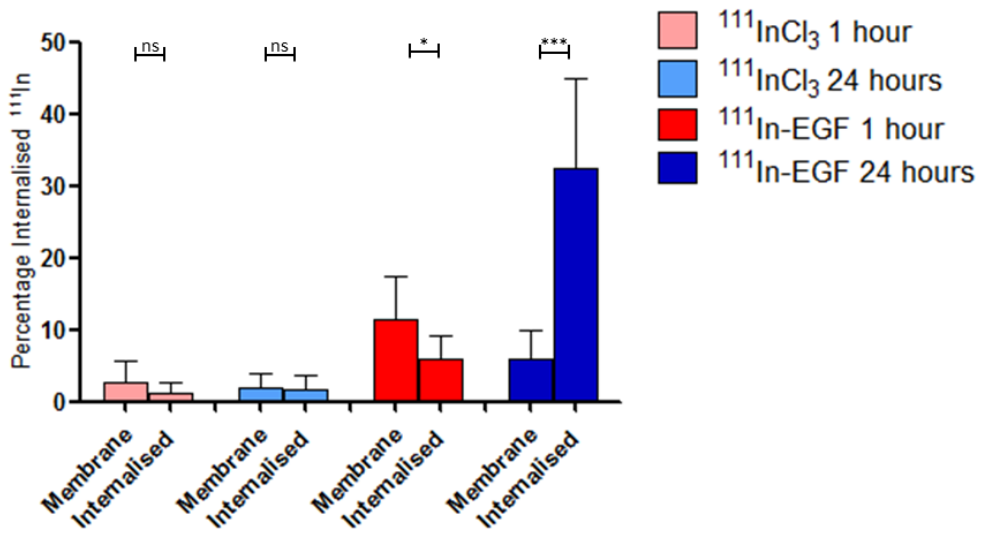

Figure 3.3: Internalization studies of ^{111}In-DTPA-hEGF in SQ20B cells
SQ20B cells were incubated for either 1 or 24 hours with either $^{111}InCl_3$ or ^{111}In-DTPA-hEGF. Cells were washed and lysed, and the proportion of internalized radioactivity determined by gamma-counting. Experiments were carried out in triplicate; data represents at least three independent repeat experiments. Significance from t-tests shown: * $P \leq 0.05$, *** $P \leq 0.001$; ns not significant. Mean plus standard deviation plotted.

There was no statistical difference in the amount of $^{111}InCl_3$ associated with the membrane-bound or internalised fractions at 24 hours compared to 1 hour. In contrast, for ^{111}In-DTPA-hEGF, the amount of membrane-bound radioactivity was greater at 1 hour versus 24 hours (** $P \leq 0.01$). By 24 hours the amount of internalised radioactivity had increased markedly compared to 1 hours (*** $P \leq 0.001$).

3.3 Discussion

3.3.1 The Variability in Epidermal Growth Factor Receptor Expression

A factor which affects the uptake of ^{111}In-DTPA-hEGF is the number of EGFR that are expressed on the cell surface (Hu et al., 2007). Therefore, to determine the number of receptors on the surface of the cell line a competition binding assay and BSA assay were used (Figure 3.1).

To validate the methodology used here in determining the number of surface-bound receptors, experiments were done with a previously well-described and receptor number quantified cell line MDA-MD-468 cells, as well as SQ20B cells. The number of receptors was approximately 1.28 x 10^6 for SQ20B cells and 1.14 x 10^6 for MD-MA-468. These values are in agreement with reported results at 1x10^6 receptor per cell, (Filmus et al., 1987, Cornelissen et al., 2011). These values have large standard deviations which is due to the variation in the number of receptors on the cell line.

The variation in the number of receptors can be seen in Figure 3.2 and shows that the data are markedly skewed. Since only single cells are analysed using FACs, the long tail on the right of the distribution is not attributable to double cells being counted but rather indicates that within the cell population there are cells with very high EGFR expression. As the heterogeneity of uptake increases, the tumour control is reduced (O'Donoghue and Wheldon, 1996). It is those cells which have a low level of EGFR expression that will have a lower uptake of the radiopharmaceutical and reduce tumour control. However, there appears to be less heterogeneity at lower levels of EGFR expression.

3.3.2 The Variability in Uptake of ^{111}In-DTPA-hEGF

The uptake of ^{111}In-DTPA-hEGF in SQ20B cells as shown in Figure 3.3 is similar to the uptake of ^{111}In-DTPA-hEGF in MDA-MD-468 cells. The internalized fraction, as a percentage of total bound ^{111}In-DTPA-hEGF for MDA-MD-468 was 70 % after 15 minutes and this increased to 80 % at 4 hours, and remained constant after 24 hours. For SQ20B cells, the values are 35 % at 1 hour and 85 % at 24 hours. For studies with MDA-MD-468 cells, the nucleus fraction was also determined: after 1 hour incubation with ^{111}In-DTPA-hEGF, 8 % of the internalized indium was localized in the cell nucleus, and after 24 hours this increased to 15 % (Reilly et al., 2000a). These studies used a specific activity of 3.7 to 11.1 MBq/μg and 5 ng of ^{111}In-DTPA-hEGF, less than used in experiments with SQ20B cells. This led to an average of 24.7 Gy cell dose, with 19.3 Gy of this being delivered to the cell nucleus. The proportion of ^{111}In-DTPA-hEGF that was localized to the nucleus (15 %) accounted for 80 % of the total radiation dose to the cell nucleus. The indium-111 associated with the cytoplasmic and membrane fractions accounted for 18 % and 3 % of the radiation dose to the nucleus respectively. Being able to account for these variations across the cell population will demonstrate how this dose varies.

If it is assumed that there is a uniform amount of radioactivity in all cells, the mean activity present in an SQ20B cell is approximately 180 mBq $\pm$ 30 mBq at 1 hour and approximately 400 mBq $\pm$ 180 mBq at 24 hours. This suggests that, as the incubation time increases, there is much greater variation in internalized radioactivity. These results are similar to the mean radioactivity present in MDA-MD-468 cells: the internalized activity ranges from approximately 200 to 350 mBq for 1- and 20-hour-exposure respectively in the cell and approximately 100 to 150 mBq for 1- and 20-hour-

exposure respectively in the cell nucleus (Cai et al., 2008). These results were obtained using internalization studies with $1x10^6$ cells. Since this information is averaged over a large number of cells it is indicative of the situation across a cell population, rather than individual cells.

3.4 Conclusions

A number of biological factors lead to variation in uptake of ^{111}In-DTPA-hEGF. Among the most important are the incubation time and the number of EGFR per cell. However, there is not a method which allows for the number of receptors on an individual cell to be known. FACs analysis allows for the variation between a large number of cells to be determined. Likewise, internalisation studies only look at the uptake across the cell population.

Chapter 4:
Poly (methyl methacrylate) Photoresists: A Novel System for the Detection of Auger Electron-Emitting Radionuclides

Chapter 4

Poly (methyl methacrylate) Photoresists: A Novel System for the Detection of Auger-Electron Emitting Radionuclides

4.1 Introduction

This chapter describes and validates the photoresist autoradiography technique (PAR). Firstly, the choice of photoresist material is discussed and a description of the PAR technique is given, together with a summary of previous results. Secondly, results are shown that validate the technique using electron beam lithography and then ^{111}In-labelled microspheres. The PAR technique is demonstrated using a radiopharmaceutical, ^{111}In-DTPA-human epidermal growth factor (^{111}In-DTPA-hEGF; DTPA is diethylenetriaminepentaacetic acid). Limitations of the technique are identified and the method is refined to allow for further improvement of the image quality.

4.1.1 The Choice of Photoresist Substrate

Photoresists are photosensitive materials and there are three main types of photoresists: chemically amplified photoresists (CARs), inorganic and organic. CARs have a high resolution with a low exposure dose. For example, dots with a 15 nm diameter and 35 nm pitch (steepness of the slope), have been fabricated in a calixarene resist layer (Fujita et al., 1996). Inorganic resists have a higher contrast compared to inorganic resists but a lower sensitivity and require high electron doses for exposure. Organic resists are a less sensitive resist material and have a lower contrast compared other to polymeric resist types (Grigorescu and Hagen, 2009). Poly (methyl methacrylate) (PMMA) is currently the highest resolution commercially available organic photoresist

(del Campo and Arzt, 2008), and as such is, by far, the most widely used resist for high resolution lithography (Solak et al., 2007).

Previously, Falzone et al. have looked at using chemically amplified photoresists (CARs,) AZ40XT and UV1116 and the organic resists PMMA as a positive tone resists (Falzone et al., 2011).

PMMA, can be both a negative and positive tone resist, as a negative tone resist PMMA has been shown to reproducibly obtain patterns of 2 to 5 nm in size. However, these patterns have been isolated. Therefore, the ultimate resolution test (writing of lines and spaces) has not been reached yet when using PMMA for lithography (Grigorescu and Hagen, 2009). The resolution can be improved by adjusting different parameters of the processing conditions (Reichmanis and Thompson, 1989).

However, the main reasons for using PMMA in PAR are its structural integrity (Grigorescu and Hagen, 2009), ease of handling over CARs, which have previously been used and being more tolerant of minor variations in processing parameters (Falzone et al., 2011, Falzone et al., 2012). These are important considerations when developing a straightforward method to evaluate the distribution of radionuclides at the subcellular level.

The resolution can be limited by the swelling of the PMMA and intermolecular forces, which are exerted on exposed resist molecules by unexposed molecules. Across the exposed region there can be incomplete and inconsistent removal. If there are large numbers of patterns in a small area with a high aspect ratio they can collapse (Grigorescu and Hagen, 2009).Development of the Processing Conditions

The electron beam lithography system was used to create a pattern of known electron fluence (exposure dose in $\mu C/cm^2$) (Royle, 2012). The electron beam was used to determine the photoresist design (substrate layers and thickness of the resist film and resist type) and the processing conditions (developer concentration and time). These conditions were used in later experiments. The photoresist was designed using either PMMA 495 K or PMMA 950 K (two different molecular weights), then with a 100 nm gold layer, a 10 nm chrome layer and then a silicon substrate. Photoresists without the gold layer were shown to have a lower sensitivity and higher resolution. The PMMA was spin-coated onto the gold at 4000 rpm, to give a layer 1.4 μm thick layer for PMMA 950 K and a 0.5 μm thick layer for PMMA 495 K. Thicker photoresists (1.5 μm, 1.9 μm for PMMA 950 K) were previously tested. These showed a reduction in sensitivity (Royle, 2012).

Different development conditions were tested. Various developer ratios (3:1, 2:1, and 1:1) were used and two development times (60 and 90 seconds) (Royle, 2012). In subsequent experiments, the development time was 60 seconds, and the concentration of developer used was 2:1 4-Methyl-2-pentanone (MIBK) to isopropyl alcohol (IPA). This allowed for a compromise between sensitivity (depth of pattern) and resolution, which was limited by the surface roughness.

Previous work, (Royle, 2012) using electron beam calibration showed that both resist formulations were sensitive enough to be used with PAR with there being a compromise between resolution and sensitivity: PMMA 495 K being more able to detect lower fluence due to is reduce surface roughness but PMMA 950 K producing deeper patterns. It was therefore determined that both PMMA 950 K and PMMA 495 K would be used for PAR. In general, an increase in sensitivity, achieved by refining

processing conditions, leads to a decrease in resolution and vice-versa. The two different molecular weights allow there to be optimisation of sensitivity and contrast. The resolution, contrast and sensitivity are dependent on the processing conditions.

4.1.2 Aim and Outline

The overall aim was to investigate PAR as a means to detect and quantify the internalisation of radiopharmaceuticals in cancer cells. To do this, calibration results are shown that validate the technique using electron beam lithography with CASINO (Demers et al., 2011) Monte Carlo (MC) modelling to show the physical interactions which have created these patterns. The technique is then further validated using ^{111}In-labelled microspheres. The PAR technique is then demonstrated using a radiopharmaceutical and then refined to improve image quality.

4.2 Results

4.2.1 Calibration using the Electron Beam

The electron beam data shown has been adapted from previous work submitted for the degree of Master of Engineering, at the University of Oxford, with further analysis to allow for better interpretation of the images obtained during cellular experiments (Royle, 2012). Patterns for the relevant range of fluence, (1–34 μC/cm^2 at logarithmic intervals, corresponding to 6.2x10^4–2.1x10^7 e$^-$/μm^2) were obtained and analysed. The energy dependence was explored by comparing the response of the two PMMA formulations (of molecular weight 495 K and 950 K, respectively) for energies of 25 and 50 keV.

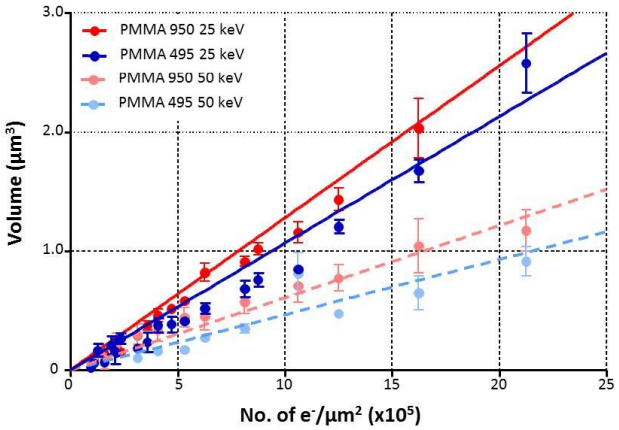

Figure 4.1: Electron beam calibrations
The response of PMMA 950 K and 495 K resists to 25 and 50 keV electron beam exposure. The volume removed (μm^3) versus number of electrons per unit area (e$^-$/μm^2) for patterns in PMMA 950 K and 495 K generated by a 25 keV and 50 keV electron beam. Work adapted with permission (Royle, 2012, Royle et al., 2015).

Electron beam patterns from fluences as low as 1-2 μC/cm^2 (0.6-1.2 x 10^5 e$^-$/μm^2), for PMMA 950 K and 495 K, were readily detectable and quantifiable by AFM analysis (Figure 4.1). Figure 4.1 shows that the higher molecular weight PMMA 950 K resist is more sensitive as compared to PMMA 495 K. The pattern depth as a function of fluence per unit area can be calculated from the slopes of the lines, while the volume of resist

that has been removed, per incident electron, can be determined. These factors are listed in Table 4.1, and were used in subsequent investigations.

Table 4.4.1: Summary of conversion factors for the electron beam calibration
Conversion factors relating the depth of a resist pattern to the fluence per unit area, and the volume of resist that has been removed per incident energetic electron

Resist	Energy (keV)	Pattern depth per electron per area ($nm/e^- \mu m^2$, $x10^{-5}$)	Volume removed per electron ($\mu m^3/e^-$)
PMMA 950 K	25	5.1	$5.1x10^{-8}$
PMMA 495 K	25	4.1	$4.3x10^{-8}$
PMMA 950 K	50	2.3	$2.4x10^{-8}$
PMMA 495 K	50	1.8	$1.9x10^{-8}$

4.2.2 CASINO Modelling of PMMA Resist Exposure to an Electron Beam

To gain a better understanding of the interaction of the electrons with the sample, MC modelling was carried out, using CASINO MC code (Demers et al., 2011). CASINO allows accurate simulation of electron beam and sample interactions and a geometry can be defined. The cut-off energy is 50 eV. For these simulations, a geometry was designed that modelled the photoresist structure. This was a silicon substrate with a 10 nm chrome and a 100 nm gold layer, and a 1.4 μm PMMA layer. The energy deposited in the resist is dependent on the chemical structure; it does not distinguish between PMMA 495 K and 950 K. The variation in the depth of the patterns etched is due to the number PMMA chains which are broken. PMMA 950 K creates deeper patterns as there is a greater number of bonds which are broken and then the PMMA is removed by the developer. This is not modelled by CASINO.

Modelling of 25 keV and 50 keV Electron Beams

To gain an understanding of what percentage of the total energy of the 25 keV and 50 keV electron beam was used to create the patterns seen in the experimental data, a PAR resist was modelled using CASINO.

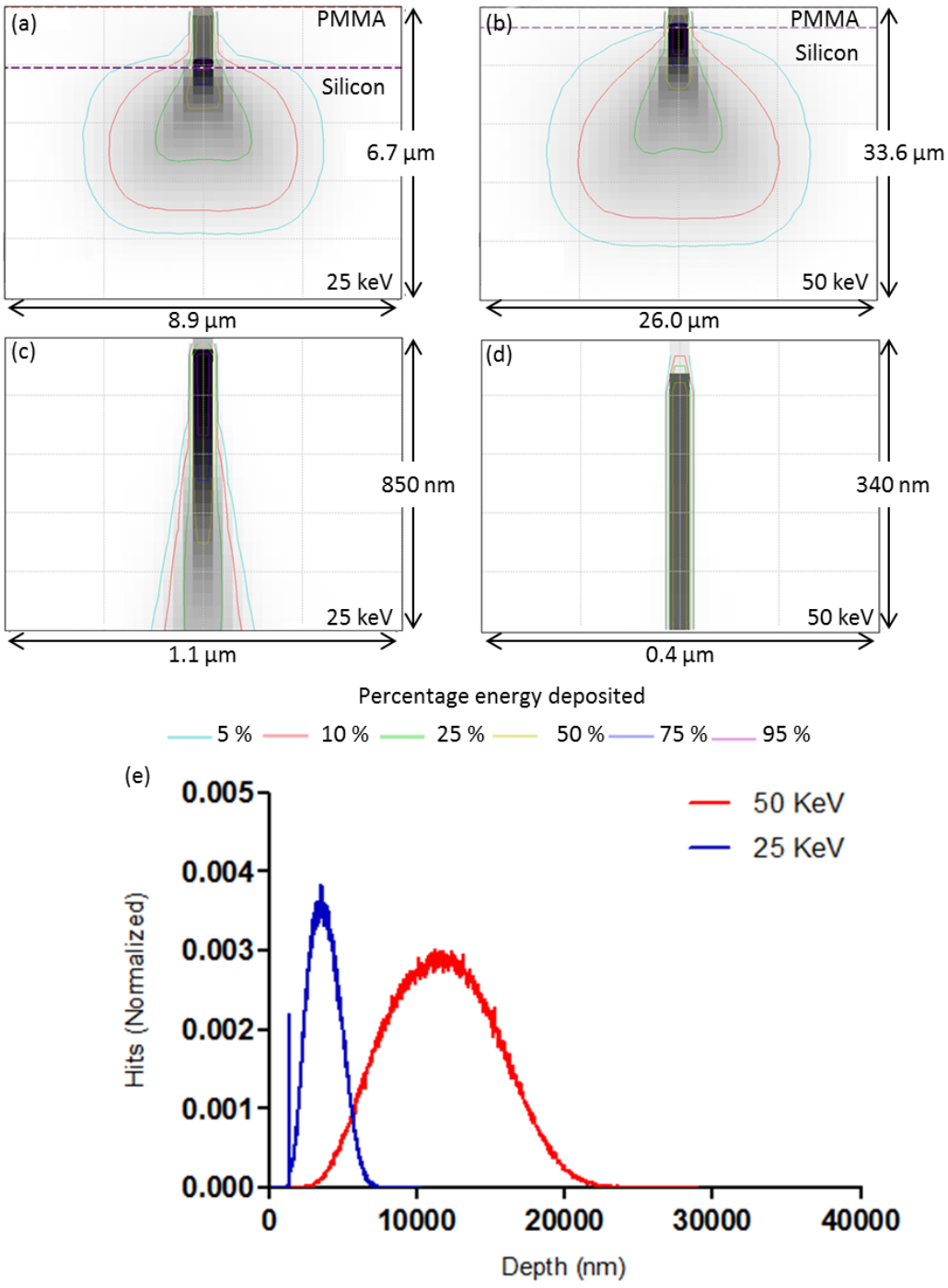

Figure 4.2: CASINO model of the 25 keV and 50 keV electron beams
A model of the 25 keV and 50 keV electron beams carried out using CASINO, showing the energy deposited by the (a) 25 keV and (b) 50 keV electron beam and (c) & (d) which demonstrate the straggling of the electron beam into the PMMA before reaching the gold layer. (e) shows the normalized hits (hits being the number of interactions within the modelled photoresist) vs the depth within the photoreists. The beam radius was 10 nm and 6 x 10^5 electrons were simulated.

Figure 4.2 shows that the electron beam only deposits a proportion of its total energy in the PMMA substrate. As the fluence to which the photoresist is exposed increases, the same percentage of total energy is transferred to the PMMA carbon bonds. However, the amount of energy transferred to the PMMA increases with increasing fluence, while the distribution of energy deposited in the PMMA remains the same. This causes the deeper patterns seen in the experimental data as the fluence increases.

The difference between the 25 keV beam and the 50 keV beam shows that the 25 keV electrons inherently have less energy and more energy in total is deposited within the PMMA resist, as shown in Figure 4.2. Figure 4.2 also shows the straggling of the electron beam. This will reduce the overall resolution. The 25 keV electron beam spreads more than the 50 keV electron beam in the PMMA layer. However, the spreading of the electron beam does not occur at the surface of the resist. For imaging using an AFM, this is important as the AFM is only able to image the surface of the PMMA. It is therefore unable to detect the spreading of the electrons. Likewise, the developer is only able to develop those regions which are exposed at the surface.

Monte Carlo Modelling of Relevant Electron Energies from Indium-111

The AE are emitted from indium-111 with a range of energies (0.345–25.58 keV). The energy of many of the electrons is lower than 25 keV (Eckerman and Endo, 2008). Figure 4.3 shows the interaction of these lower energy electrons with the photoresist.

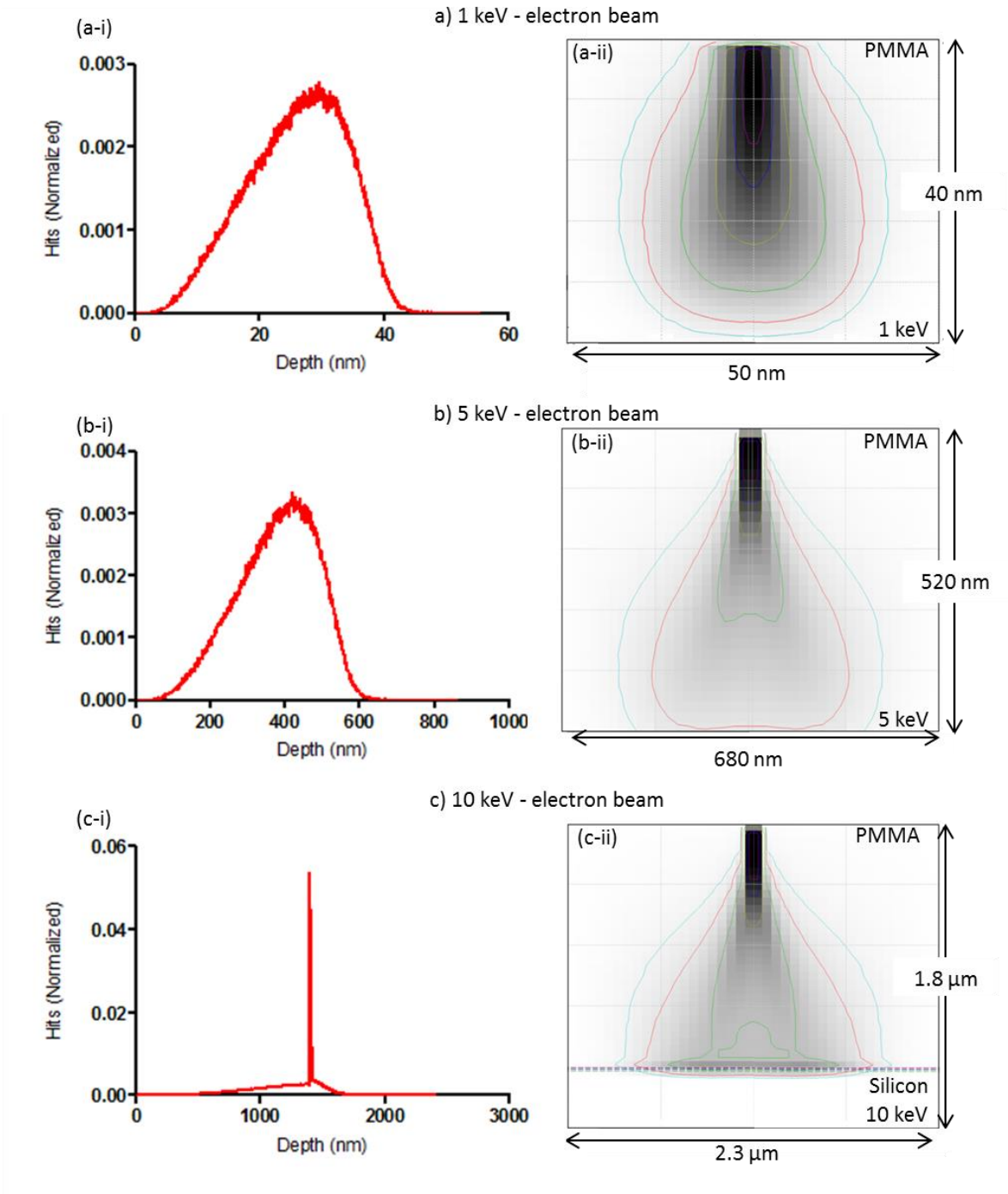

Figure 4.3: Monte Carlo modelling of relevant electron energies from indium-111
The percentage energy deposited in the PAR photoresists, from of electron beam of different energies (a) 1 keV, (b) 10 KeV and (c) 15 keV. (i) shows the normalized hits (hits being the number of interactions within the modelled photoresist) against the distance within the resist substrate and (ii) shows a visual representation of this data. The beam radius was 10 nm and 6 x 10^5 electrons simulated.

Figure 4.3 shows how the spatial distribution of the absorbed energy changes with increasing electron beam energy. A 1 keV electron beam deposits all of its energy

within 40 nm of the surface of the PMMA layer (Figure 4.3a) and for a beam radius of 10 nm, the energy is deposited over an area four times larger than the cross section of the incident electron beam (Figure 4.3a).

When the energy beam energy is increased to 5 keV, the depth of the energy deposited increases to 600 nm (Figure 4.3b) and the spread increased to 68 times the beam radius. This beam spreading occurs within the main body of the PMMA, at a depth of 70 nm. The curvature in the electron beam is as a result of back-scattering from the gold layer (Figure 4.3b (ii)), due to electrons being reflected back from the gold layer and hence depositing their energy in the PMMA layer.

As the electron beam energy is increased further, it is possible to see more of the backscatter effect of the gold and chrome layers. This is shown by the spreading out of the electron beam at the interface between the gold, chrome and PMMA. This occurs as the back-scatter electrons rebound at varying angles, not necessarily back into the electron beam path. There is also an increase in energy deposited at this point, as seen by the normalized hits of the 10 keV beam (Figure 4.3 c (ii)). The spreading of the beam occurs after an approximate depth of 300 nm for the 10 keV beam.

CASINO Modelling of the Electron Beam through Different Thicknesses of Water

Electrons that are internalised into cells pass through biological material before they interact with the PMMA photoresist. To consider these factors, CASINO modelling was performed with varying thicknesses of water, simulating a tissue equivalent material.

Figure 4.4 shows the relationship between the electron energy and the distance travelled in water, PMMA and a thin layer (0.01 nm) of water, placed on the upper surface of the photoresist. This thin layer of water was used to investigate the interface between the

biological material and the photoresist including any backscatter effects. Figure 4.4c shows there is an exponential relationship between the energy and the depth of penetration of electrons. From Figure 4.4, it is shown that adding a thin layer of water has little noticeable effect on the distance travelled by the electrons. Figure 4.4a shows that when an electron beam energy of 1 keV is modelled, the difference between adding a thin layer of water is insignificant to the distance travelled and energy deposition in the PMMA. As the electron beam energy is increased to 25 keV (Figure 4.4b), the difference between the PMMA and the PMMA with a thin layer of water is only noticeable at depth much greater than the thickness of the PMMA photoresist layer.

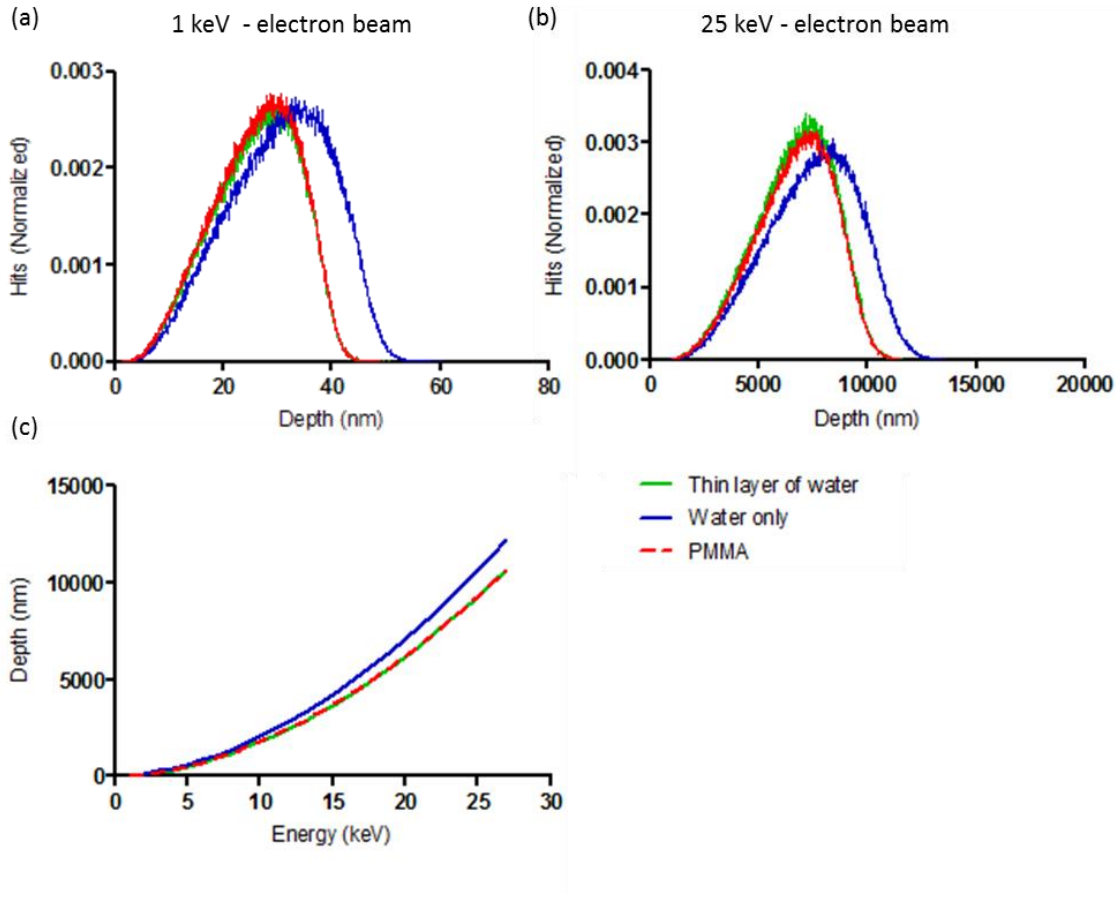

Figure 4.4: Electron beam travel through water
A graph of the initial electron energy plotted against the distance it will travel in water, in PMMA and when a thin layer of water is placed on top of a substrate of PMMA, modelled using CASINO. (a) A 1 keV electron beam and (b) a 25 keV electron beam vs hit ((hits being the number of interactions within the modelled photoresist). (c) A graph of the initial electron energy against the distance it will travel. The maximum distance travelled was calculated and

determined as the depth where 95 % of the total energy deposited had been deposited. The beam radius was 10 nm and 6 x 10^5 electrons were simulated.

As well as the surface effects which occur by the electrons which are travelling from the cell or isolated cell nuclei to the PMMA, there will also be the effects of the electrons travelling through the biological material. This can be modelled as a thicker layer of water.

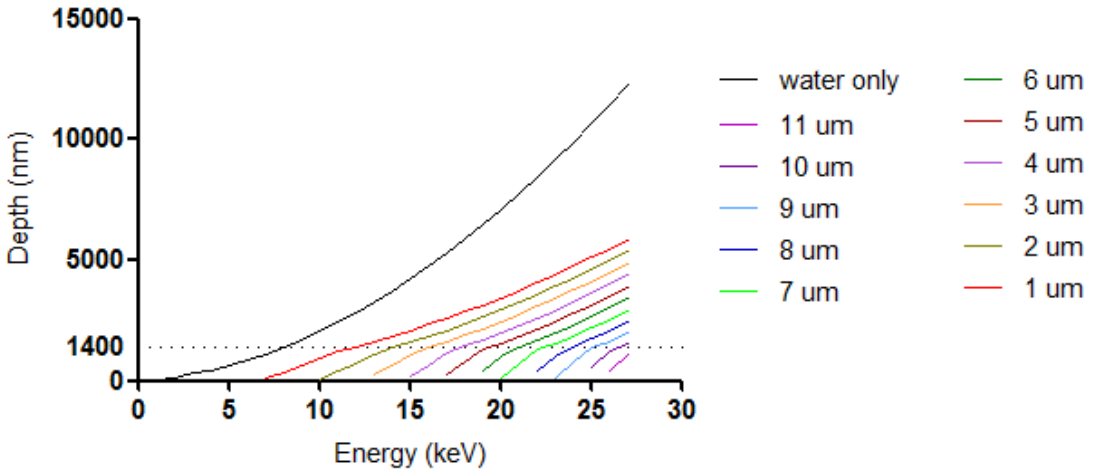

Figure 4.5: Electron travel through a thick layer of water
A graph of the initial electron energy against the depth of penetration the in PAR substrate, showing the distance electrons will travel in PMMA after travelling through various depths of water, modelled using CASINO. The maximum distance travelled was calculated and determined as the depth where 95 % of the total energy deposited had been deposited. The beam radius was 10 nm and 6 x 10^5 electrons were simulated. Dotted line at 1.4 µm depth is the change in substrate.

Figure 4.5 shows the total distance travelled for increasing electron energies when a thick layer of water up to 12 µm is placed between the source and the PMMA. The PMMA has a greater stopping power than the water. It shows that even the highest energy (25.58 keV) AE emitted by indium-111 are predicted not to reach the surface of the photoresists, if they originate at approximately 11 µm away from the surface of the resist. As the energy increases, there is uniform increase in the distance travelled. At 1.4 µm depth in the PMMA, there is a change in gradient of the line due to the change as

the electrons transverse the PMMA and start depositing their energy in the silicon substrate.

Travelling through biological material will also affect the resolution, since the further an electron has travelled through the biological material, the more that it will have spread before reaching the PMMA. Figure 4.6 shows the width of the electron beam as it enters the PMMA after travelling through different depths of water.

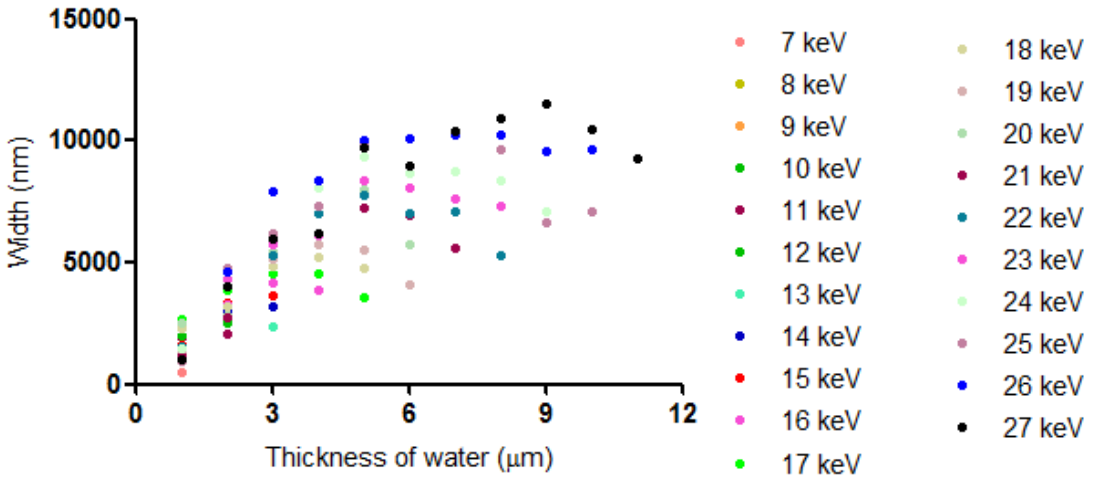

Figure 4.6: The electron beam spread through water
The spread of 95 % of the energy deposited at surface of PMMA photoresist, after electrons with different energies have passed through a layer of water of different thicknesses. The beam radius was 10 nm and 6 x 10^5 electrons were simulated. The maximum distance travelled was calculated and determined as the depth where 95 % of the total energy deposited had been deposited

Figure 4.6 shows the spread of the electron beam as it passed through layers of water of various thicknesses. As the thickness of the water increased, the width of the cross-section of the electron beam also increased. However, due to the bulb shape of the electron energy spread and the interaction of the electrons with the gold layer, the relationship between the thickness of water and the width is difficult to quantify.

If the electron beam energies which only interact with the PMMA layer are looked at, as shown in Figure 4.7, there is a linear relationship as the thickness of the layer of water increases.

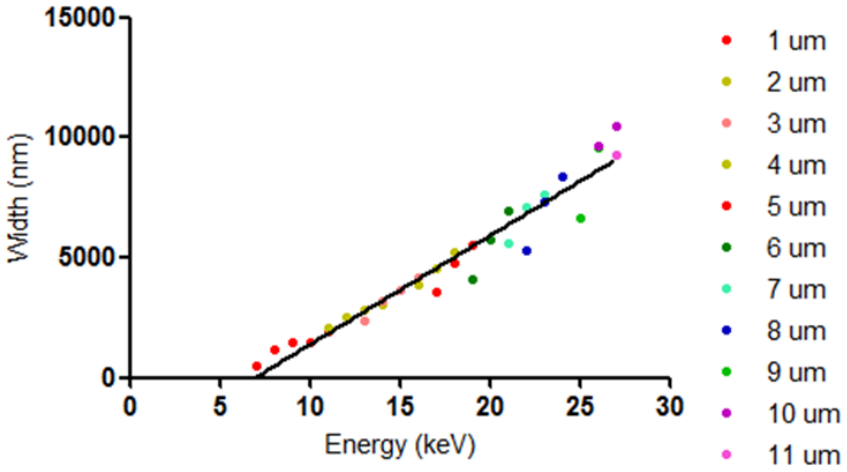

Figure 4.7: The electron beam spread in the PMMA
The spread of 95 % of the energy at surface of PMMA photoresist, after electrons of various energies have travelled through different thickness of water, looking at the interactions of electrons which only interact with the PMMA layer. The beam radius was 10 nm and 6 x 10^5 electrons were simulated. The maximum distance travelled was calculated and determined as the depth where 95 % of the total energy had been deposited.

4.2.3 The Microsphere Model

To validate the technique using indium-111, functionalized polystyrene microspheres were used, as they have a size and geometry comparable to that of a cell. Different concentrations of indium-111, corresponding to activities typically internalised in a cancer cell (100-600 mBq), were attached to the surface. The indium-111 constitutes a distribution of isotropic AE emitters, and with the microspheres there is a known geometrical relationship to the PMMA substrate surface.

A linear relationship was observed between the activity and the volume of resist removed, as expected (Figure 4.8a). The data points refer to average initial activities of

210 mBq, 300 mBq, 410 mBq and 640 mBq, respectively, for batches of labelled microspheres. The inserts in Figure 4.8a, firstly, show an optical image of the microspheres before washing; the second insert shows the footprint of the pattern. This is smaller than the area subtended by an individual sphere and is the direct result of the reduction of the fluence as a function of distance. The centre-to-centre spacing of the pits was between 6.5 and 7.5 µm, which is in approximate agreement with the average stated diameter of a microsphere (6.77 µm). The average radius of the radiation pattern patterns was 0.5 µm. The red line in Figure 4.8a is the theoretical line based on PMMA 950 K being 25 % more sensitive than PMMA 495 K.

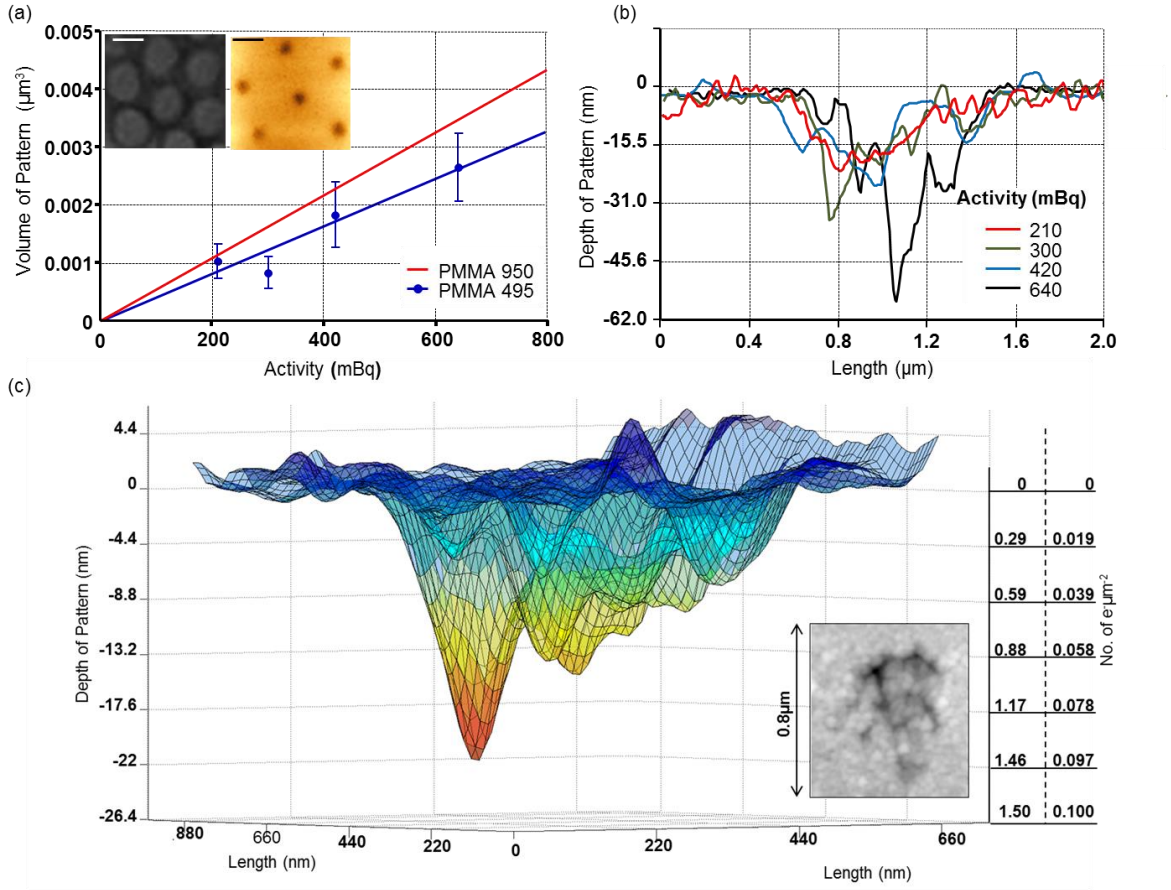

Figure 4.8: The microsphere model
(a) Volume (µm^3) removed, versus average initial activity per microsphere, for patterns on PMMA 495 K, when the microspheres were labelled with different amounts of radioactivity and the theoretical curve for PMMA 950 K. The optical image of the microspheres and the AFM image of the resultant patterns are shown in the inset (scale bar 5 µm). (b) Line contours showing the depths of the patterns in the PMMA 495 K resist, resulting from individual microspheres labelled with different specific activities (mBq). (c) A 3-D generated surface

contour of a high resolution AFM image showing the variability in depth resulting from radionuclides bound to the surface (300 mBq) for a single microsphere resting on a PMMA 495 K resist. The inset shows the pattern in grey-scale representation. The volume removed was $4.9x10^{-4}$ μm^3 (Royle et al., 2015 adapted with permission).

The error bars in Figure 4.8a show considerable variation in the labelling efficiency of individual microspheres. Moreover, indium-111 is non-uniformly distributed over the surface area of the microspheres, as demonstrated by the pattern shown in Figure 4.8c and by the line scans (Figure 4.8b). When a 3-D image of a microsphere footprint is rendered (Figure. 4.8c) the complexity of patterns resulting from the decay of isotropic indium-111 point sources distributed irregularly is apparent. The volume removed per electron is $2.3x10^{-9}$ $\mu m^3/e^-$.

4.2.4 Demonstration Photoresist Autoradiography Technique: Direct Application Method

SQ20B cells were treated with ^{111}In-DTPA-hEGF for 1 hour and then fixed in methanol or 4 % PFA, before being directly placed on a PMMA photoresist, known as the direct application method (DM). After washing and developing, the resulting patterns, arising from the exposure by the internalised radionuclides, were analysed by AFM. Initial experiments were carried out with cells directly placed on the photoresists. AFM scans of the patterns are shown in Figures 4.9–4.12.

Figure 4.9 shows the different types of conditions that can be used with the PAR technique. Most of the patterns have some features that are above the surface of the resist. The patterns are of a non-uniform shape for Figure 4.9 (a), (b) and (c) but Figure 4.9 (d) shows a uniform shape suggesting uniform dose distribution across the cell nuclei. Similar patterns were not seen on control resists Figure 4.14.

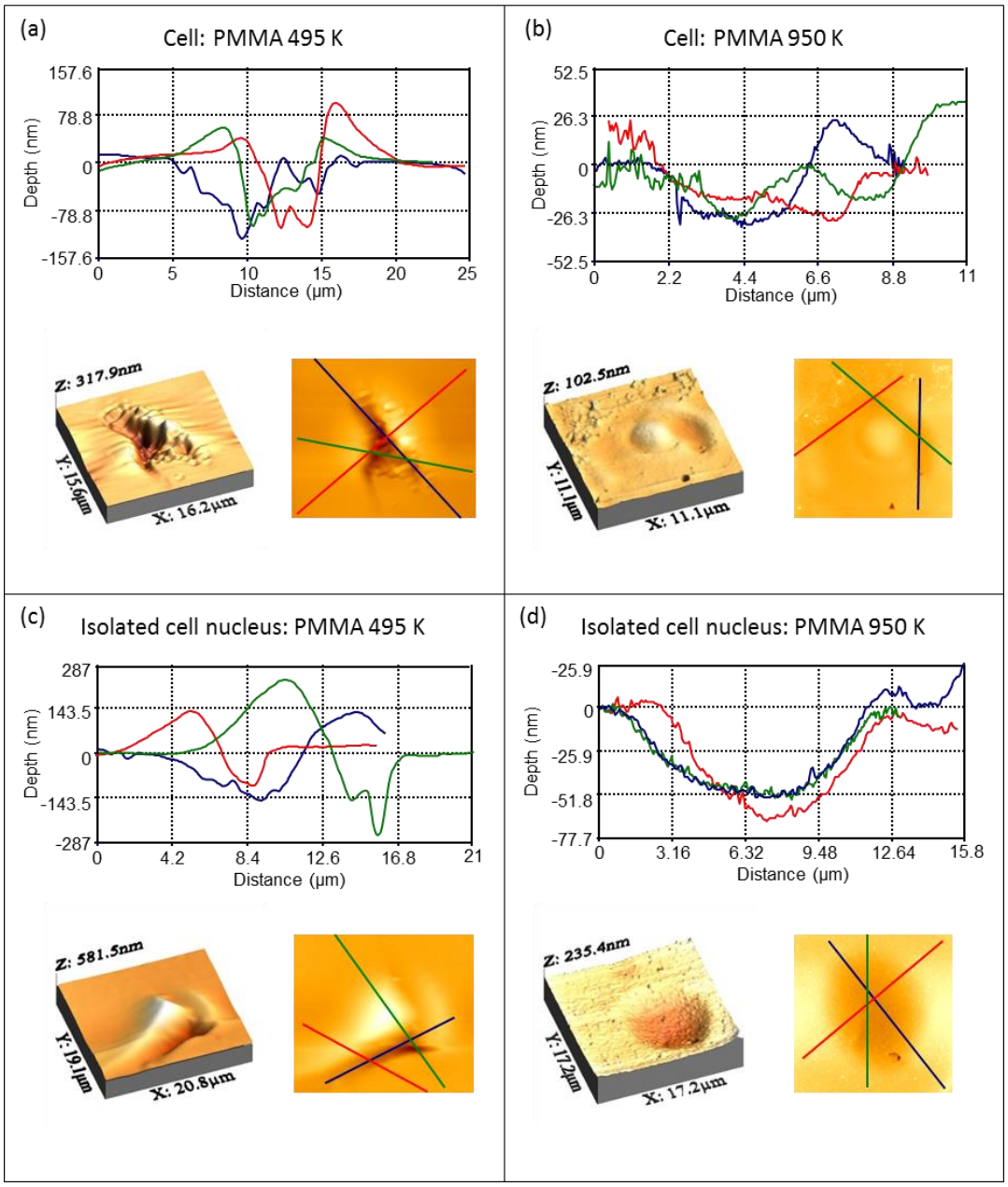

Figure 4.9: Demonstration of the direct application method: Patterns seen on photoresists when cells and isolated cell nuclei were fixed in 4 % paraformaldehyde

The PAR technique, (a) & (b) cells and (c) & (d) isolated cell nuclei, treated with ^{111}In-DTPA-hEGF for 1 hour before being fixed in 4 % PFA and directly place on (a) & (c) PMMA 495 K; or (b) & (d); PMMA 950 K photoresists.

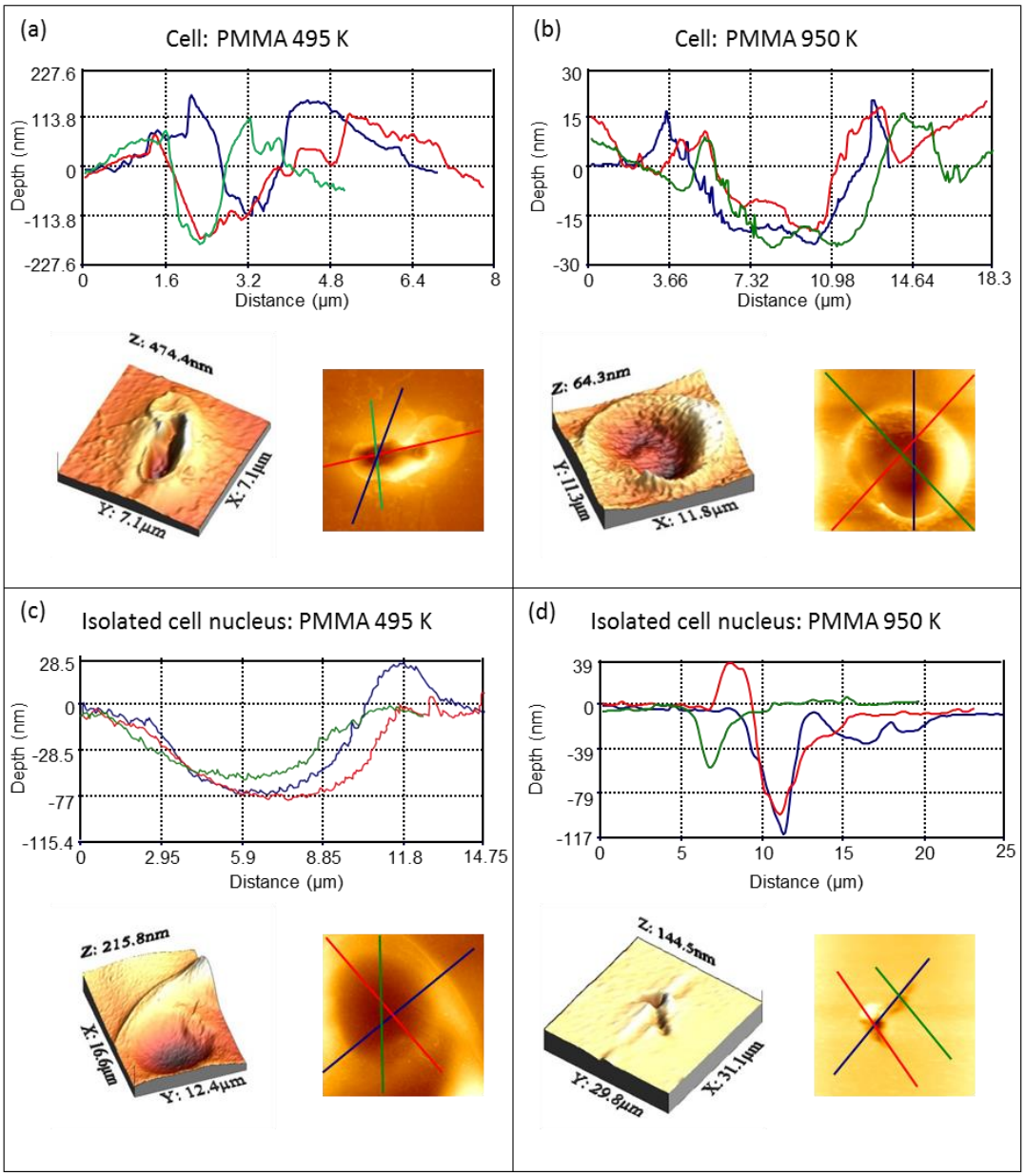

Figure 4.10: Demonstration of the direct application method: Patterns seen on photoresists when cells and isolated cell nuclei were fixed in methanol
(a) & (b) cells and (c) &(d) isolated cell nuclei treated with ^{111}In-DTPA-hEGF for 1 hour before being fixed in methanol and directly placed on PMMA 495 K (a) & (c) or PMMA 950 K (b) & (d) photoresists.

Figure 4.10 shows very similar patterns to those in Figure 4.9: they have a range of sizes. Figure 4.10 (a) shows cellular features which have a diameter of less than an SQ20B cell (20 µm). No patterns were seen on control resists (Figure 4.13).

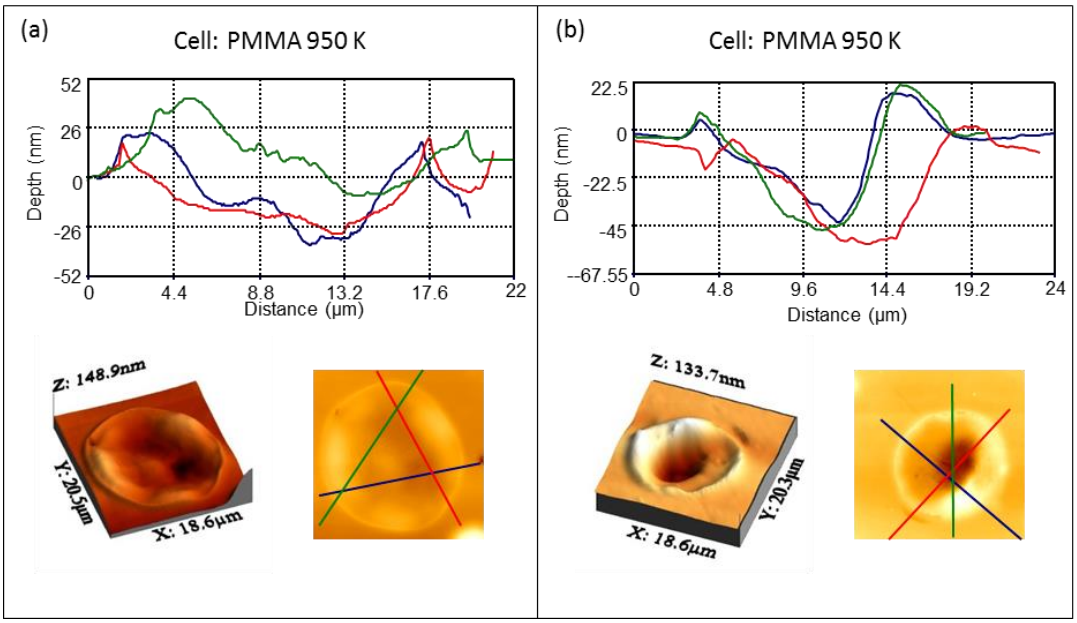

Figure 4.11: Direct application method: Patterns seen on photoresists when exposed to cells
PAR showing differences in the patterns which are seen with the PAR technique, PMMA 950 K photoresists with cells treated with ^{111}In-DTPA-hEGF for 1 hour before being fixed in methanol.

Figure 4.11 shows that for cells which have undergone the same treatment, 1 hour incubation with ^{111}In-DPTA-hEGF, and fixed in methanol, different radiation footprints are imaged using the AFM, with a range of depths and radii.

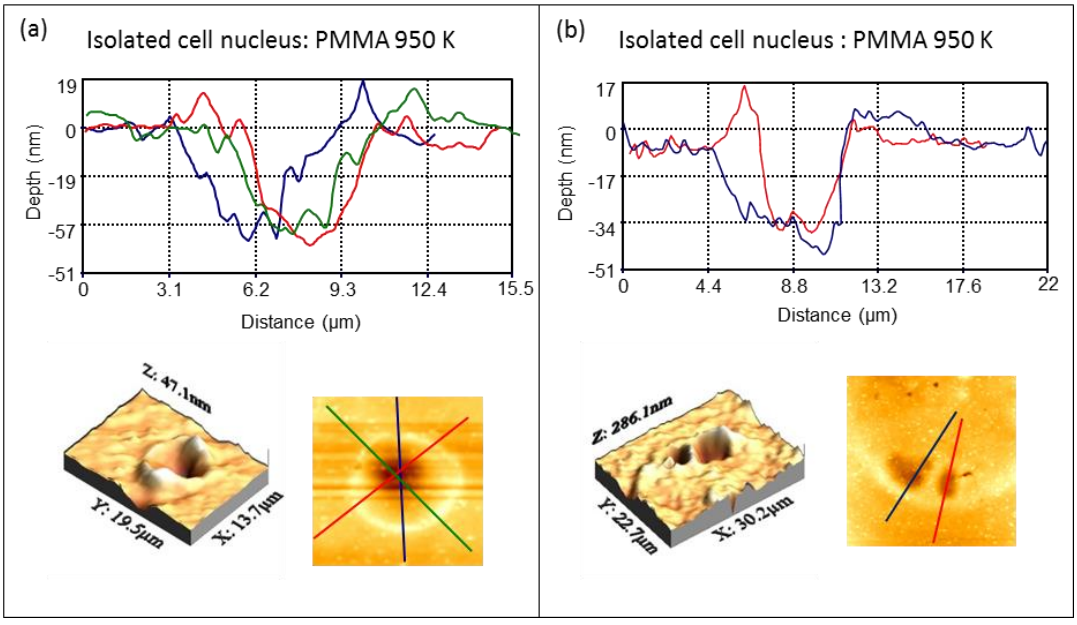

Figure 4.12: Direct application method: Patterns seen on photoresists when exposed isolated cell nuclei
Two different types of patterns which are seen with the PAR technique (a) & (b) PMMA 950 K photoresists with isolated cell nuclei treated with ^{111}In-DTPA-hEGF for 1 hour before being fixed in 4 % PFA.

Figure 4.12 shows two different types of patterns which are seen for isolated cell nuclei which have been treated the same way–1 hour incubation, fixed in 4 % PFA–showing that there are different types of patterns that can be seen.

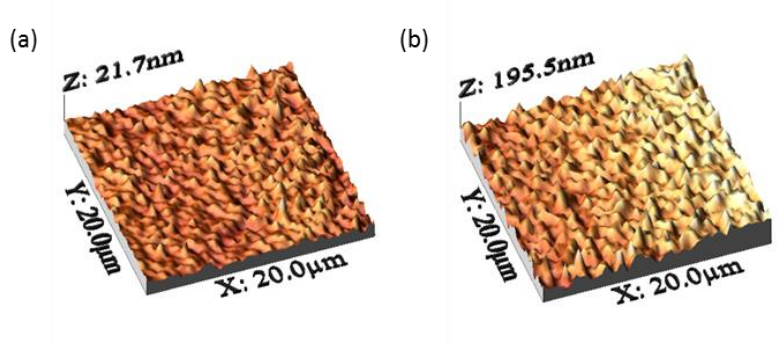

Figure 4.13: Direct application method: Atomic force microscope scans of control resists
AFM scan of PMMA 950 K resists which had control cells placed on them (a) fixed in 4 % PFA, (b) fixed in methanol.

Figures of the patterns (Figures 4.9, 4.10, 4.11, 4.12) show both PMMA 495 K and PMMA 950 K are exposed by internalised indium-111. Even under the same conditions, the patterns vary in depth and radius. There are no features on the control resists (Figure 4.13).

4.2.5 The Photoresist Autoradiography Technique: The Presence of Raised Features

A feature frequently seen in most AFM images of cells and isolated cell nuclei treated with ^{111}In-DTPA-hEGF (but absent in AFM images of untreated control cells) using the DM, are raised areas. These features have a range of heights. To explain this phenomenon we explored three possible explanations that might account for the raised features: 1) cross-linking, 2) ingress of fluid and 3) biological debris remaining after exposure and processing.

Cross-linking of the PMMA

The PAR technique uses PMMA as a positive tone resist where the exposed area has been removed by the developer after electron exposure. Although at the same time,

cross-linking occurs, but when being used as a positive tone resist, there is more chain-scission than cross-linking. However, at higher fluences, PMMA undergoes contrast-reversal due to there being more cross-linking, than chain-scission of the chemical bonds (Ziler et al., 1996, Corelli et al., 1987). By changing the development conditions, the unexposed resist is removed and the exposed resist remains, leading to features which are above the main surface of the resist. Cross-linking has been shown when using CARs with PAR (Falzone et al., 2011). The range of fluences that are emitted by indium-111 could cause a cross-linking reaction. To test whether there is more cross-linking than chain scission at higher exposure doses, which would lead to the PMMA acting as a negative tone resist and raised features, photoresists were exposed to a high electron dose. To do this, a 30 keV electron dose, from a scanning electron microscope (SEM) of approximately 1 x 10^8 electrons, was used.

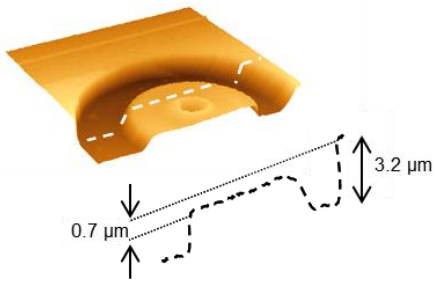

Figure 4.14: A photoresist exposed to a high electron beam dose
A 3.2 µm thick PMMA 950 K layer was exposed to a 30 keV electron dose of approximately 1 x 10^8. The feature was subsequently developed using standard processing conditions. Carried out by Dr Sverre Myhra, Department of Materials, University of Oxford.

Figure 4.14 is an AFM image which shows that the central circular feature which has received the highest dose has been heavily cross-linked, leading to the exposed region of the PMMA not being completely removed by the developer. The height of the central feature is 0.7 µm lower than the surrounding resist, thus demonstrating that cross-linking under the development conditions used does not lead to raised features that have a height greater than the non-exposed regions. This is unlike the raised features seen in

cell images. The ring region, which has a greater depth, has received a much lower dose. This is due to the Gaussian beam shape and electrons scattering out of the central feature.

Ingress of Fluid into the PMMA

Ingress of fluid occurs at a very low dose due to the developer penetrating the PMMA. While the dose is insufficient for normal lithographic development of a pattern, the developer becomes trapped within the PMMA causing it to swell (Junarsa et al., 2005). The effect was seen when using CARs with PAR (Falzone et al., 2011). Post-baking (100°C, 90 seconds) allows the developer to evaporate and remove swelling.

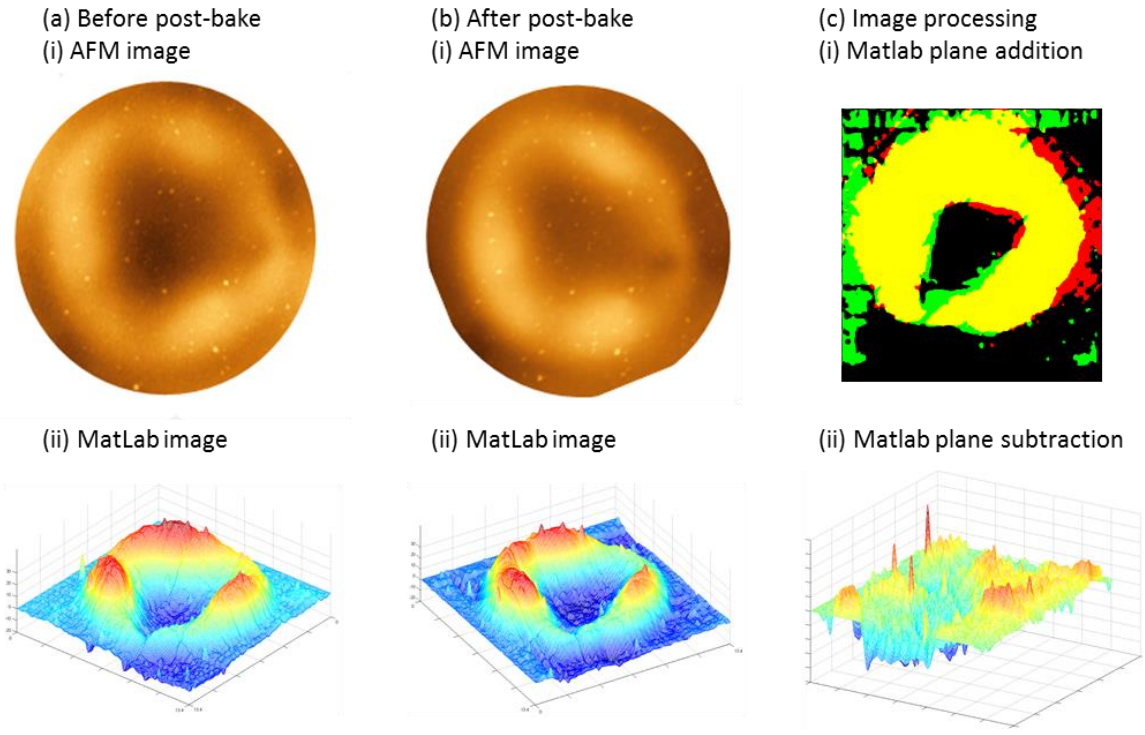

Figure 4.15: Radiation patterns before and after a post-bake
AFM Images obtained out before and after a post-bake on the same cell with prominent raised features. a) Images before post bake, b) Images after post bake c)i) Matlab reconstruction showing regions where the two images have similar heights (yellow/black), red is before post bake, green is after post-bake ii) A Matlab image after the post-bake image has been subtracted from the non-baked image showing no features.

However, raised features were seen both after an immediate post-baking (Figure 4.15) and when resists were imaged using the AFM before and after post-bake (Figure 4.16). This suggests that ingress of fluid is not a reason for raised features. Comparing the differences in the resist surface before and after post-bake shows that in Figure 4.15c (ii) there is a still a slightly raised structure, after subtraction of the two patterns. This effect is probably due to polymer relaxation, causing the patterns to change over time.

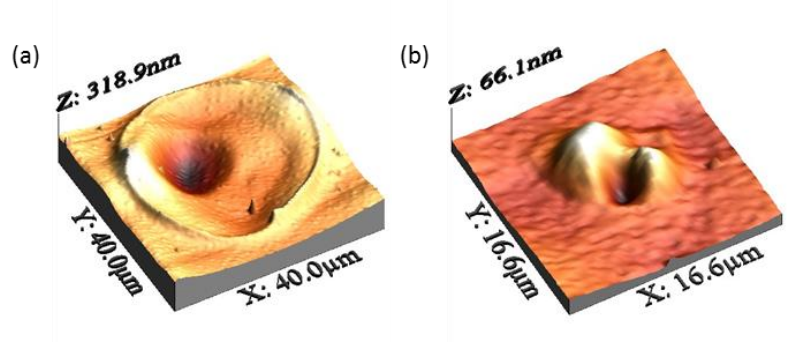

Figure 4.16: Radiation patterns after an immediate post-bake
AFM resist post-baked immediately after developing showing raised features. (a) A cell fixed in methanol placed on PMMA 950 K and (b) an isolated cell nucleus fixed in 4 % PFA before being placed on a PMMA 495 K.

Biological Debris

Biological debris remaining after chemical processing could contribute to the raised features observed. A series of washing experiments were carried out to test this hypothesis.

Figure 4.17 shows the various washing stages of the PMMA resist. This causes AFM features which are not similar to the features seen when surrounding the patterns when exposed to ^{111}In-DTPA-hEGF. Figure 4.17 shows that washing the photoresist does have an effect on the removal of the biological material. An incomplete wash would leave cellular debris on the resist, this debris has a significant height, larger than what is seen with the raised features imaged from patterns after cells are treated with ^{111}In-DTPA-hEGF (Figure 4.17a). If a partial wash is carried out, the pattern which remains

on the resist looks spikey (Figure 4.17b). However, further washing results in the removal of the resist material itself, as characterized by a very flat contour in a line scan (Figure 4.17b).

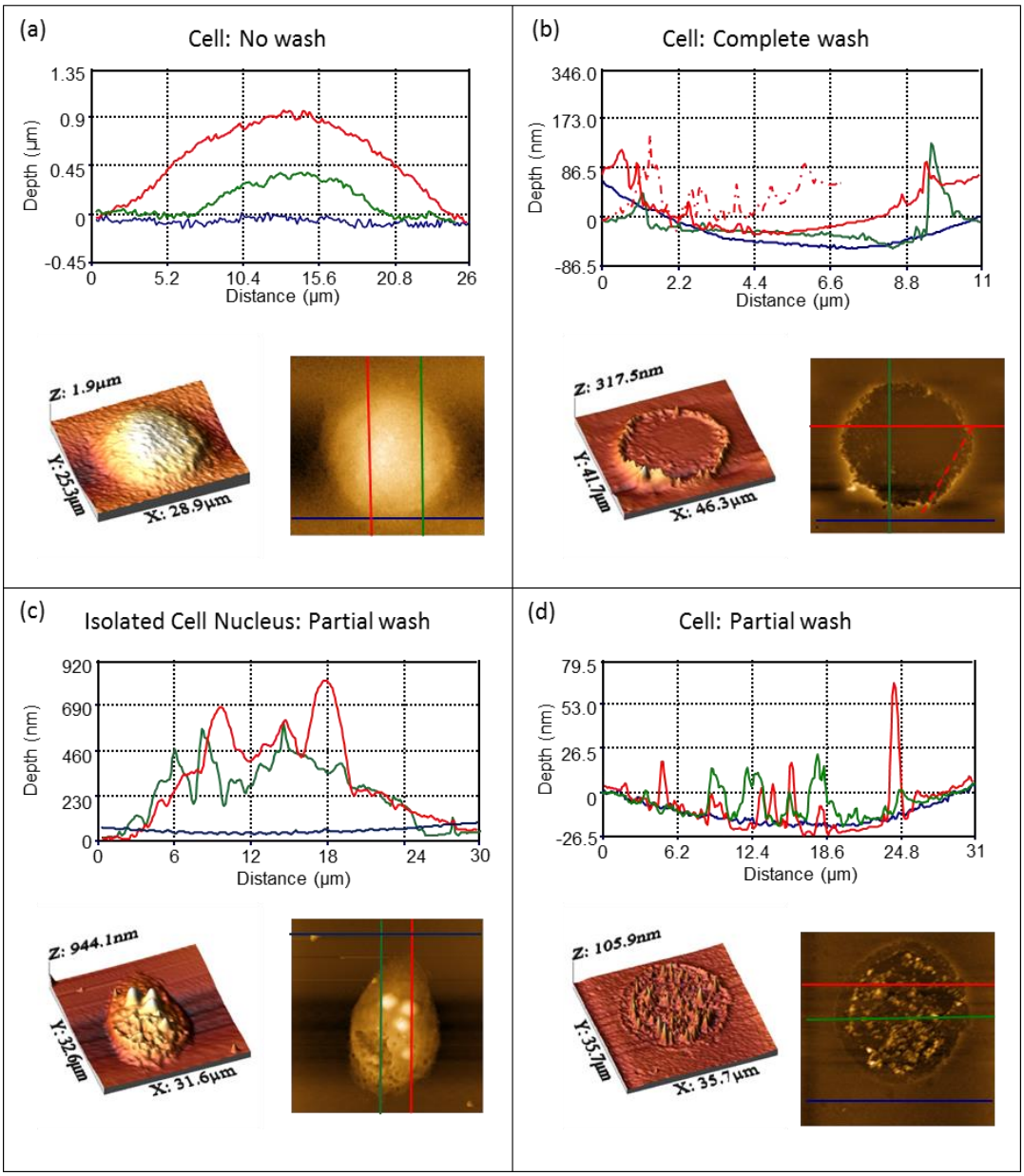

Figure 4.17: A series of washing steps
a) ^{111}In-DTPA-hEGF exposed cell on PMMA 950 K, fixed in 4 % PFA which has not undergone any wash, b) the remains of an ^{111}In-DTPA-hEGF exposed cell on PMMA 950 K, fixed in 4 % PFA which has undergone a complete wash so that the resist has been removed, c) a ^{111}In-DTPA-hEGF exposed nucleus on PMMA 950 K, fixed in 4 % PFA which has undergone a partial wash. d) An ^{111}In-DTPA-hEGF exposed cell on PMMA 950 K, fixed in 4 % PFA which has undergone a partial wash.

While several theories about the raised features have been disproven, other reasons for these raised features now have to be considered. One of these is radiation grafting. This is where the radiation causes the surface of the polymer to become more chemically reactive, and improves the surface bonding. This causes the surface to bond to a variety of materials, hence causing the raised features seen as biological material bonds to the surface. To avoid this effect, the method was adapted and the photoresist was inverted on top of a monolayer of cells, thus reducing the interaction between the two.

4.2.6 Demonstration of the Photoresist Autoradiography Technique: Indirect Application Method

To remove the likelihood that the biological material was causing radiation grafting (where the PMMA and biological materials have chemically bonded together) or other effects due to the interaction of the biological material with the PMMA surface, a new method was proposed where the resist was inverted onto a monolayer of cells: the indirect application method (IM). The cells will still be in contact with the photoresists, but a much smaller fraction of them will be. The experimental design is demonstrated in Figure 4.18. Due to its increased sensitivity and non-visible difference in image resolution only PMMA 950 K was used for experiments.

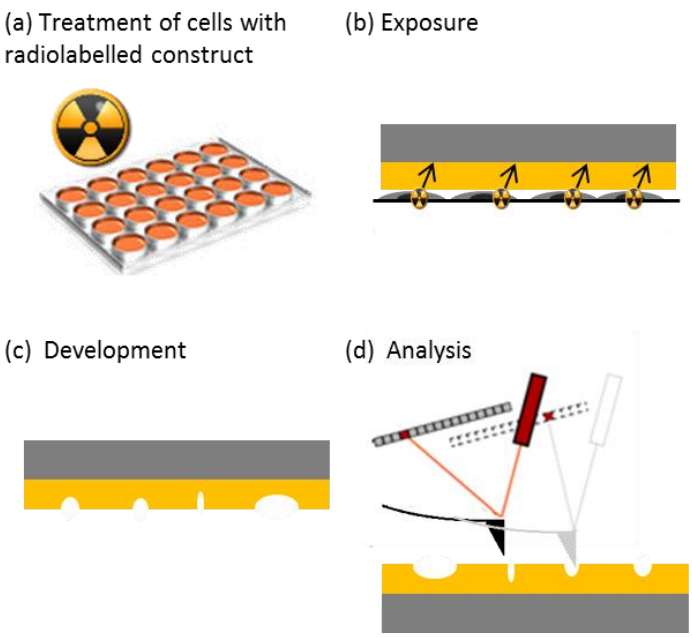

Figure 4.18: The indirect application method
Schematic representation of the new experimental sequence. (a) Cells are incubated with an AE-emitting radionuclide. (b) Exposure of a PMMA photoresist film in close proximity to the cells or isolated cell nuclei. (c) Chemical development of the latent images. (d) Topographic imaging by AFM to reveal the 3-D structure of the pattern.

The experimental condition for the incubation of the radiopharmaceutical were kept the same as the DM: 40 nM/mL of ^{111}In-DTPA-hEGF at a specific activity of 8 MBq and incubated for 1 hour. The pre-expose conditions (thickness of resist film and gold layer) and the post-expose processing of the photoresists (development, time and concentration) were kept the same. Patterns are shown in Figures 4.19–4.21.

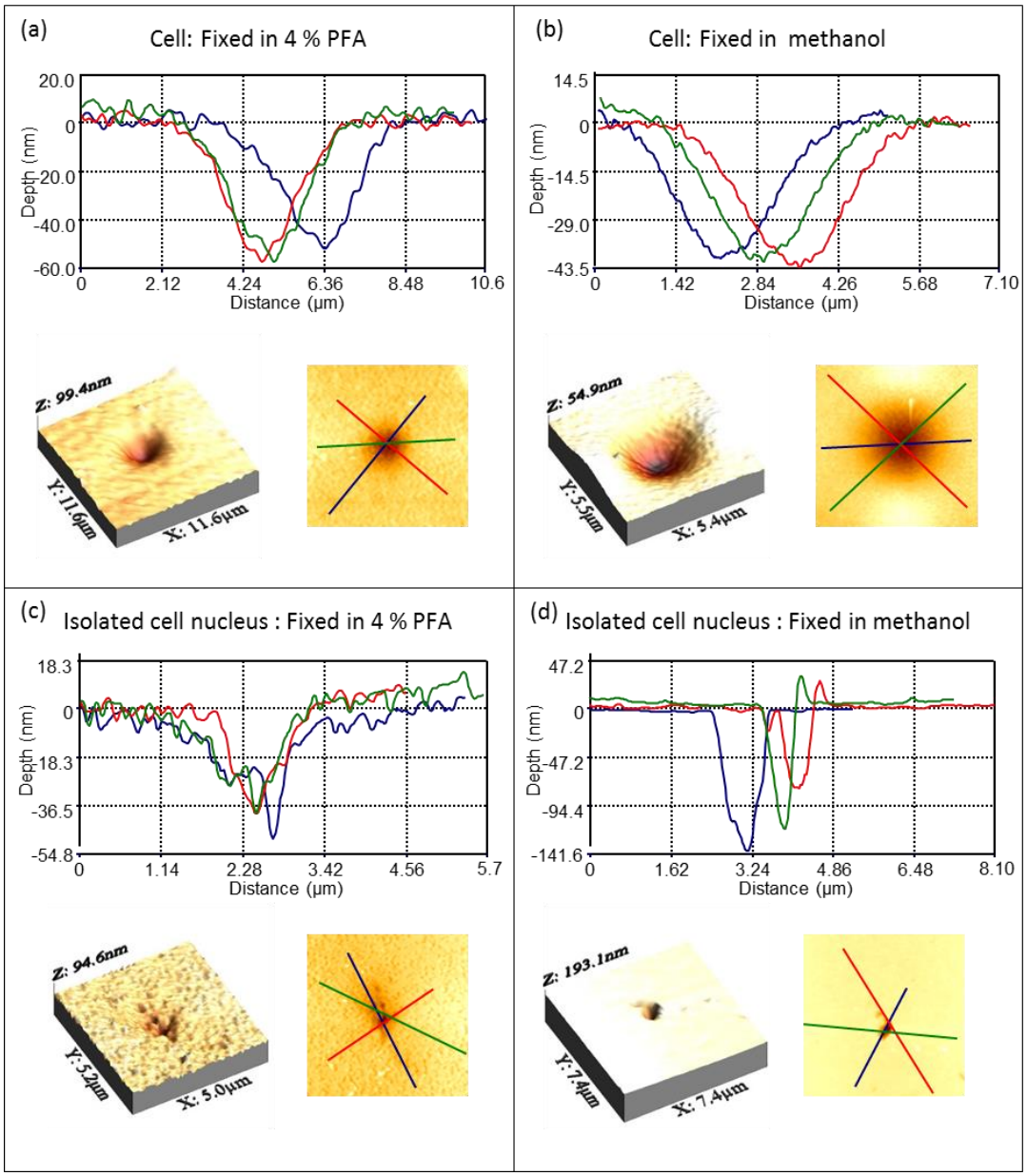

Figure 4.19: Indirect application method: Patterns seen on photoresists
(a) & (b) Cells and (c) & (d) isolated cell nuclei; treated with ^{111}In-DTPA-hEGF for 1 hour before being fixed (a) & (c) in 4 % PFA or (b) & (d) in methanol before PMMA 950 K photoresists were inverted and placed onto the cells.

Figure 4.19 shows that when the cells are not directly placed on the resist there is no swelling present. The patterns appear smaller than when seen with the original PAR method. The patterns seen in the photoresists have a range of sizes. Figure 4.20 shows two examples for cells and Figure 4.21 shows two examples for isolated cell nuclei. There are no features seen on the control resist Figure 4.22.

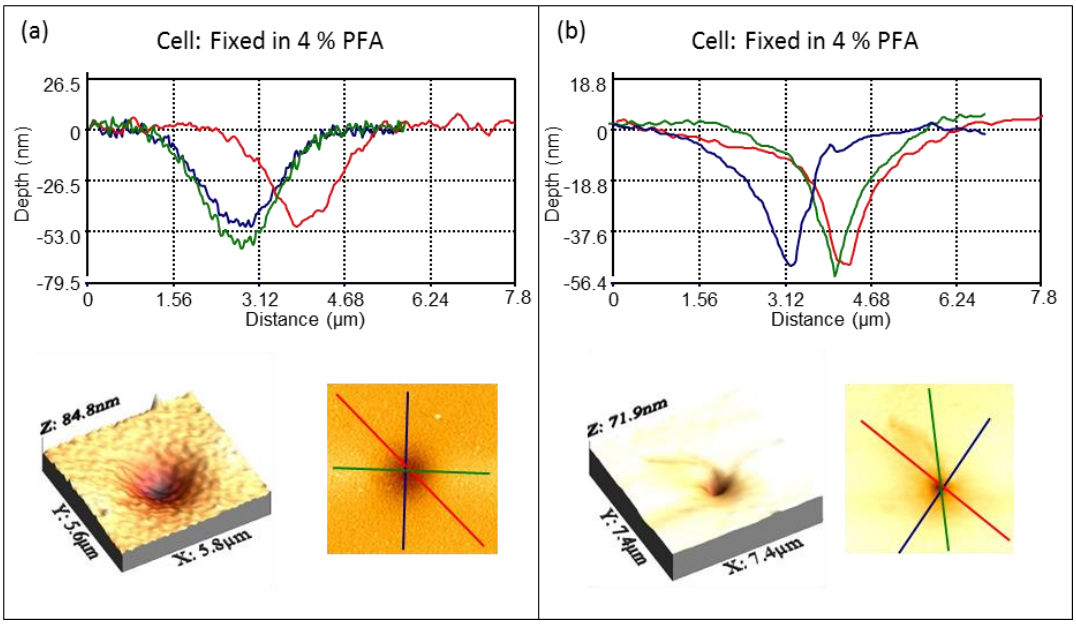

Figure 4.20: Indirect application method: Patterns seen when photoresists were exposed to cells

Different patterns that are seen with the PAR technique, (a) & (b) cells treated for 1 hour with ^{111}In-DTPA-hEGF were fixed in 4 % PFA before a PMMA 950 K photoresist was inverted and placed on the cells.

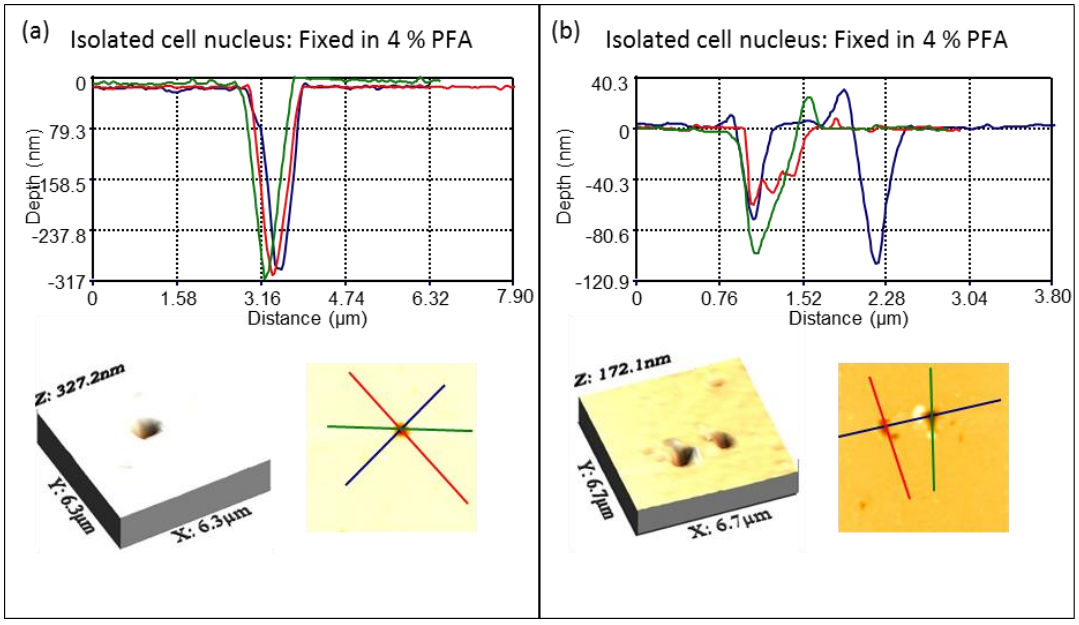

Figure 4.21: Indirect application method: Patterns seen when photoresists where exposed to isolated cell nuclei

Different patterns that are seen with the PAR technique, (a) & (b) isolated cell nuclei treated with ^{111}In-DTPA-hEGF, fixed in methanol before PMMA 950 K photoresists was inverted and placed on the cells.

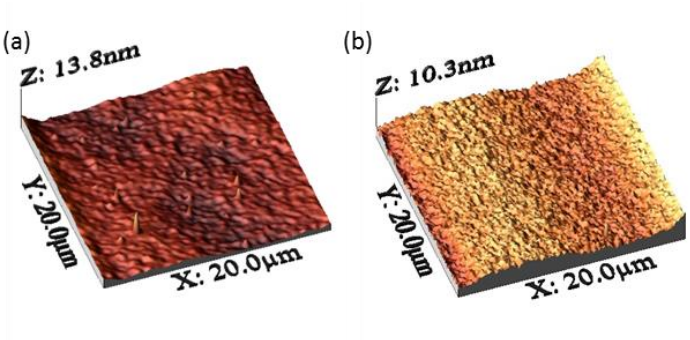

Figure 4.22: Atomic force microscope scan of control resists from the indirect application method

AFM scan of PMMA 950 K resists which had control cells placed on them (a) fixed in 4 % PFA, (b) fixed in methanol.

4.3 Discussion

4.3.1 Electron Beam Calibration

PMMA 950 K was the more sensitive photoresist with patterns which were 25 % deeper for both the 25 keV and 50 keV electron beams as shown in Figure 4.1. PMMA 950 K could detect a fluence as low as 1.0 x 10^5 $e^-/\mu m^2$ (Royle, 2012, Royle et al., 2015). The reason for this is that PMMA 950 K has a higher density thus leading to a greater number of carbon backbones which could be broken by the electrons in the same area. Both PMMA formulations were sensitive enough to have electron beam patterns written into their surface and read by the AFM after development.

It is believed that the electron beam calibration system provides robust calibration data as each electron which is emitted by the electron beam will have an effect on the photoresist surface, as experiments are carried out in a vacuum. Therefore, it allows for a relationship to be established between the incident energy and the volume of resist removed. For the development conditions described, the factors which link these parameters have been calculated and are shown in Table 4.1.

However, the electron beam used was only able to generate monoenergetic 25 keV and 50 keV beams, limiting the calibration experiments to these energies. Indium-111 emits electrons with energies ranging from a few eV up to 26 keV (AE and Coster-Kronig electrons) and internal conversion electrons up to 250 keV. Ideally, the response of the photoresist should be calibrated using an electron beam or beams with energies identical to those of the electrons emitted by the radionuclide of interest. However, available electron beam lithography systems only operate at beam energies ranging from 10–100 keV (Grigorescu and Hagen, 2009). This is less of a limitation when using the PAR technique with indium-111, as 35 keV is the approximate weighted average

energy of indium-111 per decay (excluding X-rays and gamma emissions) which is similar to the electron beam energies used (Royle et al., 2015). However, the majority (97 %) of the AE have an energy less than 4 keV and the internal conversion electrons have an energy much greater than the weighted average (144.6 and 245 keV).

4.3.2 CASINO Monte Carlo Modelling of the Photoresists

Modelling of the electron beam using CASINO MC Code allows for a better understanding of the interaction of the electrons with the PAR substrate.

Monte Carlo Modelling of 25 keV and 50 keV Electron Beams

The electron beam data showed that the 25 keV electron beam created deeper patterns compared with 50 keV (Figure 4.1). CASINO modelling of these two beam energies demonstrates why this is the case since a higher percentage of the total energy from the 25 keV beam has been deposited in the PMMA layer (Figure 4.2). The CASINO modelling does not show how deep developed patterns are, as they are dependent on the removal of the photoresist during development and cannot be modelled using the programme. However, the CASINO modelling does show that the majority of the energy from the electron beam will not be deposited within the photoresist, which may lead to the electron beam calibration being an overestimate of the number of electrons which are required to create a pattern.

PMMA 495 K will have a thinner resist layer than modelled using CASINO, all the analysis with CASINO was carried out using a PMMA layer of 1.4 µm. This is the thickness of the PMMA 950 K resist after spin coating at 4000 rpm. However, for PMMA 495 K, the layer is 0.5 µm thick after spinning at 4000 rpm (MicroChem, 2001). Since there is a relatively uniform deposition of the energy in the PMMA modelling with a PMMA layer of 0.5 µm thick, it is expected to produce similar results.

If we were able to model PMMA 495 K and 950 K separately, it would be expected that there would be more energy deposited in PMMA 950 K compared to PMMA 495 K. As PMMA 950 K has a greater density it has a greater stopping power, it therefore demonstrated deeper patterns in the electron beam experiments.

Monte Carlo Modelling of Relevant Electron Energies from Indium-111

Modelling of lower electron energies emitted by indium-111, as shown in Figure 4.3, shows that these will have more effect at the surface of the resist, since all of their energy is deposited close to the surface. Similar results have also been obtained by using the MC code PENElope (Falzone et al., 2012). Here it was shown that the Auger and Coster-Kronig electrons from indium-111 deposited 26.0 % of their energy within 0.5 μm^2 compared to 14.8 % and 4.1 % for a 25 keV and 50 keV beam. When the PMMA thickness was increased to 1.5 μm^2 the percentage incident energy increased to 33.5 %, 30.4 % and 9.6 % for indium-111, 25 keV and 50 keV beams respectively. From this information, it would therefore be expected for cellular patterns from indium-111 to be deeper if there were no other factors to consider in comparison to the electron beam.

If individual electrons energies, also shown in Figure 4.3, are looked at, a 1 keV electron beam will deposit all of its energy within 40 nm of the surface of the PMMA photoresist. While it could be predicted that all of this pattern would be developed, imaging the lateral spread may not occur. The AFM is a surface imaging technique and as such, is unable to image this spreading of the electron beam within the photoresists. This may mean that when individual cells are imaged, the volume of the pattern may not be the total volume which has been developed. This may be a factor which leads to washed out cellular patterns (as shown in cellular images) as individual point sources

overlap underneath the surface. The developer may then dissolve this volume between individual point sources, leading to the surface of the PMMA collapsing, reducing the resolution of the technique. This effect may also lead to patterns much larger than expected, as whole cellular patterns merge.

CASINO Modelling of the Electron Beam through Water

When transferring from one medium to another, there may be surface effects such as back-scattering. This is shown in Figure 4.3c (ii) by the change in shape of the deposited energy. Although PMMA and water (as a model for biological material) have a similar density (1 g/cm^3 for water compared to 1.18 g/cm^3 for PMMA), there could still be an effect. Figure 4.4 shows that when electrons transverse from water to PMMA, there is no decrease in the distance that these electrons travel, compared to electrons of the same energy which have not changed the material through which they travelled. It is therefore assumed that there will not be a dramatic change in the energy deposited in the PMMA, due to the electrons travelling between two materials, and that very few will be reflected back off the surface of the PMMA into the biological material.

Since electrons arriving at the PMMA surface will have travelled through a biological material, a demonstration of this is shown in Figure 4.5. There is a maximum distance that the AE emitted from indium-111 will be able to travel through biological material and this distance depends on their energy. The highest energy AE emitted from indium-111 atoms, have an energy of 25.58 keV and have a range in biological equivalent material of less than 11 µm. Indium-111 atoms further away than this from the surface will not interact with the resist and therefore will not contribute to a pattern. However, if the cells have collapsed into the surface of the photoresist, they are expected to be

less than this distance from the surface of the resists. An AFM image of a cell (Figure 4.17) shows that the cell collapses to approximately 1 μm.

These electrons which were emitted with a high energy and have travelled through the biological material will have lost energy as they reach the PMMA. They will behave like lower energy electrons. This increases the energy that they deposit close to the PMMA surface, leading to deeper patterns, as compared to them not traversing the biological material. However, these electrons will have spread out. The spreading out of the electrons will, firstly, greatly have an impact on the resolution that can be achieved with the PAR technique. It is assumed that the resolution of these patterns will be reduced, since the electron beam has effectively become defocussed, as shown in Figures 4.6 and 4.7. Secondly, since the electrons will now cover a larger area of the photoresist, they will have a lower density of interactions on the PMMA layer, which may lead to there not being a sufficient fluence to create a pattern. It is expected that this reduction in fluence will be offset by more electron energy being deposited in the surface region of the PMMA, leading to the creation of radiation footprints within the photoresist.

Electron beam calibration experiments and modelling with CASINO was carried out using parallel electron beams, in comparison electrons emitted from indium-111 will be emitted isotopically. However, unlike solid-state nuclear track detectors, which have an upper angular limit of approximately (<60◦) (Myhra et al., 2014), detection of electrons with PMMA is independent of the angle of incident of the electron but rather a function of the electron energy.

4.3.3 Functionalized Microspheres as a Demonstration of Photoresist Autoradiography

Functionalized polystyrene microspheres provide a realistic approximation of cells *in vitro*, by virtue of having known sizes and shapes that are comparable to a cancer cell. The results in Figure 4.8 are indicative of the extent to which the method can accommodate and reveal variability in total uptake, and in the spatial distribution of uptake in cancer cells.

AFM analysis of the radiolabelled microsphere footprints in the PMMA 495 K resist was capable of resolving individual "hot-spots" on the resist. The resolution in the z-direction is limited by the root mean square (RMS) surface roughness, which under favourable conditions is comparable to the radius of gyration (the distribution of the polymer around a central axis) of the polymer molecules (10's of nanometres).

Although the electron energies are different and will therefore individually remove different volumes of the photoresist, it is possible to compare the average volume removed per electron, for the microsphere and the 25 keV beam. This is done by comparing the gradient of the graphs in Figures 4.1 and 4.8. The volume removed on average per electron for a microsphere is approximately 6 % of the volume removed, by a 25 keV e-beam, for a similar fluence of incident radiation. Thus, a greater number of electrons would be required to create a pattern of the same depth. This is contradictory to the CASINO modelling where, because a greater percentage energy for the indium-111 is deposited closer to the surface of the photoresist, it was believed the patterns produced by indium-111 would be deeper. However, the total number of electrons which have interacted with the surface will be much lower than stated. Firstly, the electrons will be emitted around a 4π solid angle so half of the electrons will not

interact with the photoresist. As well as this, the whole surface of the microsphere will have indium-111 attached to it but not all of the electrons will interact with the surface. The fluence which reaches the surface will be reduced as there is $1/R^2$ dependence.

To take these factors into account, a more accurate way of determining the number of electrons which contributed to the patterns would be to look at the number of indium-111 atoms per unit area of the surface (of the microsphere). For an initial activity per microsphere of 300 mBq , the volume of the pattern is 4.9×10^{-4} μm^3 and there is approximately 1.3×10^4 e^- per unit area of the microsphere. The area in the x–y plane of a typical pattern is approximately 0.5 μm^2, as shown in the inset in Figure 4.8(c). It is therefore assumed that only an area of microsphere 0.5 μm^2 has contributed to a pattern, which is approximately only 2 % of the electrons. This assumption can be made as while electrons from outside this 0.5 μm^2 area may contribute, there will be an approximately equal number of electrons which have been emitted within this 0.5 μm^2 area which will deposit their energy outside this area. Therefore, the number of electrons needed to create this pattern is 6.5×10^3 e^-. This is in closer agreement with the 25 keV model, where, for a pattern of this volume, 1.1×10^4 e^- would be required. If we then consider the electrons being emitted around a 4π solid angle and thus only 50 % of them contributing to a pattern, this value becomes closer in agreement to the 25 keV beam. While these calculations are simplistic, they do determine that the 25 keV electron beam is an appropriate calibration scale.

4.3.4 Variability of Patterns from the Photoresist Autoradiography Technique

The patterns from cells and isolated cell nuclei demonstrate the inherent variability in outcomes for biosystems that nominally have been subjected to identical treatment, as they have a range of depths, areas and volumes. The regions in patterns with darker

contrast (deeper) show that there are particular locations in the x–y plane that have been exposed to a higher fluence compared to other locations.

The difference in the topography of the images (Figures 4.9–4.12 and Figures 4.19–4.21), could be a result of a number of factors. Firstly, the total amount of ^{111}In-DTPA-hEGF in individual cells is likely to be different due to differences in the number of receptors on the cells. Secondly, while hEGF will locate to similar regions within cells, the orientation of a population of cells on the resist substrate is probably random. This will lead to variability of the location of source terms in relation to the surface of the photoresist. The differences in this relationship will affect the scattering and absorption of the AE between different cells travelling through the biological material to the photoresist surface. This scattering and absorption will affect the geometry and volume of the patterns on the photoresist surface. Thirdly, while the decay of radioactive isotopes is a well-defined stochastic process, the angles at which the electrons will be emitted will be a 4π angle. However, since we are detecting relatively low numbers of emissions, there may be a non-uniform distribution of electron emissions. This fluctuation in angles of emissions could lead to a variation in the patterns on the photoresist surface.

The relative lack of detailed structure in the patterns, compared to those of the radiolabelled microspheres, is most likely due to the internalised source terms, which undergo more scattering, therefore patterns have less internal structure compared to the microsphere model. This model was able to show higher detail as source terms on the surface of the microsphere undergo less scattering. CASINO modelling of electron beam energy shows that after 1 μm of travel through a biological equivalent material (water), the maximum spreading of a 10 keV beam is approximately 180 times larger

than the original beam radius (Figure 4.3). The increase in resolution which is achieved by using the PMMA 495 K may therefore be limited and thus using a more sensitive resist may lead to the detection of more patterns.

Comparing the fluence of to a SQ20B cell and the electron beam – a SQ20B internalises 400 mBq after 24 hours incubation (Figure 3.3), this would correspond to 1 $x10^5$ disintegrations emitting approximately 8 x 10^5 electrons exposed over a period of 4 half-lives. Assuming a SQ20B has a diameter of 20 µm (data not shown), this would give an electron fluence of 2.5 x 10^3 $e^-/\mu m^2$ for a cell compared to the minimal detectable fluence of the electron beam of 1.0 x 10^5 $e^-/\mu m^2$. This suggest that the lower energy electrons emitted by indium-111 have a greater effect than is accounted for in the electron beam calibration. However, since AE have a short range many of the AE emitted will not traverse the cell boundary and therefore will not contribute to the pattern in the PMMA.

4.3.5 The Photoresist Autoradiography Technique: The Presence of Raised Features

There are several possible explanations for the raised features seen in images using the DM. These include the PMMA acting as a positive-tone resist leading to cross-linking and therefore to an increase in the polymer volume or the swelling of the PMMA due to ingress of the liquid developer. These methods were discounted (Figures 4.14–4.17). It was therefore assumed that the raised features were due to radiation grafting between the PMMA and the biological material. To avoid this, the IM was used.

4.3.6 Adaptation of the Method to Remove the Raised Features

Experiments were carried out using the IM rather than by directly placing the cells on the photoresist. The cells will still have some contact with the photoresist surface but this is expected to be greatly reduced. When using this method, the features caused by swelling were no longer observed (Figures 4.19–4.21). Patterns shown using this technique appeared to be smaller but have a range of areas, depths and volumes which were again associated with them due to the factors previously mentioned in section 3.3.4. These factors include: there being a range in uptake of ^{111}In-DTPA-hEGF; variability of the location of source terms in relation to the surface of the photoresist; and fluctuation in angles of emission of indium-111.

4.4 Conclusions

This chapter has shown that the PAR technique is quantifiable using an electron beam and ^{111}In-labelled microspheres. The lateral (10–20 nm) and vertical (1–3 nm) spatial resolutions are determined from the microsphere model. The CASINO modelling describes the physical interactions of electrons with the PMMA and gives some information on the limitation of PAR as a detection system and reason why the patterns from cellular models are less detailed. Finally, biological experiments were carried out and adapted and showed that the PAR technique can be used with PMMA to determine the distribution of radioactivity within individual cells after treatment with ^{111}In-DTPA-hEGF.

Further work needs to look at the quantitative information which can be gained from the patterns and how this information can be used to inform modelling of the PAR technique. Further validation of the system is required which would determine if there is one processing condition which improves the detection of patterns and if the technique is able to demonstrate differences in uptake, such as after a longer incubation period.

Chapter 5:
Exploration of Photoresist Autoradiography for Quantitative Single Cell Dosimetry

Chapter 5:

Exploration of Photoresist Autoradiography for Quantitative Single Cell Dosimetry

5.1 Introduction

5.1.1 The Variability in Uptake of ^{111}In-DTPA-hEGF

Every cell in Auger electron (AE) targeted radiotherapy (TRT) needs to be targeted as AE have an extremely short range (Kassis et al., 1987). This largely prevents a cross-fire effect depending on the spatial distribution of the AE emitter (Humm, 1986), although there can be a bystander effect (Cai et al., 2010). Therefore, for AE TRT the therapeutic outcome will be dominated by the sub-populations of tumour cells with insufficient accumulation of radionuclide and relatively reduced adverse biological effects (O'Donoghue and Wheldon, 1996).

There is variation in uptake of radiopharmaceuticals at whole body, organ, cellular and subcellular levels (Howell et al., 2012, Bolch, 2008, Bousis et al., 2010, Rajon et al., 2011). The variation in uptake of ^{111}In-DTPA-hEGF may result in some cells receiving a low absorbed radiation dose, allowing them to continue to divide and thus maintain tumour growth. There is therefore a need for a robust technique capable of demonstrating this variability in uptake at the single cell level. This would, for example, allow accurate microdosimetric calculations using the medical internal radiation dose (MIRD) schema. An ideal technique therefore should be capable of recording the spatial distribution of radioactivity with a resolution comparable to that of the range of AE and must provide quantitative information that allows calculation of the energy that is emitted from a point source.

5.1.2 Aims and Outline

The aim of this chapter is to describe the variability in cellular internalisation of ^{111}In-DTPA-hEGF under different conditions and to show how this variability can be detected and quantified using the PAR approach. A simple model that allows determination of the fluence needed to etch specific patterns in photoresist material was derived.

5.2 Results

5.2.1 Photoresist Surface Analysis

Detailed analyses were performed to better understand the significance of the patterns observed in photoresist materials following their exposure to radioactivity. The effect of different processing conditions on pattern formation was investigated. Firstly, the surface roughness of the direct application method (DM), where cells are placed directly on the photoresists surface, was compared to the indirect application method (IM), where photoresists were inverted on top of cells grown in a monolayer.

Secondly, analysis of patterns on photoresists under different conditions (PMMA 495 K, PMMA 950 K, cells or isolated cell nuclei, fixed in methanol 4 % paraformaldehyde (PFA) and different treatment times) were analysed alongside control samples which underwent the same processing conditions.

Surface Roughness

The surface roughness is a measure of the resolution of the photoresist system. The higher the surface roughness, the more pronounced a pattern needs to be to distinguish it from the background. The surface roughness is quantified by the deviations in the direction of the normal vector to the surface. To measure the surface roughness, the root mean squared (RMS) surface roughness of control samples was measured across the atomic force microscope (AFM) scans, excluding any obvious debris or scratches on the photoresist. From this, the mean and standard deviation were calculated. Figure 5.1 shows the analysis for the DM using PMMA 495 K and 950 K and Figure 5.2 shows the analysis for the IM using PMMA 950 K.

A one-way ANOVA was carried out on the surface roughness of the DM samples (Figure 5.1). This showed that there was no significant difference in surface roughness between any samples for both types of photoresist, with one exception: PMMA 495 cells, fixed in PFA after 1 hour incubation. Unpaired t-tests showed the only significant difference for the DM was between PMMA 495 K with control cells fixed in PFA at 1 hour incubation and the 495 K with control cells fixed in methanol at 1 hour incubation (*$P \leq 0.01$).

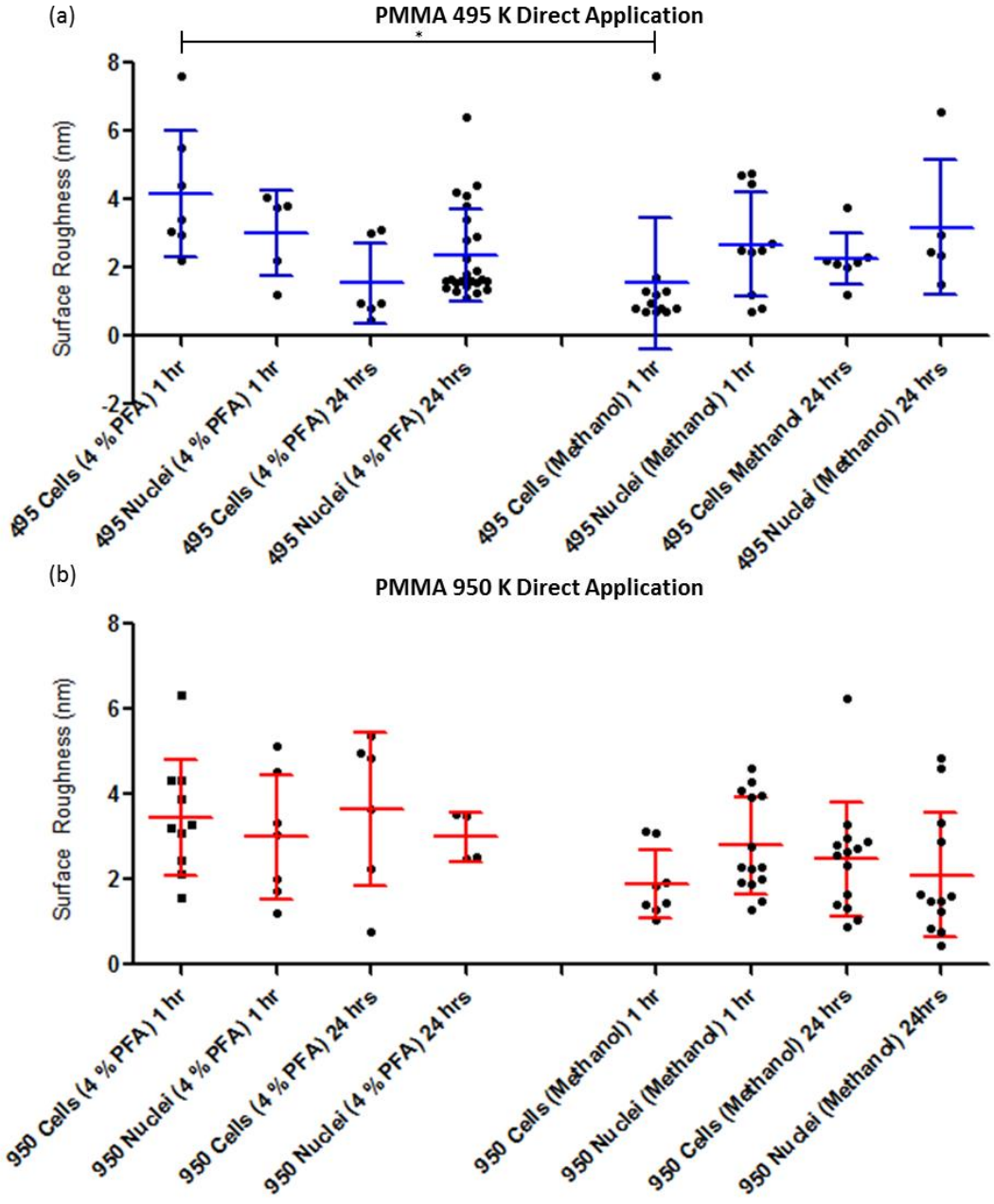

Figure 5.1: Direct Application method: The root mean squared surface roughness of control samples
The mean and standard deviation of the RMS surface roughness of DM control samples (a) PMMA 495 K and (b) PMMA 950 K. Each data set represents one experiment. Significance from unpaired t-tests shown: * P ≤ 0.05. Mean and standard deviation plotted.

A one-way ANOVA was carried out on control samples processed using the IM (Figure 5.2) which showed a significant difference between samples. Unpaired t-tests between samples using the same fixative showed a range of different significances, as shown in Figure 5.2.

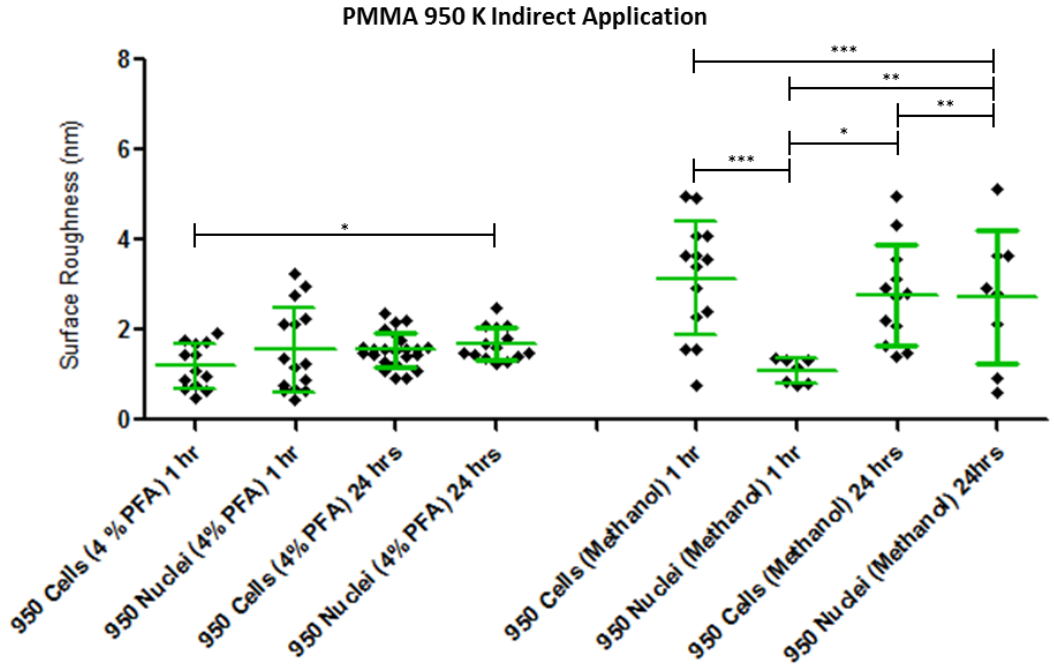

Figure 5.2: Indirect application method: The root mean squared surface roughness of control samples
The mean and standard deviation of the RMS surface roughness of IM control samples, using PMMA 950 K. Each data set represents one experiment, significance of unpaired t-test shown between samples of the same fixative: * P ≤ 0.05; ** P ≤ 0.01 *** P ≤ 0.001. Mean and standard deviation plotted.

However, if the mean and standard deviation of the samples are taken into account, as a pattern is defined as having an average surface roughness of greater than the mean plus two standard deviations (Figure 5.5). The difference between the largest and smallest

pattern depth which can be measured using the IM is 4.07 nm. Figure 5.3 demonstrates what photoresists of a high and low surface roughness look like.

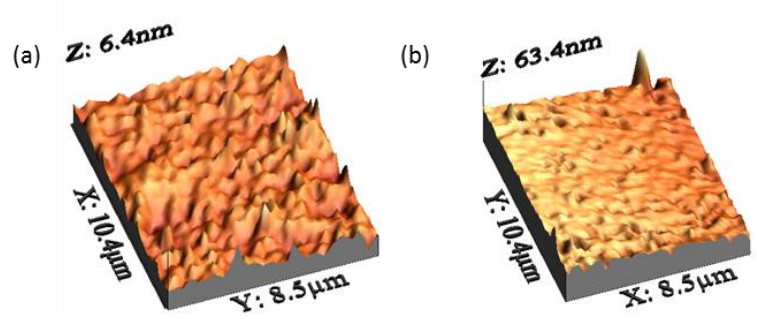

Figure 5.3: Indirect application method: Examples of high and low surface roughness
To visually see the difference between high and low surface roughness of samples prepared using the IM (a) shows a sample with a surface roughness of 0.48 nm and (b) 5.32 nm.

To compare across the different techniques, the RMS mean surface roughness from each sample and the standard deviation from each sample were plotted as well as the mean plus two times the standard deviation as shown in Figure 5.4.

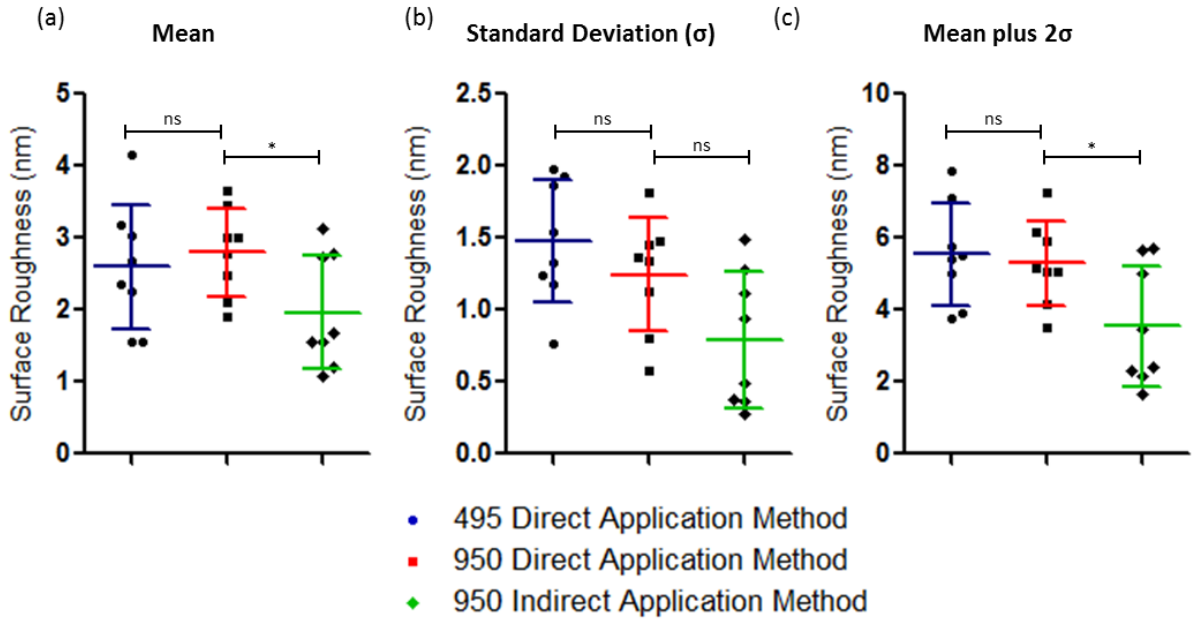

Figure 5.4: A comparison of the surface roughness of the different techniques
A comparison between the different methods (a) comparing the mean surface roughness of each sample (b) comparing the standard deviation of the surface roughness of each sample (c) comparing the mean plus two standard deviations of the sample. Significance of unpaired t-test shown: * $P \leq 0.05$; ns no significance. Mean and standard deviation plotted.

Analysis of Patterns

Different processing conditions of PMMA 495 K or PMMA 950 K (DM only) for the PAR technique were used which included cells or isolated cell nuclei fixed in methanol or in 4 % PFA and different treatment times (1 hour and 24 hours). These conditions were analysed alongside control samples which underwent the same treatment. This was to account for variations in processing conditions across the different sample batches. Analysis was carried out using WxSM software (version 5 Develop 8.2) (Horcas et al., 2007). This was used to obtain the surface roughness and the area, maximum depth, average depth and volume of patterns. A pattern was defined as having an average depth of more than the mean plus two standard deviations of the surface roughness and an area of more than 0.25 μm^2 (Figure 5.5). The reason why this area was chosen is that in the case of a circular pattern, the radius would be approximately 280 nm. The microsphere model (Figure 4.8) was used to demonstrate that a resolution of approximately 20 nm is achievable when distinguishing variation within microsphere patterns. Selecting a radius of approximately ten times this allows for the smoothing out of patterns, as shown in AFM scans from cellular experiments, to be taken into account. Analysis was carried out by using an inbuilt function that allows for the determination of holes, by selecting a plane on the photoresist. Anything below this plane is counted by the programme as a hole (Figure 5.5) and any holes which had an average depth of less than the mean plus two times the standard deviation was considered to not be a pattern. However, there were still patterns on control resists that met this criteria but were discounted as they did not look like patterns previously seen (Figure 5.6). However, they were still included in analysis. Analysis was carried out using the DM and IM. However, only shown are graphs from the IM with similar graphs being obtained for the DM.

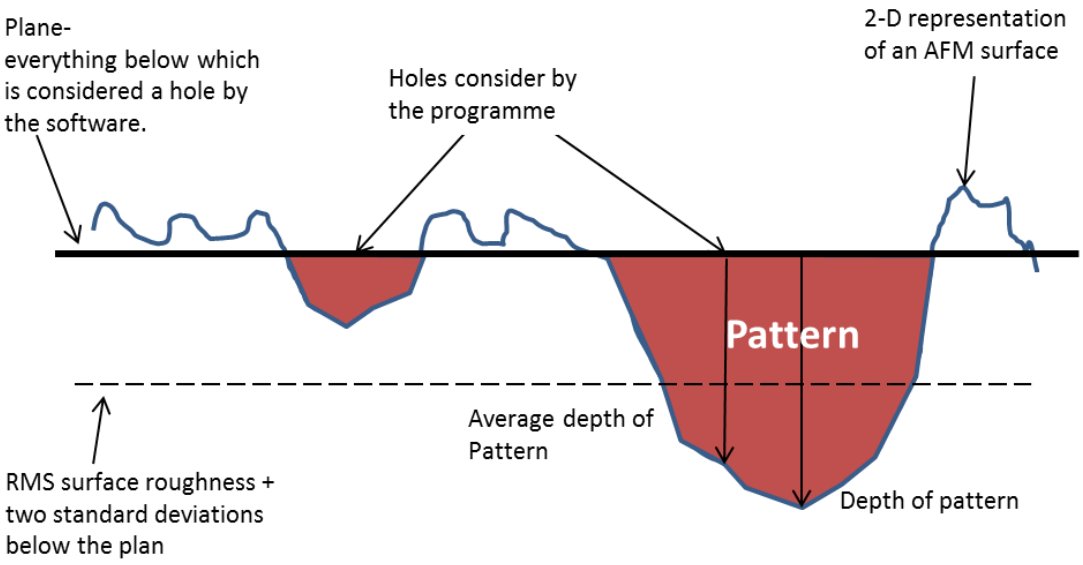

Figure 5.5: A 2-D representation of an atomic force microscope scan, showing how patterns are defined from holes

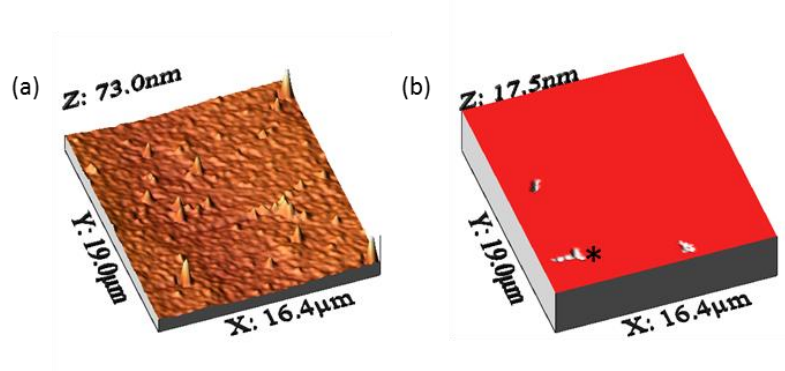

Figure 5.6: Indirect application method: A control photoresist demonstrating "patterns"
A control scan from the IM with three "patterns," (a) the photoresist scan (b) WxSM analysis of the surface showing three patterns remaining, two of them have patterns with an average depth below the mean and two standard deviations, the pattern labelled * has an area of 0.71 μm^2, a volume of 2.15 x 10^6 nm^3 and a maximum depth of 17.5 nm. It therefore is classed as a pattern.

Firstly, the number of patterns per micrometre squared was calculated. This is the total number of patterns counted divided by the area of the AFM scan; results from the IM are shown in Figure 5.7.

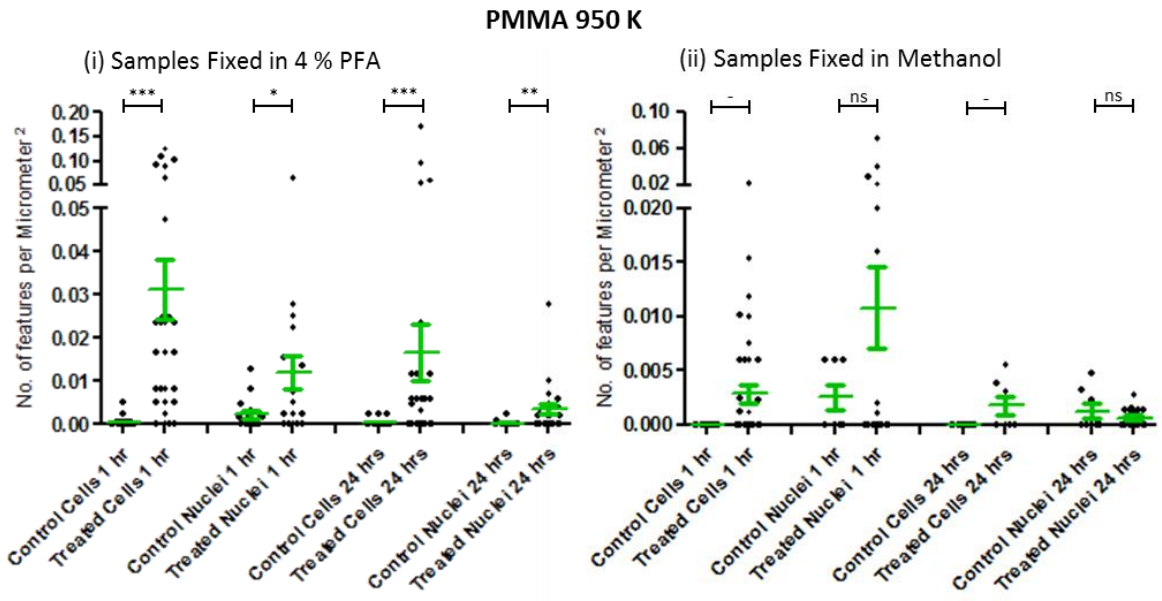

Figure 5.7: Indirect application method: The number of patterns per unit area
The number of patterns per micrometres squared present on AFM scans after SQ20B cells were incubated with ^{111}In-DPTA-hEGF for either 1 or 24 hours before being processed for PAR using PMMA 950 K. Two different fixatives were used (i) 4 % PFA and (ii) methanol. For PAR, photoresists were exposed for four half-lives, resists were then washed and developed before AFM analysis. Each data set represents one experiment. Significance of Mann-Whitney U-test is shown: * $P \leq 0.05$; ** $P \leq 0.01$ *** $P \leq 0.001$; ns not significance. - Mann-Whitney test could not be carried out. Error bars represent the mean and standard error of the mean (SE).

Figure 5.7 shows that for the IM there were more holes per unit area for treated samples compared to untreated ones, except for samples fixed in methanol after 24 hours. Similar results were seen for the DM. As the control cells fixed in methanol at 1 and 24 hours had no patterns present, a Mann-Whitney test could not be carried out.

As well as the number of patterns present there may also be a difference in the size of patterns which are observed. For example, a scan may only have one large pattern which covers the majority of the photoresist thus reducing the overall number of patterns which are counted. Figure 5.8 shows the area of individual patterns from the IM.

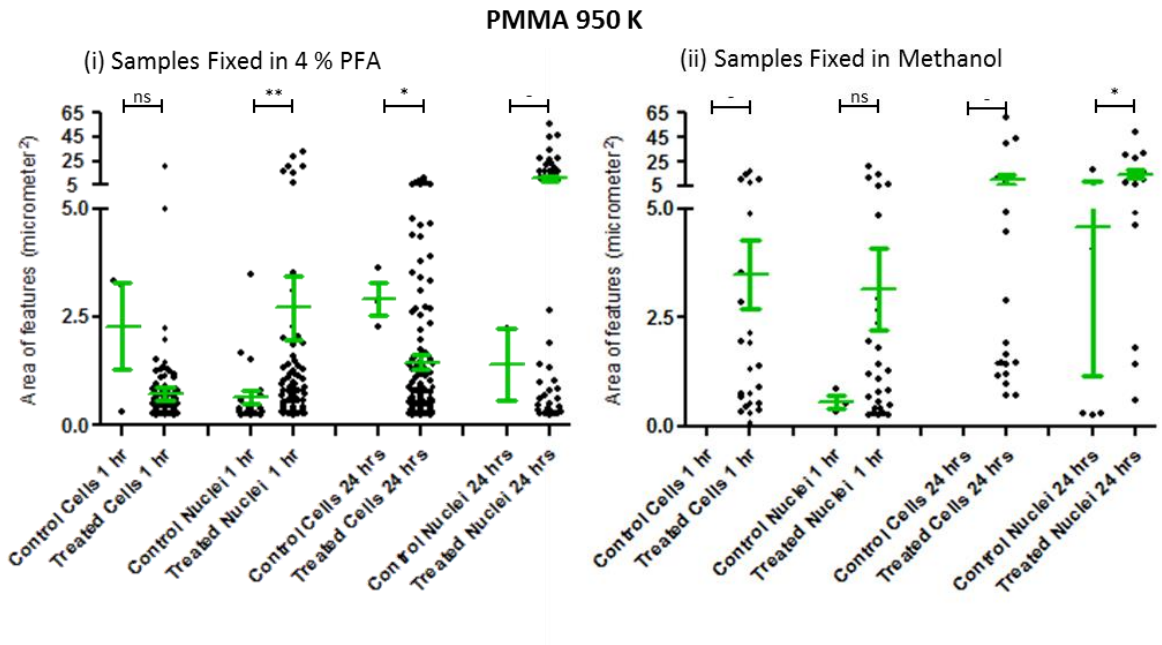

Figure 5.8: Indirect application method: The area of individual patterns
The area of individual patterns on AFM scans after SQ20B cells were incubated with ^{111}In-DPTA-hEGF for either 1 or 24 hours before being processed for PAR using PMMA 950 K. Two different fixatives were used (i) 4 % PFA and (ii) methanol. For PAR, photoresists were exposed for four half-lives, resists were then washed and developed before AFM analysis. Each data set represents one experiment. Significance of Mann-Whitney U-test is shown: * $P \leq 0.05$; ** $P \leq 0.01$; ns not significance. - Mann-Whitney test could not be carried out. Error bars represent the mean and SE.

Figure 5.8 appears to show that the control photoresists from the IM have a greater area. However, when the absolute average number of patterns is compared, it is less than five for the control resists but 57 for treated samples. The results from the DM are similar although the area of the patterns is larger. On photoresists which have been processed using the DM, there were no patterns on control samples greater than 10 μm^2; for the IM this value is reduced to 3.5 μm^2. Due to clustering effects, where there are many small patterns close together as demonstrated in Figure 5.9, these patterns below these two sizes were not excluded from analysis.

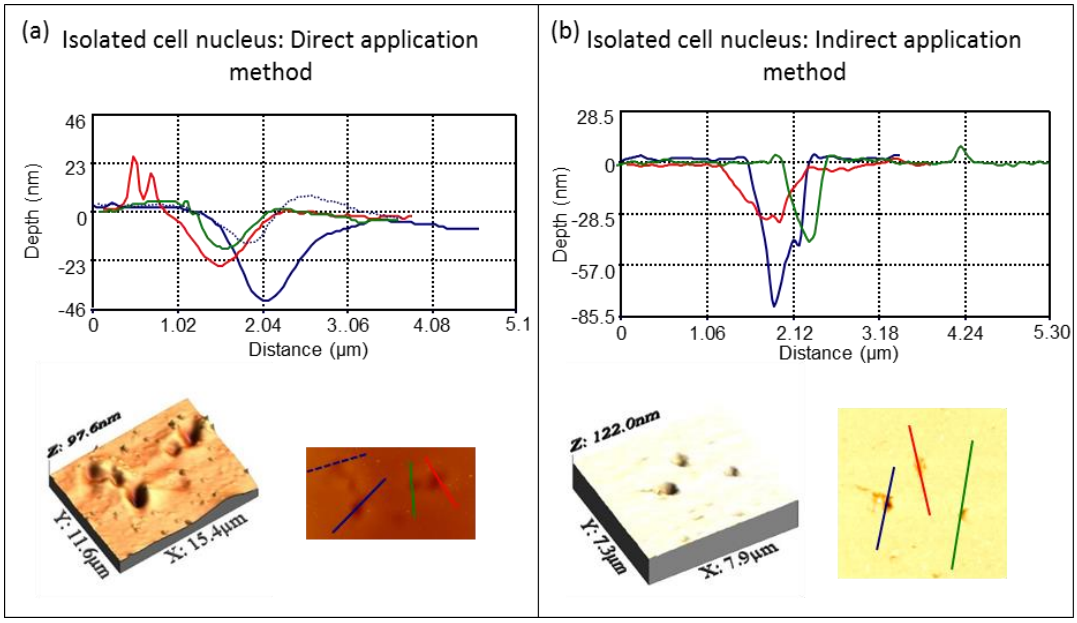

Figure 5.9: Photoresist scans demonstrating clustering
PMMA 950 K photoresists with isolated cell nuclei treated with ^{111}In-DTPA-hEGF for 1 hour before being fixed in 4 % PFA (a) DM (b) IM, which show several small features clustered together.

Figure 5.10 shows the percentage area of the photoresists which is considered to be patterns. This is the total area of all the patterns divided by the area of the photoresist scan. It shows that under all the conditions tested the mean is greater for treated samples compared to the control samples. Similar results were seen for the DM, although the mean percentage area was greater. For IM, the Mann-Whitney U-test does give some significant values but due to the large standard deviations in the samples, there is not a significant difference across all of the samples.

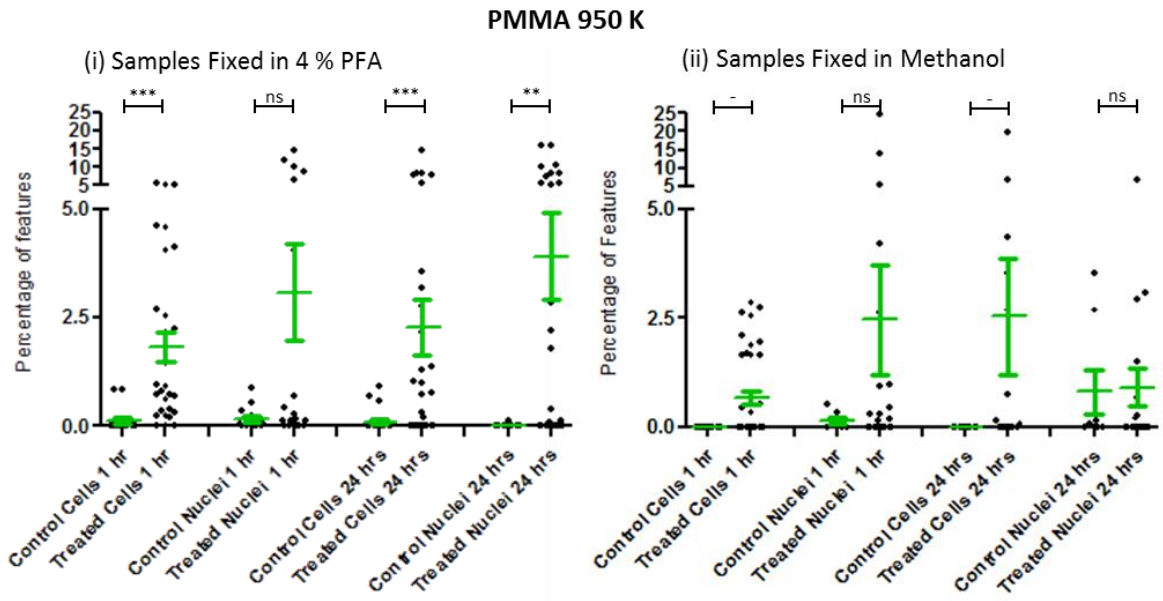

Figure 5.10: Indirect application method: The percentage area of resists scans which is occupied by patterns

The percentage of the photoresist surface that is occupied by patterns, on AFM scans after SQ20B cells were incubated with ^{111}In-DPTA-hEGF for either 1 or 24 hours before being processed for PAR using PMMA 950 K. Two different fixatives were used (i) 4 % PFA and (ii) methanol. For PAR, photoresists were exposed for four half-lives, resists were then washed and developed before AFM analysis. Each data set represents one experiment. Significance of Mann-Whitney U-test is shown: * $P \leq 0.05$; ** $P \leq 0.01$ *** $P \leq 0.001$; ns not significance; - Mann-Whitney test could not be carried out. Error bars represent the mean and standard error of the mean (SE).

The electron beam and microsphere modelling showed that there was a relationship between the fluence and the depth of the pattern. Figure 5.11 shows the maximum depths of individual patterns. In all cases, except cell nuclei treated for one hour fixed in PFA, the mean maximum depth is greater for the treated sample. However, the samples have a large standard deviation and hence Mann-Whitney U-Tests do not show differences between the samples or in other cases there are not enough data points to make a direct comparison.

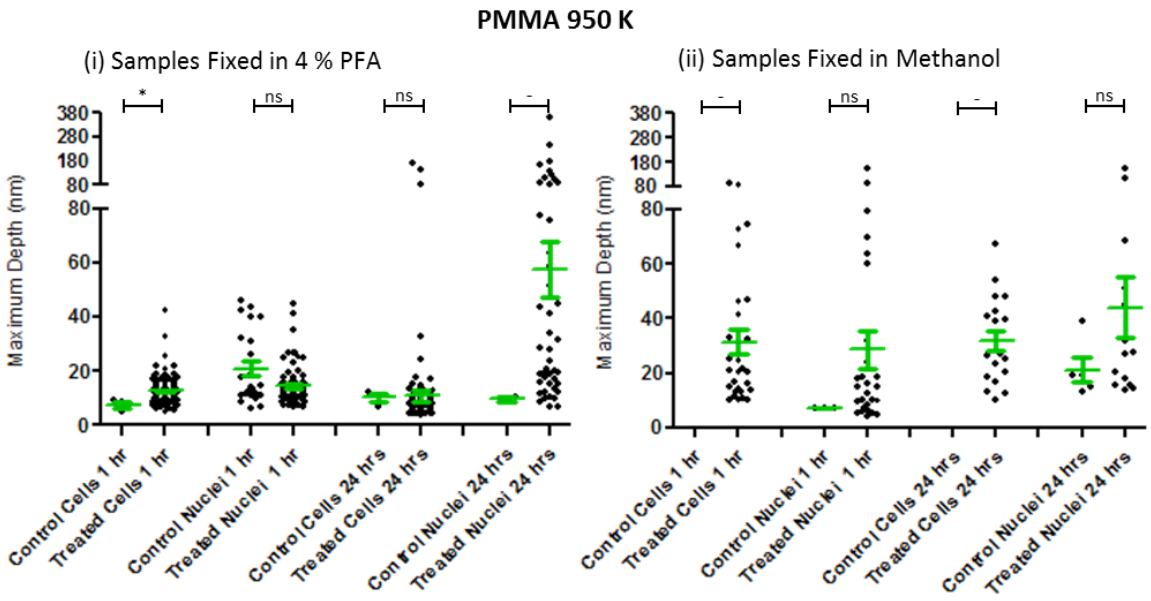

Figure 5.11: Indirect application method: The maximum depth of individual patterns
The maximum depth of individual patterns on AFM scans after SQ20B cells were incubated with ^{111}In-DPTA-hEGF for either 1 or 24 hours before being processed for PAR using PMMA 950 K. Two different fixatives were used (i) 4 % PFA and (ii) methanol. For PAR, photoresists were exposed for four half-lives, resists were then washed and developed before AFM analysis. Each data set represents one experiment. Significance of Mann-Whitney U-test is shown: * $P \leq 0.05$; ns not significance; - Mann-Whitney test could not be carried out. Error bars represent the mean and SE.

The volume of the pattern will take into account the area and the depth of the pattern, and therefore contains more information about the total fluence needed to create the pattern seen. Figure 5.12 shows the volume of individual patterns. Figure 5.12 shows that the mean volume for all treated samples is greater than the control samples.

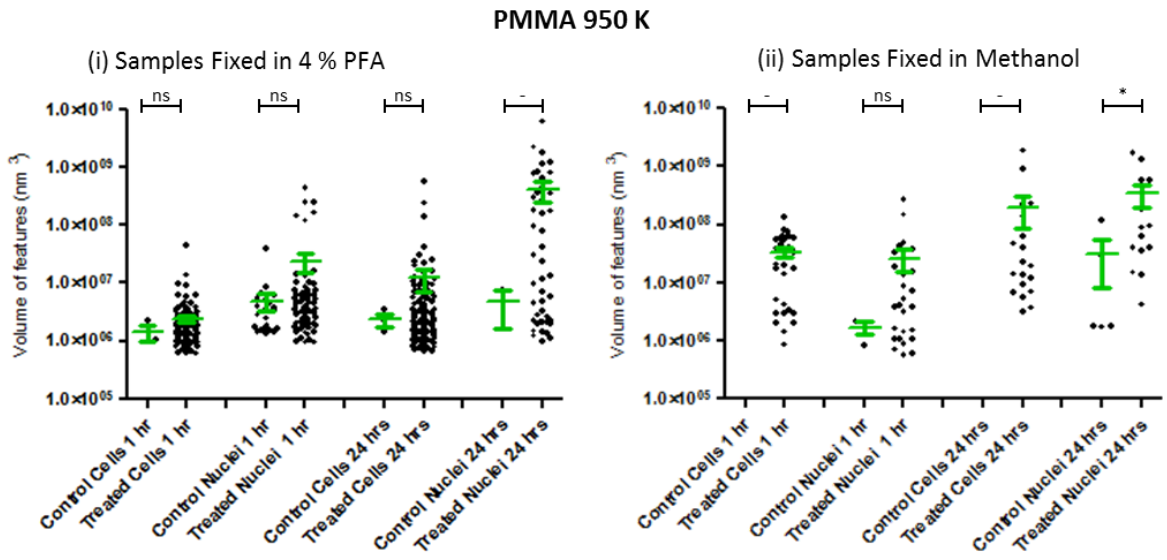

Figure 5.12: Indirect application method: The volume of individual patterns
The volume of individual patterns on AFM scans after SQ20B cells were incubated with ^{111}In-DPTA-hEGF for either 1 or 24 hours before being processed for PAR using PMMA 950 K. Two different fixatives were used (i) 4 % PFA and (ii) methanol. For PAR, photoresists were exposed for four half-lives, resists were then washed and developed before AFM analysis. Each data set represents one experiment. Significance of Mann-Whitney U-test is shown: * $P \leq 0.05$; ns not significance; - Mann-Whitney test could not be carried out. Error bars represent the mean and SE.

Statistical analysis of the patterns was carried out using a linear mixed model. The explanatory variables were the different conditions (control or treated, PMMA 495 K or PMMA 950 K photoresists, cells or isolated cell nuclei, fixed in 4 % PFA or in methanol and 1 or 24 hours treatment time) and a random effect variable is built into the model to account for the differences between samples and to resolve non-independency in the data. The assumptions of the linear mixed model are that the effect is a linear combination of the variables, that there is no collinearity between the variables, that there is an absence of heteroscedasticity (that there is equal variance across the range of predicted values) and that there is a normal distribution of the residuals. A log transformation of the data was carried out. Plots of the residuals from the regressions showed that there were no patterns in the residuals and that there was

random scatter. This shows that the model assumptions are plausible. A summary of the linear mixed model is shown in Table 5.1 for the DM and Table 5.2 for the IM.

Table 5.1: Direct application method: A summary of the information gain from the linear mixed model

A summary of the information gained from the linear mixed model, control vs treated significance determined by a likelihood ratio test: *** P ≤ 0.001. The condition which is marked in the cell the one that gives the greatest value. Significance of other variables determined by 97.5 % confidence intervals: P ≤ 0.025; ns not significance. Calculated by Dr Cristiana Kartsonaki, Nuffield Department of Population Health, University of Oxford.

	No. of features per unit area	**Area of features**	**Percentage of resist which is features**	**Maximum depth of features**	**Volume of features**
Controls vs treated	*** treated	*** treated	*** treated	*** treated	*** treated
PMMA 495 K vs PMMA 950 K	ns	Yes: PMMA 495 K	ns	Yes: PMMA 950 K	ns
Cells vs isolated cell nuclei	ns	Yes: Cells	ns	ns	Yes: Cells
4 % PFA vs methanol	ns	Yes: Methanol	ns	ns	Yes: Methanol
1 hour vs 24 hours incubation	Yes: 24 hours	ns	ns	Yes: 24 hours	No

Table 5.2: Indirect application method: A summary of the information gain from the linear mixed model

A summary of the information gained from the linear mixed model, control vs treated significance determined by a likelihood ratio test: * P ≤ 0.05; ** P ≤ 0.01 *** P ≤ 0.001 ns not significance. The condition which is marked in the cell the one that gives the greatest value. Significance of other variables determined by 97.5 % confidence intervals: P ≤ 0.025; ns not significance. Calculated by Dr Cristiana Kartsonaki, Nuffield Department of Population Health, University of Oxford.

	No. of features per unit area	**Area of features**	**Percentage of resist which is features**	**Maximum depth of features**	**Volume of features**
Controls vs treated	*** treated	* treated	*** treated	ns	** treated
Cells vs isolated cell nuclei	ns	ns	ns	ns	Yes: Nuclei
4 % PFA vs methanol	ns	Yes: Methanol	Yes: 4 % PFA	ns	Yes : Methanol
1 hour vs 24 hours incubation	ns	Yes: 24 hours	ns	Yes: 24 hours	Yes 24 hours

Comparison between the Direct and Indirect Applications Methods

A comparison between the DM and IM is shown in Table 5.3. Since the IM was not used with PMMA 495 K, DM samples used with PMMA 495 K were excluded from the analysis.

Table 5.3: A comparison of the direct application and indirect application methods
A summary of the information gained from the linear mixed model, DM vs IM, significance determined by a likelihood ratio test: *** $P \leq 0.001$. The condition which is marked in the cell the one that gives the greatest value. Calculated by Dr Cristiana Kartsonaki, Nuffield Department of Population Health, University of Oxford.

	Area of features	Maximum depth of features	Volume of features
Direct vs Indirect	*** Direct	*** Direct	*** Direct

5.2.2 Modelling of the Major Patterns

To provide a quantifiable technique, patterns created in the photoresist surface need to be related to the fluence that was required to create them. As shown in Figure 4.1, the local depth of a pattern in the resist is linearly dependent on the local fluence. The sensitivity of the resist imposes the lower limit on the detectability of fluence. The electron beam calibration data shows that patterns of less than approximately 2 nm, corresponding to a fluence of 1×10^5 $e^-/\mu m^2$ cannot be detected reliably on PMMA 950 K (Figure 4.1). To use this information to provide quantitative information, four underlying assumptions are made: a) the fluence arising from internalized indium-111 is approximated as a 25 keV mono-energetic electon beam (Appendix 1, page 237); b) contributions to the total fluence from separate point sources are additive; c) radiation is emitted isotropically d) the number of PMMA carbon bonds broken (depth of pattern) is independent of the angle of incidence. Thus the fluence from a point source falls off as the inverse square of the distance from the source.

Using these assumptions, an intuitive and simple formalism for modelling the topographic patterns in the developed resist following exposure from a radionuclide treated cell or isolated cell nucleus can be developed. The simplicity is derived from the placement of one or more point sources, each emitting a total electron fluence, F_i, at a distance, Z_i, above a location in the x-y plane of the resist (Figure 5.13). The parameters F_i and Z_i and the x-y locations can be adjusted for a best fit to the topography of the pattern.

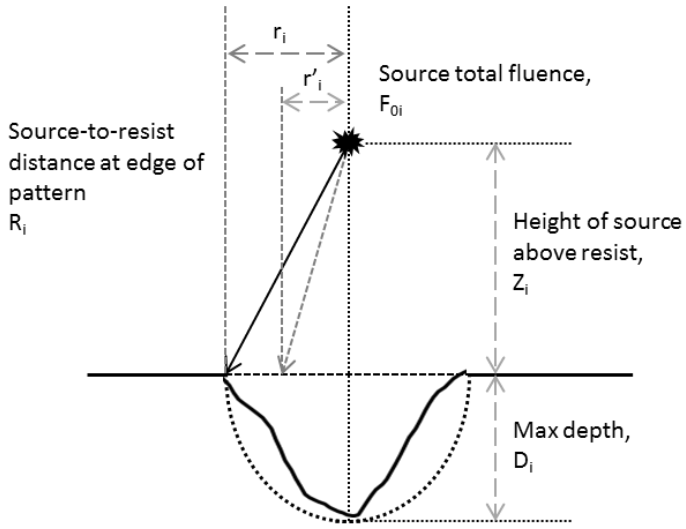

Figure 5.13: A schematic showing a simple representation of a pattern
The schematic shows, a simple representation of a pattern, which has been caused by a point source delivering a fluence F_i into the 4π solid angle from a location a distance Z_i above the plane of the resist. The radius of the resultant pattern in the x-y plane, r_i, is defined by the resist having received a fluence per unit area greater than 1 x 10^5 $e^-/\mu m^2$ (from calibration data, Figure 4.1). The greatest depth of the pattern, D_i, is measured from the original height of the resist surface. The local depth of the pattern is linearly related to the local fluence incident. Work adapted with permission (Royle et al., 2016).

The fluence a distance R from a point source is:

$$F_{iR} = \frac{F_i}{4\pi R^2} \quad \text{in } e^-/\mu m^2 \qquad (5.1)$$

The two unknowns, Z_i and F_i, can be determined from two experimental observables. These are the radius of the pattern, r_i, bounded by the minimum detectable local fluence, 1x10^5 $e^-/\mu m^{-2}$, and the greatest depth of the pattern, D_i, corresponding to the

maximum local fluence at the original surface of the resist. At the boundary of the pattern, the fluence is:

$$1x10^5 = \frac{F_i}{4\pi(Z_i^2+r_i^2)} \quad (5.2)$$

At the deepest part of the pattern we have:

$$F_i(r_i' = 0) = \frac{F_i}{4\pi Z_i^2} \quad (5.3)$$

From the calibration data in Figure 4.1 we see that the local fluence, $F_i(r_i')$, is linearly dependent on the local depth of the pattern; therefore it is convenient to replace $F_i(r_i')$ at an arbitrary point along a contour line defining the pattern by $10^{-5}C_i(r_i')$, where $C_i(r_i')$ can range from 1 to 1250 (Falzone et al., 2011). Therefore Equation (5.3) can be rewritten as:

$$F_{0i} = 4\pi x10^5 C_i(r_i')Z_i^2 \text{ , for } r_i' = 0 \quad (5.4)$$

Thus Equation (5.2) can be rewritten as:

$$C_i(r_i')Z_i^2 = (Z_i^2 + r_i'^2) \quad (5.5)$$

Solving for Z_i at the deepest point of the pattern:

$$Z_i = \sqrt{\frac{r_i^2}{C_i(r_i'=0)-1}} \quad (5.6)$$

Equations (5.4) and (5.6) can now be used to determine numerical values for Z_i and F_{0i} (the locations of point sources in the z-direction and the total fluence of the respective sources). The depth of the pattern along a contour line at locations defined by $r_i > r_i' > 0$ can then be determined from the following expression:

$$C_i(r_i') = \frac{C_i(r_i'=0)Z_i^2}{Z_i^2+r_i'^2} \quad (5.7)$$

A nomogram of Equation 5.7 is shown in Figure 5.14. The height of a point source is plotted as a function of greatest depth of the pattern with the radius of the pattern as a parameter. The family of curves allows a more rapid approximate modelling of any

pattern without recourse to the detailed formalism. It is particularly useful when multiple point sources are required in order to obtain a reasonably good fit.

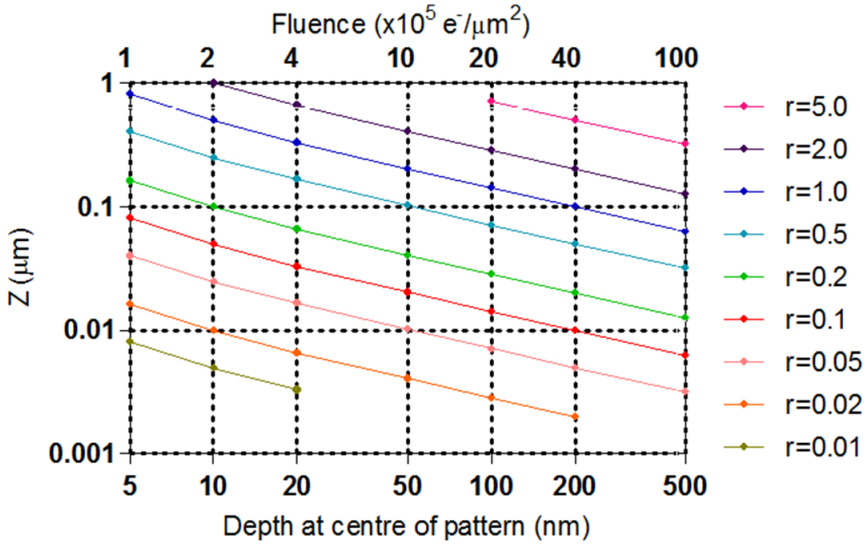

Figure 5.14: Nomogram showing the relationship between experimental observables
Nomogram showing the relationship between experimental observables (depth at centre of pattern, in nm, and radius of pattern, in µm) and location of a point source above the plane of the resist. Interpolation between the curves allows for quick interpretation of patterns in an image. Work adapted with permission (Royle et al., 2016).

Having identified the height of the point source above the resist plane, the total number of electrons emitted by the point source can be determined by:

$$F_{0i} = 4\pi x 10^5 C_i(r_i' = 0)Z_i^2 \text{ (electrons)} \qquad (5.8)$$

The shape of the pattern resulting from the placement of a point source above a plane resist surface was calculated from the formalism, and is shown as a dotted grey line in Figure 5.15. It can be seen from the formalism that the shape defined by two concave lines remains the same for all point sources, regardless of location and activity. The formula can be used with simple patterns, as demonstrated in Figure 5.15, and progressing to more detailed patterns, shown in Figure 5.16. In the case of the pattern shown in Figure 5.15, the estimated value of Z_1 of 500 nm was obtained from the

nomogram, while the total number of electrons emitted by the point source, F_1 = 8 x 10^6, was calculated from Equation 5.8.

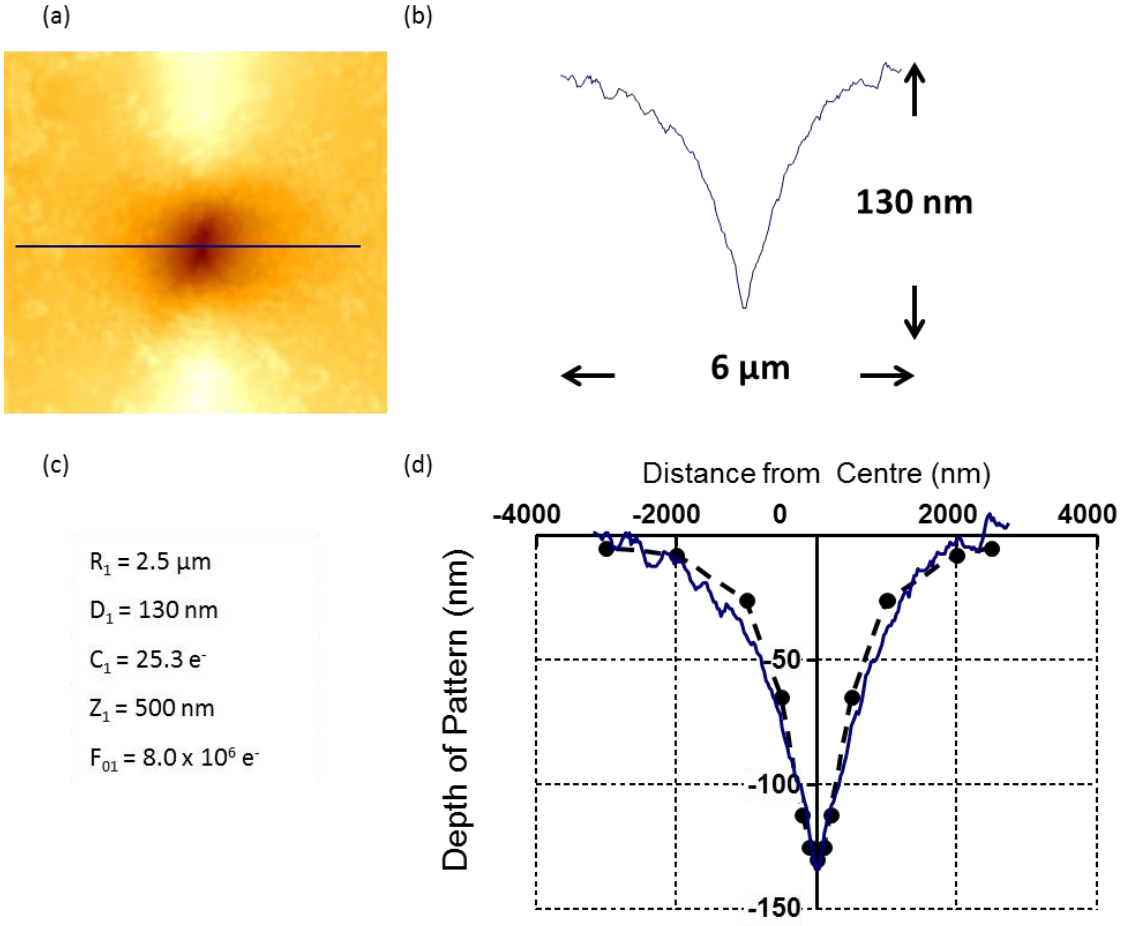

Figure 5.15: Modelling a representative simple pattern
An example of a simple pattern, (a) AFM image of a pattern from a cell nucleus with after 24 hour incubation with ^{111}In-DTPA-hEGF. The AFM-derived contour line through the centre of the pattern is shown in (b). The measured depth and radius were 130 nm and 2.5 µm, respectively. Using equations (5.6) and (5.8), the information shown in the table (c) can be obtained. (d) demonstrates the goodness of fit from placement of a single point source emitting 8.0 x 10^6 electrons (F_{01}), at a height 500 nm above the resist (Z_1). The theoretical shape of a contour line was modelled from Equation 5.7 and is shown as the broken grey line and shows a good fit between the experimental data and model. Work adapted with permission (Royle et al., 2016).

More complex patterns of cell nuclei resulting from exposure to the ^{111}In-DTPA-hEGF for 24 hours are demonstrated in Figure 5.16. To arrive at a better fit, more than one point source was used. Contour lines were used to identify the optimal locations in the

x-y plane for sources to be placed; these were placed above the different positions of maximum depth. A summary of the data obtained is shown in Table 5.4.

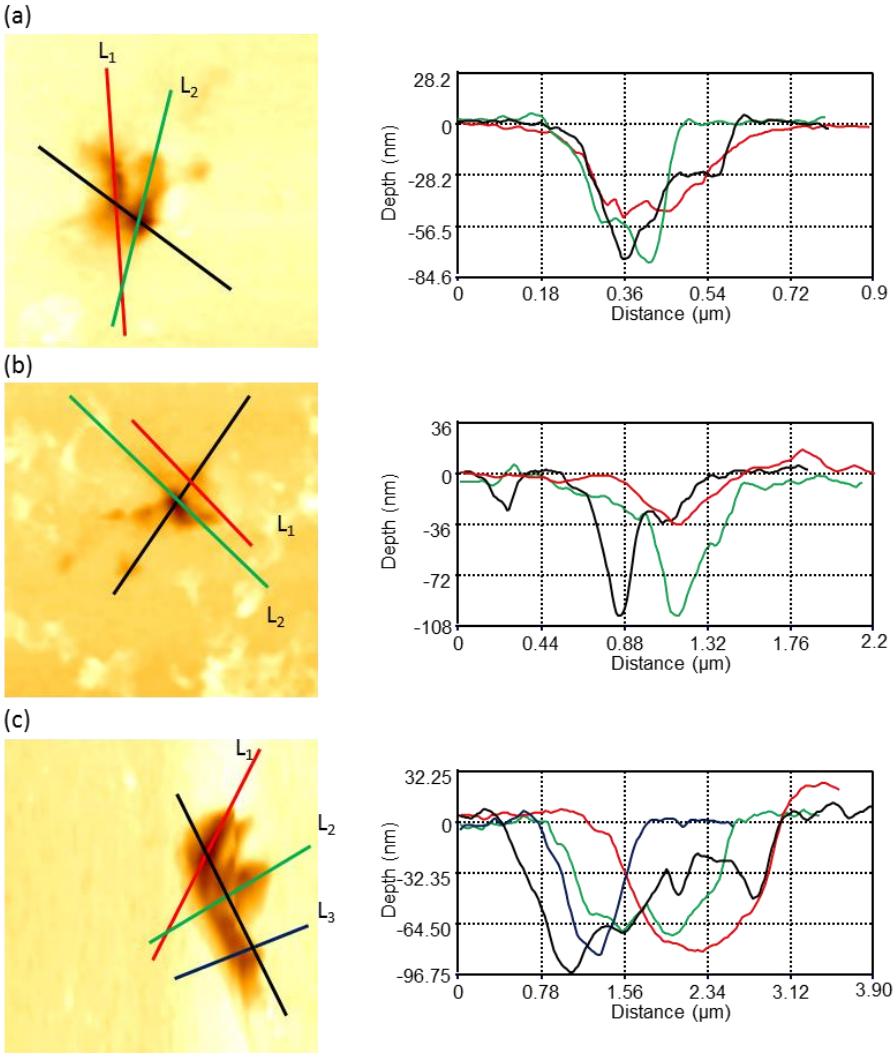

Figure 5.16: Modelling of increasingly complex patterns from isolated cell nuclei
Modelling of increasingly complex patterns from isolated cell nuclei fixed in methanol incubated with ^{111}In-DTPA-hEGF for 24 hours. The actual patterns are shown, with line scans ($L_{1,2,3}$) representing the regions of greatest depth. Work adapted with permission (Royle et al., 2016).

Table 5.4: A summary of the experimental and modelling information obtained from demonstration scans

A summary of the experimental and modelling information obtained from the representative scan shown in Figure 5.16: $R_{x,}$ the radius, $D_{x,}$ the maximum depth of a pattern obtained from experimental data and the parameters that can be obtained from modelling; C_x, the local fluence, Z_x, the height that the source is above the surface of the resist, and F_x, the total number of electrons emitted from the point source. Work adapted with permission (Royle et al., 2016).

	Pattern (a)		**Pattern (b)**		**Pattern (c)**		
	L_1	L_2	L_1	L_2	L_1	L_2	L_3
Radius($R_{x,}$ μm)	0.6	0.5	0.6	1.1	2.4	2.1	1.4
Depth ($D_{x,}$ nm)	50	74	36	95	68	66	75
Fluence ($C_{x,}$ $e^-/\mu m^2$)	10	15	7.0	19	14	13	15
Height(Z_x, nm)	200	130	240	260	600	420	360
Electrons emitted ($F_{x,}$ e^-)	$5.0x10^5$	$3.2x10^5$	$5.1x10^5$	$1.6x10^6$	$6.3x10^6$	$2.9x10^6$	$2.4x10^6$

5.3 Discussion

5.3.1 Surface Analysis of Photoresists

Surface Roughness

One of the factors that could limit the usefulness of the PAR technique is the ability of the AFM to distinguish patterns in the photoresist surface due to the inherent unevenness of the photoresist surface (surface roughness). This defines the resolution of the photoresists, as radiation-induced patterns that are of similar size and depth to minor flaws in the resist surface will be indistinguishable from the background. The surface roughness, therefore, is a measure of the resolution that can be achieved. Previously, it was shown that when photoresists are exposed to an electron beam, PMMA 495 K has a lower surface roughness compared to PMMA 950 K and hence has a greater resolution (Royle, 2012). RMS roughness results showed that the surface roughness of the photoresists was similar for the different processing conditions that were used for both the DM and IM (Figures 5.1, 5.2 and 5.3), suggesting that changing the processing condition does not reduce the resolution of the PAR method.

Due to the lower polymer chain length and density of PMMA 495 K, PMMA 495 K would be expected to have a lower surface roughness and hence higher resolution. However, as shown in Figure 5.4, there was no significant difference between the surface roughness measurements of the two photoresists. This means that the increase in resolution of the PMMA 495 K has no advantage. Therefore, it is better to use a more sensitive photoresist, PMMA 950 K, as demonstrated by the electron beam. When comparing PMMA 950 K and 495 K, 950 K showed smaller area patterns. However, it produced deeper patterns and hence can be considered more sensitive. Using the linear mixed model, there was no difference in the volume of patterns, in the number of patterns per unit area or the percentage of resist which is patterns, when comparing the

two different types of photoresist. This confirms that there is no benefit to one photoresist formulation over the other.

The reason for there being a greater surface roughness for PMMA 495 K could be due to the processing of the samples leading to an increase in surface roughness. When comparing the DM and IM, the IM has a significantly lower surface roughness (* $P \leq 0.05$, Figure 5.4). The resolution as defined by mean plus two standard deviations is significantly better when using the IM. Since these characteristics determine the resolution of the PAR technique, the IM should be able to distinguish smaller patterns. This is not a surprising result due to the reduction in the interaction of the cells with the photoresists.

Analysis of Patterns

Many different processing conditions were tested. Firstly, the number of patterns per micrometre squared. There was a significantly (*** $P \leq 0.001$) greater number of patterns for treated samples for both the DM and IM. For the DM and IM using the linear mixed model there was no significant difference in any of the processing conditions (fixative, cells or isolated cell nuclei and for the DM PMMA type). This suggests that the sensitivity of the photoresists does not depend on the processing conditions.

The area of patterns when using the DM (*** $P \leq 0.001$) and the IM (* $P \leq 0.005$) were significantly greater for treated versus control samples. Using the DM, none of the patterns derived from control (untreated) samples exceeds 10 μm^2; for IM this value is 3.5 μm^2. This suggests that the minimum size of the pattern selected, 0.25 μm^2 is too small. However, the limit of the size of the patterns was not reduced because of clustering effects (Figure 5.6). The clustering effects are seen on photoresists that were

processed using the DM and IM. Clusters occur when several small patterns lie close together. Clusters result from a single cell containing several 'hot spots" of radioactivity or from two or more cells being located close to each other. It is not possible to determine which of these accounts for a specific cluster since the PAR technique does not allow simultaneous visualisation of cells and the radiation patterns that they cause. While there were features present as determined by WxSM, on control samples they do not have the same appearance of the patterns seen on the treated samples (Figure 5.6), but were included in analysis.

The area of cellular patterns is larger than the isolated cell nuclei for the DM, as expected, but they are similar for the IM. This suggests that for the IM, the photoresist is detecting emissions from a similar area. The area of the pattern is not the footprint of the cell but a footprint of the radiation that has reached the photoresist which has a high enough fluence to cause a pattern. This could occur if the cells and isolated cell nuclei have a similar curvature and the photoresist does not detect emissions from the whole cell but only a smaller percentage (Figure 5.17). This would lead to a greater percentage of the emissions, from indium-111 within cell nuclei, being detected.

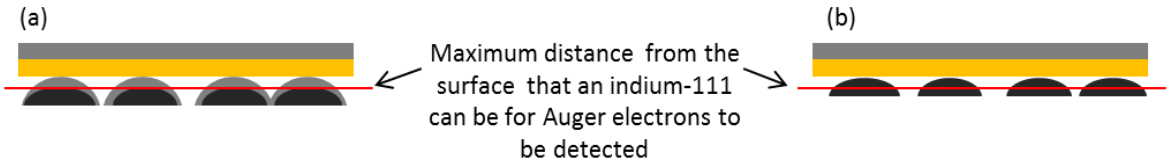

Figure 5.17: An explanation of why cells and isolated cell nuclei have features of a similar area
(a) Cells and (b) isolated cell nuclei which have a photoresist invert on top. The photoresist only detected emissions from indium atoms located above the red line hence the areas of the patterns are similar.

The photoresists with cells fixed in methanol showed on average larger patterns than those fixed with PFA, for both the IM and DM. This is expected, as methanol is a dehydration fixative rather than a cross-linking fixative like PFA. Methanol-treated

cells are expected to shrink as they lose water. This increases the likelihood that a greater proportion of the internalised indium-111 will be closer to the surface leading, in turn, to a larger pattern.

To compare both the number of patterns and the size of the patterns, the percentage of the photoresist area which is occupied by patterns was used. There were significant differences (*** $P \leq 0.001$) between controls and treated samples. For the DM, there were no significant differences when comparing the effect of photoresist type, fixative or cells and isolated cell nuclei. However, for the IM there were differences in the fixative, with PFA giving rise to a greater percentage being patterns but no difference between cells and isolated cell nuclei. The observation that the percentage area occupied by patterns is generally rather similar across all samples again suggests that the sensitivity of the photoresists is similar for the different processing conditions that were tested.

The lack of difference in the percent of the photoresist which is a pattern between cells and isolated cell nuclei in both the DM and IM is surprising, as cells are larger and hence it would be expected to see larger patterns. The reason why this may not be seen is that there is currently no way of correlating the area of the photoresist scanned with the location of individual cells or isolated cell nuclei. Therefore, the patterns which have been described as individual patterns may be caused by AE from several adjacent cells or isolated cell nuclei or may be a smaller part of a larger pattern such as the clustering effects seen in Figure 5.9. Clustering effects would lead to more smaller patterns for both cells and isolated cell nuclei, skewing the data. This may be the reason why there is no difference between cells and isolated cell nuclei using the linear mixed model.

A possible reason why PFA gave rise to a greater percentage of resists being features for the IM method could be because the photoresist is resting on top of the cells; those cells which are PFA-fixed retain their structure and are therefore more likely to be of a similar height as they have been fixed using a cross-linking fixer. They therefore could be equally close to the photoresist. When using the methanol method, cells are dehydrated and this may lead to them collapsing with a range of different heights above the surface of the photoresists; hence, on average, they are further away from the photoresist (Figure 5.18). This would lead to the PFA cells having a greater number of smaller patterns giving rise to a greater percentage of the photoresist being patterns, but those methanol-fixed cells and isolated cell nuclei which have collapsed down to form a "fried egg" shape, and are closer than average to the photoresist surface, will give larger features. This is shown by the linear mixed model.

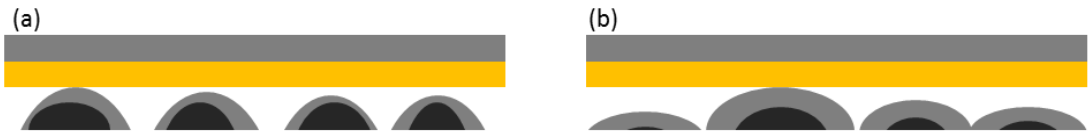

Figure 5.18: An explanation of why paraformaldehyde fixation may lead to a greater percentage of the photoresist being a pattern.
(a) PFA-fixed cells which have retained their shape and are all a similar distance away from the photoresist surface, (b) methanol-fixed cells which have collapsed down becoming flatter, with on average a greater distance from the photoresist surface.

The electron beam data showed that the depth of the pattern was related to the fluence. The maximum depth of the DM was significantly (*** $P \leq 0.001$) greater for the treated samples but there was no difference for the IM, using the linear mixed model. The lack of difference between the maximum depths may be due to selecting patterns above a threshold (mean plus two times the standard deviation). However, if the average number of patterns is compared, it is less than five patterns on a control resist compared with 57 patterns for treated samples. There are also control photoresists, for both the

DM and IM, which do not have enough “patterns” on to carry our Mann-Whitney U-tests with the corresponding treated sample. This suggests a difference between control and treated photoresist, even if the linear mixed model does not demonstrate this.

The maximum depth of the patterns for both the DM and IM is not affected by the fixation method. A possible explanation for this is that while the surface area of the cell or isolated cell nuclei in contact with the photoresist is greater for methanol-fixed samples. The height of the collapsed cell is still larger than the distance the AE travel in biological material, and hence the patterns are still only made from the emissions of the indium-111 that are close enough to the surface of the photoresist. This is a similar percentage for PFA- and methanol-fixed cells. This is similar to the reason why cells and isolated cell nuclei have the same area of features for the IM as shown in Figure 5.17.

There was no difference in the maximum depth for cells and isolated cell nuclei for the DM or IM. Since the cells contain more radioactivity, it would be expected that these would give rise to deeper patterns. An explanation for this is that the biological material the AE needs to transverse before reaching the photoresist surface is reduced when there are isolated cell nuclei. Hence, it is more likely the AE will interact with the surface, leading to patterns of similar depths.

A comparison of the volume which takes into account the area and maximum depth of the features shows a significant difference for DM (*** $P \leq 0.001$) and IM (** $P \leq 0.01$) between treated and untreated samples. For the DM, as expected due to their greater area, methanol-fixed samples and cell samples produced patterns of larger volume. However, for the IM nuclei and PFA-fixation, caused patterns on the

photoresist with a larger volume. The reason why PFA fixation may cause a greater volume is that it is on average closer to the photoresist, as explained previously (Figure 5.18). Cell nuclei may give rise to large volumes as the area from which the indium-111 emission is detected is the same and the distance the AE have to travel through the biological material is reduced, hence there is a greater concentration of radioactivity.

The internalisation data showed that at between 1 and 24 hours there was a difference in the amount of indium-111 internalised. For the DM, as treatment time increased, there was an increase in the number of features per micrometre squared, which suggests that there are more cells which have taken up indium-111 to above the threshold needed for detection. However, there was no increase in the area or the volume of the pattern. This may be due to the effects seen previously (Figure 5.17) or may be because a large proportion of the radioactivity is membrane-bound and so in direct contact with the photoresist at 1 hour, leading to a large area of a pattern at 1 hour that does not change as incubation time increases. However, the volume may not be significantly larger since as the area is much greater than the depth so it influences the volume more. Therefore, an increase in maximum depth does not necessarily lead to an increase in volume.

However, when using the IM, the length of exposure has no effect on the number of patterns. This suggests that the increase in radioactivity after 24 hours is offset by it being further away from the photoresist. An increase in the area of patterns between 1 hour and 24 hours is seen for the IM but not the DM. This could be due to the membrane-bound activity having less of an effect on the photoresist for the IM at 1 hour compared to the DM. This increase in area for IM after 24 hours also leads to an increase in the volume of the patterns seen. For both techniques, there is a greater depth of pattern after 24 hours, indicative of more radioactivity being present.

As expected, the DM produced deeper patterns with a larger area and greater volume than the IM. Since for the IM the cells are further away, it is assumed more radioactivity is required to produce a pattern which has the same dimensions, and hence why the features are smaller. It is expected that since the photoresist is further away from the surface for the IM, higher energy electrons will contribute more to the patterns than lower energy electrons, emitted by indium-111.

An issue with analysing samples in this way is that since there is no optical information about the location of the cells, the area of the photoresist to be scanned is selected randomly and individual patterns cannot be directly related to a specific cell or isolated cell nucleus. To image the photoresists for the DM, this means sampling the area closest to the centre where the droplet of cells was placed. For the IM, it is assumed that the whole photoresist surface would have been exposed to the same number of cells per unit area. However, for consistency, areas close to the centre of the photoresist were scanned. This means a scanned area may have not either been close enough to a cellular location or one scan may contain more than one cell which gives rise to differing patterns. Many of the scanned areas contained no patterns, an outcome that could be the result of there having been no cells within this area or to a lack sensitivity of the photoresist. However, since patterns were seen in resists exposed to microspheres (Figure 5.5) as well as obvious patterns with cells and isolated cell nuclei (Figures 5.6–9 and Figures 5.16–18), it is assumed that the reason for the lack of patterns is the radioactivity is not located close enough to the surface to create a pattern or no cells were present. This means that on all the samples, there are large standard deviations leading to inconsistent results when comparing the controls and the treated samples

using a Mann-Whitney U-test. The Mann-Whitney U-test was used as the number of patterns and their size do not conform to a Gaussian distribution.

Another drawback of carrying out PAR with whole cell sections is there is attenuation of the AE in the biological material. Patterns are then etched into the photoresist by AE with a lower energy close to the surface or higher energy electrons originating from radioactive atoms that are further away from the surface. The techniques cannot currently distinguish between the two.

Analysis of the patterns shows that there are significant differences when comparing controls with treated samples for all the conditions tested. The DM and IM show similar results although, as expected, patterns on photoresists treated using the DM have a greater area, deeper patterns and a large volume of the photoresist removed. However, when comparing 1 and 24 hours, it would be expected to see a greater difference (in the number of features for the IM, the area and the volume for the DM and the percentage that is patterns for both methods) than has been shown, as the internalisation data demonstrates a large difference in uptake at different incubation times (Figure 3.3). The reason why differences between 1 and 24 hours may not have been shown may be due to internal scattering and attenuation of the electrons. The large variation in pattern sizes and depths has made it difficult to directly compare samples and hence a linear mixed model effect has been used. This variation was expected partly due to the difference in uptake which depends on the number of EGFR. FACs analysis demonstrates this variation (Figure 3.2). However, variation also depends on the distance of the radioactivity from the photoresist which cannot be determined from the radiation patterns and hence a simple model was developed to quantify this effect.

5.3.2 Modelling of the Major Patterns

The variability in patterns can arise from differences in the amount of internalised radioactivity or the distance of the internalised radioactivity above the z-plane. For example, if two identical sources are located at different heights above the resist surface and assuming there are no interactions before the photoresists surface, the one which is closer to the photoresist surface will produce a pattern that is smaller in area but deeper than the other, both would have the same volume. The development of a simple model allows for a quantitative approach for analysis of the patterns. This model allows the two parameters, area and depth, to be taken into account. These parameters relate to the total volume of the pattern and the total fluence which has caused a pattern in the photoresist surface. However, this method can only assist with the interpretation of individual patterns and cannot provide collective information for all patterns on a particular resist. Nonetheless, this formalism can be applied to simple patterns as demonstrated in Figure 5.15 or to more complex patterns as demonstrated in Figure 5.16.

When cells are incubated with ^{111}In-DTPA-hEGF, the receptors bind the ^{111}In-DTPA-hEGF which then internalizes and translocates to the cell nucleus (Bailey et al., 2007, Cai et al., 2008). It is expected and demonstrated by internalisation experiments (Figure 3.3) that there is a non-uniform distribution of radiation sources throughout all of the cellular compartments (i.e. cell membrane, cytoplasm and nucleus) (Bolch, 2008, Bousis et al., 2010, Rajon et al., 2011). The modelling results are based on placement of point sources within the cells or isolated cell nuclei, which may not give a true representation of the distribution of the ^{111}In-DTPA-hEGF within the cell comparement.

Figure 5.15 shows a simple pattern and the equation fits the shape of the pattern well. Although nearer the edges of the patterns the fit is not as robust. This may be due to the

lower energy electrons near the edge of the pattern which have a shorter residual range and inelastic mean free path (IMFP). For instance, a 20 keV electron slowing down in an organic material has a range of approximately 3 μm and an IMFP of 10 nm. For an energy of 100–200 eV the range is 10 nm and the IMFP is 1 nm (Seah and Dench, 1979). Accordingly, a primary electron will enter the PMMA resist with lower energy towards the edges of a pattern, in comparison with electrons that enter the PMMA at perpendicular incidence. Although the fluence decreases towards the edges, due to the $1/\text{radius}^2$ factor, those electrons which impact the resist with a lower energy have a shorter IMFP, and will therefore be more efficient at producing chain scissions per unit path length in the PMMA. Another contributing factor is that small-angle scattering will make a marginal contribution towards the broadening of a pattern. This is due to a very slight excess fluence near the boundary of a pattern, mainly as a consequence of the additional path length being the cause of additional scattering.

Conversion of the fluence to Becquerel can be calculated by using the half-life and number of electrons emitted by each decay i.e. 7.6 electrons for indium-111 (Eckerman and Endo, 2008). Approximately 1×10^6 electrons emitted by indium-111 over a period of four half-lives corresponds to an initial activity of 500 mBq in a single cell (Royle et al., 2015). Converting initial activity to total number of electrons suggests that the patterns that we have evaluated tend to be those with higher than average initial internalized activity. This is further supported by comparing the minimal detectable fluence 2.5×10^3 $e^-/\mu m^2$ for a cell incubated for 24 hours with minimal detectable fluence of the electron beam of 1.0×10^5 $e^-/\mu m$.

The other possibility is that the monoenergetic electron beam overestimates the number of electrons that are required to create a pattern when compared to the range of

electrons emitted from indium, since the CASINO modelling showed that only a small percentage of the 25 keV electron beam deposited its energy in the photoresist surface (Figure 4.2). The ^{111}In-labelled microspheres showed that the volume removed by an electron emitted from an ^{111}In-labelled microsphere is lower than a 25 keV electron beam (Royle et al., 2015), hence a greater number of electrons would be required to form a pattern of the same volume. Therefore, further investigation is required to better define a conversion factor. However, while it may not be possible to definitively determine the actual number of internalized atoms, the variation in pattern depth, and hence fluence from one cell to another, provides a useful basis for dosimetric modelling.

The choice of using a 25 keV electron beam to calibrate the photoresists was informed by both the yield and energies of electrons emitted by indium-111 which gave an average weighted electron energy of 35 keV (Royle et al., 2015). The straightforward modelling approach based on the 25 keV electron beam calibration method provides a good match for the experimental data (Figure 5.15). Further modelling could be carried out using Monte Carlo (MC) analysis with multiple electron energies as an approach to infer the 3-D isotope distribution in cells from AFM images and may be particularly suitable for the interpretation of complex patterns.

5.3.3 Limitation of Photoresist Autoradiography

PAR is able to provide information about the fluence which has led to a creation of a pattern. However, since the biological material has been removed, it is not possible to work out if it is a single cell providing many individual point sources of radioactivity or if a larger pattern is seen if this is from one or multiple cells. A solution to this problem would need to be created; for example, a grid which would allow for individual cells to

be grown in wells before being fixed and the photoresist inverted on top. This would allow for areas to be scanned which were known to contain individual cells. However, if individual cells were grown in culture, they may not have the same biological properties as cells which are grown in a monolayer.

When using AFM to image nanoscale surface patterns, the resolution of the image may be limited by the shape of the tip of the AFM probe in relation to the shape of the pattern itself. A routine probe tip has a radius of curvature at the apex of about 10 nm. The pattern can interact with the sides of the probe, leading to an image which is a combination of the actual topography of the pattern and the probe geometry (Dufrêne, 2002). Likewise, the shaft of the tip has an opening half-angle of 20^{o}, which places a limit on the steepness of slope that can be tracked by the tip apex. Variations from this angle will cause artefacts in the imaging of the photoresist surface (Calabri et al., 2008).

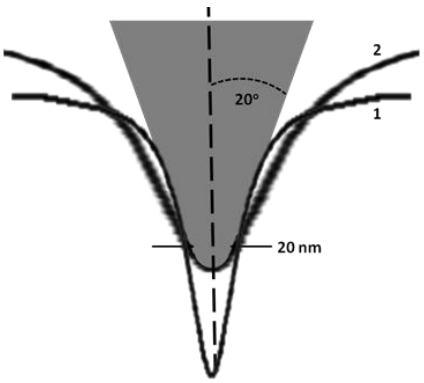

Figure 5.19: Schematic illustration of convolution of tip shape with object shape
The effect constitutes a limit on the ability of AFM to produce a 'true' 3-D map of a surface pattern. In the present case it may become a significant factor for deep and narrow patterns, when a point source is close to the resist surface.

In the present case, the effects of convolution are illustrated in Figure 5.19. The two examples, curves 1 and 2, show that imaging will be reliable for shallow and broad patterns, due to point sources located more than 150 nm above the resist surface. On the other hand, when a pattern is deep and narrow with a radius of less than 0.5 µm due to sources in close proximity to the resist, the tip cannot access the central part of the pit.

When using AFM, there is a limited size of the microscope scan and the total area scanned of the photoresist is extremely small. The photoresists have an approximate area of 15 mm^2. However, the area of an individual AFM scan is only 400 μm^2. Therefore, it is possible to only scan a small percentage of the photoresist.

Another limitation of the PAR technique is its inability to detect sources which are further away from the cell surface and have attenuated within the cell. This issue could possibly be overcome by using ultramicrotomed cells i.e. cells which have been sectioned to approximately 100 nm. Since the cells would be embedded in polymer sections, it may be possible to use the DM without the effect of radiation grafting. However, this would also increase the number of photoresists that would need to be imaged in order to provide information for modelling and reduce the likelihood of being able to correlate the pattern with the location it came from in a cell. While it has been shown here that the photoresist have processing consistency (Figures 5.1, 5.2 and 5.3) by having individual electron beam patterns printed on each photoresist, it would be possible to quality check the processing condition for individual photoresists.

Therefore, if the several improvements to the experimental design were made, principally having a technique which allows the location of individual cells to be known and an automated imaging process, the PAR technique would be able to provide accurate quantifiable information about the variation and distribution of TRT for microdosimetric modelling. It is expected that this model could better determine the differences between 1 hour and 24 hours as demonstrated by internalisation data (Figure 3.3).

5.4 Conclusions

Analysis of photoresists by AFM has shown that the different processing conditions are able to provide consistent results, with clear differences between control and treated resists. There does not appear to be a processing condition which improves the detection of patterns on the photoresist surface.

An intuitive and simple procedure has been developed for identifying the locations and strengths of AE-emitting radionuclides internalized within cancer cells. The procedure consists of matching an experimental 3-D pattern in a photoresist film detector by the placement of one, or more, point sources at locations, and with strengths that can be inferred from experimental parameters. The model can provide information about the subcellular radioactivity in the whole cell and cell nucleus for MIRD calculations.

While the PAR technique is able to provide a quantitative method, improvements to the experimental design would allow for patterns to be correlated with individual cells and hence provide more reliable information about individual cells.

Chapter 6:
Microautoradiography using the Transmission Electron Microscope

Chapter 6:

Microautoradiography using the Transmission Electron Microscope

6.1 Introduction

This chapter describes the methods developed for microautoradiography (MAR) using a transmission electron microscope (TEM). TEM is able to provide high resolution images of cells and has previously been used to determine the subcellular distribution of radioactivity from targeted radiotherapy (TRT) agents (Janson et al., 2000). However, the micrographs showed poor staining. Apart from this example, there has been limited use of the electron microscope-microautoradiography (EM-MAR) technique for determining the spatial distribution of radiopharmaceuticals. The main use of the EM-MAR technique is to use radioisotopes of common elements or radiolabelled common compounds found within cells in order to determine the biological processes which occur within cells. For example, the EM-MAR technique has been used for the studies of cell kinetics and cell distribution using indium-111 labelled leukocytes and platelets and mononuclear phagocytes (Davis et al., 1980). Tritium has been used to determine the location of dhurrin by tritium labelling its precursor (Saunders and Conn, 1977). In another example, ^{3}H-4-thymdine and ^{3}H-uridine were used to establish the amount of DNA synthesis and ribonucleic acid (RNA) synthesis respectively, using EM-MAR, this was to determine the presence and characteristics of amitosis, or direct nuclear division, in amitotic hepatocytes, obtained from mice livers. The ^{3}H-4-thymdine and ^{3}H-uridine were injected into mice at various ages (19 days to 2 years) before sacrifice. Micrographs showed there were very few MAR grains in the amitotic hepatocytes compared with the mononucleate and binucleate hepatocytes from the liver, suggesting

that nucleic acid syntheses of both DNA and RNA in amitotic cells are less than in the other mononucleate and binucleate cells (Nagata and Ma, 2003). Attempts have been made to quantify the EM-MAR technique using a radioactive “hot line” containing tritium and then creating a density distribution map, as the distance away from the source increases, counting 1,000 developed grains per line (Salpeter, 1969). However, this quantification is only accurate for the same radioisotope, exposure and development conditions.

6.1.1 Microautoradiography as a Technique

As described in the Introduction, MAR uses a silver bromide emulsion which, when exposed to a source of radiation, causes the bromide crystals to convert to metallic silver, providing spatial information about the location of the radioactive source causing the change. In the emulsion, each crystal of silver halide is an independent detector insulated from the rest of the structure by a layer of gelatine which surrounds a lattice of silver and bromine atoms. This isolates the grains from other grains so that a crystal does not catalyst the development of the surrounding crystal. The record provided by the emulsion is cumulative and spatially accurate (Rogers, 1979). To carry out MAR, cells are fixed and processed before an emulsion is applied. During the exposure period, the radioactive emission from the sample causes a latent image to form. This will not be visible until development.

In the emulsion, the silver bromide crystals are in a cubic lattice with imperfections such as dislocations, known as sensitivity specks. In this lattice, they share electrons between adjacent ions. If the electrons in the lattice are given an energy of approximately 5 eV or greater from radioactive emissions, they are able to enter the conduction band and can therefore travel large distances through the crystal, causing the

silver to be deposited at these sensitivity specks; this causes a latent image to form. If only one silver halide atom has been converted to silver, it is very unstable at room temperature. However, if two or more electrons have converted to silver at the sensitivity speck, the silver is much more stable. The energy of the isotope is inversely related to the resolution of the resulting MAR image. The lower the energy of the source, the higher the resolution of the autoradiogram (Nielsen and Nielsen, 2005).

In choosing an emulsion for EM-MAR, the smaller the mean diameter of the silver halide crystal in the emulsion, the higher the spatial resolution. For this reason, Ilford nuclear emulsion type L4 was used with a grain size of 0.11 μm (Ilford, 2015), as it is the emulsion with the smallest crystals. However, the smaller the silver halide crystal, the more difficult it becomes to achieve a high sensitivity. The smaller the crystal grains, the lower the chance the trajectory of a radioisotope emission has in interacting with the crystal at a sensitivity speck, reducing the sensitivity (Rogers, 1979).

During development, as more metallic silver is deposited at the original sensitivity speck, bromine atoms migrate out of the crystal. Also, during development, the metallic silver, which has been converted by the exposure of the electron, acts as a catalyst to convert the rest of the silver bromide into silver and hydrogen bromide.

The development is stopped by lowering the pH and then the sample is fixed. During fixation, the bromide crystals which have not been reduced to silver are dissolved out of the emulsion. Washing allows them to be removed from the sample. The basic MAR protocol is shown in Figure 6.1.

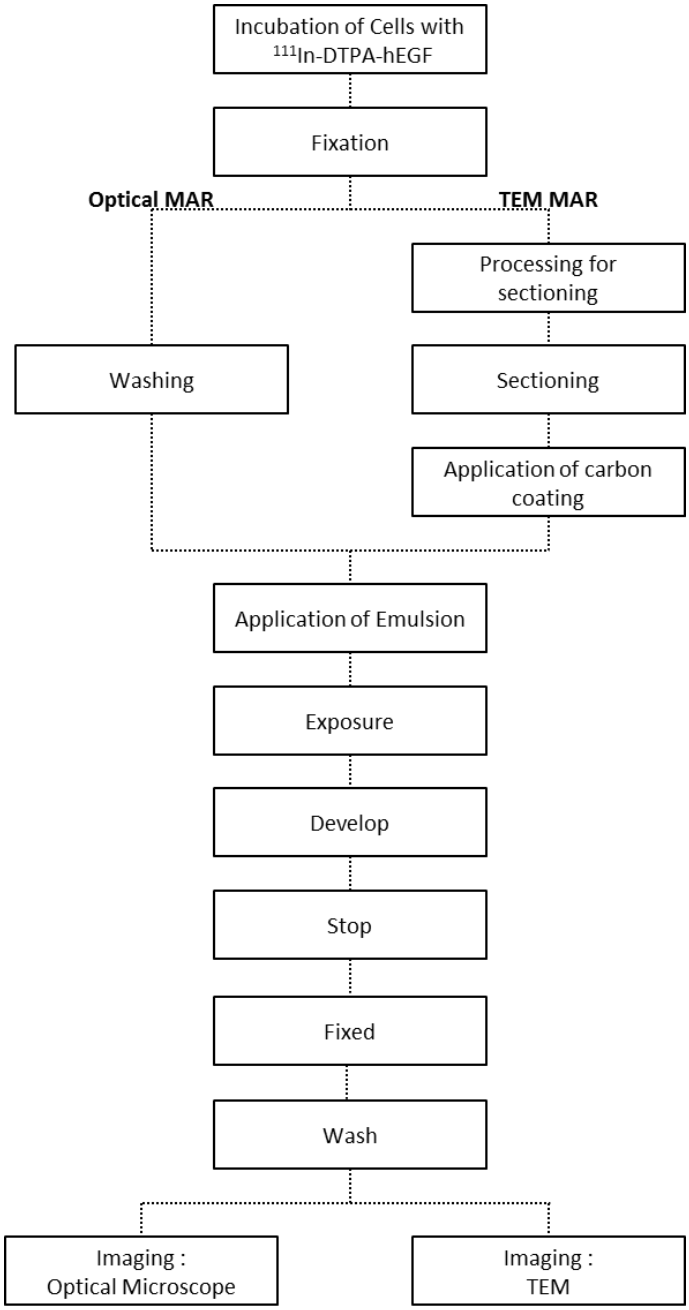

Figure 6.1: An outline of the microautoradiography techniques

6.1.2 The Transmission Electron Microscope and Resolution

A TEM uses a beam of electrons that passes through the specimen, so the sample needs to be ultrathin. For biological samples, cells are processed in such a way as to allow ultramicrotomy, which generates sections that can be less than 50 nm in thickness. The beam of electrons is then imaged, usually using a charge-coupled device. Like optical microscopy, where the theoretical resolution is limited by the wavelength light, the

theoretical maximum resolution of TEM is limited by the wavelength of the electron. Atomic resolution has been achieved with the imaging of several different types of atom including oxygen, and it is also possible to image an atom's position in its crystal lattice (Urban, 2009). However, this resolution limit is not achievable for biological samples where the resolution is determined by the sample. This depends on the processing and staining and section thickness as thicker sections lead to more scattering and lower resolution. However, with good sample preparation, the resolution is approximately 2 nm, and with good staining the subcellular organelles within the cell can be imaged (Cooper, 2000).

6.1.3 Aims and Outline

The aim of the research reported in this chapter is to demonstrate that EM-MAR is a viable method for evaluating the spatial distribution of radioisotopes in single cells and to improve on the information that can be obtained using optical MAR. This chapter firstly demonstrates the current image quality and information which can be gained from the optical MAR technique. It then describes the development of the method for EM-MAR, looking at the various factors which affect the image quality of TEM images and the factors which affect the quality of the of the MAR grains. Finally, images from a time course are analysed, demonstrating the quality of images and type of information which can be gained from these experiments.

6.2 Results

6.2.1 Microautoradiography using Optical Microscopy

MAR using optical microscopy was carried out for comparison with EM-MAR. Representative images are shown in Figure 6.2. Cells were incubated with indium labelled human epidermal growth factor (^{111}In-DTPA-hEGF, DTPA is diethylenetriaminepentaacetic acid) for 1 or 24 hours before being fixed and processed for optical MAR. Controls showed fewer grains than the cells which had been incubated with ^{111}In-DTPA-hEGF. More grains were present at 24 hours than at 1 hour.

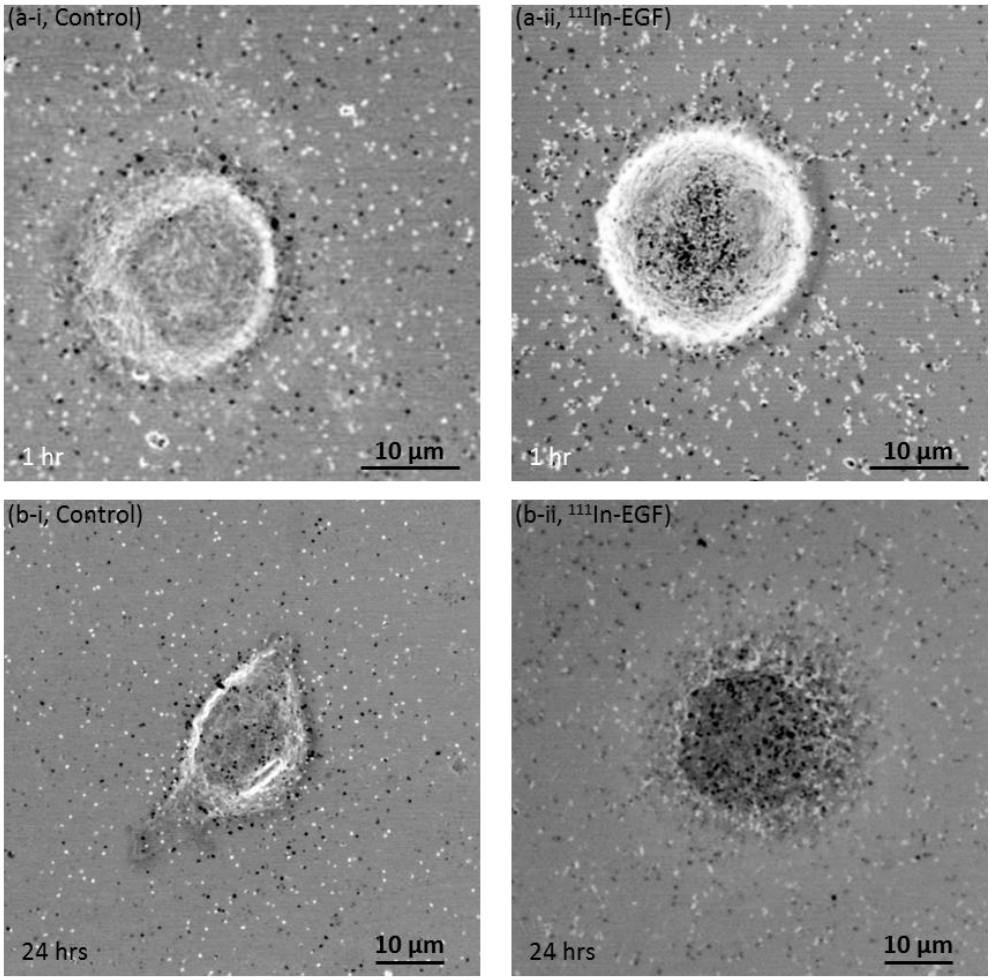

Figure 6.2: A demonstration of optical microautoradiography
Optical micrographs of SQ20B (i) control cells and (ii) cells incubated with ^{111}In-DTPA-hEGF for (a) 1 hour and (b) 24 hours. The silver grains are shown as dark spots.

6.2.2 Development of a Robust Method for Microautoradiography based on Transmission Electron Microscopy

6.2.2.1 Determination of an Optimised Transmission Electron Microscopy Preparation Technique

Numerous refinements and modifications to standard MAR techniques were introduced to enable analysis of autoradiographic samples by TEM. The two techniques, microwave preparation and oven preparation, are briefly reviewed below plus the two methods of applying the emulsion. A summary of these methods is shown in Table 6.1, with Figures 6.3–6.5 showing the quality of the images.

Microwave Preparation Technique

When using Auger electron (AE) emitting radioisotopes with a short half-life, minimising the preparation time will lead to an increase in the chance of detecting radioactive sources. To increase the chance of obtaining a signal from the indium-111, a fast preparation technique using a microwave for the polymerisation stage was developed. This shortens processing of samples to 1 day. Briefly, cells were incubated with the ^{111}In-DTPA-hEGF in flasks before being fixed in paraformaldehyde (PFA) and glutaraldehyde and then osmium tetroxide. After fixation, cells were scraped from the flask using a cell scraper and dehydrated in an ascending series of acetone. Cells were then infiltrated with resin and polymerised in a microwave (Chapter 2, Section 2.5.2.1.) Preliminary results obtained with this method are shown in Figure 6.3.

Oven Preparation Technique

The oven preparation technique has two key differences. Firstly, the processing for this technique took 3 days and cells were grown and processed on coverslips; secondly, resin was polymerised in an oven. Briefly, cells were fixed in PFA and glutaraldehyde and then in osmium tetroxide. There was a tertiary fixation in uryal acetate and a longer

dehydration series and resin embedding. The resin was then polymerised in an oven (Chapter 2, Section 2.5.2.2).

Chien Staining Pad

This is a piece of TEM equipment that has been designed for the post-staining of cell sections, once they have been placed on TEM grids. The TEM grids are "stood up" in the staining pad to allow the sections to be in contact with the stain. For use in EM-MAR, the stain was the MAR emulsion. This was placed in a Petri dish and the grids in the Chien Staining Pad were inverted into the emulsion (Chapter 2, Section 2.5.5.2.).

Wire Loop

Since there was interference from the emulsion that was affecting the cell sections, it was suggested that this was caused by the temperature of the emulsion (43°C). To reduce the temperature that the sections were exposed to, a wire loop was used to apply the emulsion. The thin layer of emulsion in the wire loop was allowed to cool, and slightly gel, before being applied to the cell sections; this firstly reduces the temperature that the cell sections are exposed to and secondly increases the heat transfer away from the cell sections. This method was tried with the microwave preparation technique but the emulsion collapsed, forming a thick uneven layer on the surface of the TEM grids. However, addition of the surfactant dioctyl sodium sulfosuccinate allowed for an even layer of the emulsion to be applied to the grid (Figure 6.5b) (Nagata, 1998). An even layer means that each indium-111 atom will be in equally close proximity to a MAR grain and so will have the same likelihood of producing a latent image, which can then be viewed in the TEM after development (Chapter 2, Section 2.5.5.2.). A carbon layer was also added when using the wire loop method to prevent chemographic interactions between the sections and the autoradiographic emulsion and to provide more support for the emulsion (Somogyi and Chubb, 1976).

Table 6.6.1: Adaptation of the electron microscope-microautoradiography protocol

A table showing the various TEM processing techniques which were used

Protocol	Reason for using	Result	Problems	Solution	Figure
Microwave preparation technique	To increase the chance of obtaining a signal from the indium-111	EM-MAR was sensitive enough to detect radioactivity from internalised ^{111}In-DTPA-hEGF	Poor staining, poor cell structure	Oven preparation	Figure 6.3
Oven preparation technique: Chien staining grid	Improve cell structure	When no MAR emulsion was applied, cells showed good contrast with staining allowing the identification of internal cell structures	Cells sections with emulsion applied showed the section had been corrupted and no longer demonstrates a smooth surface or the presence of cells.	Addition of carbon layer; wire loop technique to apply emulsion	Figure 6.4
Oven preparation technique: wire loop method	Stop corruption of cell sections	With the wire loop technique the emulsion can be applied to cells without causing the sections to be corrupted; There is an even layer of emulsion across the section.	-	-	Figure 6.5

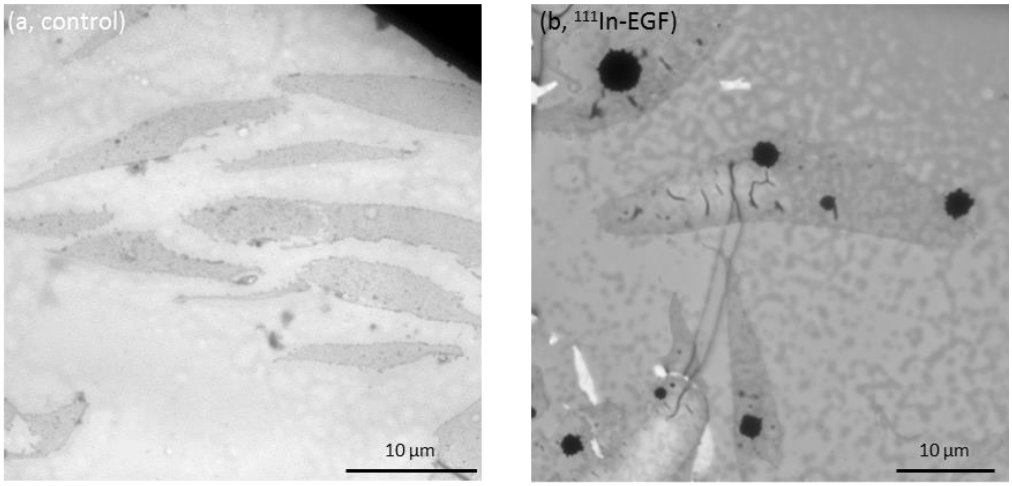

Figure 6.3: Demonstration of the microwave transmission electron microscope cell preparation technique

TEM Micrographs of (a) control cells and (b) cells incubated with ^{111}In-DTPA-hEGF. Emulsion was applied using the Chien staining pad, sections were left to expose the emulsion for 5 days and the sections were developed for 180 seconds in Ilford Phenisol developer.

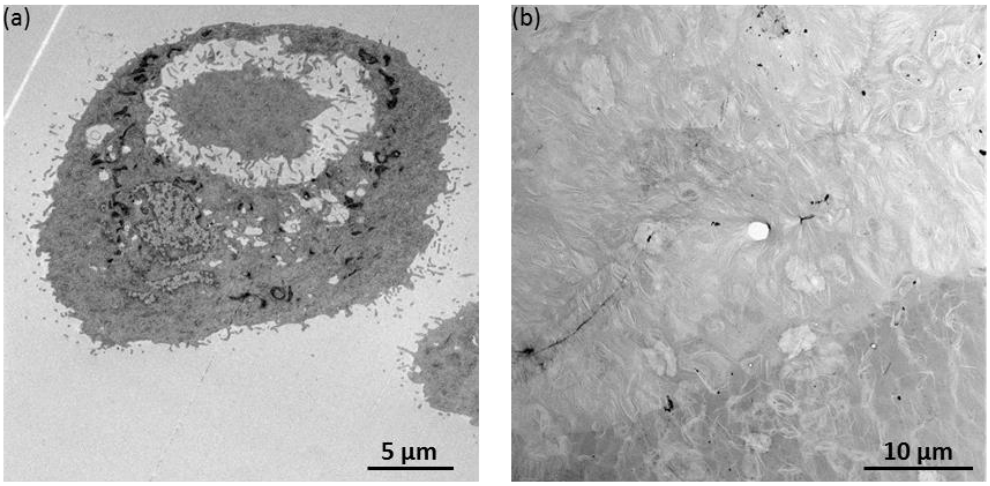

Figure 6.4: Demonstration of the oven transmission electron microscope cell preparation technique

TEM micrographs of the oven (longer) preparation technique, (a) an image showing that the cell preparation technique works and (b) showing that when the emulsion is applied there is destruction of the cell sections.

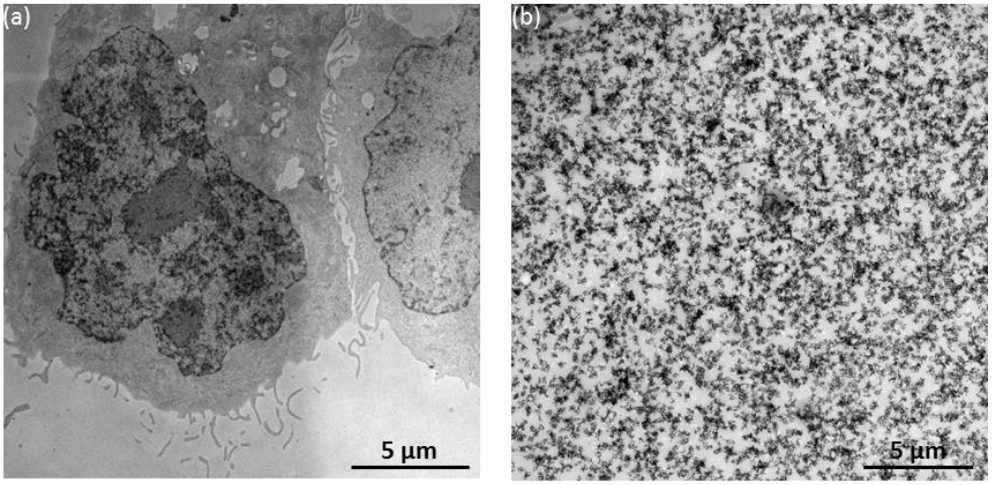

Figure 6.5: Alterations to the oven transmission electron microscope cell preparation technique

TEM micrographs of (a) control cells after application of a carbon layer (b) an even layer of the MAR emulsion on a positive control (exposed to white light) section**.**

6.2.2.2 Optimisation of Exposure Time and Development Time

Both the duration of the exposure time that the MAR emulsion is exposed to radioactive biomaterial and the length of time for development of the emulsion affect the quality of the final MAR images and, therefore, the information that can be gained from them. Table 6.2 shows a summary of different exposure and development times and the results obtained. Figure 6.6 shows images of these conditions.

Table 6.6.2: Determination of the expose and development time

Exposure time	Development time			Figure
	60 seconds	90 seconds	120 seconds	
5 days	No grains	n/a	No grains	Not shown
7 days	No grains	n/a	Over-developed	Figure 6.6a
10 days	Developed	n/a	Over-developed	Figure 6.6b
12 days	Developed	Over-developed	n/a	Figure 6.6c
14 days	Developed	Over-developed	n/a	Not shown

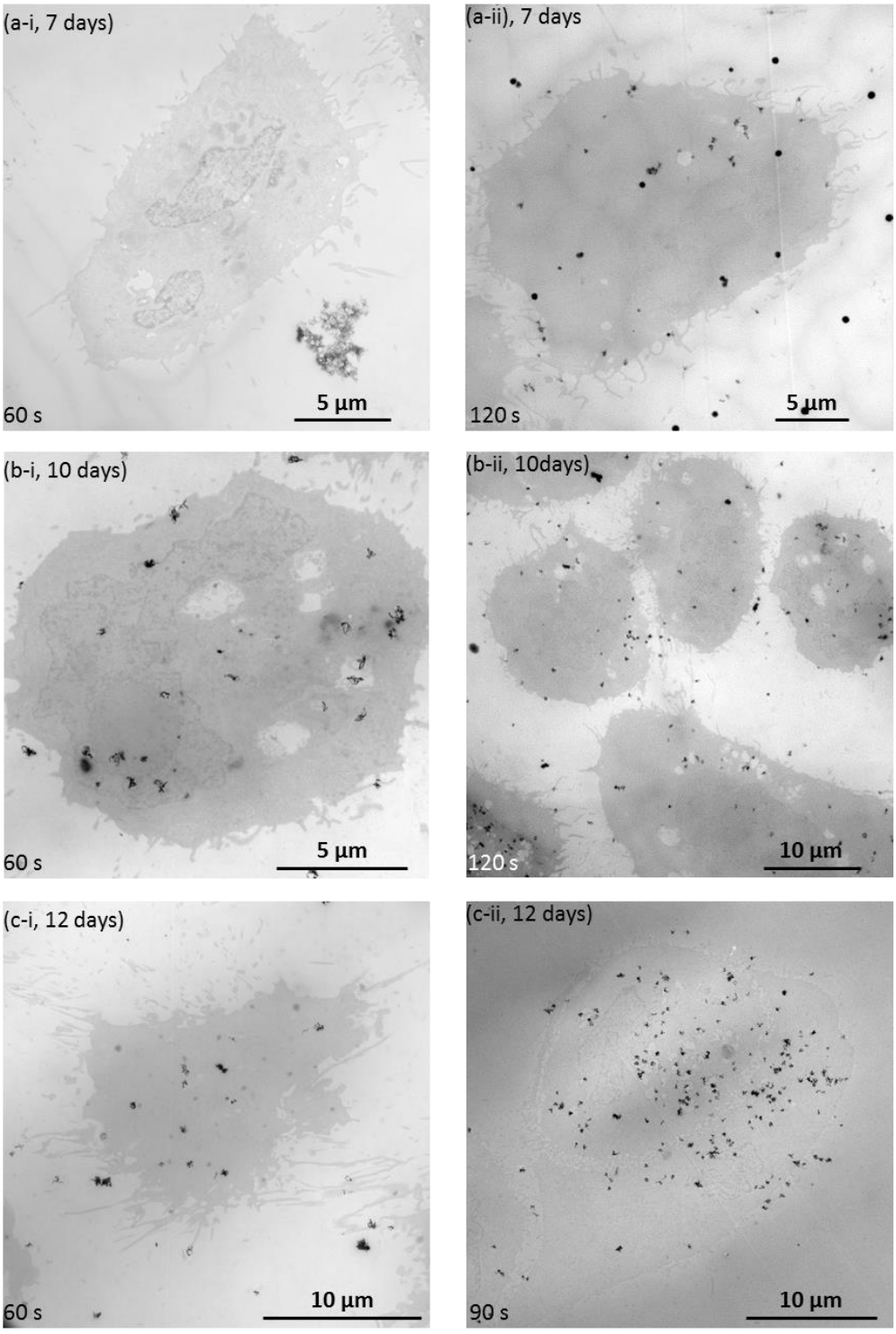

Figure 6.6: The determination of exposure period and development time

Cells which had been incubated with ^{111}In-DTPA-hEGF for 24 hours were prepared for TEM using the oven preparation protocol. Cells were sectioned and placed on TEM grids and exposed to the MAR emulsion for (a) 7 days, (b) 10 days (c) 12 days. They were then developed for (i) 60 seconds or (ii) 120 seconds (a), (b) or for 90 seconds (c).

A short exposure time will not allow for there to be enough interaction of the electrons with the silver bromide crystals and therefore will not lead to the formation of a latent image. Increasing the length of exposure will allow for more emissions of indium-111 and increase the chance of silver halide being converted to silver. Increasing the exposure time further increases the background noise. It is, therefore, important to develop the samples at the shortest exposure time which produces developed grains and for this reason 10 days of exposure was chosen instead of 12 or 14 days (Table 6.2).

Full development occurs when all the silver available in the crystal has been converted to metallic silver. At this point, all the developed grains look like coiled filaments and occupy a space three times the size of the original crystal volume (Rogers, 1979). For the Ilford L4 emulsion, a fully-formed grain should therefore have a diameter of approximately 0.2 μm. As the development time increases, the background noise also increases, which reduces the quality of the images.

Table 6.6.3: Determination of the development time

Exposure Time	Results	Figure
30 seconds	No developed grains are seen and the gelatine which surrounds the silver halide crystals in the emulsion can still be seen suggesting a too short fixation time	Figure 6.7a
60 seconds	After 1 minute, ribbon like grains are seen which have not started to coalesce, approximate size 0.2 μm- grains considered developed.	Figure 6.7b
90 seconds	After 90 seconds of development grains appear in ribbon like structures but do appear to have started to coalesce	Figure 6.7c
120 seconds	Overdeveloped and are seen as circular grains	Figure 6.7d

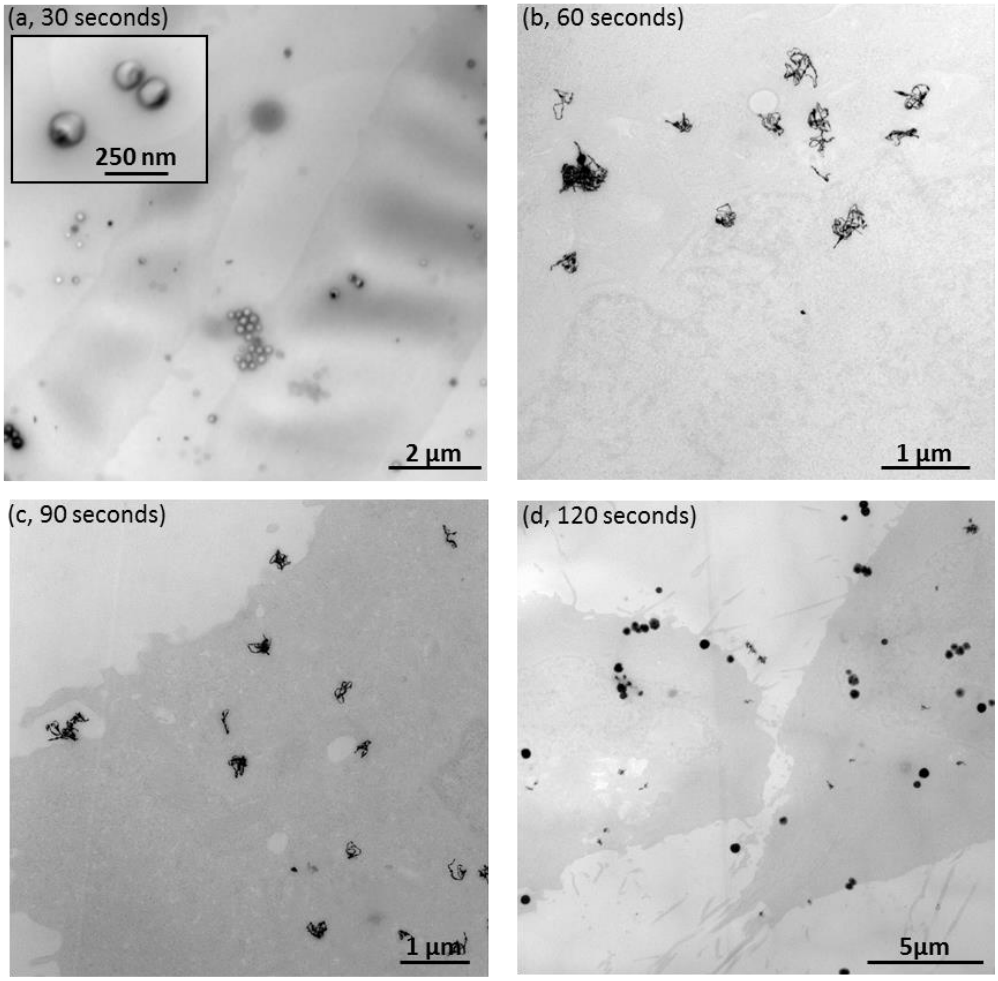

Figure 6.7: Determining the development time
Experiments were carried out to determine the optimal development time (a) 30 seconds, insert showing gelatine still present (b) 60 seconds (c) 90 seconds (d) 120 seconds.

6.2.2.3 Determining the Staining Technique

The quality of the TEM micrographs will be influenced by the quality of the staining of the cell sections, as this allows the subcellular structures to be visualised. Staining of the sections is carried out to provide contrast of the cell structures during TEM. Samples can either be stained before but are most commonly stained after, the application of emulsion (Leslie et al., 1985, Falette et al., 1989, Tovey and Kendall, 1979).

Table 6.6.4: Determination of the staining technique

Stain	Results			Figure
	Control: No emulsion	**Control: No indium-111**	**Treated samples: ^{111}In-DTPA-hEGF**	
Pre-stained before emulsion vs post-stained after application of emulsion	Both pre- and post-staining showed poor staining of the TEM grids and there did not appear to be a difference in the number or quality of grains if cells were pre-stained or if they were post-stained with lead citrate after development of the MAR emulsion.			n/a
5 minutes lead citrate	There was good staining across the cells	There was slightly worse staining	The contrast was greatly reduced	Figure 6.8a
10 minutes uryal acetate, 10 minutes lead citrate	Improved contrast	Improved contrast	Improved contrast–still poor staining	Figure 6.7b
En-bloc stained	Improved the contrast and allowed for subcellular structures including nucleoli, cell nucleus, nuclear membrane, ribosomes, mitochondria and lysosomes to be seen.			Figure 6.7c

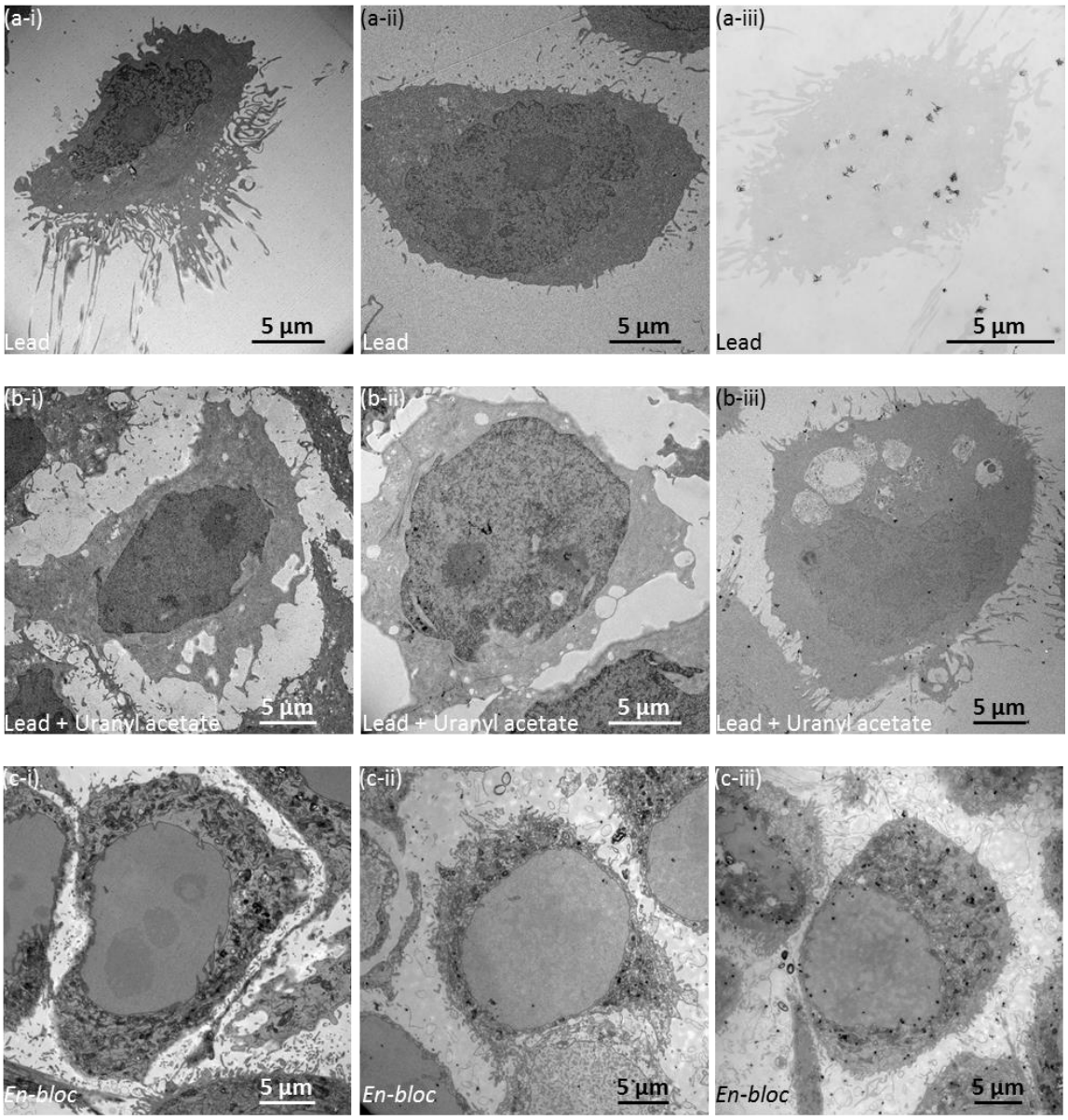

Figure 6.8: Determination of the staining technique

To obtain the best contrast in the TEM, different staining techniques were tried. (a) lead citrate staining only, (b) lead citrate and uryal acetate staining, (c) *en-bloc* staining; (i) no emulsion applied to untreated cells (ii) MAR emulsion applied to untreated cells and (iii) MAR emulsion applied to cells after incubation with ^{111}In-DTPA-hEGF.

Negative staining is usually carried out with lead citrate and uranyl acetate and the secondary fix in osmium tetroxide also increases contrast. These are heavy elements that react to varying degrees with cell structures. For example, osmium tetroxide as well as fixing lipids stain them and stains the plasma membrane due to its reaction with phospholipids and the reduction of the osmium tetroxide. Uranyl ions (UO_2^+) bind to

proteins and lipids and to nucleic acid phosphate groups of DNA and RNA and hence membranes and nucleic acids. Nucleic acids containing protein complexes such as ribosomes show good contrast when stained with uranyl acetate, due to the electrostatic interactions. Lead citrate enhances the contrasting effect for a wide range of cellular structures such as ribosomes, lipid membranes, cytoskeleton and other compartments of the cytoplasm, as lead is a cation and binds via the electrostatic interaction. Those that react more will appear darker in the TEM. Application of the MAR emulsion has been shown previously to affect the contrast in the TEM (Janson et al., 2000).

6.2.2.4 Summary

These results allowed for the selection of the MAR processing conditions to be determined. These were: the wire loop method was used to apply the emulsion, the grids were exposed for 10 days and there was a 60 second development. The *en bloc* staining method described, improved the quality of the image and hence it was used for further experiments (Ramcharan and Matthews, 1996, Gould and Armstrong, 1989).

6.2.3 Time course

To investigate whether the spatial resolution of EM-MAR is sufficiently sensitive to allow visualisation of differences in intracellular distribution of indium-111 under different conditions, a time course experiment was carried out. Two time points were used: 15 minutes to determine if the EM-MAR technique could determine rapid uptake of indium-111, and 24 hours as a contrasting time point to see if the EM-MAR technique was able to distinguish between differences in uptake. Untreated cells were fixed immediately and $^{111}InCl_3$ was used for controls at both time points. The first was to obtain the background density of grains and $^{111}InCl_3$ was used to see if the technique

could determine the differences in two sources of indium-111. A summary of results is shown in Figure 6.9, with more detailed micrographs shown in Figures 6.10 to 6.15. Analysis of the results is shown in Figures 6.16 to 6.18

Figure 6.9 shows that that there has been good fixation and processing of the cells leading to good contrast, with subcellular structures easily identifiable. These include the nucleoli, cell nucleus, nuclear membrane and filopodia. Figure 6.9(i) shows cells incubated with $^{111}InCl_3$ showing no grains present at 15 minutes or 24 hours. When cells were incubated with ^{111}In-DTPA-hEGF, MAR grains were present. After 15 minutes, there were grains associated with the filopodia, around the cell membrane, in the cytoplasm with a few associated with the cell nucleus. At 24 hours there are more grains present in the cell nucleus and in the cytoplasm of the cells. There are no grains present in the resin surrounding the cells. The epidermal growth factor (EGF) and epidermal growth factor receptor (EGFR) complexes are internalised via receptor binding (Jorissen et al., 2003). These complexes are carried in budding vesicles to cellular localisations including the Golgi, endoplasmic reticulum and mitochondria as well as the cell nucleus (Wang and Hung, 2012).

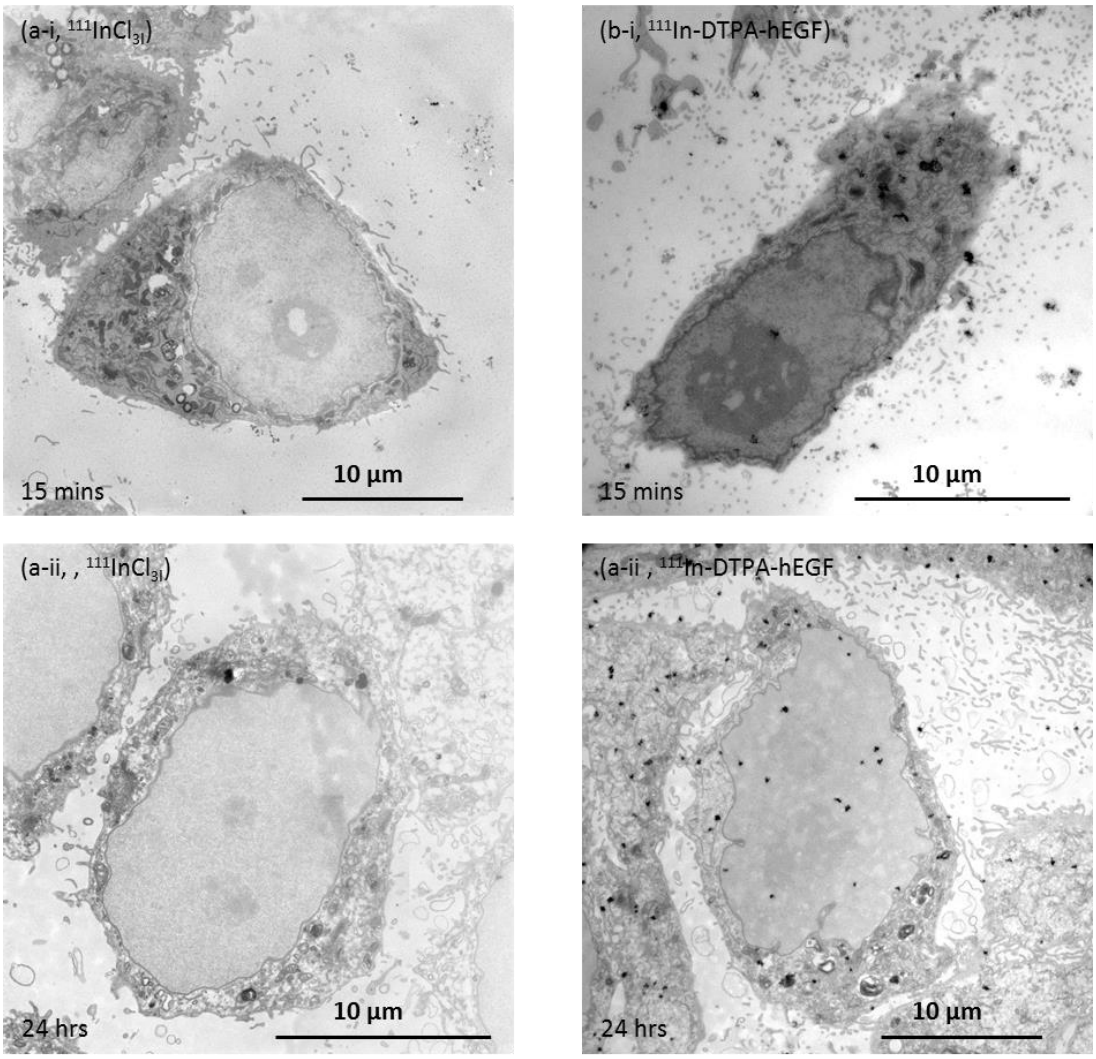

Figure 6.9: Demonstration of a time course
TEM micrographs showing SQ20B cells incubated with either (a) $^{111}InCl_3$ or (b) ^{111}In-DTPA-hEGF for (i) 15 minutes, (ii) 24 hours.

Figure 6.10 shows two cells sections. The first is a section of a cell incubated with ^{111}In-DTPA-hEGF for 15 minutes (Figure 6.10a) and shows only five grains present across the whole cell section labelled "☼", with the nucleus having no grains associated with it. The second is a section of a cell incubated with ^{111}In-DTPA-hEGF for 24 hours and has 70 grains associated with it, in the cell nucleus and cytoplasm.

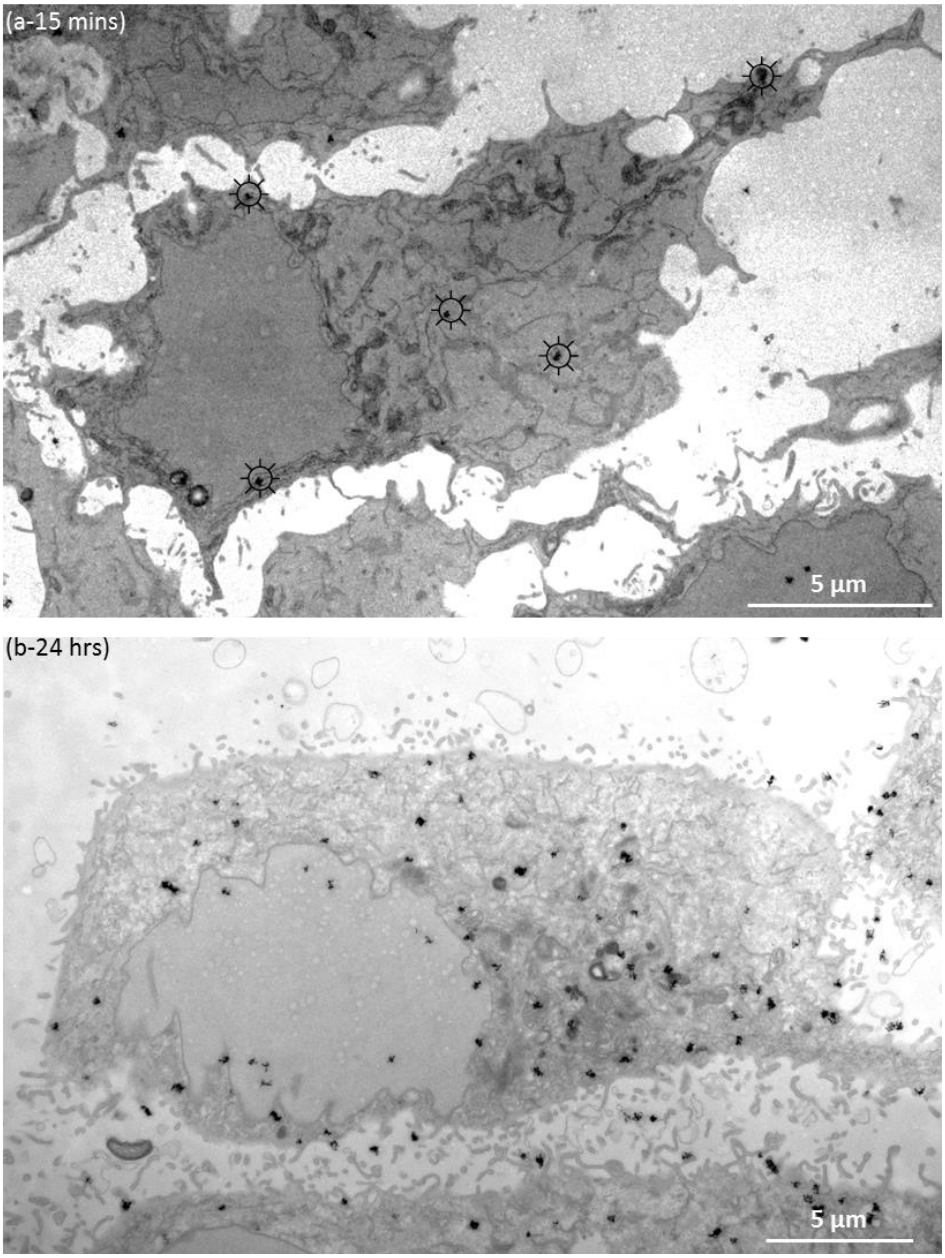

Figure 6.10: Comparison of 15 minutes and 24 hours
TEM micrographs showing SQ20B cells incubated with ^{111}In-DTPA-hEGF for either (a) 15 minutes where grains are labelled ☼ (b) 24 hours.

Time Point: 15 minutes

Figures 6.11 and 6.12 show images of representative cells that have been incubated with ^{111}In-DTPA-hEGF for 15 minutes. The cells have varying amounts of grains associated with them, with no grains associated with the polymer resin which supports the cells.

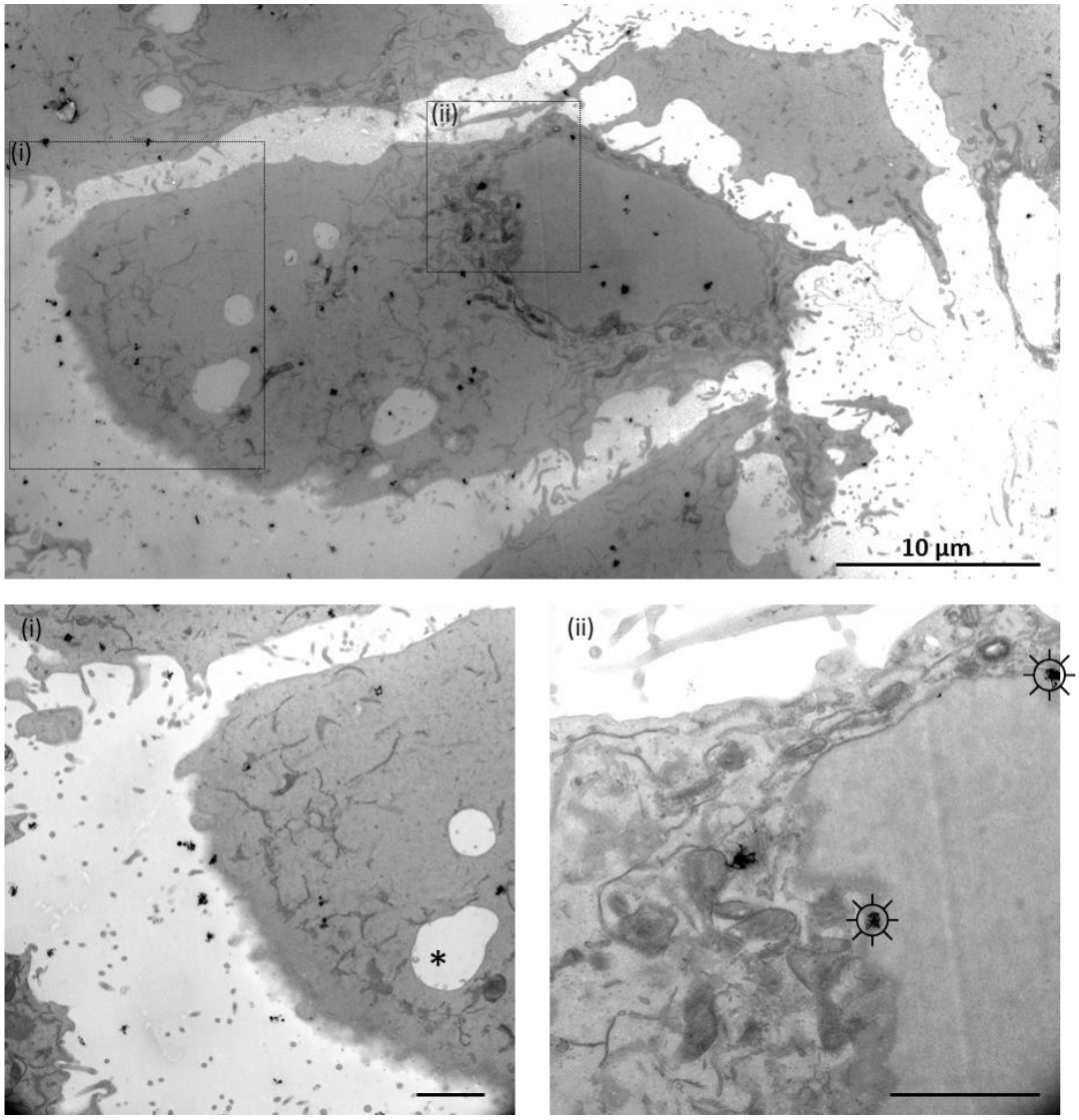

Figure 6.11: Cells incubated with ^{111}In-DTPA-hEGF for 15 minutes
TEM micrographs of SQ20B cells incubated with ^{111}In-DTPA-hEGF for 15 minutes. (i) Grains are only present in resin close to the cell surface. (*) indicates biological material in vacuoles, (ii) Grains (☼) are not associated with cell organelles and are present on the nuclei membrane. Scale bar of inserts 2 µm.

Figure 6.11 shows a large cell; the nucleus has grains associated with it. There are subcellular structures around the nuclear membrane. Several large vacuoles containing biological material (*) are present. This cell has a large number of grains associated with it across the whole of the cell as well as two grains, shown in Figure 6.11(ii) which are located on nuclear membrane (☼). The grains that appear to be located in the space between cells are likely a result of radioactivity in filopodia which, although protruding

from the cell itself, cannot be seen in this particular section. Alternatively, some grains may be due to non-specific, background changes in the emulsion. However, since the majority of grains that are seen in spaces between cells are not randomly dispersed but appear to be located close to cells (image not shown) it is most likely that the majority of them are the result of intracellular radioactivity.

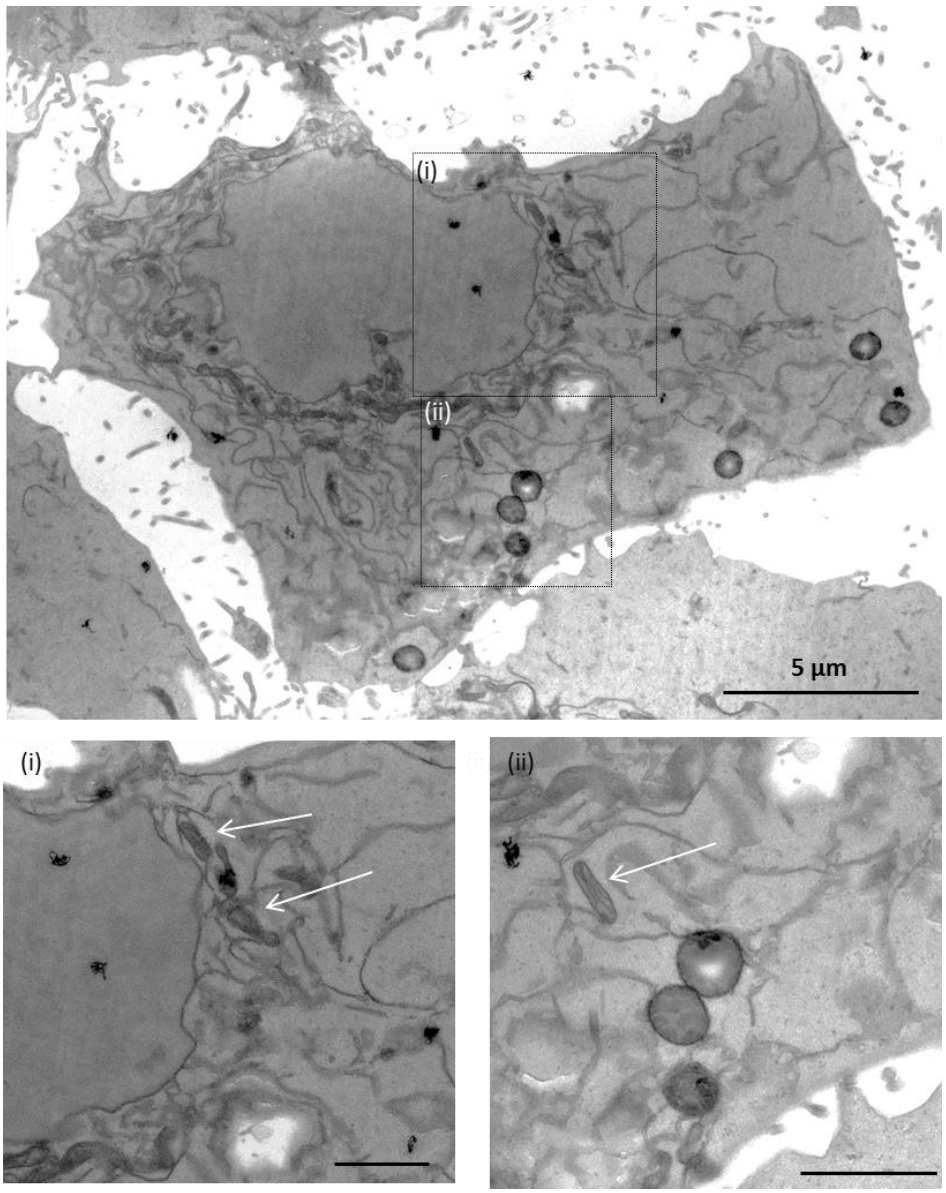

Figure 6.12: Grains in the cell nucleus after incubation with ^{111}In-DTPA-hEGF for 15 minutes
TEM micrographs of SQ20B cells incubated with ^{111}In-DTPA-hEGF for 15 minutes, (a) MAR grains are seen overlying the cell nucleus and also associated with (i) mitochondria (arrows) and (ii) lysosomes (identified by their single membrane). Scale bar of inserts 1 µm.

Figure 6.12 shows a cell which has a few MAR grains associated with it. Figure 6.12 shows that some grains are associated with mitochondria and lysosomes. In all images at 15 minutes, there do not appear to be multiple grains in close contact with each other, suggesting that one source of indium-111 leads to one grain being developed.

Time Point: 24 hours

Figures 6.13 to 6.15 show a range of cells which have been incubated with ^{111}In-DTPA-hEGF for 24 hours. The cells have varying amounts of grains associated with them and like previous examples there are few grains in the polymer resin.

Figure 6.13 shows the varying number of grains which are associated with the cell. This number varies but all cells have a higher number of grains associated with the cell compared to 15 minutes incubation. There are still grains in the filopodia and cell membrane, suggesting that uptake of ^{111}In-DTPA-hEGF is still occurring. There are no grains associated with the polymer resin. There appears to be some association of MAR grains with the mitochondria (Figure 6.13a and 5.13b, Figure 6.14 and Figure 6.15(i)) and Figures 6.14 (i) and 6.15 (i) have autophagosomes present. In some images there are multiple grains in close contact with each other.

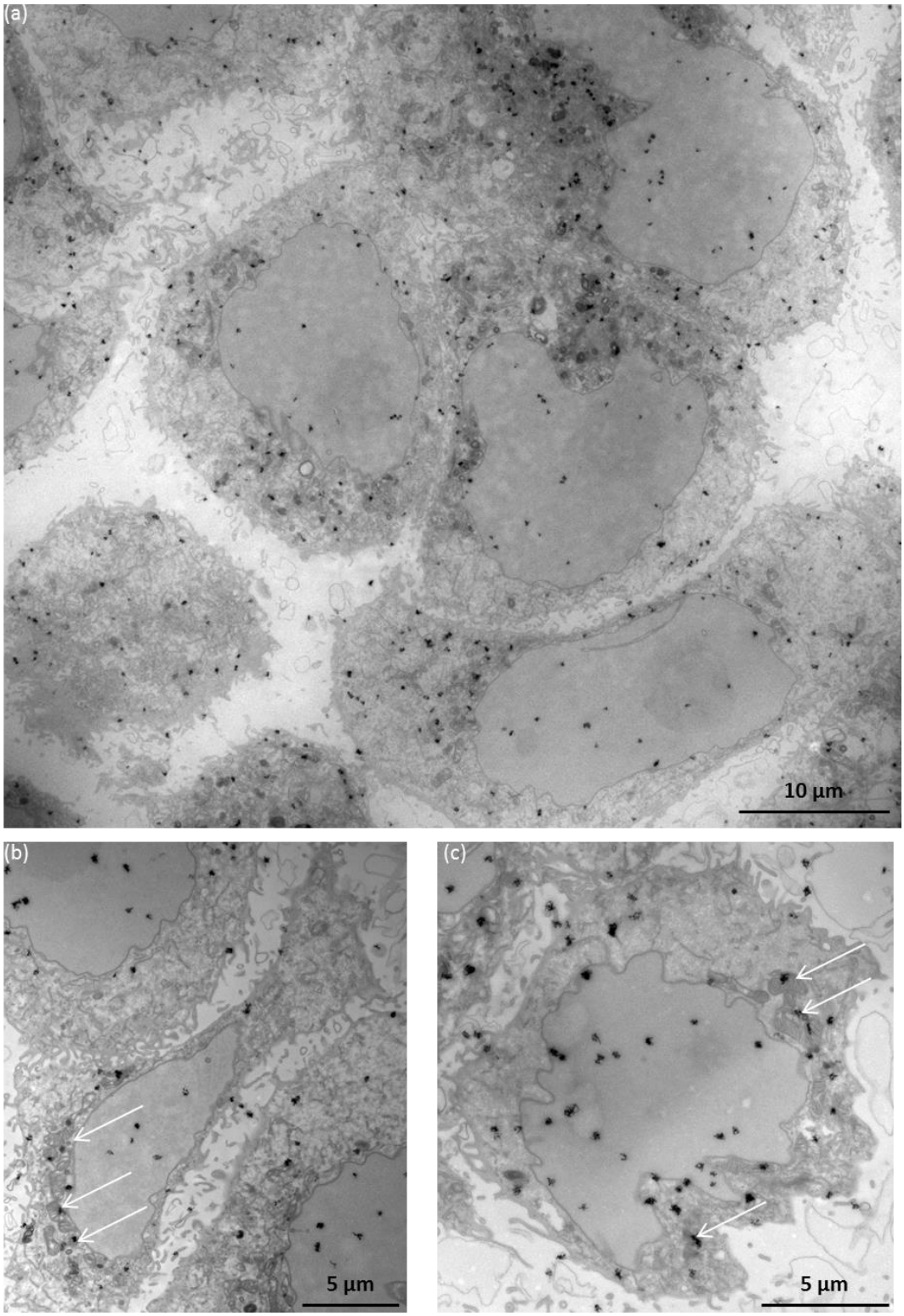

Figure 6.13: Cells incubated with ^{111}In-DTPA-hEGF for 24 hours

TEM micrographs of cells incubated with ^{111}In-DTPA-hEGF for 24 hours, (a) cells showing variation in the number of grains associated with different cells, with high levels of MAR grains in the cell nucleus, and the cell cytoplasm, with a few grains associated with cellular debris outside the main cells or in the polymer resin support. (b) & (c) single cells which are showing uptake in the cell nucleus and in the mitochondria as shown by arrows.

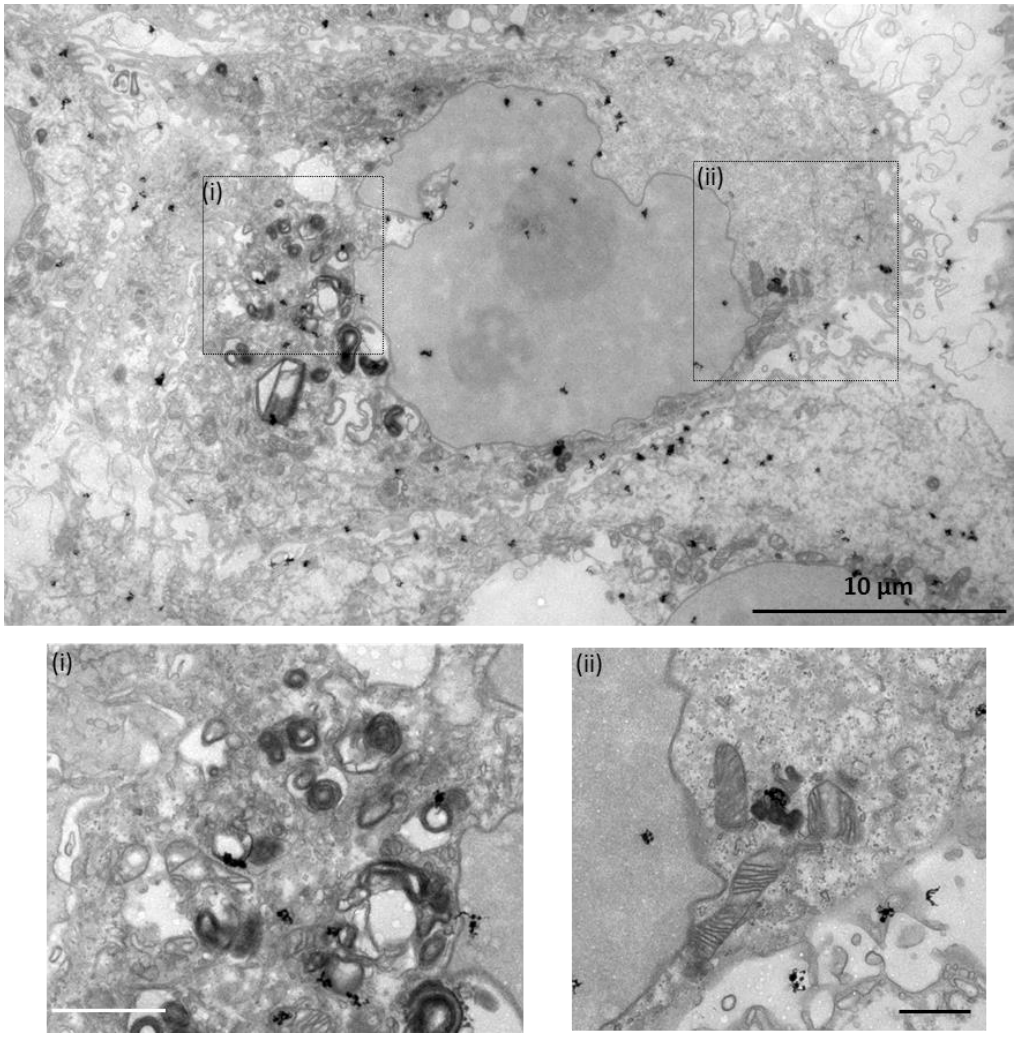

Figure 6.14: A cell showing autophagy after incubation with ^{111}In-DTPA-hEGF for 24 hours
TEM micrographs of a cell incubated with ^{111}In-DTPA-hEGF for 24 hours. There are MAR grains associated with the cell nucleus (including nucleoli) and the cell cytoplasm (including mitochondria). There are (i) autophagosomes present (as demonstrated by a double membrane, and semi-circular shape) and (ii) grains in the filopodia. Scale bar in inserts 2 µm.

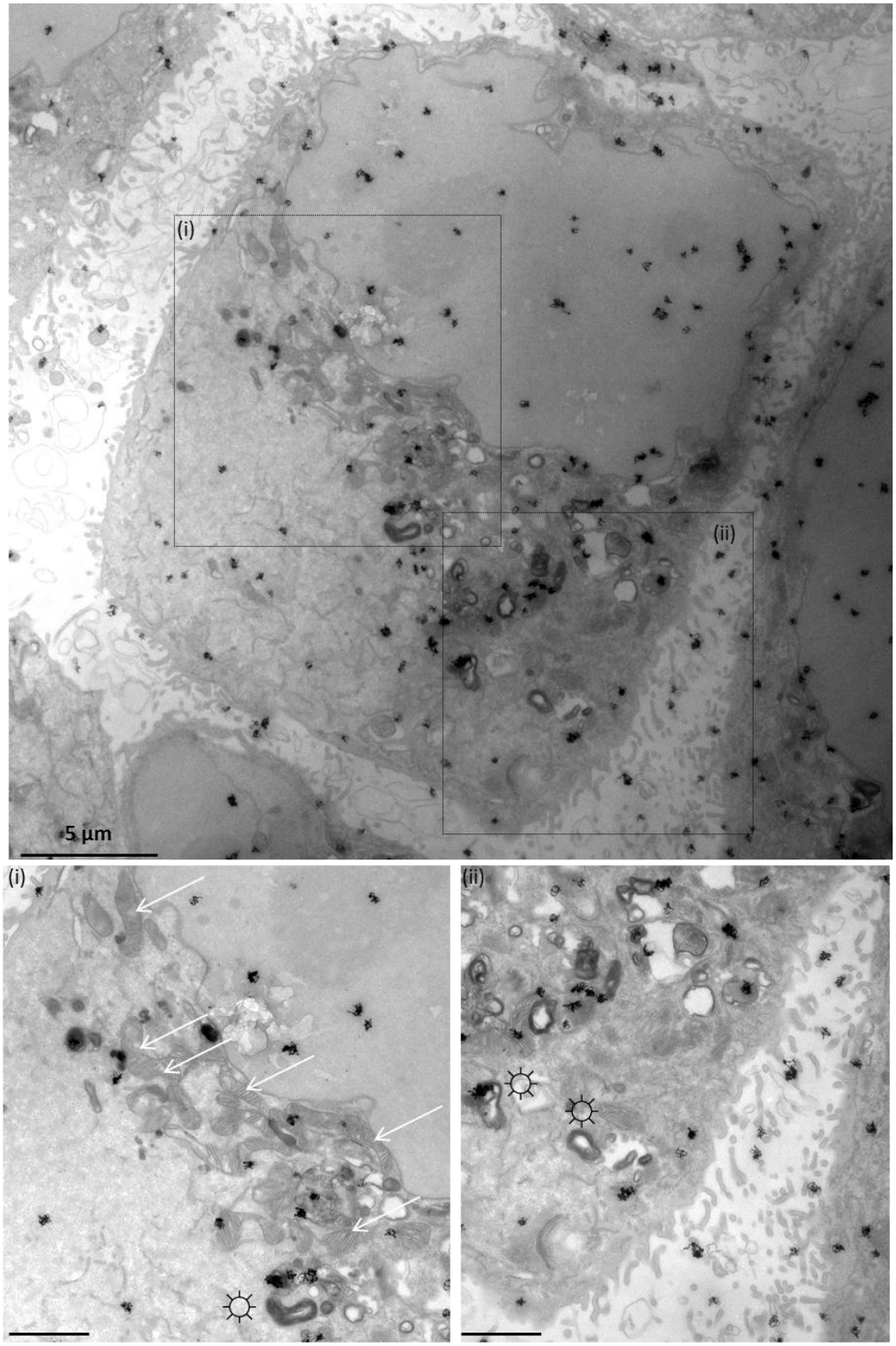

Figure 6.15: A cell showing silver grains associated with it and features of autophagy after incubation with ^{111}In-DTPA-hEGF for 24 hours

Grains are associated with compartments throughout the cell, including the nucleoli, nucleus, cytoplasm and mitochondria. (i) shows grains associated with mitochondria as shown by arrows (not all labelled) and both (i) and (ii) show autophagosomes as demonstrated by a double membrane, and semi-circular shape as shown by ☼ (not all labelled). Scale bar in inserts 2 µm.

Analysis of Time Course Data

To analyse the information, the grain density per unit area was calculated. To obtain the area of the cells, the total cell area and the cell nucleus were measured. For the cell nucleus, the boundary was drawn around the nucleus membrane. For the total cell area, the boundary was drawn around the outside of the cell, including any filopodia which were extending from the cell, but excluding any that were not attached. Inclusion and exclusion criteria were set as follows: grains were counted as in the nucleus if they were on the nuclei membrane and in the cytoplasm if they were on the cell membrane or associated with filopodia even if the filopodia were not associated with the cell. If grains were between two cells, the closest cell was considered to contain them. For example, the cell in Figure 6.10 contained nine in the cell nucleus and 22 in the cytoplasm.

Figure 6.16 shows the grains per micrometre squared for cells under different treatment conditions; untreated cells, cells incubated with $^{111}InCl_3$ for 15 minutes and 24 hours and cells incubated with ^{111}In-DTPA-hEGF for 15 minutes and 24 hours. Mann-Whitney U-tests showed that when comparing untreated samples with everything there was a significant difference (*** $P \leq 0.001$) between the blank samples and all other samples. This was across all cell compartments (cytoplasm, nucleus and whole cell), except $^{111}InCl_3$ at 24 hours, where there was no significance for the cytoplasm, nucleus or the whole cell.

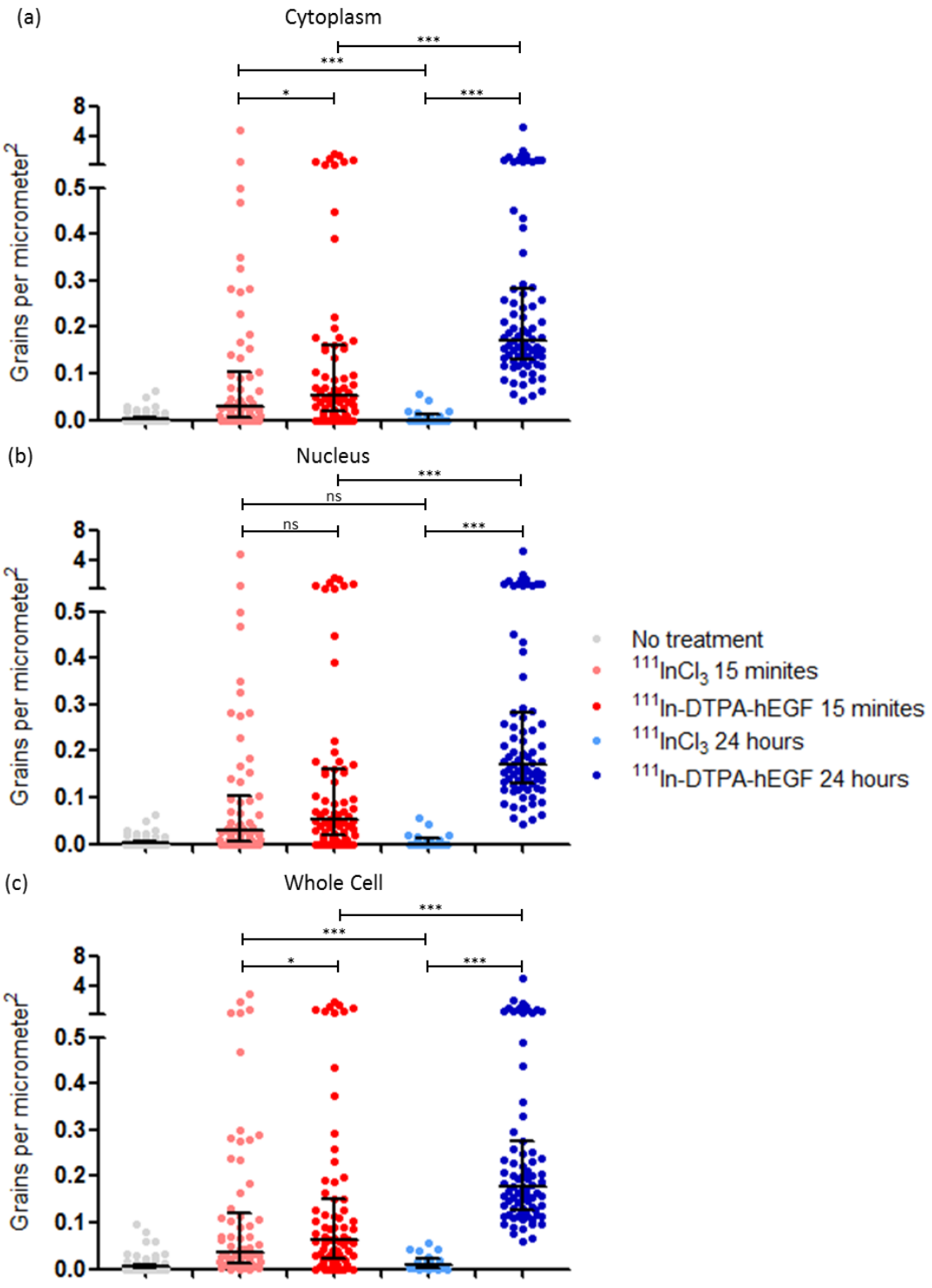

Figure 6.16: Analysis of transmission electron microscope time course data
Quantitative analysis of TEM time course data showing the number of grains per micrometre squared for (a) the cytoplasm, (b) the nucleus and (c) the whole cell. Significance from Mann-Whitney U-test: * $P \leq 0.05$; *** $P \leq 0.001$; ns no significance. Error bars represent mean and interquartile range.

Table 6.6.5: A summary of Mann-Whitney U-test values comparing the cell compartments

Significance from Mann-Whitney U-test; ns no significance;** P ≤ 0.01; *** P ≤ 0.001

Sample	Cytoplasm vs Nucleus
Untreated	***
$^{111}InCl_3$: 15 minutes	ns
^{111}In-DTPA-hEGF: 15 minutes	ns
$^{111}InCl_3$: 24 hours	**
^{111}In-DTPA-hEGF: 24 hours	ns

Table 6.6.6: The area of cells

Sample	No. of cells	Area of Cytoplasm (μm^2)	Area of Nucleus (μm^2)	Total Area (μm^2)
Untreated	67	282±172	98±68	395±204
$^{111}InCl_3$: 15 minutes	66	225±329	70±68	395±372
^{111}In-DTPA-hEGF: 15 minutes	69	296±260	83±90	296±260
$^{111}InCl_3$: 24 hours	17	395±204	148±100	379±247
^{111}In-DTPA-hEGF: 24 hours	79	232±134	103±76	336±201

Table 6.6 shows the area of cells which were scanned. When comparing the areas of the different cells sections that were analysed, there was no significant difference in the area of the cytoplasms by a one-way ANOVA test. For different cell nuclei there were significant differences (* $P \leq 0.05$) between the area of the $^{111}InCl_3$ nuclei at 24 hours and the rest of the samples when carrying out an unpaired t-test. When a one-way ANOVA test was carried out for the whole area of the cell section, there was no significant difference.

Further analysis was carried out on cells incubated with ^{111}In-DTPA-hEGF. The cells were divided into five compartments: cell nucleus, nuclear membrane, cytoplasm, filopodia and cell membrane and mitochondria. The area of these compartments was not calculated. For example, the cell in Figure 6.10 contained seven grains in the cell

nucleus, two on the nuclear membrane, 14 in the cytoplasm, eight in the filopodia and cell membrane and zero in the mitochondria. The compartment that a grain was selected to be in was the compartment which had more than 50 % of the MAR grain within that compartment, grains were determined to be on the cell membrane if a portion of them was located outside the cell.

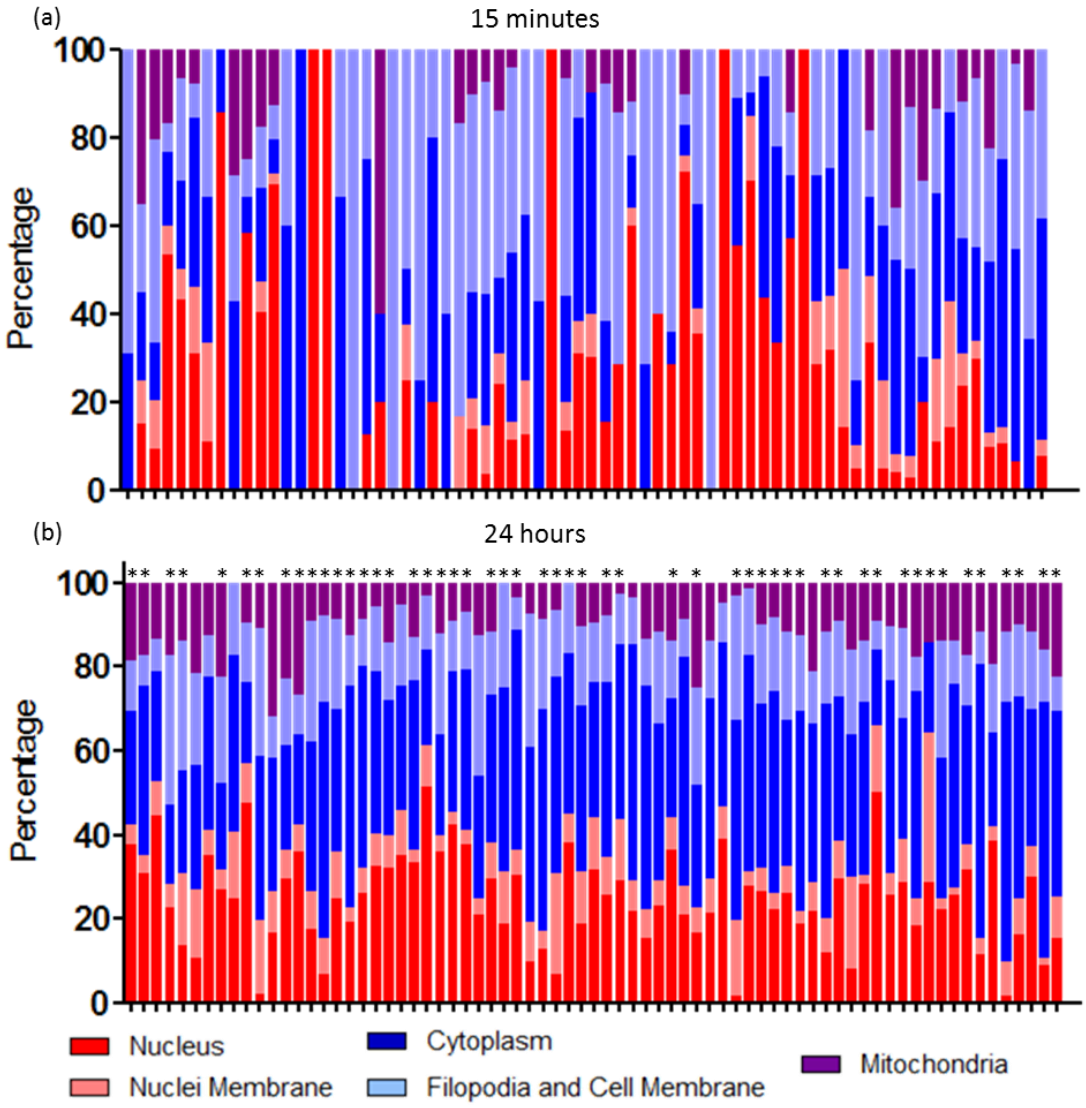

Figure 6.17: An analysis of grains in five individual cell compartments

The number of grains in individual cell compartments, the cell nucleus, nuclei membrane, cytoplasm, the filopodia and cell membrane and in the mitochondria were counted and the percentage of the grains in these compartments was plotted for SQ20B cells incubated with ^{111}In-DTPA-hEGF for (a) 15 minutes and (b) 24 hours. Not shown are the five cells after 15 minutes incubated which contained zero grains. (*) at the top indicates autophagy occurring in cells, as determines by one or more autophagosomes being present.

Figure 6.17 shows the percentage of grains which were in each cell compartment for individual cells at (a) 15 minutes and (b) 24 hours incubation, to demonstrate the variation between cells. Figure 6.18 shows a summary of this data.

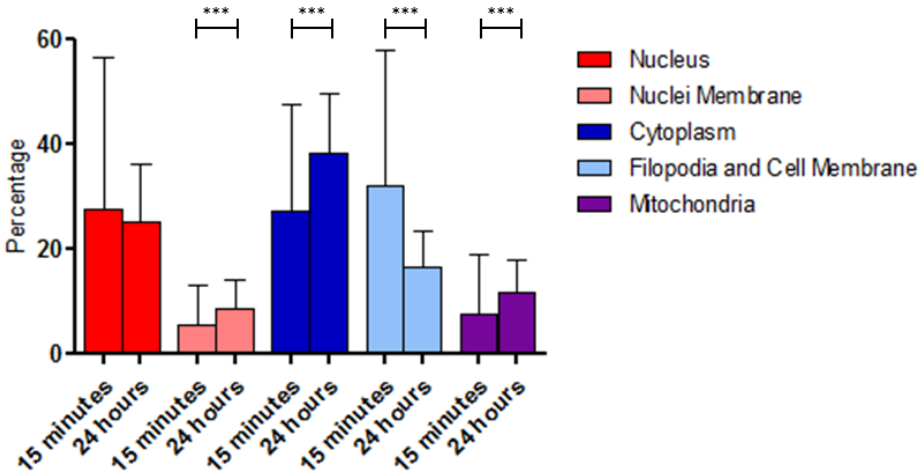

Figure 6.18: A summary of the number of silver grains in different cell compartments
A summary of the number of MAR grains in different cell compartments after 15 minutes and 24 hours incubation with ^{111}In-DTPA-hEGF. Significance from Mann-Whitney U-test is shown: ** $P \leq 0.01$ *** $P \leq 0.001$; ns no significance. Bars represent mean plus standard deviation.

6.3 Discussion

6.3.1 Microautoradiography using the Optical Microscope

MAR using an optical microscopy was carried out with whole cell samples. This means that the indium-111 atoms which are located within the cell can be shielded from interactions with the emulsion, firstly, by the cytoplasm as the short range AE cannot reach the emulsion and secondly by other indium-111 sources. This happens as the grains are a binary detection system; they have either been converted to silver or not. This means that sources which are further away are shielded by emissions that are closer and that have already converted the silver bromide to sliver.

In Figure 6.2b (ii) at 24 hours where there is more internalised radioactivity (Figure 3.3), the technique is unable to distinguish between the radioactivity which is surface bound and that which is internalised. Between the 1 hour and 24 hour incubation it is difficult to distinguish if there are more grains present at 24 hours due to the differences in background. Therefore, while MAR using the optical microscope is able to distinguish if there is radioactivity present in the cells or not, it is difficult to distinguish if there are different levels of radioactivity at different time points without densitometry measurements of controls and treated samples.

Experiments have been carried out using optical MAR on single cell sections (Puncher and Blower, 1994). Frozen sections of leukocytes from homogenized rat liver were mixed with indium-111 which was labelled to oxine. Using an ultramicrotome, 6 µm-thick sections were cut. Using MAR, it was possible to distinguish between grains in the cell nucleus and cell cytoplasm, as there was a high nuclear-to-cytoplasmic grain density ratio (2.23 ±1.07 for granulocytes and 2.24 ±0.67 for mononuclear cells) with

significantly greater radioactive concentration inside nuclei than outside (60 %) after a first triton wash (Puncher and Blower, 1994).

Sectioning cells will allow for more information to be obtained using optical MAR. However, as the grains cover the cell structure, the differences in uptake between the cell cytoplasm and cell nucleus is only noticeable when there is a large difference in the distribution of the radioisotope. When obtaining high resolution images it would still only be possible to distinguish between the cell cytoplasm and the cell nucleus.

6.3.2 Development of the Electron Microscope-Microautoradiography Technique

The oven preparation technique with *en-bloc* staining produced high quality TEM images with good contrast. A carbon layer was applied to cell sections on the TEM grid and the emulsion was applied with a wire loop. The exposure time was 10 days and the development time was 60 seconds.

6.3.3 Resolution of the Electron Microscope-Microautoradiography Technique

Although the micrographs clearly show grains associated with cellular compartments, the resolution can be affected by the biological preparation and the MAR technique. Firstly, the resolution is limited to approximately 2 nm due to artefacts introduced into the sample during preparation of the cells for TEM, such as fixation, dehydration, staining and embedding (Hayat, 2000). For example, chemical fixation using a cross-linking fixer can cause aggregation of protein, collapse of highly hydrated glycans and loss of lipids (Łukasz Mielańczyk et al., 2015). Heavy metals, precipitated from stains, can cause additional artefacts in the form of precipitates (Dubochet and Sartori Blanc, 2001, Massover, 2011). As well as this, processing for TEM could affect the cellular location of the ^{111}In-DTPA-hEGF. To confirm that this is not the case, subcellular

fractionation studies should be carried out to confirm that the radioactivity is located in the same cell compartments as shown by EM-TEM.

Secondly, the resolution of MAR depends on the distance the AE has transversed to intersect with a silver bromide grain, and the size of the developed grains. The distance an electron will have travelled is dependent on the thickness of the MAR emulsion layer and the thickness of the sections. As the grains of the MAR emulsion get larger during development, the location of the indium-111 atom, which led to the formation of the grain, becomes harder to define. This is because, during development, more silver is added to the silver sensitivity speck which produces a ribbon of silver growing out from the speck. However, the ribbon of silver halide does not grow uniformly in all directions and so the centre of the ribbon does not correspond to the location of the sensitivity speck which was activated by the radioactive emissions.

It appears that under the EM-MAR conditions used in the experiments reported here, that one source of indium-111 leads to the development of one grain or fewer, directly above the location of the radioactivity in the cell section. This assumption is made because of the following: firstly, due to the short path length of the AE which are emitted, the radius will be less than the size of an individual grain and so the AE will only develop one grain. Secondly, due to the distribution of the grains as seen in the micrographs of the time course (Figures 6.9–6.15), with micrographs at 15 minutes and 24 hours showing isolated grains. An even layer of emulsion has been demonstrated (Figure 6.5). If each source of indium-111 was producing more than one grain it would be expected to see grains present in a circle around the point source, rather than individual grains, as all the grains close enough are developed. Janson et al. under similar MAR conditions describe each grain as being caused by a single ^{111}In-

radionuclide, but they do not attempt to define the diameter from which the electron could originate (Janson et al., 2000). In further discussion, for simplicity, it is assumed that the grains are located directly above the location of the ^{111}In-DTPA-hEGF in the resin.

6.3.4 Time Course

After the optimum TEM preparation protocol and MAR processing was defined, a time course experiment was carried out. The aim of this experiment was to investigate whether the technique can be used to provide information about the increase in radioactivity present and the differences in uptake of between 15 minutes and 24 hours.

Figure 6.9 provides an overview of the differences between $^{111}InCl_3$ and ^{111}In-DTPA-hEGF at 1 hour and 24 hours. No grains are present in the cell sections incubated with $^{111}InCl_3$ and there are more grains in cells incubated for 24 hours with ^{111}In-DTPA-hEGF compared to those exposed to ^{111}In-DTPA-hEGF for 15 minutes. The presence of grains at 15 minutes shows that the EM-MAR is able to detect extremely low levels of radioactivity, as a section is only a small slice of a cell. For example, if a cell is assumed to have shrunk by approximately 20 % (Lee et al., 1982) and originally had a volume of approximately 4,200 μm^3 (diameter of SQ20B cell 20 µm data not shown), then after processing for TEM, the depth would be approximately 8 µm. Therefore, nearly 90 sections with a thickness of 90 nm would be required to cut through the whole sample and as such the radioactivity activity detected at 15 minutes in a single cell slice is approximately 2 mBq. This is assuming from internalisation studies (Figure 3.3) that there is the same amount of radioactivity (180 mBq per cell) at 15 minutes incubation compared to as 1 hour's incubation. The detection of radioactivity in the cell nucleus is not surprising after a short incubation and has been seen previously (Lin et al., 2001).

The micrographs of cells at 24 hours (Figures 6.13–6.15) allow the assumption to be made that the saturation of the MAR grains has not occurred. Figure 6.5b shows that there is an even layer of MAR grains. If saturation of the MAR grains had occurred then, it is expected that a similar result to Figure 6.5b would be seen, with grains covering the whole cell section. However, while the MAR technique as a whole is not saturated, it is possible that in regions where there is a higher concentration of indium-111, the MAR grains have been saturated. This is seen after 24 hours' incubation, where there are grains which are close together (Figures 6.13c, 6.15), which may suggest we are reaching the maximum limit of detectability under these conditions. By altering the conditions, such as reducing the exposure time, the detection range of MAR can be altered.

Figure 6.16 provides information about what is seen in the cell micrographs. The grains per micrometre squared increases for 24 hours compared to 15 minutes and significantly fewer grains are present in $^{111}InCl_3$ samples and untreated samples. This is expected from the internalisation data shown in Figure 3.3. The data does not fit a Gaussian distribution and there are some cell sections with a much larger density of grains compared to the average. This is expected from the FACs analysis seen in Figure 3.2

The area of cell sections was determined to be similar, except cell nuclei in the 24 hour $^{111}InCl_3$ samples. This is likely due to sectioning through a different part of the cell. If the average of the other cell areas is used instead, which is smaller, the mean grain per micrometre squared changes from 0.02 to 0.03, which is still small compared to treated samples. So while analysis only compares cell sections, these are of a similar size and so they are likely to contain a similar subcellular structure. It is important to note that

the TEM images of cells show only a single thin section through a cell and that radioactivity is likely to be heterogeneously distributed in the cell. Therefore, counting the grains associated with a single section may not represent the level of radioactivity in the whole cell. However, by counting grains associated with a large number of cells, this source of uncertainty should be reduced.

The Mann-Whitney U-tests were carried out on data as the number of grains per micrometre squared does not conform to a Gaussian distribution. Figure 6.16 shows varying levels of significance. None of these values is surprising, except that there is no difference $^{111}InCl_3$ at 15 minutes and ^{111}In-DPTA-hEGF at 15 minutes. This may be due to a higher number of grains present in the $^{111}InCl_3$ or that after such a short time period, transport into the cell by receptor binding is not significant and this only becomes a factor after longer periods. However, the results in Figure 6.18, which show similar internal distribution of grains after different incubations of ^{111}In-DTPA-hEGF for different time periods, suggest that it is likely not this reason. Table 6.5 shows that there is not a significant difference in the grains per unit area between the cytoplasm and nucleus, so while there are grains in the nucleus, there is the same relative proportion of grains compared to the area of the nucleus.

Figure 6.17 shows the distribution of the grains in cells treated with ^{111}In-DTPA-hEGF. This information is limited because it does not take into account the variation in the number of grains between samples and does not account for the size of the compartments. It does, however, show that there is a variation in uptake between cell sections. This variation appears to be greater at 15 minutes with only 45 % and 46 % of cell sections having grains in the cell nucleus or in mitochondria respectively, whereas at 24 hours, all cells have grains in the cell nucleus and most (95 %) of the cells contain

some grains in the mitochondria. The level of damage across the cell population is also demonstrated with 70 % of cells having autophagy occurring at 24 hours compared to zero at 15 minutes. There appears to be some association with mitochondria as approximately 15 % of the grains after 24 hours were associated with the mitochondria. EGF/EGFR are known to be carried in vesicles to the mitochondria (Wang and Hung, 2012), which is a radiation-sensitive target (Murphy et al., 2005).

Figure 6.17 shows that when comparing between samples the distribution of grains varies between 15 minutes and 24 hours. There is also a greater number of grains present after 24 hours. Since the cell size was determined to be similar (Table 6.5), it is expected that the cell compartments will have a similar distribution between the cells and different samples. The lack of a significant difference between the number of grains associated with the cell nucleus at 15 minutes and 24 hours suggests that the mechanism of the internalisation of ^{111}In-DTPA-hEGF is extremely fast and can occur after 15 minutes. This is in agreement with Lin et al. who, after targeting EGFR, detected nuclear radioactivity in the cell nucleus within 5 minutes at 37° (Lin et al., 2001).

The internalisation studies (Figure 3.3) show that at 1 hour there is a similar amount of radioactivity attached to the cell membrane as there is in the rest of the cell. Figure 6.18 does agree with these data as less than 50 % of grains are in the cell membrane and fillopodia. It would be expected results from an internalisation study at 15 minutes would expect to show more membrane-bound radioactivity. However, this may not be seen because the technique is only looking at single cell sections which are cut close to the cell centre and contain a relatively small percentage of the cell membrane.

Figure 6.18 shows that there is large amount of variation in these samples, with more variation at 15 minutes. This suggests that in a single cell population, variation in uptake can be reduced with an increase in incubation times.

While it has been assumed that one source of indium leads to the development of one grain, an approximate calculation determined the number of electrons which leads to the development of each grain. Assuming that the average number of grains per cell section at 15 minutes is 19 grains which corresponds to approximately 2 mBq, this is approximately 300 days (after 10 days exposure, when the exposure has started after 1 half-life), this leads to a developed grain representing 15 decays, although this is an overestimate the 2 mBq is based on 1 hour incubation period. The same calculation can be done for 24 hours incubation with the activity per slide being 4.5 mBq, (605 decays) the average number of grains per slide being 64, leading to each grain representing approximately 10 decays. While these figures are approximate, as it is likely that the cell section was through the centre of the cell (due to the techniques used to get cell sections) and therefore will have more than the average radioactivity per slide, the two number being in close agreement suggests the technique can be consider accurate, although it can no longer be assumed that one source of indium leads to the development of one grain.

6.4 Conclusions

The EM-MAR technique developed is able to show the variation in the subcellular distribution of ^{111}In-DTPA-hEGF. EM-MAR images provided confirmation that ^{111}In-DTPA-hEGF translocates in part to the cell nucleus. It provided evidence that, as well as uptake into the cell nucleus, the mitochondria are also targeted and harbour indium-111 following exposure of cells to ^{111}In-DTPA-hEGF. That uptake of ^{111}In-DTPA-hEGF into mitochondria has not been observed previously is likely because subcellular biodistribution experiments have relied on fractionation in which the mitochondrial fraction has not been isolated. This is also the first time that cells incubated with ^{111}In-DTPA-hEGF have been shown to exhibit some of the features of autophagy, suggesting a cell death mechanism that has not previously been seen with any radiopharmaceutical, although it is presumed other cell death mechanisms such as apoptosis and mitotic catastrophe will also play a significant role, they have not been fully explored in this work. The mode of cell death will depend on the cell type as well as the radiopharmaceutical. However, this technique has not been fully quantified and only looks at small sections of the cell. The EM-MAR technique can provide more information about the location of the radioactivity at the cellular level compared to other techniques.

These results could be confirmed by carrying out further internalisation studies which look at subcellular fractions. If these experiments were carried out alongside studies which determine the purity of these fractions, they would further validate EM-MAR as a technique that determines the subcellular location of radioactivity within single cells. Further work will look at confirming the results which have been shown, to consist of repeats of the time course, experiments using a different target and quantification and resolution experiments.

Chapter 7:
Discussion

Chapter 7:

Discussion

7.1 Summary of Results

The current techniques which are available to determine the spatial distribution of Auger electrons (AE) emitters used in (TRT) are not able to provide quantitative information about the spatial distribution of AE at a resolution similar to their range in biological material.

The aim of the research presented in this thesis was to develop novel techniques which provide a high spatial resolution, of the order of nanometres, to determine the location of radioactive atoms within cells. The selection of these techniques was motivated by the need for quantitative data that could be used as the basis for nano- to micrometre scale dosimetry. They would aim to show the variation in uptake at the cellular and subcellular level and provide information for small-scale dosimetry.

Firstly, the photoresist autoradiography (PAR) technique using poly (methyl methacrylate) (PMMA) was shown to be a quantitative technique, with the spatial resolution in the lateral (10–20 nm) and vertical (1–3 nm) dimensions determined by the microsphere model. Analysis of the surface established that altering the processing conditions did not affect the images obtained, demonstrating the robustness of the detection system. Modelling provides information about the fluence which was required to produce these individual patterns. The rate-limiting aspect of this methodology is the time required for atomic force microscope (AFM) image analysis. This limits the amount of samples and hence individual cells which can be analysed.

Secondly, a technique which has been used to a very limited extent in the detection of radioisotopes uses electron microscope-microautoradiography (EM-MAR). This technique was refined and optimised to provide high quality transmission electron microscope (TEM) images. While this technique has previously been used for similar experiments, the quality of images in the published literature was poor, thus limiting the amount and quality of information obtained from them. The improvements to this technique were such that information about the location of ^{111}In-DTPA-human epidermal growth factor (^{111}In-DTPA-hEGF, DTPA is diethylenetriaminepentaacetic acid) in subcellular organelles was obtained as well as information about cells exhibiting some of the features of autophagy, suggesting a cell death mechanism that has not previously been seen with radiopharmaceuticals.

These two techniques do provide more information than the current techniques which are used for determining and quantifying the spatial distribution of TRT agents. However, a limitation of quantifiable small-scale dosimetry techniques is that imaging techniques which are able to provide high resolution images are slow and have a limited field of view. This means that, in order to get statistical information under a large number of conditions, experiments will be extremely time consuming. This is likely to limit the use of both the EM-MAR and the PAR technique.

7.2 Comparison of the Photoresist Autoradiography and the Electron Microscope-Microautoradiography Techniques

Both techniques provide information about the subcellular distribution of ^{111}In-DTPA-hEGF. PAR provides quantitative information about the amount of radioactivity that was internalised to obtain a pattern, but does not provide precise spatial information about the location of radioactivity within the cell. It is not always possible to distinguish whether a PAR radiation footprint is due to a single cell or multiple cells. The EM-MAR technique is able to provide the cellular location of the radioactivity. However, it is not clear how the presence, number and distribution of silver grains can be used to provide quantitative dosimetric information. Unlike PAR, the EM-MAR technique only provides two-dimensional information, whereas PAR patterns reflect the radioactivity in a whole cell. This may not necessarily be an advantage of PAR as the AE which we are trying to detect have only a short range and may be attenuated within the cell.

With the PAR technique, an 25 keV electron beam fluence as low as 1 x 10^5 $e^-/\mu m^2$ is detectable in PMMA 950 K. The sensitivity of the EM-MAR technique has not been determined. However, assuming that the cell slices shown only contain a fraction of the radioactivity, the EM-MAR technique is able to detect approximately 2 mBq or approximately 300 decays or 4 x 10^3 electrons of varying energies in a cell section. This suggests that the EM-MAR technique may be more sensitive compared with PAR. The sensitivity is inversely related to the resolution and the intrinsic resolution of PAR is much greater, as the polymer molecules which are the equivalent of the EM-MAR grains are much smaller. The detection range of these techniques is determined by the processing conditions. Suitable processing conditions for both techniques were established but further refinement could change the range of detection to allow for more information to be obtained.

Quantification of the EM-MAR technique could be achieved with $^{111}InCl_3$ in resin and this quantification may be considered to be more accurate than the monoenergetic electron beam quantification of the PAR technique, since the AE will come from the same type of radioactive source. However, the electron beam quantification for PAR is robust, as all electrons emitted by the electron beam will interact with the photoresist. PAR calibration using the electron beam could be used for other radioactive isotopes. However, if either technique has to be calibrated by direct application of a radioactive isotope, this procedure would have to be repeated for all isotopes of interest.

The variation in the uptake of ^{111}In-DPTA-hEGF is much easier to describe when using the EM-MAR technique rather than PAR, as the EM-MAR technique is able to provide visual information about the distribution, although the TEM micrographs only look at single cell sections. Therefore, as well as being used for quantifiable dosimetry (if calibration can be achieved), it can also be used to demonstrate targeting to subcellular compartments or whether biological processes such as autophagy are occurring in cells.

Since the processing of the cells for PAR is simple and can be carried out on the same day, PAR may be suitable for those radioactive isotopes that have a short half-life. It may not be possible to carry out EM-MAR on isotopes that have a short half-life due to the lengthy processing time, this may cause there to be not be enough radioactive emissions to cause a latent image, after the processing time.

In summary, while the PAR technique has shown the ability to produce more robust results, it does not currently allow assessment of accumulated radioactivity in individual cell compartments beyond the whole cell and cell nucleus. The EM-MAR technique demonstrates the variation between cell sections and provides detailed information about the spatial distribution of radioactivity.

7.3 Benefits of Novel Techniques over Current Methods

Current techniques: internalisation studies, autoradiography techniques, electron beam electron microprobe analysis (EMPA), secondary ion mass spectrometry (SIMS) and Nanoscale SIMS (NanoSIMS) have been used as methods to investigate the spatial distribution of radiopharmaceuticals. They all have limitations. Mainly, they are not quantitative or have a resolution greater than the distance AE travel in biological material. Clonogenic assays, imaging with biomarkers and internalisation studies will always play a role in the development of TRT agents. However, these do not describe the heterogeneity of uptake of the radionuclide within a population of cells, which can lead to inaccurate dose calculations. Both the PAR and EM-MAR techniques are able to account for this variation across the cell population and also within cells.

Optical microautoradiography (MAR) can be used to visualise this variation, but can only distinguish between the number of grains in the cell nucleus and in the cytoplasm and the technique is difficult to quantify (Puncher and Blower, 1995). EMPA, SIMS and NanoSIMS have been used to analyse biological samples but with much lower resolution than TEM (Guerquin-Kern et al., 2004). Therefore, the EM-MAR technique is able to image the distribution of radioisotopes at a higher resolution than these techniques. SIMS and EBMA have the ability to detect the radioactive isotope within individual cells, but the techniques have so far had limited use. Improvements in these techniques, such as NanoSIMS, could lead to their application in the future. However, expense may limit their use in small-scale dosimetry.

Chemically amplified photoresists (CARs) have previously been used for PAR (Falzone et al., 2011). Rather than using electron beam modelling of the resist, the Monte Carlo (MC) code PENELOPE was used. This allowed for more accurate simulations as

multiple energies, which are emitted from indium-111, were included. The development process when using CARs is required to be better controlled, compared to organic photoresists, as it can affect the complex chemical structure of the resists (Yasin et al., 1999). This means it could be affected by the biological material that is present when using the PAR technique, even with the indirect application method (IM). PMMA is therefore a more suitable photoresist material. Under the development conditions used by Falzone et al. for PMMA, cellular patterns were not imaged with the AFM Falzone et al., 2011). However, in this work the resolution is comparable to that previously reported for the CAR UVIII (Falzone et al., 2012).

Although ^{111}In-DTPA-hEGF was used as the exemplar radiopharmaceutical, the EM-MAR technique could be used to investigate the intracellular distribution of other radiopharmaceuticals. It could be used to determine whether a radiopharmaceutical is reaching its intended intracellular target or, conversely, whether there is unexpected concentration in off-target sites. This level of information can inform microdosimetric studies and may also provide information about why a radiopharmaceutical is ineffective when tested in animal models or in clinical trials.

However, these techniques may not be required if radiolabelled gold (or other metal) nanoparticles are used for therapy, as their exact location can be known within the cell by conventional TEM (Chithrani et al., 2006, Shukla et al., 2005). Another technique which would use the resolution of the TEM and gold is immunogold labelling. This is similar to fluorophore labelling for confocal microscopy, but instead of using a fluorophore, gold-conjugated streptavidin is used. However, these methods are not a direct detection of the radioisotope and so if the radioisotope is detached from the carrier molecule then the location of the radioactivity would not be accurately known.

7.4 Further Developments of the Techniques

The techniques described are still in development. PAR using cell sections could improve the resolution by reducing attenuation in the cell and a way of relating the location of the radioactivity to an individual cell could be developed. For example, the cells could be grown in individual cell compartments which can then be related to a position on the photoresist surface. A way of automating the scanning of the photoresists would need to be developed to facilitate collecting the data, if this technique were to be used on large data sets.

To further explore the EM-MAR technique, the resolution in the lateral plane as well as the z-direction would have to be determined. It would need to be confirmed that the emissions from indium-111 lead to the development of number of silver grains calculated. To provide dosimetric information, this technique must be quantified and the minimum and maximum limits of detection would also have to be determined. These quantification experiments could be carried out using $^{111}InCl_3$ in resin and sectioning the resin to different thicknesses to determine the resolution.

These techniques could also be adapted for use with tissue samples from animal models or human patients. This would allow for more information to be gained from tumour models. Multiple cell models could be used to validate the use of single cell systems to evaluate (novel) radiopharmaceuticals; for example, to confirm whether the location of radionuclides within the cells are similar between single cell and multicellular models. This would validate single cell experiments and microdosimetry as a technique which can predict information about the effects of TRT agents before animal studies or clinical trials.

7.5 Conclusions

PAR is a novel technique for AE dosimetry. It is quantitative and has a high lateral spatial resolution. It is able to show the distribution of the AE emitted from radionuclide sources distributed within a cell or a cell nucleus. The EM-MAR technique is able to show the distribution of the AE emitted from radionuclide sources distributed within a cell section. The technique provides new information about the subcellular location of ^{111}In-DTPA-hEGF, which was previously not known to be in the cell mitochondria. Both techniques are able to provide information about the subcellular radioactivity at a higher resolution than current techniques are able to provide.

Primarily, these techniques have been developed for acquiring information for microdosimetric calculations. The quality of microdosimetric calculations is limited by the biological information which is used to inform the calculations. Therefore, these techniques, which have led to improved biological distribution information, will enable more accurate microdosimetric calculations to be made.

References

ADELSTEIN, S. J. 1993. Merrill C. Sosman Lecture. The Auger process: a therapeutic promise? *American Journal of Roentgenol,* 160, 707-13.

AGHEVLIAN, S., BOYLE, A. J. & REILLY, R. M. In Press. Radioimmunotherapy of cancer with high linear energy transfer (LET) radiation delivered by radionuclides emitting α-particles or Auger electrons. *Advanced Drug Delivery Reviews*. Available online 17 December 2015

AHNESJÖ, A. & ASPRADAKIS, M. M. 1999. Dose calculations for external photon beams in radiotherapy. *Physics in Medicine and Biology,* 44, R99-155.

ALBERTS, B. 2002. *Molecular biology of the cell.* New York: Garland Science.

ALPER, T. 1963. Effects on irradiated micro-organisms of growth in the presense of acriflavine *Nature,* 200, 534-6.

ANTONELLI, F., BELLI, M., CUTTONE, G., DINI, V., ESPOSITO, G., SIMONE, G., SORRENTINO, E. & TABOCCHINI, M. A. 2005. Induction and repair of DNA double-strand breaks in human cells: dephosphorylation of histone H2AX and its inhibition by calyculin A. *Radiation Research,* 164, 514-7.

AUDINOT, J., SCHNEIDER, S., YEGLES, M., HALLEGOT, P., WENNIG, R. & MIGEON, H. 2004. Imaging of arsenic traces in human hair by nano-SIMS 50. *Applied Surface Science,* 231, 490-496.

BAILEY, K. E., COSTANTINI, D. L., CAI, Z., SCOLLARD, D. A., CHEN, Z., REILLY, R. M. & VALLIS, K. A. 2007. Epidermal growth factor receptor inhibition modulates the nuclear localization and cytotoxicity of the Auger electron emitting radiopharmaceutical 111In-DTPA human epidermal growth factor. *Journal of Nuclear Medicine,* 48, 1562-70.

BAL, H., GUERIN, L., CASEY, M. E., CONTI, M., ERIKSSON, L., MICHEL, C., FANTI, S., PETTINATO, C., ADLER, S. & CHOYKE, P. 2014. Improving PET spatial resolution and detectability for prostate cancer imaging. *Physics in Medicine and Biology,* 59, 4411-26.

BANÁTH, J. P., MACPHAIL, S. H. & OLIVE, P. L. 2004. Radiation sensitivity, H2AX phosphorylation, and kinetics of repair of DNA strand breaks in irradiated cervical cancer cell lines. *Cancer Research,* 64, 7144-9.

BARD, J. B. & ABBOTT, A. S. 1979. Matrices containing glycosaminoglycans in the developing anterior chambers of chick and Xenopus embryonic eyes. *Developmental Biology,* 68, 472-86.

BEHR, T. M., BÉHÉ, M., LÖHR, M., SGOUROS, G., ANGERSTEIN, C., WEHRMANN, E., NEBENDAHL, K. & BECKER, W. 2000. Therapeutic advantages of Auger electron-over beta-emitting radiometals or radioiodine when conjugated to internalizing antibodies. *European Journal of Nuclear Medicine,* 27, 753-65.

BERMUDEZ, V. 1999. Low-energy electron-beam effects on poly(methyl methacrylate) resist films. *Journal of Vacuum Science & Technology B,* 17, 2512-2518.

BERRY, J. P., ESCAIG, F., POUPON, M. F. & GALLE, P. 1983. Localization of gallium in tumor cells. Electron microscopy, electron probe microanalysis and analytical ion microscopy. *International Journal of Nuclear Medicine and Biology,* 10, 199-204.

BISHAYEE, A., RAO, D. V. & HOWELL, R. W. 2000. Radiation protection by cysteamine against the lethal effects of intracellularly localized Auger electron, alpha- and beta-particle emitting radionuclides. *Acta Oncologica,* 39, 713-20.

BLOOMER, W. D. & ADELSTEIN, S. J. 1977. 5-125I-iododeoxyuridine as prototype for radionuclide therapy with Auger emitters. *Nature,* 265, 620-1.

BODEI, L., KASSIS, A. I., ADELSTEIN, S. J. & MARIANI, G. 2003. Radionuclide therapy with iodine-125 and other auger-electron-emitting radionuclides: experimental models and clinical applications. *Cancer Biotherapy and Radiopharmaceuticals,* 18, 861-77.

BOLCH, W. 2008. Further explorations of cellular uptake of radioactivity. *Journal of Nuclear Medicine,* 49, 869-870.
BOLCH, W. E., BOUCHET, L. G., ROBERTSON, J. S., WESSELS, B. W., SIEGEL, J. A., HOWELL, R. W., ERDI, A. K., AYDOGAN, B., COSTES, S., WATSON, E. E., BRILL, A. B., CHARKES, N. D., FISHER, D. R., HAYS, M. T. & THOMAS, S. R. 1999. MIRD pamphlet No. 17: the dosimetry of nonuniform activity distributions--radionuclide S values at the voxel level. Medical Internal Radiation Dose Committee. *Journal of Nuclear Medicine,* 40, 11S-36S.
BOLCH, W. E., ECKERMAN, K. F., SGOUROS, G. & THOMAS, S. R. 2009. MIRD pamphlet No. 21: a generalized schema for radiopharmaceutical dosimetry--standardization of nomenclature. *Journal of Nuclear Medicine,* 50, 477-84.
BOSCH, F. & ROSICH, L. 2008. The contributions of Paul Ehrlich to pharmacology: a tribute on the occasion of the centenary of his Nobel Prize. *Pharmacology,* 82, 171-9.
BOUSIS, C., EMFIETZOGLOU, D., HADJIDOUKAS, P. & NIKJOO, H. 2010. Monte Carlo single-cell dosimetry of Auger-electron emitting radionuclides. *Physics in Medicine and Biology,* 55, 2555-72.
BOYD, M., ROSS, S. C., DORRENS, J., FULLERTON, N. E., TAN, K. W., ZALUTSKY, M. R. & MAIRS, R. J. 2006. Radiation-induced biologic bystander effect elicited in vitro by targeted radiopharmaceuticals labeled with alpha-, beta-, and auger electron-emitting radionuclides. *Journal of Nuclear Medicine,* 47, 1007-15.
BRADLEY, E. W., CHAN, P. C. & ADELSTEIN, S. J. 1975. The radiotoxicity of iodine-125 in mammalian cells. I. Effects on the survival curve of radioiodine incorporated into DNA. *Radiation Research,* 64, 555-63.
BUCHEGGER, F., PERILLO-ADAMER, F., DUPERTUIS, Y. M. & DELALOYE, A. B. 2006. Auger radiation targeted into DNA: a therapy perspective. *European Journal of Nuclear Medicine and Molecular Imaging,* 33, 1352-63.
BURNS, M. S. 1988. Biological microanalysis by secondary ion mass spectrometry: status and prospects. *Ultramicroscopy,* 24, 269-81.
BURNS, M. S., FILE, D. M., DELINE, V. & GALLE, P. 1986. Matrix effects in secondary ion mass spectrometric analysis of biological tissue. *Scanninf Electron Microscopy*, 1277-90.
CAI, Z., CHEN, Z., BAILEY, K. E., SCOLLARD, D. A., REILLY, R. M. & VALLIS, K. A. 2008. Relationship between induction of phosphorylated H2AX and survival in breast cancer cells exposed to 111In-DTPA-hEGF. *Journal of Nuclear Medicine,* 49, 1353-61.
CAI, Z., PIGNOL, J. P., CHAN, C. & REILLY, R. M. 2010. Cellular dosimetry of (111)In using monte carlo N-particle computer code: comparison with analytic methods and correlation with in vitro cytotoxicity. *Journal of Nuclear Medicine,* 51, 462-70.
CALABRI, L., PUGNO, N., MENOZZI, C. & VALERI, S. 2008. AFM nanoindentation: tip shape and tip radius of curvature effect on the hardness measurement. *Journal of Physics: Condensed Matter,* 20, 474208.
CAPELLO, A., KRENNING, E. P., BREEMAN, W. A., BERNARD, B. F. & DE JONG, M. 2003. Peptide receptor radionuclide therapy in vitro using [111In-DTPA0]octreotide *Journal of Nuclear Medicine*, 44, 98-104.
CARPENTER, G. & COHEN, S. 1976. Human epidermal growth factor and the proliferation of human fibroblasts. *Journal of Cellular Physiology,* 88, 227-37.
CARPENTER, G., LEMBACH, K. J., MORRISON, M. M. & COHEN, S. 1975. Characterization of the binding of 125-I-labeled epidermal growth factor to human fibroblasts. *Journal of Biological Chemistry,* 250, 4297-304.
CHAN, P. C., LISCO, E., LISCO, H. & ADELSTEIN, S. J. 1976. The radiotoxicity of iodine-125 in mammalian cells II. A comparative study on cell survival and cytogenetic responses to 125IUdR, 131TUdR, and 3HTdR. *Radiation Research,* 67, 332-43.

CHAN, P. C., LISCO, E., LISCO, H. & ADELSTEIN, S. J. 1978. Cell survival and cytogenetic responses to 125I-UdR in cultured mammalian cells. *Current Topics in Radiation Research Quarterly,* 12, 426-35.

CHANDRA, S. 2003. SIMS ion microscopy as a novel, practical tool for subcellular chemical imaging in cancer research. *Applied Surface Science,* 203, 679-683.

CHARLTON DE, BOOZ J, FIODORA J, SMIT TH & LE, F. Microdosimetry of radioactive nuclei incorporated into the DNA of mammalian cells. *In: BOOZ J, EBERT & HG, eds. 6th Symposium on Microdosimetry,* 1978 Brussels, Belgium. London: Harwood Academic Publishers, 625-638.

CHÉHADÉ, F., DE LABRIOLLE-VAYLET, C., MOINS, N., MOREAU, M. F., PAPON, J., LABARRE, P., GALLE, P., VEYRE, A. & HINDIÉ, E. 2005. Secondary ion mass spectrometry as a tool for investigating radiopharmaceutical distribution at the cellular level: the example of I-BZA and (14)C-I-BZA. *Journal of Nuclear Medicine,* 46, 1701-6.

CHÉHADÉ, F., MAURIZIS, J. C., PUCCI, B., PAVIA, A. A., OLLIER, M., VEYRE, A., ESCAIG, F., JEANGUILLAUME, C., DENNEBOUY, R., SLODZIAN, G. & HINDIÉ, E. 1996. Subcellular distribution of a new fluorinated, biocompatible, non-ionic telomeric carrier: a study in cultured B16 melanoma and rat skin fibroblasts. *Cellular and Molecular Biology (Noisy-le-grand),* 42, 335-42.

CHITHRANI, B., GHAZANI, A. & CHAN, W. 2006. Determining the size and shape dependence of gold nanoparticle uptake into mammalian cells. *Nano Letters,* 6, 662-668.

CLERC, J., HALPERN, S., FOURRÉ, C., OMRI, F., BRIANÇON, C., JEUSSET, J. & FRAGU, P. 1993. SIMS microscopy imaging of the intratumor biodistribution of metaiodobenzylguanidine in the human SK-N-SH neuroblastoma cell line xenografted into nude mice. *Journal of Nuclear Medicine,* 34, 1565-70.

CLERC, J., MARDON, K., GALONS, H., LOC'H, C., LUMBROSO, J., MERLET, P., ZHU, J., JEUSSET, J., SYROTA, A. & FRAGU, P. 1995. Assessing intratumor distribution and uptake with MBBG versus MIBG imaging and targeting xenografted PC12-pheochromocytoma cell line. *Journal of Nuclear Medicine,* 36, 859-66.

COHEN, S. & CARPENTER, G. 1975. Human epidermal growth factor: isolation and chemical and biological properties. *Proceedings of the National Academy of Sciences of the United States of America,* 72, 1317-21.

COLE, A. 1969. Absorption of 20-eV to 50,000-eV electron beams in air and plastic. *Radiation Research,* 38, 7-33.

COOPER, G. M. 2000. *The cell: a molecular approach.* Washington, D.C.; Sunderland, Mass.: SM Press; Sinauer Associates.

CORELLI, J., STECKL, A., PULVER, D. & RANDALL, J. 1987. Ultralow dose effects in ion-beam induced grafting of polymethylmethacrylate (PMMA). *Nuclear Instruments & Methods in Physics Research Section B-Beam Interactions With Materials and Atoms,* 19-20, 1009-1012.

CORNELISSEN, B., DARBAR, S., HERNANDEZ, R., KERSEMANS, V., TULLIS, I., BARBER, P. R., SMART, S., VOJNOVIC, B., REILLY, R. & VALLIS, K. A. 2011. ErbB-2 blockade and prenyltransferase inhibition alter epidermal growth factor and epidermal growth factor receptor trafficking and enhance (111)In-DTPA-hEGF Auger electron radiation therapy. *Journal of Nuclear Medicine,* 52, 776-83.

CORNELISSEN, B., KERSEMANS, V., MCLARTY, K., TRAN, L. & REILLY, R. M. 2009. 111In-labeled immunoconjugates (ICs) bispecific for the epidermal growth factor receptor (EGFR) and cyclin-dependent kinase inhibitor, p27Kip1. *Cancer Biotherapy Radiopharmaceuticals,* 24, 163-73.

CRANE, P., LALIBERTÉ, R., HEMINWAY, S., THOOLEN, M. & ORLANDI, C. 1993. Effect of mitochondrial viability and metabolism on technetium-99m-sestamibi myocardial retention. *European Journal of Nuclear Medicine,* 20, 20-5.

DATTA, K., JARUGA, P., DIZDAROGLU, M., NEUMANN, R. D. & WINTERS, T. A. 2006. Molecular analysis of base damage clustering associated with a site-specific radiation-induced DNA double-strand break. *Radiation Research,* 166, 767-81.

DAVIS, H. H., SENIOR, R. M., GRIFFIN, G. L. & KUHN, C. 1980. 111Indium-labeled human alveolar macrophages and monocytes: function and ultrastructure. *Journal of Immunological Methods,* 36, 99-107.

DEL CAMPO, A. & ARZT, E. 2008. Fabrication approaches for generating complex micro- and nanopatterns on polymeric surfaces. *Chemical Reviews,* 108, 911-945.

DEMEKHIN, P. V., SCHEIT, S. & CEDERBAUM, L. S. 2009. Recoil by Auger electrons: Theory and application. *Journal of Chemical Physics,* 131, 164301.

DEMERS, H., POIRIER-DEMERS, N., COUTURE, A. R., JOLY, D., GUILMAIN, M., DE JONGE, N. & DROUIN, D. 2011. Three-dimensional electron microscopy simulation with the CASINO Monte Carlo software. *Scanning,* 33, 135-46.

DOMINGUES, I., RINO, J., DEMMERS, J. A., DE LANEROLLE, P. & SANTOS, S. C. 2011. VEGFR2 translocates to the nucleus to regulate its own transcription. *PLoS One,* 6, e25668.

DUBOCHET, J. & SARTORI BLANC, N. 2001. The cell in absence of aggregation artifacts. *Micron,* 32, 91-9.

DUFRÊNE, Y. F. 2002. Atomic force microscopy, a powerful tool in microbiology. *Journal of Bacteriology,* 184, 5205–5213.

ECHLIN, P. 2001. Biological X-ray Microanalysis: The past, present practices, and future prospects. *Microscopy and Microanalysis,* 7, 211-219.

ECKERMAN, K. & ENDO, A. (eds.) 2008. *Radionuclide Data And Decay Schemes.* Reston, VA: The Society of Nuclear Medicine.

ELBAST, M., WU, T. D., GUIRAUD-VITAUX, F., PETIET, A., HINDIÉ, E., CHAMPION, C., CROISY, A., GUERQUIN-KERN, J. L. & COLAS-LINHART, N. 2008. Kinetics of intracolloidal iodine within the thyroid of newborn rats. Direct imagery using secondary ion mass spectrometry. *Comptes Rendus Biologies,* 331, 13-22.

ERIKSSON, B., KLÖPPEL, G., KRENNING, E., AHLMAN, H., PLÖCKINGER, U., WIEDENMANN, B., ARNOLD, R., AUERNHAMMER, C., KÖRNER, M., RINDI, G., WILDI, S. & PARTICIPANTS, F. C. C. 2008. Consensus guidelines for the management of patients with digestive neuroendocrine tumors--well-differentiated jejunal-ileal tumor/carcinoma. *Neuroendocrinology,* 87, 8-19.

ESHLEMAN, J. S., CARLSON, B. L., MLADEK, A. C., KASTNER, B. D., SHIDE, K. L. & SARKARIA, J. N. 2002. Inhibition of the mammalian target of rapamycin sensitizes U87 xenografts to fractionated radiation therapy. *Cancer Research,* 62, 7291-7.

FALETTE, N., FRAPPART, L., LEFEBVRE, M. F. & SAEZ, S. 1989. Increased epidermal growth factor receptor level in breast cancer cells treated by 1,25-dihydroxyvitamin D3. *Molecular and Cellular Endocrinology,* 63, 189-98.

FALZONE, N., FERNÁNDEZ-VAREA, J. M., FLUX, G. & VALLIS, K. A. 2015. Monte Carlo Evaluation of Auger Electron-Emitting Theranostic Radionuclides. *Journal of Nuclear Medicine,* 56, 1441-6.

FALZONE, N., MYHRA, S., CHAKALOVA, R., HILL, M. A., THOMSON, J. & VALLIS, K. A. 2013. Characterization of single α-tracks by photoresist detection and AFM analysis-focus on biomedical science and technology. *Physics in Medicine and Biology,* 58, 7673-82.

FALZONE, N., MYHRA, S., CHAKALOVA, R., ROYLE, G., ALTEBAEUMER, T., NATHAN, R. & VALLIS, K. A. 2012. Photoresists as a high spatial resolution autoradiography substrate for quantitative mapping of intra- and sub-cellular distribution of Auger electron emitting radionuclides. *International Journal of Radiation Biology,* 88, 933-40.

FALZONE, N., NATHAN, R., MYHRA, S., CHAKALOVA, R., ALTEBAEUMER, T. & VALLIS, K. 2011. Chemically amplified photoresist for high resolution autoradiography in targeted radiotherapy. *Biomaterials,* 32, 6138-44.

FILMUS, J., TRENT, J. M., POLLAK, M. N. & BUICK, R. N. 1987. Epidermal growth factor receptor gene-amplified MDA-468 breast cancer cell line and its nonamplified variants. *Molecular and Cellular Biology,* 7, 251-7.

FIRTH, S. M. & BAXTER, R. C. 2002. Cellular actions of the insulin-like growth factor binding proteins. *Endocrine Reviews,* 23, 824-54.

FOURRÉ, C., HALPERN, S., JEUSSET, J., CLERC, J. & FRAGU, P. 1992. Significance of secondary ion mass spectrometry microscopy for technetium-99m mapping in leukocytes. *Journal of Nuclear Medicine,* 33, 2162-6.

FOURRÉ, C., PETIET, A. & COLAS-LINHART, N. 1996. Mutual contribution by "track" microradioautography method (MRA) and secondary ion mass spectrometry (SIMS) microscopy: prospects in technetium dosimetry at-the cellular level. *Cellular and Molecular Biology (Noisy-le-grand),* 42, 385-93.

FUJITA, J., OHNISHI, Y., OCHIAI, Y., NOMURA, E. & MATSUI, S. 1996. Nanometer-scale resolution of calixarene negative resist in electron beam lithography. *Journal of Vacuum Science & Technology B,* 14, 4272-4276.

FUNARO, A., HORENSTEIN, A. L., SANTORO, P., CINTI, C., GREGORINI, A. & MALAVASI, F. 2000. Monoclonal antibodies and therapy of human cancers. *Biotechnology Advances,* 18, 385-401.

GALLE, P., LEVI-SETTI, R., LAMPERTI, A., BOURAHLA, K. & ESCAIG, F. 2004. Subcellular localization of aluminum and indium in the rat kidney. *Applied Surface Science,* 231, 475-478.

GALLI MARXER, C., KRAFT, M. L., WEBER, P. K., HUTCHEON, I. D. & BOXER, S. G. 2005. Supported membrane composition analysis by secondary ion mass spectrometry with high lateral resolution. *Biophysical Journal,* 88, 2965-75.

GAO, C., LEYTON, J. V., SCHIMMER, A. D., MINDEN, M. & REILLY, R. M. 2016. Auger electron-emitting (111)In-DTPA-NLS-CSL360 radioimmunoconjugates are cytotoxic to human acute myeloid leukemia (AML) cells displaying the CD123(+)/CD131(-) phenotype of leukemia stem cells. *Applied Radiation and Isotopes,* 110, 1-7.

GARDIN, I., FARAGGI, M., LE GULUDEC, D. & BOK, B. 1999. Cell irradiation caused by diagnostic nuclear medicine procedures: dose heterogeneity and biological consequences. *European Journal of Nuclear Medicine,* 26, 1617-26.

GINJ, M., CHEN, J., WALTER, M. A., ELTSCHINGER, V., REUBI, J. C. & MAECKE, H. R. 2005. Preclinical evaluation of new and highly potent analogues of octreotide for predictive imaging and targeted radiotherapy. *Clinical Cancer Research,* 11, 1136-45.

GODDU, S. M., HOWELL, R. W. & RAO, D. V. 1994a. Cellular dosimetry: absorbed fractions for monoenergetic electron and alpha particle sources and S-values for radionuclides uniformly distributed in different cell compartments. *Journal of Nuclear Medicine,* 35, 303-16.

GODDU, S. M., HOWELL, R. W. & RAO, D. V. 1996. Calculation of equivalent dose for Auger electron emitting radionuclides distributed in human organs. *Acta Oncologica,* 35, 909-16.

GODDU, S. M., RAO, D. V. & HOWELL, R. W. 1994b. Multicellular dosimetry for micrometastases: dependence of self-dose versus cross-dose to cell nuclei on type and energy of radiation and subcellular distribution of radionuclides. *Journal of Nuclear Medicine,* 35, 521-30.

GOULD, R. M. & ARMSTRONG, R. 1989. Use of lead aspartate block staining in quantitative EM autoradiography of phospholipids: application to myelinating peripheral nerve. Journal of Histochemistry & Cytochemistry, 37, 1393-9.

GRIGORESCU, A. E. & HAGEN, C. W. 2009. Resists for sub-20-nm electron beam lithography with a focus on HSQ: state of the art. *Nanotechnology,* 20, 292001.

GUERQUIN-KERN, J. L., HILLION, F., MADELMONT, J. C., LABARRE, P., PAPON, J. & CROISY, A. 2004. Ultra-structural cell distribution of the melanoma marker iodobenzamide: improved potentiality of SIMS imaging in life sciences. *Biomedical Engineering Online,* 3, 10.

GUERQUIN-KERN, J. L., WU, T. D., QUINTANA, C. & CROISY, A. 2005. Progress in analytical imaging of the cell by dynamic secondary ion mass spectrometry (SIMS microscopy). *Biochimica et Biophysica Acta,* 1724, 228-38.

HAYAT, M. A. 2000. *Principles and techniques of electron microscopy: biological applications,* Cambridge: Cambridge University Press.

HINDIE, E., COULOMB, B., BEAUPAIN, R. & GALLE, P. 1992. Mapping the cellular distribution of labelled molecules by SIMS microscopy. *Biology of the Cell,* 74, 81-8.

HOANG, B., REILLY, R. M. & ALLEN, C. 2012. Block copolymer micelles target Auger electron radiotherapy to the nucleus of HER2-positive breast cancer cells. *Biomacromolecules,* 13, 455-65.

HOFER, K. G. 1980. Radiation biology and potential therapeutic applications of radionuclides. *Bulletin du Cancer,* 67, 343-53.

HOFER, K. G., HARRIS, C. R. & SMITH, J. M. 1975. Rdiotoxicity of intracellular 67Ga, 125I and 3H. Nuclear versus cytoplasmic radiation effects in murine L1210 leukaemia. *International journal of radiation biology and related studies in physics, chemistry, and medicine,* 28, 225-41.

HOFER, K. G. & HUGHES, W. L. 1971. Radiotoxicity of intranuclear tritium, 125 iodine and 131 iodine. *Radiation Research,* 47, 94-101.

HORCAS, I., FERNANDEZ, R., GOMEZ-RODRIGUEZ, J., COLCHERO, J., GOMEZ-HERRERO, J. & BARO, A. 2007. WSXM: A software for scanning probe microscopy and a tool for nanotechnology. *Review of Scientific Instruments,* 78, 013705.

HOWELL, R. W. 1994. The MIRD Schema: from organ to cellular dimensions. *Journal of Nuclear Medicine,* 35, 531-3.

HOWELL, R. W., NARRA, V. R., SASTRY, K. S. & RAO, D. V. 1993. On the equivalent dose for Auger electron emitters. *Radiation Research,* 134, 71-8.

HOWELL R. W., G, B. L., BOLCH, W. E. & V., R. D. 1997. *MIRD cellular S. values: Self-absorbed dose per unit cumulated activity for selected radionuclides and monoenergetic electron and alpha particle emitters incorporated into different cell comparments*, Reston, VA: The Society of Nuclear Medicine.

HOWELL, R. W., RAJON, D. & BOLCH, W. E. 2012. Monte Carlo simulation of irradiation and killing in three-dimensional cell populations with lognormal cellular uptake of radioactivity. *International Journal of Radiation Biology,* 88, 115-22.

HSU, S. C. & HUNG, M. C. 2007. Characterization of a novel tripartite nuclear localization sequence in the EGFR family. *Journal of Biological Chemistry,* 282, 10432-40.

HU, M., SCOLLARD, D., CHAN, C., CHEN, P., VALLIS, K. & REILLY, R. M. 2007. Effect of the EGFR density of breast cancer cells on nuclear importation, in vitro cytotoxicity, and tumor and normal-tissue uptake of [111In]DTPA-hEGF. *Nuclear Medicine and Biology,* 34, 887-96.

HUMM, J. L. 1986. Dosimetric aspects of radiolabeled antibodies for tumor therapy. *Journal of Nuclear Medicine,* 27, 1490-7.

ILFORD. 2015. *Ilford Nuclear Emulsions* [Online]. Available: http://www.agarscientific.com/media/import/Ilford-Nuclear-Emulsions-Technica-Information_v2.pdf [Accessed 05/07/2016 2016].

JANSON, E. T., WESTLIN, J. E., OHRVALL, U., OBERG, K. & LUKINIUS, A. 2000. Nuclear localization of 111In after intravenous injection of [111In-DTPA-D-Phe1]-octreotide in patients with neuroendocrine tumors. *Journal of Nuclear Medicine,* 41, 1514-8.

JIANG, H., FAVARO, E., GOULBOURNE, C. N., RAKOWSKA, P. D., HUGHES, G. M., RYADNOV, M. G., FONG, L. G., YOUNG, S. G., FERGUSON, D. J., HARRIS, A. L. & GROVENOR, C. R. 2014. Stable isotope imaging of biological samples with high resolution secondary ion mass spectrometry and complementary techniques. *Methods,* 68, 317-24.

JOHANSSON, P., FASTH, A., EK, T. & HAMMARSTEN, O. 2016. Validation of a flow cytometry-based detection of γ-H2AX, to measure DNA damage for clinical applications. *Cytometry Part B Clinical Cytometry,* 00B, 000–000.

JOHNSTRÖM, P., BIRD, J. L. & DAVENPORT, A. P. 2012. Quantitative phosphor imaging autoradiography of radioligands for positron emission tomography. *Methods in Molecular Biology,* 897, 205-20.

JONES, J. W., SCOTT, A. J., TUDOR, G., XU, P. T., JACKSON, I. L., VUJASKOVIC, Z., BOOTH, C., MACVITTIE, T. J., ERNST, R. K. & KANE, M. A. 2014. Identification and quantitation of biomarkers for radiation-induced injury via mass spectrometry. *Health Physics,* 106, 106-19.

JORISSEN, R. N., WALKER, F., POULIOT, N., GARRETT, T. P., WARD, C. W. & BURGESS, A. W. 2003. Epidermal growth factor receptor: mechanisms of activation and signalling. *Experimental Cell Research,* 284, 31-53.

JUNARSA, I., STOYKOVICH, M., NEALEY, P., MA, Y. & CERRINA, F. 2005. Hydrogen silsesquioxane as a high resolution negative-tone resist for extreme ultraviolet lithography. *Journal of Vacuum Science & Technology B,* 23, 138-143.

KASSIS, A. I. 2003. Cancer therapy with Auger electrons: are we almost there? *Journal of Nuclear Medicine* , 44, 1479-81.

KASSIS, A. I. 2004. The amazing world of auger electrons. *International Journal of Radiation Biology,* 80, 789-803.

KASSIS, A. I. 2011. Molecular and cellular radiobiological effects of Auger emitting radionuclides. *Radiation Protection Dosimetry,* 143, 241-7.

KASSIS, A. I., ADELSTEIN, S. J., HAYDOCK, C. & SASTRY, K. S. 1980. Radiotoxicity of 75Se and 35S: theory and application to a cellular model. *Radiation Research,* 84, 407-25.

KASSIS, A. I., ADELSTEIN, S. J., HAYDOCK, C. & SASTRY, K. S. 1983. Thallium-201: an experimental and a theoretical radiobiological approach to dosimetry. *Journal of Nuclear Medicine,* 24, 1164-75.

KASSIS, A. I., ADELSTEIN, S. J., HAYDOCK, C., SASTRY, K. S., MCELVANY, K. D. & WELCH, M. J. 1982. Lethality of Auger electrons from the decay of bromine-77 in the DNA of mammalian cells. *Radiation Research,* 90, 362-73.

KASSIS, A. I., FAYAD, F., KINSEY, B. M., SASTRY, K. S. & ADELSTEIN, S. J. 1989. Radiotoxicity of an 125I-labeled DNA intercalator in mammalian cells. *Radiation Research,* 118, 283-94.

KASSIS, A. I., FAYAD, F., KINSEY, B. M., SASTRY, K. S., TAUBE, R. A. & ADELSTEIN, S. J. 1987. Radiotoxicity of 125I in mammalian cells. *Radiation Research,* 111, 305-18.

KHALIL, M. M., TREMOLEDA, J. L., BAYOMY, T. B. & GSELL, W. 2011. Molecular SPECT imaging: An overview. *International Journal of Molecular Imaging,* 2011, 796025.

KOPPE, M. J., POSTEMA, E. J., AARTS, F., OYEN, W. J., BLEICHRODT, R. P. & BOERMAN, O. C. 2005. Antibody-guided radiation therapy of cancer. *Cancer Metastasis Reviews,* 24, 539-67.

LECHENE, C., HILLION, F., MCMAHON, G., BENSON, D., KLEINFELD, A. M., KAMPF, J. P., DISTEL, D., LUYTEN, Y., BONVENTRE, J., HENTSCHEL, D., PARK, K. M., ITO, S., SCHWARTZ, M., BENICHOU, G. & SLODZIAN, G. 2006. High-resolution quantitative imaging of mammalian and bacterial cells using stable isotope mass spectrometry. *Journal of Biological Chemistry,* 5, 20.

LEE, E., RAO, G. & MANSUR, L. 1999. LET effect on cross-linking and scission mechanisms of PMMA during irradiation. *Radiation Physics and Chemistry,* 55, 293-305.

LEE, R. M., MCKENZIE, R., KOBAYASHI, K., GARFIELD, R. E., FORREST, J. B. & DANIEL, E. E. 1982. Effects of glutaraldehyde fixative osmolarities on smooth muscle cell volume, and osmotic reactivity of the cells after fixation. *Journal of Microscopy,* 125, 77-88.

LESLIE, C. C., MCCORMICK-SHANNON, K., ROBINSON, P. C. & MASON, R. J. 1985. Stimulation of DNA synthesis in cultured rat alveolar type II cells. *Experimental Lung Research,* 8, 53-66.

LEYTON, J. V., HU, M., GAO, C., TURNER, P. V., DICK, J. E., MINDEN, M. & REILLY, R. M. 2011. Auger electron radioimmunotherapeutic agent specific for the CD123+/CD131- phenotype of the leukemia stem cell population. *Journal of Nuclear Medicine,* 52, 1465-73.

LIN, S. Y., MAKINO, K., XIA, W., MATIN, A., WEN, Y., KWONG, K. Y., BOURGUIGNON, L. & HUNG, M. C. 2001. Nuclear localization of EGF receptor and its potential new role as a transcription factor. *Nature Cell Biology,* 3, 802-8.

ŁUKASZ MIELAŃCZYK, NATALIA MATYSIAK, KLYMENKO, O. & WOJNICZ, R. 2015. Transmission electron microscopy of biological samples. *In:* MAAZ, K. (ed.) *The transmission electron microscope - theory and applications.* 1 ed.: InTech.

LUNDBERG, C., FIELD, P. M., AJAYI, Y. O., RAISMAN, G. & BJÖRKLUND, A. 1996. Conditionally immortalized neural progenitor cell lines integrate and differentiate after grafting to the adult rat striatum. A combined autoradiographic and electron microscopic study. *Brain Research,* 737, 295-300.

MACAPINLAC, H. A., KEMENY, N., DAGHIGHIAN, F., FINN, R., ZHANG, J., HUMM, J., SQUIRE, O. & LARSON, S. M. 1996. Pilot clinical trial of 5-[125I]iodo-2'-deoxyuridine in the treatment of colorectal cancer metastatic to the liver. *Journal of Nuclear Medicine,* 37, 25S-29S.

MACPHAIL, S. H., BANÁTH, J. P., YU, T. Y., CHU, E. H., LAMBUR, H. & OLIVE, P. L. 2003. Expression of phosphorylated histone H2AX in cultured cell lines following exposure to X-rays. *International Journal of Radiation Biology,* 79, 351-8.

MAEDA, H., WU, J., SAWA, T., MATSUMURA, Y. & HORI, K. 2000. Tumor vascular permeability and the EPR effect in macromolecular therapeutics: a review. *Journal of Controlled Release,* 65, 271-84.

MAGHRAOUI, S., AYADI, A., BEN AMMAR, A., JAAFOURA, M. H., EL HILI, A., GALLE, P. & TEKAYA, L. 2011. Microscopy and microanalysis study of the indium (In) behavior in the intestinal mucosa, the liver, the kidney and the testicle. *Journal of Electron Microscopy (Tokyo),* 60, 183-90.

MAH, L. J., ORLOWSKI, C., VERVERIS, K., VASIREDDY, R. S., EL-OSTA, A. & KARAGIANNIS, T. C. 2011. Evaluation of the efficacy of radiation-modifying compounds using γH2AX as a molecular marker of DNA double-strand breaks. *Genome Integrity,* 2, 3.

MAIRS, R. J., ANGERSON, W., GAZE, M. N., MURRAY, T., BABICH, J. W., REID, R. & MCSHARRY, C. 1991. The distribution of alternative agents for targeted radiotherapy within human neuroblastoma spheroids. *British Journal of Cancer,* 63, 404-9.

MAIRS, R. J., FULLERTON, N. E., ZALUTSKY, M. R. & BOYD, M. 2007. Targeted radiotherapy: microgray doses and the bystander effect. *Dose Response,* 5, 204-13.

MARC, R. E. & LIU, W. L. 1984. Horizontal cell synapses onto glycine-accumulating interplexiform cells. *Nature,* 312, 266-9.

MARIANI, G., DI SACCO, S., VOLTERRANI, D., DI LUCA, L., BURALLI, S., DI STEFANO, R., BARANOWSKA-KORTYLEWICZ, J., BONORA, D., MATTEUCCI, F., RICCI, S., BELLINA, C. R., FALCONE, A., SALVADORI, P. A., MOSCA, F., ADELSTEIN, S. J. & KASSIS, A. I. 1996. Tumor targeting by intra-arterial infusion of 5-[123I]iodo-2'-deoxyuridine in patients with liver metastases from colorectal cancer. *Journal of Nuclear Medicine,* 37, 22S-25S.

MARTIN, R. F. & HASELTINE, W. A. 1981. Range of radiochemical damage to DNA with decay of iodine-125. *Science,* 213, 896-8.

MASSOVER, W. H. 2011. New and unconventional approaches for advancing resolution in biological transmission electron microscopy by improving macromolecular specimen preparation and preservation. *Micron,* 42, 141-51.
MAUCKSCH, U., RUNGE, R., WUNDERLICH, G., FREUDENBERG, R., NAUMANN, A. & KOTZERKE, J. 2016. Comparison of the radiotoxicity of the (99m)Tc-labeled compounds (99m)Tc-pertechnetate, (99m)Tc-HMPAO and (99m)Tc-MIBI. *International Journal of Radiation Biology*, 92, 698-706.
MCGOWAN, D. R. & GUY, M. J. 2015. Time to demand dosimetry for molecular radiotherapy? *British Journal of Radiology,* 88, 20140720.
MCGRAW-HILL 2005. *McGraw-Hill concise encyclopedia of physics.* New York, NY, McGraw-Hill.
MICHEL, R. B., BRECHBIEL, M. W. & MATTES, M. J. 2003. A comparison of 4 radionuclides conjugated to antibodies for single-cell kill. *Journal of Nuclear Medicine,* 44, 632-40.
MICROCHEM. 2001. *NANO™ PMMA and Copolymer* [Online]. Available: http://microchem.com/pdf/PMMA_Data_Sheet.pdf [Accessed 20 June 2016].
MIYAZAKI, N. & SHINOHARA, K. 1993. Cell killing induced by decay of 125I during the cell cycle: comparison of 125I-antipyrine with 125I-bovine serum albumin. *Radiation Research,* 133, 182-6.
MOHAN, R., BAREST, G., BREWSTER, L. J., CHUI, C. S., KUTCHER, G. J., LAUGHLIN, J. S. & FUKS, Z. 1988. A comprehensive three-dimensional radiation treatment planning system. *International Journal of Radiation Oncology • Biology • Physics,* 15, 481-95.
MONROE, E. B., JURCHEN, J. C., LEE, J., RUBAKHIN, S. S. & SWEEDLER, J. V. 2005. Vitamin E imaging and localization in the neuronal membrane. *Journal of the American Chemical Society,* 127, 12152-3.
MOSES, W. W. 2011. Fundamental Limits of Spatial Resolution in PET. *Nuclear Instruments and Methods in Physics Research Section A,* 648 Supplement 1, S236-S240.
MURPHY, J. E., NUGENT, S., SEYMOUR, C. & MOTHERSILL, C. 2005. Mitochondrial DNA point mutations and a novel deletion induced by direct low-LET radiation and by medium from irradiated cells. *Mutation Research,* 585, 127-36.
MUSAT, N., HALM, H., WINTERHOLLER, B., HOPPE, P., PEDUZZI, S., HILLION, F., HORREARD, F., AMANN, R., JØRGENSEN, B. B. & KUYPERS, M. M. 2008. A single-cell view on the ecophysiology of anaerobic phototrophic bacteria. *Proceedings of the National Academy of Sciences of the United States of America,* 105, 17861-6.
MYHRA, S., FALZONE, N. & CHAKALOVA, R. 2014. Alpha and recoil track detection in poly(methyl methacrylate) (PMMA)--towards a method for in vitro assessment of radiopharmaceuticals internalized in cancer cells. *Review of Scientific Instruments,* 85, 034302.
NAGATA, T. 1998. Techniques of radioautography for medical and biological research. *Brazilian Journal of Medical and Biological Research,* 31, 185-95.
NESHASTEH-RIZ, A., ANGERSON, W. J., REEVES, J. R., SMITH, G., RAMPLING, R. & MAIRS, R. J. 1997. Incorporation of iododeoxyuridine in multicellular glioma spheroids: implications for DNA-targeted radiotherapy using Auger electron emitters. *British Journal of Cancer,* 75, 493-9.
NESHASTEH-RIZ, A., MAIRS, R. J., ANGERSON, W. J., STANTON, P. D., REEVES, J. R., RAMPLING, R., OWENS, J. & WHELDON, T. E. 1998. Differential cytotoxicity of [123I]IUdR, [125I]IUdR and [131I]IUdR to human glioma cells in monolayer or spheroid culture: effect of proliferative heterogeneity and radiation cross-fire. *British Journal of Cancer,* 77, 385-90.
NETTLETON, J. S. & LAWSON, R. S. 1996. Cellular dosimetry of diagnostic radionuclides for spherical and ellipsoidal geometry. *Physics in Medicine and Biology,* 41, 1845-54.

NIELSEN, J. L. & NIELSEN, P. H. 2005. Advances in microscopy: microautoradiography of single cells. *Methods in Enzymology,* 397, 237-56.
NIKJOO, H., O'NEILL, P., TERRISSOL, M. & GOODHEAD, D. T. 1999. Quantitative modelling of DNA damage using Monte Carlo track structure method. *Radiation and Environmental Biophysics,* 38, 31-8.
NILSSON, S., FRANZÉN, L., PARKER, C., TYRRELL, C., BLOM, R., TENNVALL, J., LENNERNÄS, B., PETERSSON, U., JOHANNESSEN, D. C., SOKAL, M., PIGOTT, K., YACHNIN, J., GARKAVIJ, M., STRANG, P., HARMENBERG, J., BOLSTAD, B. & BRULAND, O. S. 2007. Bone-targeted radium-223 in symptomatic, hormone-refractory prostate cancer: a randomised, multicentre, placebo-controlled phase II study. *Lancet Oncology,* 8, 587-94.
O'DONOGHUE, J. A. 1999. Implications of nonuniform tumor doses for radioimmunotherapy. *Journal of Nuclear Medicine,* 40, 1337-41.
O'DONOGHUE, J. A. & WHELDON, T. E. 1996. Targeted radiotherapy using Auger electron emitters. *Physics in Medicine and Biology,* 41, 1973-92.
OLIVE, P. L. & BANÁTH, J. P. 2004. Phosphorylation of histone H2AX as a measure of radiosensitivity. *International Journal of Radiation Oncology • Biology • Physics,* 58, 331-5.
OSTROWSKI, S. G., KURCZY, M. E., RODDY, T. P., WINOGRAD, N. & EWING, A. G. 2007. Secondary ion MS imaging to relatively quantify cholesterol in the membranes of individual cells from differentially treated populations. *Analytical Chemistry,* 79, 3554-60.
OSTROWSKI, S. G., VAN BELL, C. T., WINOGRAD, N. & EWING, A. G. 2004. Mass spectrometric imaging of highly curved membranes during Tetrahymena mating. *Science,* 305, 71-3.
PANYUTIN, I. G. & NEUMANN, R. D. 1994. Sequence-specific DNA double-strand breaks induced by triplex forming 125I labeled oligonucleotides. *Nucleic Acids Research,* 22, 4979-82.
PANYUTIN, I. V., SEDELNIKOVA, O. A., BONNER, W. M., PANYUTIN, I. G. & NEUMANN, R. D. 2005. DNA damage produced by 125I-triplex-forming oligonucleotides as a measure of their successful delivery into cell nuclei. *Annals of the New York Academy of Sciences,* 1058, 140-50.
PAVEL, M., BAUDIN, E., COUVELARD, A., KRENNING, E., ÖBERG, K., STEINMÜLLER, T., ANLAUF, M., WIEDENMANN, B., SALAZAR, R. & PARTICIPANTS, B. C. C. 2012. ENETS Consensus Guidelines for the management of patients with liver and other distant metastases from neuroendocrine neoplasms of foregut, midgut, hindgut, and unknown primary. *Neuroendocrinology,* 95, 157-76.
PETERANDERL, R. & LECHENE, C. 2004. Measure of carbon and nitrogen stable isotope ratios in cultured cells. *Journal of the American Society for Mass Spectrometry,* 15, 478-85.
PHILLIPS, T. M., MCBRIDE, W. H. & PAJONK, F. 2006. The response of CD24(-/low)/CD44+ breast cancer-initiating cells to radiation. *Journal of the National Cancer Institute,* 98, 1777-85.
PIWNICA-WORMS, D. P., KRONAUGE, J. F., LEFURGEY, A., BACKUS, M., HOCKETT, D., INGRAM, P., LIEBERMAN, M., HOLMAN, B. L., JONES, A. G. & DAVISON, A. 1994. Mitochondrial localization and characterization of 99Tc-SESTAMIBI in heart cells by electron probe X-ray microanalysis and 99Tc-NMR spectroscopy. *Magnetic Resonance Imaging,* 12, 641-52.
PORTEOUS, D. D. 1971. The toxicity of 125 IUdR in cultured mouse BP8 tumour cells. *British Journal of Cancer,* 25, 594-7.POUGET, J. P., LOZZA, C., DESHAYES, E., BOUDOUSQ, V. & NAVARRO-TEULON, I. 2015. Introduction to radiobiology of targeted radionuclide therapy. *Frontiers in Medicine (Lausanne),* 2, 12.

POUGET, J. P., NAVARRO-TEULON, I., BARDIÈS, M., CHOUIN, N., CARTRON, G., PÈLEGRIN, A. & AZRIA, D. 2011. Clinical radioimmunotherapy--the role of radiobiology. *Nature Reviews Clinical Oncology,* 8, 720-34.

POUGET, J. P., SANTORO, L., RAYMOND, L., CHOUIN, N., BARDIÈS, M., BASCOUL-MOLLEVI, C., HUGUET, H., AZRIA, D., KOTZKI, P. O., PÈLEGRIN, M., VIVÈS, E. & PÈLEGRIN, A. 2008. Cell membrane is a more sensitive target than cytoplasm to dense ionization produced by auger electrons. *Radiatation Research*, 170, 192-200.

PUNCHER, M. R. & BLOWER, P. J. 1994. Radionuclide targeting and dosimetry at the microscopic level: the role of microautoradiography. *European Journal of Nuclear Medicine,* 21, 1347-65.

PUNCHER, M. R. & BLOWER, P. J. 1995. Frozen section microautoradiography in the study of radionuclide targeting: application to indium-111-oxine-labeled leukocytes. *Journal of Nuclear Medicine,* 36, 499-505.

PUTTARAKSA, N., UNAI, S., RHODES, M., SINGKARAT, K., WHITLOW, H. & SINGKARAT, S. 2012. Fabrication of a negative PMMA master mold for soft-lithography by MeV ion beam lithography. *Nuclear Instruments & Methods in Physics Research Section B-Beam Interactions with Materials and Atoms,* 272, 149-152.

QVARNSTRÖM, O. F., SIMONSSON, M., JOHANSSON, K. A., NYMAN, J. & TURESSON, I. 2004. DNA double strand break quantification in skin biopsies. *Radiotherapy & Oncology,* 72, 311-7.

RADFORD, I. R., HODGSON, G. S. & MATTHEWS, J. P. 1988. Critical DNA target size model of ionizing radiation-induced mammalian cell death. *International Journal of Radiation Biology,* 54, 63-79.

RAJON, D., BOLCH, W. E. & HOWELL, R. W. 2011. Lognormal distribution of cellular uptake of radioactivity: Monte Carlo simulation of irradiation and cell killing in 3-dimensional populations in carbon scaffolds. *Journal of Nuclear Medicine,* 52, 926-933.

RAMCHARAN, E. J. & MATTHEWS, M. R. 1996. Autoradiographic localization of functional muscarinic receptors in the rat superior cervical sympathetic ganglion reveals an extensive distribution over non-synaptic surfaces of neuronal somata, dendrites and nerve endings. *Neuroscience,* 71, 797-832.

RANA, S., KUMAR, R., SULTANA, S. & SHARMA, R. K. 2010. Radiation-induced biomarkers for the detection and assessment of absorbed radiation doses. *Journal of Pharmacy And Bioallied Sciences,* 2, 189-96.

RAO, D. V., NARRA, V. R., HOWELL, R. W. & SASTRY, K. S. 1990. Biological consequence of nuclear versus cytoplasmic decays of 125I: cysteamine as a radioprotector against Auger cascades in vivo. *Radiation Research,* 124, 188-93.

REDON, C. E., NAKAMURA, A. J., GOULIAEVA, K., RAHMAN, A., BLAKELY, W. F. & BONNER, W. M. 2010. The use of gamma-H2AX as a biodosimeter for total-body radiation exposure in non-human primates. *PLoS One,* 5, e15544.

REFT, C., ALECU, R., DAS, I. J., GERBI, B. J., KEALL, P., LIEF, E., MIJNHEER, B. J., PAPANIKOLAOU, N., SIBATA, C., VAN DYK, J. & 63, A. R. T. C. T. G. 2003. Dosimetric considerations for patients with HIP prostheses undergoing pelvic irradiation. Report of the AAPM Radiation Therapy Committee Task Group 63. *Medical Physics,* 30, 1162-82.

REICHMANIS, E. & THOMPSON, L. F. 1989. Polymer materials for microlithography. *Chemical Reviews,* 89, 1273-1289.

REILLY, R. M., CHEN, P., WANG, J., SCOLLARD, D., CAMERON, R. & VALLIS, K. A. 2006. Preclinical pharmacokinetic, biodistribution, toxicology, and dosimetry studies of 111In-DTPA-human epidermal growth factor: an auger electron-emitting radiotherapeutic agent for epidermal growth factor receptor-positive breast cancer. *Journal of Nuclear Medicine,* 47, 1023-31.

REILLY, R. M., KIARASH, R., CAMERON, R. G., PORLIER, N., SANDHU, J., HILL, R. P., VALLIS, K., HENDLER, A. & GARIEPY, J. 2000a. 111In-labeled EGF is selectively radiotoxic to human breast cancer cells overexpressing EGFR. *Journal of Nuclear Medicine,* 41, 429-38.

REILLY, R. M., KIARASH, R., SANDHU, J., LEE, Y. W., CAMERON, R. G., HENDLER, A., VALLIS, K. & GARIEPY, J. 2000b. A comparison of EGF and MAb 528 labeled with 111In for imaging human breast cancer. *Journal of Nuclear Medicine,* 41, 903-11.

REILLY, R. M., SCOLLARD, D. A., WANG, J., MONDAL, H., CHEN, P., HENDERSON, L. A., BOWEN, B. M. & VALLIS, K. A. 2004. A kit formulated under good manufacturing practices for labeling human epidermal growth factor with 111In for radiotherapeutic applications. *Journal of Nuclear Medicine,* 45, 701-8.

ROESKE, J. C., AYDOGAN, B., BARDIES, M. & HUMM, J. L. 2008. Small-scale dosimetry: challenges and future directions. *Seminars in Nuclear Medicine,* 38, 367-83.

ROGAKOU, E. P., BOON, C., REDON, C. & BONNER, W. M. 1999. Megabase chromatin domains involved in DNA double-strand breaks in vivo. *Journal of Cell Biology,* 146, 905-16.

ROGAKOU, E. P., PILCH, D. R., ORR, A. H., IVANOVA, V. S. & BONNER, W. M. 1998. DNA double-stranded breaks induce histone H2AX phosphorylation on serine 139. *Journal of Biological Chemistry,* 273, 5858-68.

ROGERS, A. W. 1979. *Techniques of autoradiography.* Amsterdam; New York: Elsevier/North-Holland Biomedical Press.

ROINEL, N. 1984. Electron probe analysis of biological fluids: possibilities and limitations. *Annals of the New York Academy of Sciences,* 428, 90-100.

ROTHKAMM, K. & LÖBRICH, M. 2003. Evidence for a lack of DNA double-strand break repair in human cells exposed to very low x-ray doses. *Proceedings of the National Academy of Sciences of the United States of America,* 100, 5057-62.

ROYLE, G. 2012. *Demonstration of nano-scale 3D visualisation of dose patterns from tailored radionuclides for targeted cancer therapeutics.* Unpublished Masters of Engineering thesis, University of Oxford.

ROYLE, G., FALZONE, N., CHAKALOVA, R., VALLIS, K. & MYHRA, S. 2016. Internalization of Auger electron-emitting isotopes into cancer cells: a method for spatial distribution determination of equivalent source terms. *International Journal of Radiation Biology*, 92, 633-640. http://www.tandfonline.com/doi/full/10.1080/09553002.2016.1233369

ROYLE, G., MYHRA, S., CHAKALOVA, R., VALLIS, K. A. & FALZONE, N. 2015. Spatial distribution of Auger electrons emitted from internalised radionuclides in cancer cells: the photoresist autoradiography (PAR) method. *Radiation Protection Dosimetry*, 166, 1-4.

SAK, A., GREHL, S., ERICHSEN, P., ENGELHARD, M., GRANNASS, A., LEVEGRUN, S., POTTGEN, C., GRONEBERG, M. & STUSCHKE, M. 2007. gamma-H2AX foci formation in peripheral blood lymphocytes of tumor patients after local radiotherapy to different sites of the body: dependence on the dose-distribution, irradiated site and time from start of treatment. *International Journal of Radiation Biology,* 83, 639-52.

SAK, A. & STUSCHKE, M. 2010. Use of γH2AX and other biomarkers of double-strand breaks during radiotherapy. *Seminars in Radiation Oncology,* 20, 223-31.

SASTRY, K. S. 1992. Biological effects of the Auger emitter iodine-125: a review. Report No. 1 of AAPM Nuclear Medicine Task Group No. 6. *Medical Physics,* 19, 1361-70.

SAUNDERS, J. A. & CONN, E. E. 1977. Subcellular localization of the cyanogenic glucoside of sorghum by autoradiography. *Plant Physiology,* 59, 647-52.

SCOTT, B. & SCHOLLNBERGER, H. 2000. Introducing biological microdosimetry for ionising radiation. *Radiation Protection Dosimetry,* 91, 377-384.

SEAH, M. P. & DENCH, W. A. 1979. Quantitative electron spectroscopy of surfaces: A standard data base for electron inelastic mean free paths in solids. *Surface and Interface Analysis,* 1, 2-11.

SEDELNIKOVA, O. A., ROGAKOU, E. P., PANYUTIN, I. G. & BONNER, W. M. 2002. Quantitative detection of (125)IdU-induced DNA double-strand breaks with gamma-H2AX antibody. *Radiation Research,* 158, 486-92.

SGOUROS, G., ROESKE, J. C., MCDEVITT, M. R., PALM, S., ALLEN, B. J., FISHER, D. R., BRILL, A. B., SONG, H., HOWELL, R. W., AKABANI, G., BOLCH, W. E., MEREDITH, R. F., WESSELS, B. W., ZANZONICO, P. B. & COMMITTEE, S. M. 2010. MIRD Pamphlet No. 22 (abridged): radiobiology and dosimetry of alpha-particle emitters for targeted radionuclide therapy. *Journal of Nuclear Medicine,* 51, 311-28.

SHAH, K., BOGHOZIAN, R. A., KARTSONAKI, C., SHAH, K. A. & VALLIS, K. A. 2016. γH2AX expression in cytological specimens as a biomarker of response to radiotherapy in solid malignancies. *Diagnostic Cytopathology,* 44, 141-6.

SHAO, C., FOLKARD, M., MICHAEL, B. D. & PRISE, K. M. 2004. Targeted cytoplasmic irradiation induces bystander responses. *Proceedings of the National Academy of Sciences of the United States of America,* 101, 13495-500.

SHARKEY, R. M., BLUMENTHAL, R. D., BEHR, T. M., WONG, G. Y., HAYWOOD, L., FORMAN, D., GRIFFITHS, G. L. & GOLDENBERG, D. M. 1997. Selection of radioimmunoconjugates for the therapy of well-established or micrometastatic colon carcinoma. *International Journal of Cancer,* 72, 477-85.

SHUKLA, R., BANSAL, V., CHAUDHARY, M., BASU, A., BHONDE, R. R. & SASTRY, M. 2005. Biocompatibility of gold nanoparticles and their endocytotic fate inside the cellular compartment: a microscopic overview. *Langmuir,* 21, 10644-54.

SIEGEL, J. A., THOMAS, S. R., STUBBS, J. B., STABIN, M. G., HAYS, M. T., KORAL, K. F., ROBERTSON, J. S., HOWELL, R. W., WESSELS, B. W., FISHER, D. R., WEBER, D. A. & BRILL, A. B. 1999. MIRD pamphlet no. 16: Techniques for quantitative radiopharmaceutical biodistribution data acquisition and analysis for use in human radiation dose estimates. *Journal of Nuclear Medicine,* 40, 37S-61S.

SISSON, J. C., HUTCHINSON, R. J., SHAPIRO, B., ZASADNY, K. R., NORMOLLE, D., WIELAND, D. M., WAHL, R. L., SINGER, D. A., MALLETTE, S. A. & MUDGETT, E. E. 1990. Iodine-125-MIBG to treat neuroblastoma: preliminary report. *Journal of Nuclear Medicine* 31, 1479-85.

SOLAK, H. H., EKINCI, Y., KASER, P. & PARK, S. 2007. Photon-beam lithography reaches 12.5 nm half-pitch resolution. *Journal of Vacuum Science & Technology B,* 25, 91-95.

SOMOGYI, P. & CHUBB, I. W. 1976. The recovery of acetylcholinesterase activity in the superior cervical ganglion of the rat following its inhibition by diisopropylphosphorofluoridate: a biochemical and cytochemical study. *Neuroscience,* 1, 413-21.

SONG, L., FALZONE, N. & VALLIS, K. A. 2016. EGF-coated gold nanoparticles provide an efficient nano-scale delivery system for the molecular radiotherapy of EGFR-positive cancer. *International Journal of Radiation Biology,* 1-8.

SORKIN, A. & GOH, L. K. 2008. Endocytosis and intracellular trafficking of ErbBs. *Experimental Cell Research,* 314, 3093-106.

SPEER, T. W. 2011. *Targeted radionuclide therapy.* Philadelphia, Pa.; London: Lippincott Williams & Wilkins.

TASK GROUP ON RADIATION QUALITY EFFECTS IN RADIOLOGICAL PROTECTION, C. O. R. E., INTERNATIONAL COMMISSION ON RADIOLOGICAL PROTECTION. 2003. Relative biological effectiveness (RBE), quality factor (Q), and radiation weighting factor (w(R)). A report of the International Commission on Radiological Protection. *Annals of the ICRP,* 33, 1-117.

TEPMONGKOL, S. & HEYMAN, S. 1999. 131I MIBG therapy in neuroblastoma: mechanisms, rationale, and current status. *Medical and Pediatric Oncology,* 32, 427-31; discussion 432.

TOVEY, D. G. & KENDALL, P. A. 1979. Ultrastructural autoradiography of 0.5 micron sections of tritium-labelled specimens using scanning transmission electron microscopy (STEM). *Experimental Cell Research,* 118, 401-4.

URBAN, K. W. 2009. Is science prepared for atomic-resolution electron microscopy? *Nature Materials,* 8, 260-2.

VAIDYANATHAN, G. & ZALUTSKY, M. R. 2011. Applications of 211At and 223Ra in targeted alpha-particle radiotherapy. *Current Radiopharmaceuticals,* 4, 283-94.

VALKEMA, R., DE JONG, M., BAKKER, W. H., BREEMAN, W. A., KOOIJ, P. P., LUGTENBURG, P. J., DE JONG, F. H., CHRISTIANSEN, A., KAM, B. L., DE HERDER, W. W., STRIDSBERG, M., LINDEMANS, J., ENSING, G. & KRENNING, E. P. 2002. Phase I study of peptide receptor radionuclide therapy with [In-DTPA]octreotide: the Rotterdam experience. *Seminars in Nuclear Medicine,* 32, 110-22.

VALLIS, K. A., REILLY, R. M., SCOLLARD, D., MERANTE, P., BRADE, A., VELAUTHAPILLAI, S., CALDWELL, C., CHAN, I., FREEMAN, M., LOCKWOOD, G., MILLER, N. A., CORNELISSEN, B., PETRONIS, J. & SABATE, K. 2014. Phase I trial to evaluate the tumor and normal tissue uptake, radiation dosimetry and safety of (111)In-DTPA-human epidermal growth factor in patients with metastatic EGFR-positive breast cancer. *American Journal of Nuclear Medicine and Molecular Imaging,* 4, 181-92.

VENSELAAR, J., WELLEWEERD, H. & MIJNHEER, B. 2001. Tolerances for the accuracy of photon beam dose calculations of treatment planning systems. *Radiotherapy & Oncology,* 60, 191-201.

WADAS, T. J., PANDYA, D. N., SOLINGAPURAM SAI, K. K. & MINTZ, A. 2014. Molecular targeted α-particle therapy for oncologic applications. *American Journal of Roentgenol,* 203, 253-60.

WALICKA, M. A., ADELSTEIN, S. J. & KASSIS, A. I. 1998. Indirect mechanisms contribute to biological effects produced by decay of DNA-incorporated iodine-125 in mammalian cells in vitro: clonogenic survival. *Radiation Research,* 149, 142-6.

WALICKA, M. A., ADELSTEIN, S. J. & KASSIS, A. I. 2001. Chemical modification of 5-[125I]iodo-2'-deoxyuridine toxicity in mammalian cells in vitro. *International Journal of Radiation Biology,* 77, 625-30.

WALICKA, M. A., DING, Y., ADELSTEIN, S. J. & KASSISS, A. I. 2000. Toxicity of DNA-incorporated iodine-125: quantifying the direct and indirect effects. *Radiation Research,* 154, 326-30.

WALICKA, M. A., DING, Y., ROY, A. M., HARAPANHALLI, R. S., ADELSTEIN, S. J. & KASSIS, A. I. 1999. Cytotoxicity of [125I]iodoHoechst 33342: contribution of scavengeable effects. *International Journal of Radiation Biology,* 75, 1579-87.

WANG, M., CARUANO, A. L., LEWIS, M. R., MEYER, L. A., VANDERWAAL, R. P. & ANDERSON, C. J. 2003. Subcellular localization of radiolabeled somatostatin analogues: implications for targeted radiotherapy of cancer. *Cancer Research,* 63, 6864-9.

WANG, S. C. & HUNG, M. C. 2009. Nuclear translocation of the epidermal growth factor receptor family membrane tyrosine kinase receptors. *Clinical Cancer Research,* 15, 6484-9.

WANG, Y. N. & HUNG, M. C. 2012. Nuclear functions and subcellular trafficking mechanisms of the epidermal growth factor receptor family. *Cell & Bioscience,* 2, 13.

WARTERS, R. L. & HOFER, K. G. 1977. Radionuclide toxicity in cultured mammalian cells. Elucidation of the primary site for radiation-induced division delay. *Radiation Research,* 69, 348-58.

WEBER, W., WEBER, J. & SENEKOWITSCH-SCHMIDTKE, R. 1996. Therapeutic effect of m-[131I]- and m-[125I]iodobenzylguanidine on neuroblastoma multicellular tumor spheroids of different sizes. *Cancer Research,* 56, 5428-34.

WILEY, H. S. 2003. Trafficking of the ErbB receptors and its influence on signaling. *Experimental Cell Research,* 284, 78-88.

WOO, D. V., LI, D., MATTIS, J. A. & STEPLEWSKI, Z. 1989. Selective chromosomal damage and cytotoxicity of 125I-labeled monoclonal antibody 17-1a in human cancer cells. *Cancer Research,* 49, 2952-8.

WOODWARD, W. A. & BRISTOW, R. G. 2009. Radiosensitivity of cancer-initiating cells and normal stem cells (or what the Heisenberg uncertainly principle has to do with biology). *Seminars in Radiation Oncology,* 19, 87-95.

XUE, L. Y., BUTLER, N. J., MAKRIGIORGOS, G. M., ADELSTEIN, S. J. & KASSIS, A. I. 2002. Bystander effect produced by radiolabeled tumor cells in vivo. *Proceedings of the National Academy of Sciences of the United States of America,* 99, 13765-70.

YASIN, S., HASKO, D. & AHMED, H. 1999. Comparison of sensitivity and exposure latitude for polymethylmethacrylate, UVIII, and calixarene using conventional dip and ultrasonically assisted development. *Journal of Vacuum Science & Technology B,* 17, 3390-3393.

YOSHII, Y., FURUKAWA, T., KIYONO, Y., WATANABE, R., WAKI, A., MORI, T., YOSHII, H., OH, M., ASAI, T., OKAZAWA, H., WELCH, M. J. & FUJIBAYASHI, Y. 2010. Copper-64-diacetyl-bis (N4-methylthiosemicarbazone) accumulates in rich regions of CD133+ highly tumorigenic cells in mouse colon carcinoma. *Nuclear Medicine and Biology,* 37, 395-404.

YOSHII, Y., FURUKAWA, T., MATSUMOTO, H., YOSHIMOTO, M., KIYONO, Y., ZHANG, M. R., FUJIBAYASHI, Y. & SAGA, T. 2016. (64)Cu-ATSM therapy targets regions with activated DNA repair and enrichment of CD133(+) cells in an HT-29 tumor model: Sensitization with a nucleic acid antimetabolite. *Cancer Letters*, 376, 74-82.

ZANZONICO, P. 2011. Cell-level dosimetry and biologic response modeling of heterogeneously distributed radionuclides: a step forward. *Journal of Nuclear Medicine,* 52, 845-7.

ZANZONICO, P. B. 2000. Internal radionuclide radiation dosimetry: a review of basic concepts and recent developments. *Journal of Nuclear Medicine,* 41, 297-308.

ZHANG, Y., MA, Y., LU, H. P., GAO, J. H., LIANG, C. S., LIU, C. Z., ZOU, J. T. & WANG, H. Q. 2008. Inhibition of human prostate cancer xenograft growth by 125I labeled triple-helix forming oligonucleotide directed against androgen receptor. *Chinese Medical Journal (English),* 121, 2284-9.

ZHOU, F. C., TAO-CHENG, J. H., SEGU, L., PATEL, T. & WANG, Y. 1998. Serotonin transporters are located on the axons beyond the synaptic junctions: anatomical and functional evidence. *Brain Research,* 805, 241-54.

ZILER, I., FROST, J., CHABASSEURMOLYNEUX, V., FORD, C. & PEPPER, M. 1996. Crosslinked PMMA as a high-resolution negative resist for electron beam lithography and applications for physics of low-dimensional structures. *Semiconductor Science and Technology,* 11, 1235-1238.

Appendix 1

Comparison of a 25 keV Electron Beam with Indium-111

The number of electrons per micrometer^2 entering the photoresist surface from a single decay of a point source of either indium-111 or 25 keV mono-energetic electrons placed at various distances above the photoresist surface in cell equivalent material were calculated by Monte Carlo simulation as described in Falzone et al (2011). For distances close to the photoresist surface, emissions from indium-111 are up to three-fold greater than that of 25 keV electrons. At the maximum height of the collapsed cell (1 μm: From Figure 4.17), the contributions from indium-111 decreased to approximately a third of that from the 25 keV electrons.

Appendix Table 1

A summary of the Monte Carlo simulation results comparing the fluence ($e^-/\mu m^2$) at various positions of point sources of either indium-111 or 25 keV monoenergetic electrons. Calculated by Dr Nadia Falzone, Department of Oncology, University of Oxford.

Distance (nm)	Indium-111 ($e^-/\mu m^2$)	25 keV ($e^-/\mu m^2$)	Ratio
1	4.16×10^5	1.52×10^5	2.75
10	1.77×10^5	1.47×10^5	1.20
20	1.57×10^5	1.44×10^5	1.09
50	1.23×10^5	1.39×10^5	0.89
100	8.24×10^4	1.33×10^5	0.62
150	5.46×10^4	1.28×10^5	0.43
200	4.01×10^4	1.25×10^5	0.32
500	2.95×10^4	1.09×10^5	0.27
1000	2.37×10^4	8.12×10^4	0.29

Appendix 2

Permission to use Figure 4.1 and Figure 4.8

RightsLink | Copyright Clearance Center

Thank You For Your Order!

Dear Miss. Georgina Royle,

Thank you for placing your order through Copyright Clearance Center's RightsLink service. Oxford University Press has partnered with RightsLink to license its content. This notice is a confirmation that your order was successful.

Your order details and publisher terms and conditions are available by clicking the link below:
http://s100.copyright.com/CustomerAdmin/PLF.jsp?ref=a3df4f26-bd02-49fc-a443-61e9802a7f03

Order Details
Licensee: Georgina Royle
License Date: Jul 19, 2016
License Number: 3912540110635
Publication: Radiation Protection Dosimetry
Title: Spatial distribution of Auger electrons emitted from internalised radionuclides in cancer cells: the photoresist autoradiography (PAR) method:
Type Of Use: Thesis/Dissertation
Total: 0.00 GBP

To access your account, please visit https://myaccount.copyright.com.

Please note: Online payments are charged immediately after order confirmation; invoices are issued daily and are payable immediately upon receipt.

To ensure that we are continuously improving our services, please take a moment to complete our customer satisfaction survey.

B.1:v4.2

+1-855-239-3415 / Tel: +1-978-646-2777
customercare@copyright.com
http://www.copyright.com

Order Completed

Thank you for your order.

This Agreement between Georgina Royle ("You") and Oxford University Press ("Oxford University Press") consists of your order details and the terms and conditions provided by Oxford University Press and Copyright Clearance Center.

License number	Reference confirmation email for license number
License date	Jul 19, 2016
Licensed Content Publisher	Oxford University Press
Licensed Content Publication	Radiation Protection Dosimetry
Licensed Content Title	Spatial distribution of Auger electrons emitted from internalised radionuclides in cancer cells: the photoresist autoradiography (PAR) method:
Licensed Content Author	G. Royle, S. Myhra, R. Chakalova, K. A. Vallis, N. Falzone
Licensed Content Date	Sep 1, 2015
Licensed Content Volume	166
Licensed Content Issue	1-4
Type of Use	Thesis/Dissertation
Requestor type	Academic/Educational institute
Format	Print and electronic
Portion	Figure/table
Number of figures/tables	2
Will you be translating?	No
Author of this OUP article	Yes
Order reference number	
Title of your thesis / dissertation	Towards Quantitative Intra-Nuclear Dose Mapping of Auger Emitting Radionuclides used for Targeted Radiotherapy
Expected completion date	Sep 2016
Estimated size(pages)	275
Requestor Location	Georgina Royle Trinity College Oxford, Oxon ox1 3bh United Kingdom Attn: Georgina Royle
Publisher Tax ID	GB125506730
Billing Type	Invoice
Billing address	Georgina Royle Trinity College Oxford, United Kingdom ox1 3bh Attn: Georgina Royle
Total	0.00 GBP

CLOSE WINDOW

Permission to use Figures 5.13, 5.14, 5.15, 5.16, Table 5.4 and Equations 5.1-5.8

From: Lee-ann.anderson@tandf.co.uk

To: Georgina.royle@trinity.ox.ac.uk

Our Ref: LA/IRAB/P9846

27 February 2017

Dear Georgina Royle

Material requested: Figures 1, 3-6, Table 1 and equations 1-8 (adapt), from Georgina Royle, Nadia Falzone, Radka Chakalova, Katherine Vallis & Sverre Myhra (2016) Internalization of Auger electron-emitting isotopes into cancer cells: a method for spatial distribution determination of equivalent source terms, International Journal of Radiation Biology, 92:11, 633-640

Thank you for your correspondence requesting permission to reproduce the above mentioned material from our Journal in your printed thesis entitled 'Towards Quantitative Intra-Nuclear Dose Mapping of Auger Emitting Radionuclides used for Targeted Radiotherapy' and to be posted in the university's repository - University of Oxford.

We will be pleased to grant permission on the sole condition that you acknowledge the original source of publication and insert a reference to the article on the Journals website: http://www.tandfonline.com

This is the authors accepted manuscript of an article published as the version of record in International Journal of Radiation Biology ©07 Sep 2016 http://www.tandfonline.com/doi/full/10.1080/09553002.2016.1233369

This permission does not cover any third party copyrighted work which may appear in the material requested.

Please note that this license does not allow you to post our content on any third party websites or repositories.

Thank you for your interest in our Journal.

Yours sincerely

Lee-Ann

Lee-Ann Anderson – Senior Permissions Executive, Journals
Routledge, Taylor & Francis Group
3 Park Square, Milton Park, Abingdon, Oxon, OX14 4RN, UK.
Tel: +44 (0)20 7017 7932
Fax:+44 (0)20 7017 6336
Web: www.tandfonline.com
e-mail: lee-ann.anderson@tandf.co.uk